Bulk acoustic wave resonators and oscillators at liquid helium temperatures

Maxim Goryachev

▶ **To cite this version:**

Maxim Goryachev. Bulk acoustic wave resonators and oscillators at liquid helium temperatures. Vibrations [physics.class-ph]. Université de Franche-Comté, 2011. English. NNT : . tel-00651960

HAL Id: tel-00651960

https://theses.hal.science/tel-00651960

Submitted on 14 Dec 2011

HAL is a multi-disciplinary open access archive for the deposit and dissemination of scientific research documents, whether they are published or not. The documents may come from teaching and research institutions in France or abroad, or from public or private research centers.

L'archive ouverte pluridisciplinaire **HAL**, est destinée au dépôt et à la diffusion de documents scientifiques de niveau recherche, publiés ou non, émanant des établissements d'enseignement et de recherche français ou étrangers, des laboratoires publics ou privés.

UNIVERSITÉ DE FRANCHE-COMTÉ

THÈSE

présentée à
L'UFR DES SCIENCES ET TECHNIQUES
DE L'UNIVERSITE DE FRANCHE-COMTE

pour obtenir le
GRADE DE DOCTEUR
DE L'UNIVERSITE DE FRANCHE-COMTE
spécialité Sciences Pour l'Ingénieur

par
Maxim Goryachev

Résonateurs à ondes acoustiques de volume et oscillateurs à température de l'hélium liquide

Thèse dirigée par Serge Galliou

soutenue le 3 novembre 2011 devant la commission d'examen :

Président :	B. DULMET	Professeur des universités, ENSMM, FEMTO-ST, dépt. Temps-Fréquence, Besançon
Rapporteurs :	M. TOBAR	Professor, ARC Laureate Fellow, Frequency Standards and Metrology Research Group Radio Frequency Division, School of Physics, The University of Western Australia
	O. LLOPIS	Directeur de recherche CNRS, Laboratoire d'Analyse et d'Architecture des Systèmes (LAAS), Toulouse
Examinateurs :	M. PRIGENT	Professeur des universités, Université de Limoges, IUT du Limousin, Département GEII, Brive, Xlim, Limoges
	R. BOURQUIN	Professeur Emérite, ENSMM, FEMTO-ST, dépt. Temps-Fréquence, Besançon
	S. GALLIOU	Professeur des universités, ENSMM, FEMTO-ST, dépt. Temps-Fréquence, Besançon

Dédicace
à mon père...
à ma mère...
et à Evelin...

Remerciements

The present work is made during my stay at the Time and Frequency Department of the FEMTO-ST Institute, Besançon, France. It was a pleasure for me to work with all the wonderful people from the department. The financial support is kindly granted by the Conseil Régional de Franche-Comté (Convention No. 2008C_16215) and managed by the University of Franche-Comté.

First and foremost, I would like to thank Serge GALLIOU, professor in the ENSMM, for the invitation to do this research, for enormous help in scientific work, for giving me the chance to visit several interesting conferences, and for the kind help in all aspects of my stay in France. He spend a lot of time helping me with the work and papers. Without him, his curious spirit of research and genial attitude, this work would be impossible. I learned a lot during my work with this man and I am convinced that this knowledge will help me in my future work. I am happy to have such a great supervisor. His impact into this work could not be overrated.

I am very grateful to Sergey TARARYKINE, professor, the head of the Ivanovo State Power Engineering University, for choosing me for this opportunity and his help in many administrative things in Russia. Also, I am thankful to Vadim KOMINE, researcher in the Ivanovo State Power Engineering University, for his help, discussions and assistance.

I would like to thank Philippe ABBE, assistant engineer in the ENSMM, for his everyday willingness to help with electronics stuff. His know-how in electronics and equipment helped me during all my work. I appreciate his invaluable help with cryogenerator and all other equipment.

Also, I want to express my thanks to Joël IMBAUD, maître de conférences in the ENSMM, for his explanations in cryogenic experiments and equipment and valuable help with a cryogenic oscillator development. He imparted his knowledge and experience to me.

I was happy to work along with Roger BOURQUIN, professor in the ENSMM. I appreciate his sincere interest in the present research, for valuable help and explanations in many aspects of resonator operation and construction, his irreplaceable expertise in the field. As well, I would like to thank Jean-Pierre ROMAND, assistant engineer in the ENSMM, and Xavier VACHERET, engineer in the ENSMM, for their help in production of "big" resonators.

My thanks go to Kirill VOLYANSKIY, researcher in the Saint Petersburg State University of Aerospace Instrumentation, for scientific discussions, as well as, for introduction into student's life in Besançon.

Special thanks to Bernard DULMET, professor in the ENSMM, head of the department, for the hospitable reception, huge help with many administrative questions, as well

as valuable scientific discussions. I also express my thanks to Fabienne CORNU and Sarah DJAOUTI for their help in many aspects of my work and stay in France, as well as for their everyday morning smile.

I would like to thank Marc MOUREY, research engineer, for the discussions of oscillator electronics and some valuable suggestions. Also, thanks to Pierre-Yves BOURGEOIS, CNRS researcher, Serge GROP, research engineer, and Benoît DUBOIS, research engineer, for their crucial help in vibration measurements.

I would like to say a special word of thanks to the members of the examination board: Michael TOBAR, ARC Australian Laureate Fellow, professor in Frequency Standards and Metrology Research Group, School of Physics, The University of Western Australia, Olivier LLOPIS, directeur de recherche in CNRS-LAAS, manager of the MOST group (Microondes et Opto-microondes pour Systèmes de Télécommunications), and M. PRIGENT, member of the C2S2 (Composants Circuits Signaux et Systèmes Hautes Fréquences) group in Xlim (UMR CNRS 6172), professeur in the Université de Limoges, who kindly accepted this role.

I'm also grateful to all the stuff of École Doctorale SPIM (Rachel LANGLET, Eric LANTZ) for their warm hearty welcome and organization of useful French courses.

I appreciate kindness of all the people, who gave their advises, suggests, comments, corrections, etc. My thanks to Pierre CASSARD, assistant engineer in ENSMM, Yannick GRUSON, CNRS engineer, Fabrice STHAL, professor in ENSMM, Emmanuel BIGLER, professor, Vincent GIORDANO, CNRS research head, Enrico RUBIOLA, professor, Patrice SALZENSTEIN, CNRS research engineer, Jean-Michel FRIEDT, research engineer, Rodolphe BOUDOT, CNRS researcher, Michel LENCZNER, professor, etc.

Additionally, I would like to thank my friends in the T&F Department and Besançon in general. They are Hui HUI, Raj Narayan DHARA, Bin YANG, Youssef YACOUBI, Florent BASSIGNOT, Ekaterina ERSHOVA, Dmitriy KUZIKOV, Junjie HE, Roman LAVROV, Elena TUSHKANOVA, Youssef GERGES, and many others.

I would thank each person of the ENSMM crowd, who standed the noise of the cryogenic system...

Last but not least, I wish to thank my parents Natalia and Nikolay GORYACHEV for their everyday support and their belief in me, for giving a chance of such a long study abroad. And I want to express my gratefulness and warm feelings to Evelin KARTASHOVA, one of the persons, I dedicate this work to...

Contents

List of Figures

List of Tables

Liste des abréviations

AC	Alternating Current
ADS	Advanced Design System (from Agilent)
ANN	Artificial Neural Network
BAW	Bulk Acoustic Wave
BJT	Bipolar (Junction) Transistor
BVA	Boîtier à Vieillissement Amélioré
CAD	Computer-Aided Design
DC	Direct Current
DUT	Device Under Test
EIA	Electronic Industries Alliance
HB	Harmonic Balance
HBT	Heterojunction Bipolar Transistor
HFET	Heterostructure Field Effect Transistor
HOH	Higher Order Terms
JFET	Junction gate Field-Effect Transistor
FBAR	Film Bulk Acoustic Resonator
FET	Field-Effect Transistor
FFT	Fast Fourier Transform
FLL	Frequency Locked Loop
FM	Frequency Modulation
GPIB	General Purpose Interface Bus
KLM	Krimtholz-Leedom-Matthaei (model)
LGS	Lanthanum Gallium Silicate (Langasite)
LGT	Lanthanum Gallium Tantalate (Langatate)
MELF	Metal Electrode Leadless Face
MEMS	Microelectromechanical Systems
MESFET	Metal Semiconductor Field Effect Transistor
MIMO	Multiple Input Multiple Output
MOSFET	Metal-Oxide-Semiconductor Field-Effect Transistor
NiCr	Nickel-Chromium
OCXO	Oven Controlled Crystal Oscillator
ODE	Ordinary Differential Equation
OT	Overtone
PLL	Phase Locked Loop
PM	Phase Modulation

PSD	Power Spectral Density
PTFE	Polytetrafluoroethylene
RF	Radio Frequencies
RMS	Root Mean Square
SAW	Surface Acoustic Wave
SMD	Surface-Mount Technology
TaN	Tantalum-Nitride
USO	Ultra Stable Oscillator
VCO	Voltage Controlled Oscillator

Liste des notations

a	acceleration in mechanical systems, m/s^2, or signal amplitude in electrical
$A(j\omega)$, $B(j\omega)$, $\rho(j\omega)$	transfer functions
B	susceptance, S
b_i	coefficients of the power-law approximation of $S_\phi(f)$
C	electrical capacitance, F
C_v	volumetric heat capacity, J/K
$\mathbb{E}$	mathematical expectation
f	Fourier frequency, Hz
f_c	corner frequency of the oscillator open-loop phase noise, Hz
f_L	Leeson frequency, Hz
f_r	resonance frequency, Hz
G	conductance, S
j	imaginary unit, $j = \sqrt{-1}$
s	Laplace variable
$\mathbf{k}$	wave vector
k_B	Boltzmann constant, $k_B = 1.38 \cdot 10^{-23}$ J/K
$H(s)$	transfer function
h	Planck constant
h_i	coefficients of the power-law approximation of $S_y(f)$
$\mathscr{H}(s)$	transfer function in the domain of phases and magnitudes
L	electrical inductance, H
$\mathscr{L}(f)$	single-sideband noise spectrum, dBc/Hz
M	averaged signal magnitude
m	signal magnitude
n	random noise
P	power, W
p	differentiation operator, $\frac{d}{dt}$
R	resistance, Ohm
$S_x(f)$	power spectral density of the variable x
Q	resonator quality (merit) factor
Q_L	loaded resonator quality (merit) factor
T	absolute temperature, K
t	time, sec
$\mathbb{Z}$	set of integer numbers
X	reactance, Ohm
Y	admittance, S

Z	impedans, Ohm
$\mathcal{F}(\cdot)$	Fourier transform
$\mathcal{F}^{-1}(\cdot)$	inverse Fourier transform
$\Im\{\cdot\}$	imaginary part of a complex number
$\Re\{\cdot\}$	real part of a complex number
δ	Dirac delta, oscillator damping
$\sigma_y(\tau)$	Allan deviation
τ	measurement time, sec
τ	resonator relaxation time, sec
ν_0	carrier frequency, Hz
ρ	material density, kg/m^3
γ	Grüneisen parameter
Ω	detuning angular frequency, rad/Hz
ω	angular frequency, carrier or Fourier, rad/Hz
ω_r	angular resonance frequency, rad/Hz
Φ, Θ	averaged signal phase, rad
ϕ, θ	signal phase, rad
Ψ	full signal phase, rad

Introduction

Performance of many scientific, industrial, consumer and military systems directly or indirectly depends on the performance of the utilized frequency sources. Since requirements to these systems are constantly growing, different requirements to frequency sources are also subjects of a constant growth. So, scientists and engineers are always eager to imagine new approaches and techniques which could or at least potentially could burst the performances of frequency references, i.e. to improve the frequency stability, to reduce power consumption, to reduce dimensions, etc.

Nowadays, the best short-term (typically for averaging times less than 1 minute) frequency stability performance is achieved with quartz crystal oscillators. But now it is generally believed that this family of frequency sources is almost in saturation and could not lead to considerable stability improvement with reasonable efforts in the future. So, a jump of technology is necessary. The possibility of replacement of quartz oscillators with MEMS and chip-scale atomic clocks is under discussion [5]. As for the long term stability performance, many different types of frequency sources compete. Here, atomic clocks, hydrogen masers, cryogenic sapphire systems could be found [6]. Usually, the quartz oscillator performance here is very poor and insufficient for the majority of applications. However, cryogenic[1] quartz systems (or more generally, systems based on cryogenic bulk acoustic wave devices) remain to be *a dark horse* in the race for the best stability in short, middle and moderate long terms. Indeed, up to now cryogenic quartz systems are under-investigated and their abilities and perspectives are not generally known. Majority of the works dedicated to these devices and systems are not systematic studies, and now most of them are outdated. This work is a more systematic investigation in this field and related problems, and it is supposed to shed light on this problem.

Additionally, systematic investigation of bulk acoustic wave devices (and quartz, in particular) at cryogenic temperatures can give an answer to the question about the future of this technology. Indeed, it is the order of the day to figure out if the quartz is further able to compete with emerging technologies. Furthermore, cryogenic investigation can help to deduce some new information about the devices and materials under test.

[1] Here and further, by "cryogenic" we mean liquid helium temperatures (typically 4K) if the inverse is not explicitly stated

Beyond the applications in hyper-stable frequency sources, new information on quartz devices behavior at cryogenic temperatures is useful from the point of view of many other physics experiments. Indeed, in many fields of physics scientists are looking for materials with low losses. And the quartz is a very good candidate for this role. For example, this is the case in gravitational wave experiments [7].

Speaking about cryogenic frequency sources, one has not to forget that they can require some electronic components other than crystal resonators. This fact produces the requirement for deep investigations in liquid helium electronics. Nowadays, this fields is also very under-investigated. This can be easily seen simply by comparing numbers of papers dedicated to electronics in liquid helium and liquid nitrogen. It may be concluded that the former almost does not exist. Partially this is connected with much higher difficulties associated with creation of liquid helium temperatures, as well as with much higher power consumption and equipment dimensions. This work opens the door into the world of liquid helium electronics by beginning of systematic studies in the field. The obtained results could be useful not only for applications in the time and frequency domain, but also to all other scientific and engineering applications demanding such low temperatures.

The work is organized as follows. Chapter 1 is devoted to general background in the field of time and frequency, and crystal resonators and oscillators in particular. Special attention has to be given to Chapter 2 where a new parametric model of crystal resonator and oscillator noise is proposed. The theoretical results of this chapter are used further in the work for deeper understanding of experimental results. Chapter 3 describes the cryogenic test bench which is a base for almost all experiments in this work. Sections 3.2 and 3.3 are of the special importance, because they give the analysis of the test-bench instabilities. Chapter 4 is a systematic study of many aspects of bulk acoustic wave devices at cryogenic temperatures. Components of the cryogenic electronic devices are under scope in Chapter 5. This chapter concerns both passive (section 5.1) and active (section 5.2) electronic devices. Contrary to Chapters 4 and 5 which concerns cryogenic components, next two chapters deal with cryogenic system built with these components. Thus, Chapter 6 is a study of a frequency closed loop reference system based on a crystal cryogenic resonator, i.e. a supersystem approach. The methods, adopted in this chapter, allow to measure the quartz resonator phase noise at cryogenic conditions and the derivation of its origins (see subsection 6.5.4). Next, Chapter 7 is dedicated to a cryogenic crystal oscillator design and measurements, i.e. it represents a subsystem approach. This chapter starts with the development of new approaches in very high quality factor oscillator analytical modeling (section 7.1) and numerical simulation (section 7.2). The chapter is terminated with frequency stability measurements of actual liquid helium oscillators.

Chapter 1

General Overview

1.1 Bulk Acoustic Wave Resonators

The principle of operation of all bulk acoustic wave resonators is based on the fundamental physical effect, which is called the piezoelectric effect. Piezoelectricity ('piezo', from Greek to squeeze or press) is the ability of some materials to generate an electric field or electric potential in response to an applied mechanical stress. This effect can be observed in many materials, both natural and man-made:

- natural: quartz, berlinite ($AlPO_4$), topaz, tourmaline-group minerals, cane sugar, rochelle salt, etc.
- synthetic crystals: gallium orthophosphate ($GaPO_4$), langasite ($La_3Ga_5SiO_{14}$), langatate ($La_3Ga_{5.5}Ta_{0.5}O_{14}$) etc.
- synthetic ceramics: barium titanate ($BaTiO_3$), lead titanate ($PbTiO_3$), lead zirconate titanate ($Pb[Zr_xTi_{1x}]O_3, 0 < x < 1$), potassium niobate ($KNbO_3$), lithium niobate ($LiNbO_3$), lithium tantalate ($LiTaO_3$), sodium tungstate ($Na_2WO_3$), bismuth ferrite ($BiFeO_3$) etc.
- polymers: polyvinylidene fluoride (PVDF).

Nowadays piezoelectric crystals are used in numerous ways: in high voltage and power sources, piezoelectric motors, sensors, actuators, for vibrations and noise reduction and in frequency standards. The latter systems are the subject of this work. For the time and frequency applications, the quartz is the most important amongst all piezoelectric materials. In this section main properties of quartz crystal resonators are considered.

When a crystal of quartz is properly cut and mounted, it can be made to distort in an electric field by applying a voltage to an electrode near or on the crystal. When the field is

removed, the quartz will generate an electric field as it returns to the previous geometrical shape, and this can generate a voltage. The result is that a quartz crystal behaves like a circuit composed of inductor L_x, capacitor C_x and resistor R_x, with a certain resonant frequency, which depends on the crystal geometry. Actually many resonant frequencies exist. They correspond to different modes of vibration and overtones. In addition, the electrical connection of the crystal is made by two electrodes which form a parasitic or shunt capacitance C_0 connected in parallel with the resonance branches (also called motional branches). These simple physical observations are the basis of a quartz crystal linear model also known as a Butterworth-Van-Dyke equivalent (see Fig. 1.1).

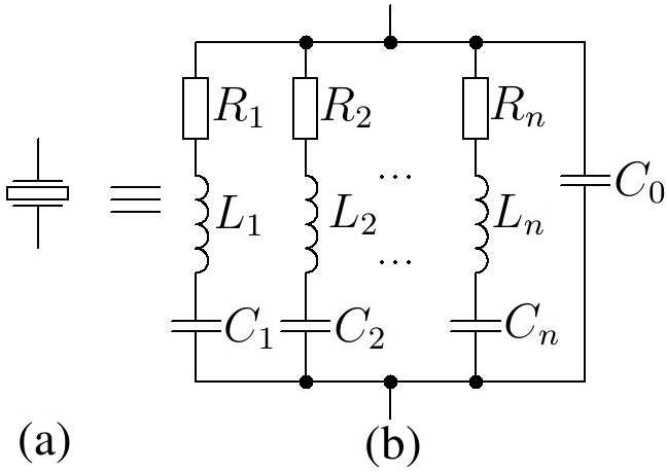

Figure 1.1: Linear model of the quartz crystal resonator

Usually in quartz crystal resonators three types of vibration exist. These types correspond to the so-called A, B and C modes of operation. Also, each mode usually may exists at several overtones: fundamental, 3rd (about 3 times the fundamental frequency), 5th, 7th, etc. In addition to this, spurious modes exist. For non-autonomous systems usually only one mode is under consideration somehow related to the input signal frequency. In the same time for autonomous application several close modes have to be considered to ensure right crystal locking.

1.1.1 Resonator Characteristics

The resonator motional (resonance) branch may be characterized by the series resonance angular frequency ω_0 and the quality factor Q:

$$\omega_0^2 = \frac{1}{L_x C_x}, \quad Q = \frac{L_x \omega_0}{R_x} = \frac{1}{R_x C_x \omega_0}. \tag{1.1}$$

where x may stand for any mode number and further is considered as the main resonator motional branch. The quality factor is inversely proportional to device losses which may

consist of material losses, mounting losses, etc. Quality factor values of room temperature BAW resonators used in ultra-stable oscillators can vary between one and two millions (for resonance frequencies of a few MegaHertz). In the same time, these values can be considerably increased by several hundred times by simply cooling the devices down to the liquid helium temperatures [8, 9, 10]. Such considerable increase inspires the researches in the field of cryogenic BAW resonators and oscillators whose performance is strongly correlated with Q values. On the other hand, physical base of the losses mechanisms as well as physical limitations of the BAW devices at very low temperature has not been analyzed or extensively studied. In addition, the comparison of resonator's different modes and overtones was made only recently [10] and has to be extended. And finally, cryogenic resonator parameters have not been discussed or analyzed from the point of view of actual applications.

Also, the resonator may be characterized by the damping δ or the relaxation time τ

$$\delta = \frac{\omega_0}{Q}, \quad \tau = \frac{Q}{\omega_0} \tag{1.2}$$

Though these parameters are not usual in the traditional design of the crystal resonator, they are widely considered in this work.

The shunt capacitance usually changes the values of the series resonance and the quality factor. The presents of C_0 may be characterized by the frequency of the parallel resonance (angular frequency: ω_{0p}) and capacitance ratio:

$$\omega_{0p}^2 = \frac{1}{L_x \frac{C_x C_0}{C_x + C_0}}, \quad \frac{C_x}{2C_0} \approx \frac{\omega_{0p} - \omega_0}{\omega_0}. \tag{1.3}$$

Up to now the linear time-invariant model of the quartz crystal is considered. In reality, equations (1.1), (1.2) and (1.3) are valid only for small values of excitation signals. In actual devices, values of the equivalent electrical parameters L_x, C_x and R_x depend on the branch current. As a result both ω_0 and Q change with the amplitude of the excitation, what is called the amplitude-frequency effect. The most common analytical model of this effect is given by the following equations [11, 12]:

$$R_x(i) = R_{x0}\big(1 + k_1 i^2\big), \quad C_x(i)^{-1} = C_{x0}^{-1}\big(1 + k_2 i^2\big). \tag{1.4}$$

where i is a current passing through the resonant branch, k_1 and k_2 are some model parameters. Usually, in actual applications BAW resonators are used in the linear regime when nonlinear terms in (1.4) could be neglected, because high driving levels are resulted in higher degradation [13] and excess phase noise [14, 15]. The usual BAW resonators at room temperature work with dissipated active power less than several hundreds of microwatts, which assures their linear behavior. The same limitations hold true for cryogenic devices. Unfortunately, no data about amplitude-frequency effect of cryogenic BAW devices is published in the literature up to now. This question is clarified in this work.

So, BAW resonator operation at liquid helium temperatures remains under-studied both from the physical point of view as well as that of possible applications.

1.1.2 Resonator Sources of Instabilities: Room and Cryogenic Temperatures

Though the resonator plate is placed in the vacuum and a special enclosure, its parameters highly depend on the environmental factors, such as temperature, pressure, vibration, stress, magnetic and electric fields, DC bias, etc [16, 15].

Temperature is one of the main destabilizing factors for the crystal resonators due to temperature dependence of the resonator parameters [15]. Generally their dependences are nonlinear and can be both positive or negative. By choosing an appropriate crystal cut and mode, one can decrease the frequency sensitivity to temperature. The frequency-temperature dependence can be analytically described in the vicinity of the temperature T_0 by a nth-order polynomial:

$$\omega_0 = \omega_{0c}\big[1 + a_0(T - T_0) + b_0(T - T_0)^2 + c_0(T - T_0)^3 + ... + k_0(T - T_0)^n\big], \qquad (1.5)$$

where ω_{0c} is an initial frequency at T_0, a_0, b_0, c_0, etc are temperature coefficients of the corresponding terms. Usually the order is limited by $n = 3$. For this case the function (1.5) has two turn-over points. Ideally the resonator should operate exactly at these points since they have zero frequency-temperature derivatives. In the actual implementations of oven controlled crystal oscillators (OCXOs) this is not possible due to technical limitations. So the crystal operates at a point close to the turn-over. Majority of the resonators are designed in such a way that they have a turn-over point above the room temperature (about $75 - 90°\mathrm{C}$). The dependence of resonance frequency on temperature has also been measured for cryogenic conditions [4, 10], though this data needs serious revision and further discussion and analysis.

Changing the temperature surrounding a crystal unit produces thermal gradients. The static frequency versus temperature characteristic is modified by the thermal-transient effect resulting from the thermal-gradient-induced stresses [17]. When an OCXO is turned on, there can be a significant thermal-transient effect. The same holds true for cryogenic use of BAW resonators. The thermal transient effects are very important for all cryogenic systems: they are clearly seen on some frequency stability measurement results. Indeed, in the case of room temperature devices the thermal transient effects have time constants of several hours. It is shown that for the cryogenic system these values can increase up to tens of hours. This effect has never been considered and studied for liquid helium devices and systems though it has a considerable influence on system performance.

The frequency versus temperature characteristics of crystal resonators do not repeat exactly upon temperature cycling, which is known as hysteresis and retrace phenomena [18]. Hysteresis is defined as the difference between the up-cycle and the down-cycle frequency-temperature characteristics, and is quantified by the value of the difference at the temperature where the difference is maximum. Hysteresis is determined during at least one complete quasi-static temperature cycle between specified temperature limits. Retrace is defined as the non-repeatability of the frequency-temperature characteristic at

a fixed temperature (which is usually the oven temperature of an OCXO) upon on-off cycling an oscillator under specified conditions.

A quartz crystal resonator subject to a steady acceleration has a slightly different series resonant frequency than the same resonator experiencing zero acceleration [19]. Furthermore, it has been observed that the magnitude of the frequency shift is proportional to the magnitude of the acceleration, and is also dependent upon the direction of the acceleration relative to a coordinate system fixed to the resonator. It has been shown, empirically, that the acceleration sensitivity of a quartz crystal resonator is a vector quantity. However, in most applications, the magnitude of the acceleration is time-dependent, so the corresponding resonance frequency is also a time-dependent quantity. This fact gives the birth to yet another source of instability, which is obviously also present in BAW devices working at cryogenic conditions. This aspect for low temperatures has never been characterized and analyzed, though appears to be critical for cryogenic frequency source performance.

The atmospheric pressure change can influence a crystal oscillator's frequency if the pressure change produces a deformation of the crystal unit's or the oscillator's enclosure (thus changing stray capacitances and stresses) [6]. The pressure change can also affect the frequency indirectly through a change in heat-transfer conditions inside the oscillator. Humidity changes can also affect the heat-transfer conditions. In addition, moisture in the atmosphere will condense on surfaces when the temperature falls below the dew point, and can permeate materials such as epoxies and polyimides, and thereby affect the properties (e.g., conductivities and dielectric constants) of the oscillator circuitry.

Gas permeation under conditions where there is an abnormally high ambient concentration of hydrogen or helium can lead to anomalous aging rates [6]. For example, hydrogen can permeate into "hermetically" sealed crystal units in metal enclosures, and helium can permeate through the walls of glass-enclosed crystal units.

Crystals undergo slow gradual change of frequency with time, known as aging [13, 20]. There are many mechanisms involved in this process. The mounting and contacts may undergo relief of the build-in stresses. Molecules of contamination either from the residual atmosphere, outgassed from the crystal, electrodes or packaging materials, or introduced during sealing the housing can be adsorbed on the crystal surface, changing its mass; this effect is exploited in quartz crystal microbalances. The composition of the crystal can be gradually altered by outgassing, diffusion of atoms of impurities or migrating from the electrodes, or the lattice can be damaged by radiation. Slow chemical reactions may occur on or in the crystal, or on the inner surfaces of the enclosure. Electrode material can react with the crystal, creating layers of metal oxide and silicon; these interface layers can undergo changes in time. Factors outside of the crystal itself are e.g. aging of the oscillator circuitry (and e.g. change of capacitances), and drift of parameters of the crystal oven. The aging of BAW devices at liquid helium temperatures has never been studied due to operational difficulties and high power consumption of cryogenic systems.

So, it is clear that even though different sources of instabilities of BAW resonators are extensively studied at room temperatures, their characteristics at very low temperatures are almost unknown or at the very beginning stage of study. These conclusions inspires new systematic research in the area of liquid-helium BAW devices and systems.

1.1.3 Resonator Cuts

The resonator plate can be cut from the source crystal in many different ways. The orientation of the cut influences the crystal's frequency, aging characteristics, quality factor, thermal characteristics, and many other parameters. The most widespread quartz crystal cuts are:

- *AT* is used for oscillators operating in wider temperature range, for the frequency range of 0.5 to 200 MHz. Sensitive to mechanical stresses, whether caused by external forces or by temperature gradients. Thickness-shear crystals typically operate in fundamental mode at $1-30$ MHz, 3rd overtone at $30-90$ MHz, and 5th overtone at $90-150$ MHz. AT-cut resonators can be manufactured either as a conventional round disk, or as a strip resonator; the latter allows much smaller size. The thickness of the quartz blank is about (1.661 mm)/(frequency in MHz), with the frequency somewhat shifted by further processing. Crystals designed for operating in overtone modes have to be specially processed for plane parallelism and surface finish for the best performance at a given overtone frequency.

- *SC* (Stress Compensated) is a special double-rotated cut for oven-stabilized oscillators with low phase noise, good aging characteristics, less sensitive to mechanical stresses. This cut has faster warm-up speed, high Q, better close-in phase noise, small sensitivity to spatial orientation against the vector of gravity, and less sensitivity to vibrations. Its frequency constant is 1.797 MHz-mm. Coupled modes are worse than the AT cut, resistance tends to be higher; much more care is required to convert between overtones. Operates at the same frequencies as the AT cut. The frequency-temperature curve is a third order downward parabola with inflection point at 95°C. Less available than AT cut, more difficult to manufacture; the order-of-magnitude parameters improvement is traded for an order of magnitude tighter crystal orientation tolerances. Aging characteristics are 2 to 3 times better than of the AT cuts. It is less sensitive to drive levels, has far fewer activity dips and several times lower motional capacitance than the corresponding AT cut. But it is sensitive to air damping, so to obtain optimum Q it has to be packaged in vacuum.

- *BT* is a special cut, similar to AT cut. It operates in thickness shear mode, in B-mode (fast quasi-shear). It has well known and repeatable characteristics. These resonators have frequency constant 2.536 MHz-mm, poorer temperature characteristics than the AT cut. Due to the higher frequency constant, can be used for crystals with higher frequencies than the AT cut.

- *AK* is a double rotated cut with better temperature-frequency characteristics than AT and BT cuts and with higher tolerance to crystallographic orientation than the AT, BT, and SC cuts (by factor 50 against a standard AT cut, according to calculations), operates in thickness-shear mode.

- *Y* is a temperature-sensitive cut, thus it can be used as a sensor. It operates at a single mode with steep frequency-temperature characteristics. The plane of the plate is perpendicular to the Y axis of the crystal. Temperature coefficient is about 90 ppm/°C.

The crystals are usually mounted in hermetically sealed glass or metal cases, filled with a dry and inert atmosphere, usually vacuum, nitrogen, or helium. Plastic housings can be used as well, but those are not hermetic and another secondary sealing has to be built around the crystal.

Several resonator configurations are possible, in addition to the classical way of directly attaching leads to the crystal. For example, the BVA resonator (Boîtier à Vieillissement Amélioré, Enclosure with Improved Aging), where the parts that influence the vibrations are machined from a single crystal (which reduces the mounting stress), and the electrodes are deposited not on the resonator itself but on inner sides of two condenser discs made of adjacent slices of the quartz from the same bar, forming a three-layer sandwich with no stress between the electrodes and the vibrating element. The gap between the electrodes and the resonator acts as two small series capacitors, making the crystal less sensitive to circuit influences. The architecture eliminates the effects of the surface contacts between the electrodes, the constraints in the mounting connections, and the issues related to ion migration from the electrodes into the lattice of the vibrating element. The resulting configuration is rugged, resistant to shock and vibration, resistant to acceleration and ionizing radiation, and has improved aging characteristics.

There is no any study which systematically compares different crystal cuts at liquid helium. Indeed, each author considers only one or two available cuts. Moreover, many of these cuts are now outdated as well as the device production technology. The present work is concentrated "good“ quality devices with the state-of-the-art cut.

1.2 Quartz Crystal Ultra-Stable Oscillators

An electronic oscillator is an autonomous electronic circuit that produces a repetitive electronic signal. There are two main types of electronic oscillator: the harmonic (or feedback) oscillator and the relaxation oscillator. Only harmonic-type oscillators are under scope of the work, since such systems show better performance. The basic form of the harmonic oscillator is an electronic amplifier $A(j\omega)$ with the output attached to an band-pass electronic filter (resonator) around a frequency ω_0 with the transfer function $\rho(j\omega)$,

and the output of the filter attached back to the input of the amplifier, in a feedback loop. When the power supply to the amplifier is first switched on, the amplifier's output consists only of noise. The noise travels around the loop, being filtered and re-amplified until it increasingly resembles the desired signal. A piezoelectric crystal (commonly quartz) resonator may take the place of the filter to stabilize the frequency of oscillation, resulting in a crystal oscillator.

Basic feedback oscillator is shown in Fig. 1.2. It consists of three parts: sustaining amplifier $A(j\omega)$, resonator $\rho(j\omega)$ and output buffer amplifier $B(j\omega)$.

Continuing discussion about harmonic oscillators, it can be said that in a steady-state regime, the sustaining amplifier A compensates losses at a given resonator frequency ω_0. Here, two conditions arise. First, for the signal to be periodic, it has to replicate itself after each loop pass. Second, the amplitude of the returned signal has to be enough to reproduce itself on another turn. This two general conditions are collectively known as Barkhausen conditions and may be mathematically written as:

$$\begin{cases} \left|A(j\omega)\rho(j\omega)\right| = 1, \\ \arg A(j\omega)\rho(j\omega) = 2\pi n, n \subset \mathbb{Z}. \end{cases} \tag{1.6}$$

Oscillation frequency is determined by the second equation of this system.

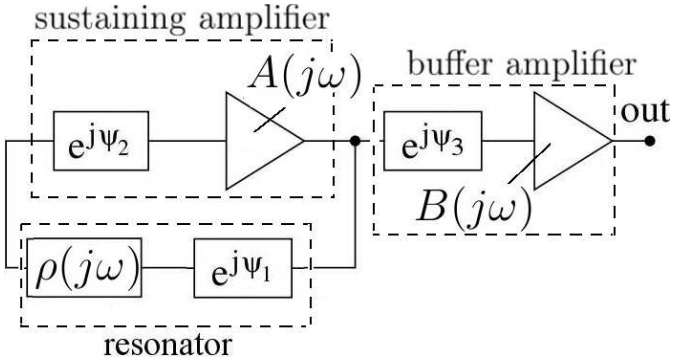

Figure 1.2: Simplified feedback oscillator: sustaining amplifier $A(j\omega)$, resonator $\rho(j\omega)$, output buffer amplifier $B(j\omega)$ with corresponding sources of instability ψ_1, ψ_2 and ψ_3

In the real world there are no ideal components. All parts of the oscillator shown in Fig. 1.2 vary or fluctuate with time. These fluctuations influence the circuit oscillation frequency. Thus, the produced frequency is not constant, it depends on some stochastic processes inside and outside the oscillating loop. This fact can be represented with sources of phase instability shown in Fig. 1.2. The frequency instability phenomenon is a subject of the next section.

Suggested linear oscillator under posed conditions 1.6 is able to oscillate infinitely in time. But, this representation leaves some questions about the oscillator start-up. As it was said above, the oscillations can be started from the residual oscillator noise or

switch-on transients. But originally only very limited energy is stored in the spectrum around an oscillation frequency ω_0. Thus, in order to amplify this region of the power spectrum, another condition is obligatory: $A(j\omega)\rho(j\omega) > 1$ for small amplitude values. This condition provides growth of the oscillation amplitude up to some value identified by some amplitude control mechanism with the condition 1.6. So, in order to make the oscillator start-up possible and to limit its amplitude the oscillator loop has to be inherently nonlinear.

The harmonic crystal oscillators may be classified according an used active element. Usually, for ultra-stable quartz resonators the active element is a bipolar transistor. The generalized scheme of one-transistor oscillator is shown in Fig. 1.3.

A basic transistor-type oscillator shown in Fig. 1.3 consists of one transistor and three impedances Z_1, Z_2 and Z_3. Each of the impedances may be of inductive or capacitive types with a phase balance condition on the π-network:

$$Z_1 + Z_2 + Z_3 = 0, \tag{1.7}$$

which has to be completed by an amplifier input-output phase relation (0 or π) in order to fulfill the Barkhausen phase condition. In the simplest case, the amplifier could be built with a single transistor.

According to the combination of capacitances and inductances one-transistor oscillators may be classified into three big groups: 1.3(b) Pierce scheme, 1.3(b) Colpitts scheme, 1.3(b) Clapp scheme. Points show corresponding connection terminals on 1.3(b). In all these schemes the resonator may be substituted by a simple inductance, since inductance mode condition (1.7) may be fulfilled only in the resonator. Depending on the zero or π phase shift between two nodes of the passive π-network, the transistor works in a common-base (zero phase shift), common-collector (zero-phase shift) or common-emitter (π phase shift) configurations.

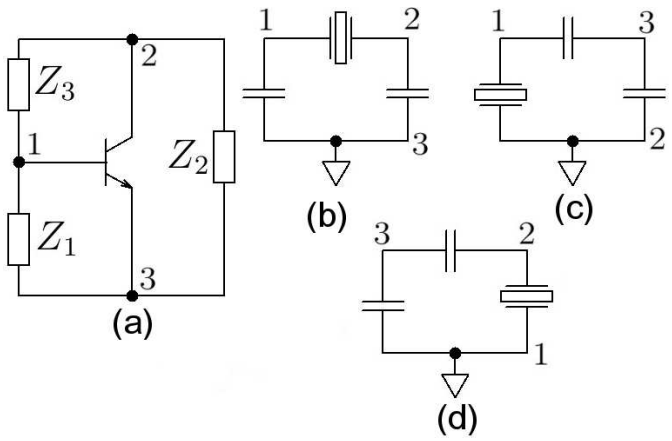

Figure 1.3: Basic transistor-type oscillator: (a) AC general view, (b) Pierce scheme, (c) Colpitts scheme, (d) Clapp scheme

1.3 Phase Noise and Frequency Stability

The ideal oscillator produces an ideal sinusoid which can be characterized by its amplitude V_0 and frequency $\omega_0 = 2\pi\nu_0$:

$$V(t) = V_0 \sin(2\pi\nu_0 t) = V_0 \sin(\omega_0 t) \tag{1.8}$$

In the frequency domain such a signal is represented by a single Dirac delta at frequency $\delta(\nu - \nu_0)$. But in reality, as it is mentioned above, deterministic and stochastic processes modify both the amplitude and the phase of the signal, hence, producing instabilities. Thus, the signal in real conditions may be written as:

$$V(t) = V_0\big[1 + \alpha(t)\big] \sin(2\pi\nu_0 t + \varphi(t)), \tag{1.9}$$

where $\alpha(t)$ and $\varphi(t)$ represent respectively amplitude and phase modulation. These components broaden the signal spectrum, which in this case is no more a Dirac function. In the majority of cases amplitude fluctuations are not considered, due to existence of limiting mechanisms. On the contrary, phase fluctuations are of the great interest, since small fluctuations can lead to unlimited phase changes.

1.3.1 Time Domain Characterization

Frequency stability may be characterized both in frequency and time domains [21]. Temporal characterization of the instabilities is maid through notation of the statistics. The principle is to repeat frequency measurements considerable number of times in order to obtain a table of its values: $\overline{\nu}_1, \overline{\nu}_2, \overline{\nu}_3 ... \overline{\nu}_N$. Each sample $\overline{\nu_k}$ is measured over time τ between the moment $k\tau$ and $(k+1)\tau$ as an average of the frequency $\nu(t)$:

$$\overline{\nu}_k = \frac{1}{\tau} \int_{k\tau}^{(k+1)\tau} \nu(t)dt. \tag{1.10}$$

More often the normalized frequency is used: $\overline{y}_k = (\overline{\nu}_k - \nu_0)/\nu_0$:

$$\overline{y}_k = \frac{1}{\tau} \int_{k\tau}^{(k+1)\tau} y(t)dt. \tag{1.11}$$

The first solution is to calculate the mean value $\langle y \rangle$ of the N samples:

$$\langle y \rangle_N = \frac{1}{N} \sum_{k=1}^{N} y_k. \tag{1.12}$$

Then the classical variance may be calculated:

$$\sigma_y^2 = \frac{1}{N-1}\sum_{k=1}^{N}\left(\overline{y}_k - \langle\overline{y}\rangle_N\right)^2. \tag{1.13}$$

The most often used tool for time-domain frequency instability characterization is the Allan Variance:

$$\sigma_y^2(\tau) = \mathbb{E}\Big\{\frac{1}{2}\big[\overline{y}_{k+1} - \overline{y}_k\big]\Big\}, \tag{1.14}$$

which is the expectation of the two contiguous sample variance. The corresponding deviation is a square root of the variance:

$$\sigma_y(\tau) = \sqrt{\sigma_y^2(\tau)}. \tag{1.15}$$

Allan variance (1.14) is equivalent to a filter with the transfer function $H_A(jf)$:

$$\sigma_y(\tau) = \int_0^\infty S_y(f)\big|H_A(jf)\big|^2 df, \quad \big|H_A(jf)\big|^2 = 2\frac{\sin^4\pi\tau f}{(\pi\tau f)^2}, \tag{1.16}$$

where $S_y(f)$ is a power spectral density (PSD) of the relative frequency fluctuations $\overline{y}$, which is a frequency fluctuation characteristic in the frequency domain.

1.3.2 Frequency Domain Characterization

Amplitude and phase noises cause distribution of the signal power in the frequency band around the central frequency ν_0. The signal spectral purity may be characterized for each (Fourier) frequency $f = \nu - \nu_0$ (distance from the central or carrier frequency to ν) by the quantity $S_\varphi(f)$ (in dBrad^2/Hz) that is defined as the one-sided power spectral density of the random phase fluctuations $\varphi(t)$ (the similar is defined for amplitude fluctuations $\alpha(t)$) [1]. The dimension of $S_\varphi(f)$ is rad^2/Hz.

In real measurements, manufacturers and engineers prefer the quantity $\mathscr{L}(f)$, which is defined as:

$$\mathscr{L}(f) = \frac{1}{2}S_\varphi(f), \tag{1.17}$$

according to the IEEE standard 1139 [22]. $\mathscr{L}(f)$ is given in dBc/Hz that relates the phase noise to the carrier in one hertz bandwidth.

Furthermore, the one-sided PSD of the random phase fluctuations may be transformed into the PSD of the fractional frequency fluctuations $S_y(t)$:

$$S_y(f) = \frac{f^2}{\nu_0^2}S_\varphi(f). \tag{1.18}$$

which is due to derivation relationship of two quantities.

Usually the oscillator phase noise may be represented in the form of the following function:

$$S_\varphi(f) = \sum_{i=-4}^{0} b_i f^i. \tag{1.19}$$

which represents 5 (there may be more than that) phase noise processes each with the slope $i \times 10$ dB/decade on a log-log scale. This corresponds to

$$S_y(f) = \sum_{i=2}^{-2} h_i f^i. \tag{1.20}$$

Table 1.1 provides some conversation relationships between spectra slopes and Allan variance. Also, this relationship can be seen on Fig. 1.4.

Table 1.1: Relationships between spectra and Allan variance

Noise Type	$S_\phi(f)$	$S_y(f)$	$\sigma_y^2(\tau)$
White PM	b_0	$\frac{b_0}{\nu_0 2} f^2$	$\frac{3 f_H h_2}{4\pi 2}\tau^{-1}$ $2\pi\tau f_H \gg 1$
Flicker PM	$b_{-1} f^{-1}$	$\frac{b_{-1}}{\nu_0 2} f$	$\left[1.038 + 3\ln(2\pi f_H \tau)\right] \frac{h_1}{4\pi 2}\tau^{-2}$
White FM	$b_{-2} f^{-2}$	$\frac{b_{-2}}{\nu_0 2}$	$\frac{1}{2} h_0 \tau^{-1}$
Flicker FM	$b_{-3} f^{-3}$	$\frac{b_{-3}}{\nu_0 2} f^{-1}$	$2\ln(2) h_{-1}$
Random walk FM	$b_{-4} f^{-4}$	$\frac{b_{-4}}{\nu_0 2} f^{-2}$	$\frac{4\pi 2}{6} h_{-2}\tau$

1.3.3 Leeson effect

Now, let us return to the frequency stability of the harmonic oscillator as a frequency source. The closed loop of such an oscillator is a subject of two random phase fluctuations $\psi_1(t)$ and $\psi_2(t)$ (Fig. 1.2). Since the model is linear we can consider a total loop phase fluctuation $\psi(t) = \psi_1(t) + \psi_2(t)$. As a result of these instabilities the output signal has the following form:

$$V(t) = V_0 \sin(2\pi\nu_0 t + \varphi(t)). \tag{1.21}$$

The interesting point here is a spectral relationship between variables $\varphi(t)$ and $\psi(t)$. To find out this relationship one must separate two cases: slow (slower than resonator relaxation time 1.2) and fast variations of $\psi(t)$.

Slow components of $\psi(t)$ can be treated as quasi-static fluctuations. Thus, frequency fluctuation is

$$\Delta\nu = \frac{\nu_0}{2Q_l}\psi(t), \tag{1.22}$$

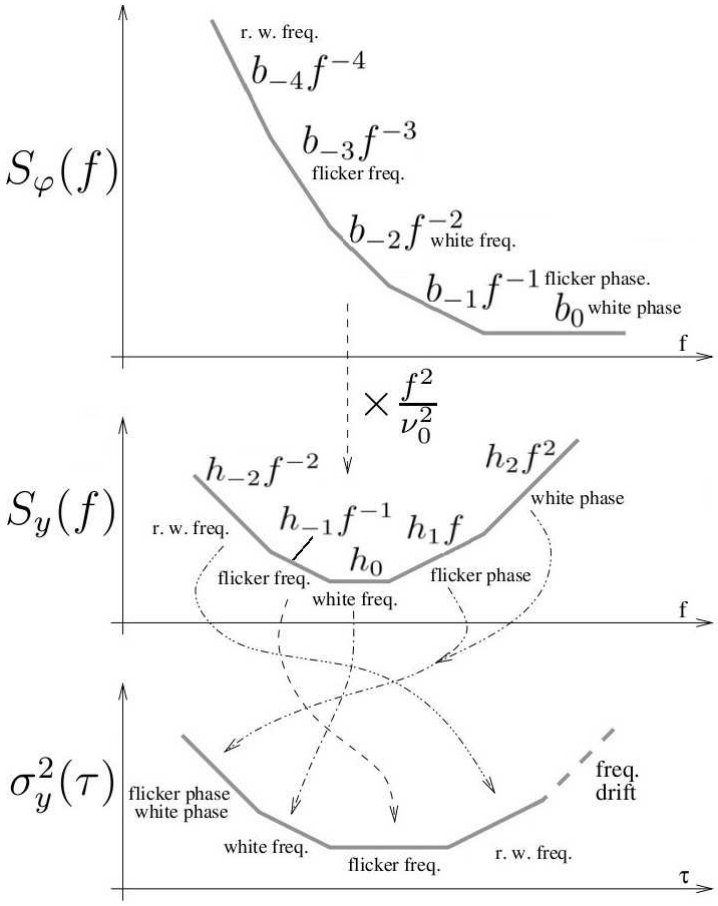

Figure 1.4: Relationships between time and frequency domain representation of oscillator instability [1, 2]

and spectral densities relate as

$$S_{\Delta\nu}(f) = \Big(\frac{\nu_0}{2Q_l}\Big)^2 S_\psi(f). \tag{1.23}$$

By definition the instantaneous phase $\varphi(t)$ of the oscillator output signal is an integral of the frequency deviation $\Delta\nu(t)$:

$$\varphi(t) = 2\pi \int \Delta\nu(t)dt. \tag{1.24}$$

This time-domain integration is equivalent to the multiplication by $\frac{1}{j\omega}$ in frequency space. Furthermore, the corresponding spectra are connected by multiplication by f^{-2}, thus the oscillator phase noise for slow-varying phase instabilities $\psi(t)$ is

$$S_\varphi(f) = \frac{1}{f^2}\Big(\frac{\nu_0}{2Q_l}\Big)^2 S_\psi(f). \tag{1.25}$$

This relation means that slow spectral components of $\psi(t)$ passes the oscillating loop without any suppression. i.e. this is the case of the noise regeneration.

For the fast-varying phase instabilities, resonator suppresses $\psi(t)$, when it passes the oscillating loop. Roughly speaking this means that the oscillating loop is open for phase fluctuations. Since regeneration is not present, the following is true for fast fluctuations:

$$S_\varphi(f) = S_\psi(f). \tag{1.26}$$

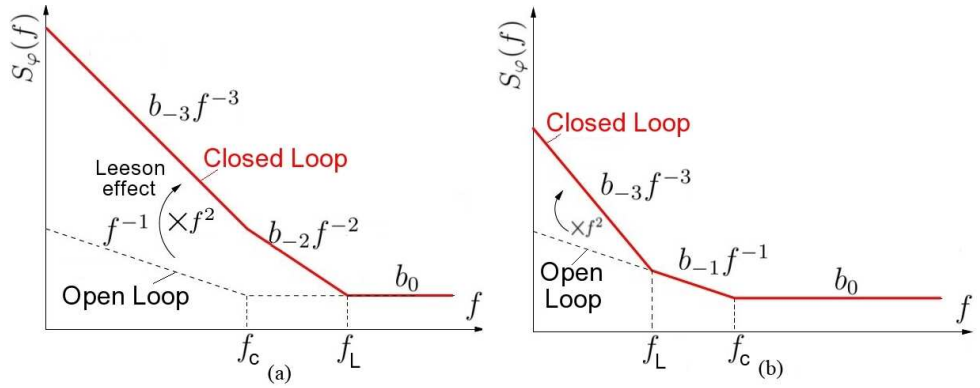

Figure 1.5: Leeson effect, shown for two typical cases

Assuming that there is no correlation between slow and fast components of $\psi(t)$, the effects of relationships (1.25) and (1.26) may be added to each other [110]:

$$S_\varphi(f) = \left[1 + \frac{1}{f^2}\left(\frac{\nu_0}{2Q_l}\right)^2\right] S_\psi(f). \tag{1.27}$$

This relationship is generally known as the Leeson formula. Its main parameter is so-called Leeson frequency (also known as resonator's half-bandwidth):

$$f_L = \frac{\nu_0}{2Q_l} = \frac{1}{2\pi\tau}. \tag{1.28}$$

Next, what is the effect of the Leeson formula on the oscillator phase noise spectra? To answer this question two cases have to be considered separately: 1) open-loop phase noise corner frequency f_c (between open-loop flicker and white noises) is less than Leeson frequency f_L (see Fig. 1.5,(a)); 2) corner frequency f_c is higher than f_L (see Fig. 1.5,(a)). Since, Leeson effect is equivalent to noise multiplication by f^{-2} for Fourier frequencies less than f_L. So, in the first case (typical for microwave oscillators), the resulting PSD consists of f^{-3}, f^{-2} and f^0 noises. But in the second case (typical e.g. for RF BAW oscillator), the spectra has f^{-3}, f^{-1} and f^0 slopes.

From the observations given above, two general methods to decrease oscillator frequency instability are clear. First, the open loop oscillator phase noise has to be reduced. Second, resonator loaded quality factor has to be augmented in order to "move" the Leeson effect to the zone of very low Fourier frequencies.

Chapter 2

Theoretical Investigations on the Phase Noise in Resonators and Oscillators

The present chapter considers the problem of the phase noise in resonators and oscillators from the theoretical point of view. The investigation is needed to understand the noise origins as well as to give associated mathematical models. These models are required for deep analysis of systems based on BAW resonators.

2.1 Parametric Model of the Quartz Crystal Resonator Phase Noise

It is generally known (and is proved in the Section 7.2) that the resonator phase noise is the main limitation of the oscillator performance close-to-carrier (i.e. oscillator long-term stability). So, its modeling is of the great interest in the corresponding areas of science. In this section a new parametric crystal phase noise model is proposed. The section follows the ideas published in [23].

Experimental and theoretical investigation on the origins of phase noises is of great interest in the recent years. It is also our interest in studying phase processes at cryogenic temperatures. The special attention is devoted to quartz resonators, because of their crucial role for many types of oscillators. Indeed, performance of ultra-stable quartz crystal oscillators (usually $5 - 10$ MHz) in terms of frequency stability is limited by the resonator noise. Recent experimental researches on high quality bulk acoustic quartz resonators [24, 3, 25, 26] provide a power spectral density (PSD) of the phase noise generated by quartz crystals. However, these results require further theoretical explanation. An explanation from a point of view of parameter fluctuations is given in this section.

There are two main approaches to a problem of quartz resonator phase noise. The first one (noise conversion method) is based on a resonator equivalent circuit and may be successfully used for phase noise PSD calculation of different oscillatory systems based on intrinsic noise sources [27, 28]. The main advantage of this approach is that it enables us to study particular finite ranges of the system PSD and all types of noise without using the corresponding differential equations. This method is rather accurate and is in a good agreement with available measurements of that time.

The essence of the second approach (here and further called the phase plane method) lies in the Laplace transform of the phase of a carrier and representation of the quartz crystal as a transfer function in a phase plane [1]. Though this method is common for different types of phase-locked loop (PLL) systems, it can also be applied to oscillatory system analysis. According to this approach phase noise is regarded as additive flicker noise at the input of the resonator transfer function. No other noise sources and phenomena are considered. Nevertheless, this model may be sufficient for many types of system level analyses.

2.1.1 Given Data

The model presented in this section is based on recent measurements of different types of $5 - 10$ MHz high quality quartz resonators from different manufacturers. Moreover, it must be an efficient tool for analyzing future results of our investigations on resonator behavior at cryogenic temperatures.

Measurements have been performed by means of a home-made state-of-the-art interferometric measurement system. Some details about the test bench are given in [26] or [25], for example. The noise floor of the bench depends on the carrier power and, as a consequence, on the power dissipated inside the couple of quartz crystal resonators. It can vary according to the motional resistance of the resonator from -143 dBc/Hz, for a typical dissipated power of 20 μW, up to -165 dBc/Hz for a typical dissipated power of 200 μW. Here and now it should be mentioned that experimental results do not exhibit any f^0 noise generated by both resonators, greater than the noise floor of the bench (so, it is also excluded from the model).

Each resonator under test is temperature-controlled at its turnover temperature, in such a way that the thermal stability is about 2 μ°C for measurement time of 1 s and about 20 μ°C over 10 s [29]. Thus, the behavior of f^{-2}-type noise PSD (see further) inside the resonators bandwidth is very limited or at least restricted to offset frequency lower than 0.01 Hz.

Moreover, ideally the resonators under tests are excited at their series resonance frequency. Actually, because both resonators never have the same resonance frequency, a series capacitor must be added at least in one branch of the bench, in order to be able to

tune the source frequency at the resonance frequency of both branches. Nevertheless, the couples of crystal resonators are always sorted to be as close as possible in terms of the resonance frequency as well as motional parameters.

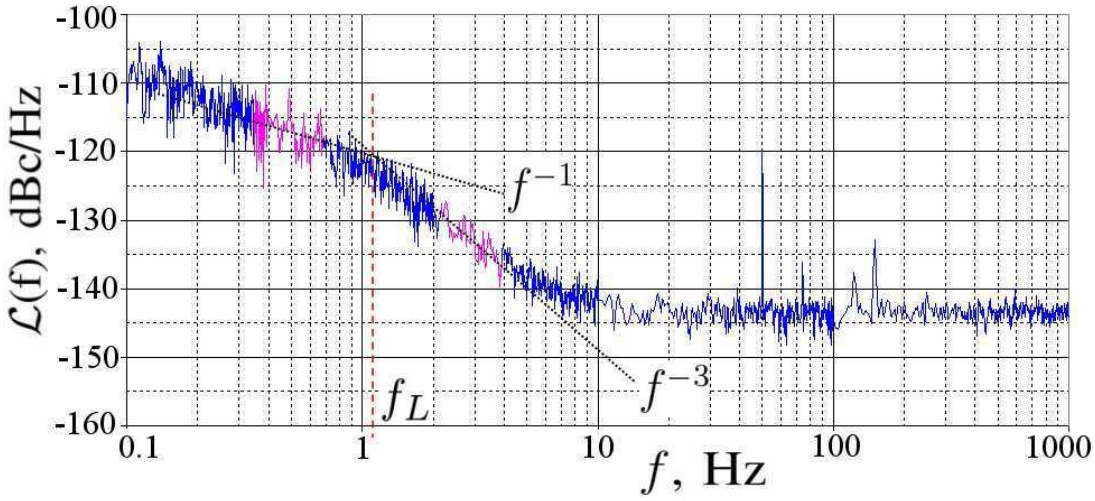

Figure 2.1: Measured phase noise of a 5 MHz high quality quartz crystal resonator. f_L denotes the so-called Leeson frequency, i.e. a half of a resonator bandwidth. The dashed line is needed to identify the PSD value at $f = 1$ Hz from the carrier which is used to calculate the corresponding Allan deviation [3]

A typical (about 90% of all measurements on various types of resonators) power spectral density plot of the quartz crystal phase noise is shown in Fig. 2.1. The curve shown in Fig. 2.1 consists of three parts: phase flicker f^{-1}, f^{-3} and white f^0 noise areas. The latter is the noise floor of the measurement test bench and not a noise generated by the resonators under test.

Such a pattern has been explained with the phase plane model [1]. According to this model the phase noise at the output of the resonator results from a flicker phase noise at the input (S_{add}) which is always present regardless the absence of the driving signal noise [1]. Thus, the power spectral density at the output of the resonator can be found in the following way:

$$S_\varphi(f) = |\mathscr{H}(f)|^2 S_{add}(f), \tag{2.1}$$

where $\mathscr{H}(f)$ is a transfer function of an ideal resonator in the phase plane and f is the Fourier frequency. Since in the absence of detuning signal this transfer function is a linear first order function, then a term $|\mathscr{H}(f)|^2$ has a spectral density with two regions: f^0 and f^{-2}. A multiplication of this term by S_{add} which follows f^{-1} law gives a power spectral density shown in Fig. 2.1 without the f^0 part. The same pattern may be easily obtained with the noise conversion method [28].

Nevertheless, in practice, for more modest resonators one can observe f^{-2} slopes instead of f^{-3} (see Fig. 2.2). This is the case of less than 10% of measured resonators and

exclusively observed on just one type of resonators. This fact can be explained with the first approach based on fluctuations of the equivalent motional resistance, i.e. the noise conversion method, but not the phase plane model.

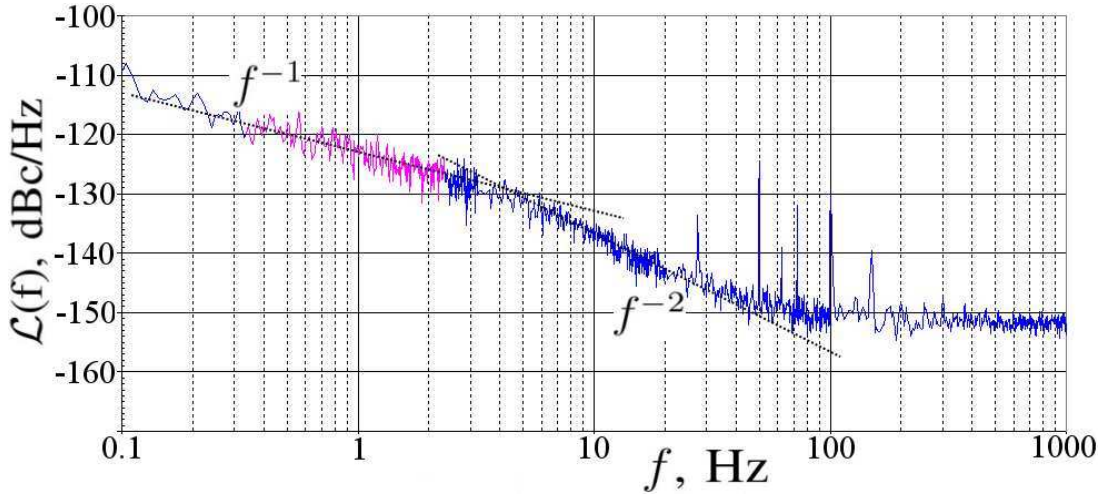

Figure 2.2: Measured phase noise of a medium quality 10MHz quartz crystal resonator. This behavior has been observed just for one type of the tested resonators.

Here we consider a model based on parameter fluctuations of differential equations, which are close in nature to the second approach (representation of quartz resonator in phase space), but based on fluctuations of parameters of the electrical equivalent model, as in the first method.

2.1.2 Parametric Fluctuations

Let's consider a simple π-network driven by an ideal sinusoid. In this case a crystal resonator can be represented by its electrical equivalent circuit (see Fig. 2.3).

In order to construct a rigorous model of parameter fluctuating system this equivalent circuit (Fig. 2.3) can be considered as a system where motional inductance L_x and capacitance C_x vary with time in such a fast way that the Laplace transform of the signals becomes irrelevant. Nevertheless, it is possible to derive ordinary differential equations (ODEs), which describe physical processes in such a system. The relations appear from the physical analysis of energy, which is stored in each of the components of the equivalent circuit. In fact, dynamic properties of a time-varying capacitance are associated with the time-varying electric charge and an inductance with magnetic flux [11]. Therefore, rigorously, the ODEs of the equivalent electrical circuit must be written and solved for the electric charge and/or magnetic flux, to fit physical processes.

This choice of fluctuating parameters is made, because an equivalent inductance and

capacitance determine the position of the system natural frequency, which is believed to be a source of generated phase noise. Also, these two sources are separated since their influences on system parameters are different. For the simplicity of the following calculations the shunt capacitance C_0 is neglected. Indeed, the absolute shift of the resonance frequency due to C_0 is estimated as follows:

$$\Delta\omega \approx \omega_x \frac{R_x^2 C_0}{L_x},$$

where ω_x is the angular resonance frequency determined by the series motional branch L_x, C_x, R_x where R_x is the resonator equivalent series resistance. As an example, for a usual high quality quartz resonator, R_x is less than 100 Ohms, L_x is about 1 H and C_0 is about 2 pF, that gives an absolute frequency shift of just about 10^{-8} of ω_x. So, fluctuations of C_0 have 10^8 lower impact on resonance frequency than that of L_x and C_x. Moreover, the shunt capacitance is a function of the BAW resonator geometry and the relative permittivity. Both can fluctuate with temperature, inducing a C_0 relative sensitivity of a few 10^{-5} per Kelvin [30], but, in this work, the device under test is temperature-controlled. For the measurements resulting in Fig. 2.1 and 2.2, temperature fluctuations of the tested resonators are typically lower than $2 \cdot 10^{-6}$K over one second [29].

A time-varying parameter of the capacitor is its amount of electric charge q stored for a given electric potential or the capacitance $C(t) = q(t)/u_c(t)$. The electrical current through the capacitor is a speed of change of its charge. From the following equation of the physical process in the capacitor can be derived:

$$i_c(t) = \frac{dq}{dt} = \frac{dq}{du}\frac{du_c}{dt} = C(t)\frac{du_c}{dt}, \tag{2.2}$$

where $u_c(t)$ is a capacitor voltage, $i_c(t)$ is a capacitor current.

In the same manner for a time-varying inductor the main parameter is the amount of magnetic flux ξ produced for a given electric current i_L in the inductance $\xi(t) = L(t) \cdot i_L(t)$.

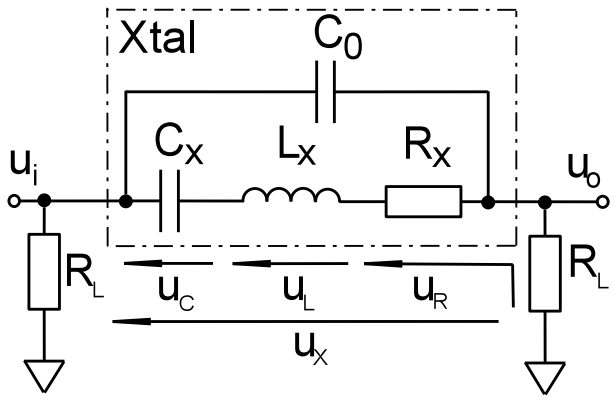

Figure 2.3: Model of the crystal resonator as a part of the π-network

The inductor voltage is a derivative of the magnetic flux:

$$u_L(t) = \frac{d\xi}{dt} = \frac{d}{dt}L(t)i_L(t) = \frac{dL(t)}{dt}i_L(t) + L(t)\frac{di_L(t)}{dt}. \tag{2.3}$$

Now, let's consider an equivalent circuit of the resonator which has time-varying components $L_x(t) = L_{x0} + \Delta L_x(t)$ and $C_x(t) = C_{x0} + \Delta C_x(t)$. So, the system governing equation can be written for a current through the crystal resonator i_x as:

$$\int_{-\infty}^{t} \frac{i_x(\tau)}{C_x(\tau)}d\tau + \frac{dL_x(t)}{dt}i_x(t) + \frac{di_x(t)}{dt}L_x(t) + R_x i_x(t) + R_L i_x(t) = u_i(t). \tag{2.4}$$

Substituting relation $u_R(t) = (R_x + R_L)i_x(t)$ into (2.4) and differentiating the result, the system equation can be written in terms of the total equivalent (motional resistance of the resonator R_x and the load resistance R_L) resistance voltage drop $u_R(t)$:

$$\ddot{u}_R(t) + \dot{u}_R(t)\frac{2\dot{L}_x(t) + R_x + R_L}{L_x(t)} + u_R(t)\Big(\frac{1}{C_x(t)L_x(t)} + \frac{\ddot{L}_x(t)}{L_x(t)}\Big) = \dot{u}_i(t)\frac{R_x + R_L}{L_x(t)}. \tag{2.5}$$

The output voltage in this case is simply:

$$u_o(t) = u_R(t)\frac{R_L}{R_x + R_L}, \tag{2.6}$$

if C_0 is neglected.

Also, from the description (2.5) one can find an actual (dynamic) natural frequency and actual loaded quality factor (both depending on time) of the resonator:

$$\omega_0(t) = \sqrt{\frac{1}{C_x(t)L_x(t)} + \frac{\ddot{L}_x(t)}{L_x(t)}}, \quad Q(t) = \frac{L_x(t)\omega_0(t)}{2\dot{L}_x(t) + R_x + R_L}. \tag{2.7}$$

If the inductance and the capacitance are time-invariant, then both formulas (2.7) give well-known expressions for the quality factor and the natural frequency of the time-invariant system.

If the time dependences of $L_x(t)$ and $C_x(t)$ are known, equation (2.5) can be solved numerically by transforming the second order ODEs into a system of first order differential equations of the Cauchy form:

$$\begin{cases} \dot{y}_1 = y_2, \\ \dot{y}_2 = -\omega_0^2(t)y_1 - 2\delta(t)y_2 + 2k(t)x(t), \end{cases} \tag{2.8}$$

where $y_1 = u_R$, $x(t) = \dot{u}_i$ and

$$\delta(t) = \frac{2\dot{L}_x(t) + R}{2L_x(t)}, \quad k(t) = \frac{R}{2L_x(t)}. \tag{2.9}$$

For the sake of simplicity all following calculations are made for the total equivalent resistance ($R = R_L + R_x$). However, this task is very time-consuming. The point is that the frequency of the input signal has to be in the vicinity of the resonance frequency of the resonator crystal, i.e. the period of change is about 10^{-7} seconds. But in the same time fluctuations of the parameters of the system are very slow. Here we are interested in the processes with time constants of tens and hundreds of seconds. Thus, a number of time steps for modeling of such a system is incredibly large. In order to avoid this drawback the method of averaging [11, 31, 32, 33] can be used.

2.1.3 System Solution with Averaging Method

Let the input signal of the π-network is described in the form of an ideal cosinusoid:

$$u_i(t) = u_a \cos(\omega t + \varphi),$$

where ω is a constant angular frequency. Then the signal $x(t)$ is a derivative of the $u_i(t)$:

$$x(t) = \dot{u}_i(t) = -u_a\omega \sin(\omega t + \varphi) = -u_a\omega \cos(\omega t + \varphi - \frac{\pi}{2}).$$

A state vector $\boldsymbol{Y} = [y_1(t), y_2(t)]^T$ shows the position of the system at the present moment t in the phase plane. These are Cartesian (rectangular) coordinates of the point. In this case both coordinates have the same rate of change. But as it is known from the control system theory a system in the phase plane can be represented by an infinite number of ways, i.e. state coordinates. For example, in the polar coordinates the system can be described by a length $m(t)$ (magnitude) and an angle $\psi(t)$ (phase) of a vector drawn from the point of origin to the current state: $\boldsymbol{M} = [m(t), \psi(t)]^T$. For the given system the transition from the Cartesian coordinates to the polar ones is done with the following expressions:

$$y_1(t) = m(t)\cos(\omega t + \phi(t)) = m(t)\cos(\psi(t)), \qquad y_2(t) = \frac{dy_1(t)}{dt} \approx -m(t)\omega \sin(\psi(t)) \quad (2.10)$$

The coordinate $y_2(t)$ is found for the case when the length of the vector $m(t)$ and the phase fluctuation $\phi(t)$ change much slower than the phase ωt. In this variant $m(t)$ and $\phi(t)$ change with the rate of parameters of the equivalent circuit $L_x(t)$ and $C_x(t)$, and the phase ωt changes with the rate of the input signal, i.e. roughly 5 MHz or 10 MHz in the present case.

Substituting expressions (2.10) to the system in Cartesian coordinates (Eq. (2.8)), reducing equal term in left-hand and right-hand sides and dividing the second equation by $-\omega$, the following system in polar coordinates is derived:

$$\begin{cases} \dot{m}\cos\psi - m\dot{\phi}\sin\psi = 0, \\ \dot{m}\sin\psi + m\dot{\phi}\cos\psi = -m\omega\cos\psi + \frac{\omega_0^2}{\omega}m\cos\psi - 2\delta m\sin\psi + 2\frac{ku_a}{m}\sin(\omega t). \end{cases} \quad (2.11)$$

This system can be transformed to the Cauchy form for slowly varying variables m and ϕ. To do this, the first equation of system (2.11) has to be multiplied by $\cos\psi$ and the second one by $\sin\psi$. After summating the results of these multiplications and taking into account the Pythagorean trigonometric identity for functions of ψ, the first equation of system (2.12) is obtained. After that the procedure needs to be repeated. This time the first equation has to be multiplied by $-\sin\psi$, and the second one by $\cos\psi$. After summation, the second equation of (2.12) is derived.

$$\begin{cases} \dot{m} = -m\omega\sin\psi\cos\psi + \frac{\omega_0^2 m}{\omega}\sin\psi\cos\psi + 2\delta m\sin^2\psi + 2ku_a\sin(\omega t)\sin\psi, \\ \dot{\phi} = -\omega\cos^2\psi + \frac{\omega_0^2}{\omega}\cos^2\psi - 2\delta\sin\psi\cos\psi + 2\frac{ku_a}{m}\sin(\omega t)\cos\psi. \end{cases} \tag{2.12}$$

System (2.12) still depends on the fast component of the phase. So, in order to spare from this constituent both parts of both equations have to be integrated over one period of the input signal $T = \frac{2\pi}{\omega}$, or just 2π for the variable ψ.

The following result is obtained with an assumption that the length m and the phase ϕ do not change during one period of the input signal. In case of parameter fluctuations of BAW resonators, this assumption holds true with good precision. Thus, swapping derivation and integration (taking in mind that $\dot{\psi} \approx \omega$, so ϕ and ψ are independent) we obtain a system for length M and phase Φ of an average vector, which describes a system state for one period of the input signal.

$$\begin{cases} 2\pi\dot{M} = -M\omega\int\limits_0^{2\pi}\sin\psi\cos\psi d\psi + \frac{\omega_0^2 M}{\omega}\int\limits_0^{2\pi}\sin\psi\cos\psi d\psi - \\ \qquad -2\delta M\int\limits_0^{2\pi}\sin^2\psi d\psi + 2ku_a\int\limits_0^{2\pi}\sin(\omega t)\sin\psi d\psi, \\ 2\pi\dot{\Phi} = -\omega\int\limits_0^{2\pi}\cos^2\psi d\psi + \frac{\omega_0^2}{\omega}\int\limits_0^{2\pi}\cos^2\psi d\psi - 2\delta\int\limits_0^{2\pi}\sin\psi\cos\psi d\psi + \\ \qquad +\frac{2ku_a}{M}\int\limits_0^{2\pi}\sin(\omega t)\cos\psi d\psi. \end{cases} \tag{2.13}$$

Each of three first integrals of both equations of system (2.13) is trivial. The last integrals are found taking into account the definition $\psi = \omega t + \phi$, which means that $\omega t = \psi - \phi$. And, so it can be found using the well-known trigonometric identities for the sinus and the cosinus of the difference:

$$\int\limits_0^{2\pi}\sin(\psi-\phi)\sin\psi d\psi = \int\limits_0^{2\pi}\sin^2\psi\cos\phi d\psi - \int\limits_0^{2\pi}\cos\psi\sin\phi\sin\psi d\psi = \pi\cos\Phi.$$

In the same way the last integral of the second equation of (2.13) gives:

$$\int\limits_0^{2\pi}\sin(\psi-\phi)\cos\psi d\psi = \int\limits_0^{2\pi}\sin\psi\cos\phi\cos\psi d\psi - \int\limits_0^{2\pi}\cos^2\psi\sin\phi d\psi = -\pi\sin\Phi.$$

And, finally, the system of differential equations for averaged values of length and phase of the vector can be written in the following way:

$$\begin{cases} \dot{M} = -\delta(t)M + K(t)u_a \cos\Phi, \\ \dot{\Phi} = \Omega(t) - K(t)\dfrac{u_a}{M}\sin\Phi, \end{cases} \tag{2.14}$$

where $\Omega = \frac{\omega_0^2(t)-\omega^2}{2\omega}$ is a detuning frequency. And M and Φ are average values of $m(t)$, $\phi(t)$ for one period of the input signal.

In order to find equilibrium points the left parts of the system (2.14) have to be set equal to zeros:

$$\begin{cases} \delta M = K u_a \cos\Phi, \\ \Omega M = K u_a \sin\Phi. \end{cases} \tag{2.15}$$

If the system is time-invariant and the frequency of the input signal corresponds to the natural frequency of the resonator (i.e. $\Omega = 0$), then the second equation of system (2.15) gives solutions for Φ in the form $\Phi = \pi n$, where $n \in \mathbb{Z}$. This solution of the first equation gives two possible variants of the first one: $M = \pm u_a$. A negative variant of the solution does not make physical sense. Moreover only one solution (on case of $n = 0$) can be explained in the physical way. This result is a solution where the BAW crystal is in the resonance, i.e. it does not give a phase shift to the input signal ($\Phi = 0$) and the input voltage equals to the total resistance voltage drop ($M = u_a$). The point $(u_a, 0)$ in (M, Φ) space is the stable equilibrium point of system (2.14).

Figures 2.1.3 and 2.5 show amplitude M and phase Φ fluctuations correspondingly produced by some random fluctuations of $L_x(t)$ and $C_x(t)$ and simulated with system (2.14), where the input amplitude is $u_a = 1V$.

Figure 2.1.3 shows that $M = u_a = 1V$ is a coordinate of the stable equilibrium point of system (2.14). From the physical point of view, M can not exceed u_a. The same result is obtained with the model. When $M = u_a$ the quartz crystal is exactly in the resonance. In all other points inductor and capacitor impedances are not compensated and the quartz crystal resonator is not working in the resonance mode.

Figure 2.5 shows that the output phase fluctuations are observed around another coordinate of the equilibrium point $\Phi = 0$. When $\Phi = 0$, the system is in the resonance mode, when impedances of the capacitor C_x and the inductance L_x are compensated and the crystal does not give a phase shift between input and output signals.

So, system of differential equations (2.14) can be used to find phase and amplitude fluctuations for given fluctuations of equivalent capacitance C_x and inductance L_x, introduced by fluctuating detuning frequency Ω and coefficients τ_1 and τ_2, and vice versa. In both cases a system of differential equations has to be solved.

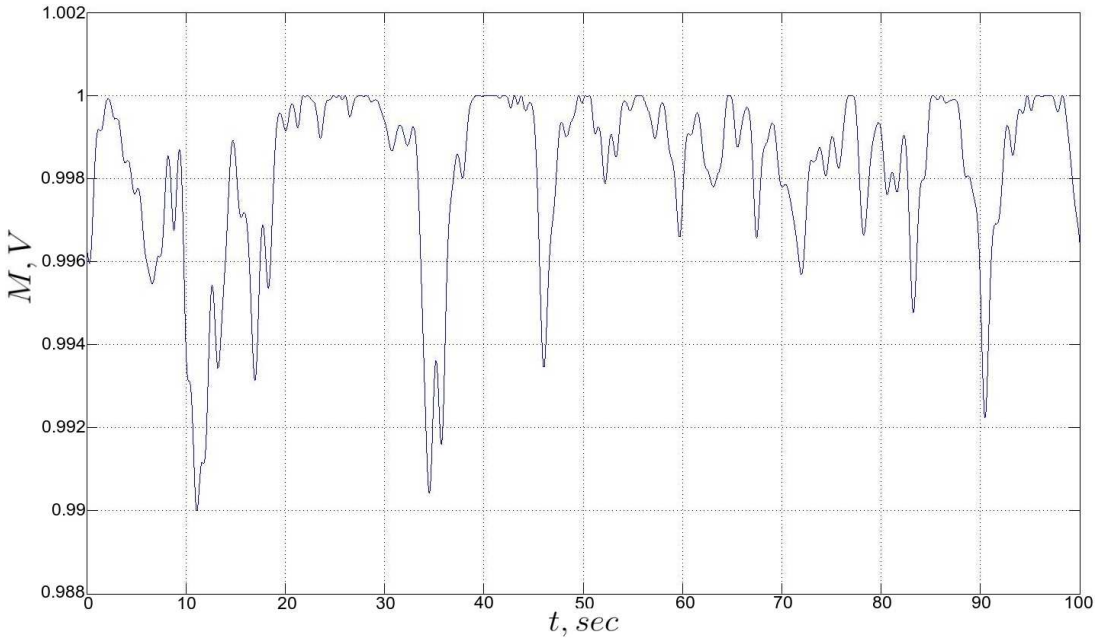

Figure 2.4: M (amplitude of the total resistance voltage drop u_R) fluctuations for some fluctuations of L_x and C_x, the input amplitude $u_a = 1V$. This curve has the same form as output amplitude (see (2.6))

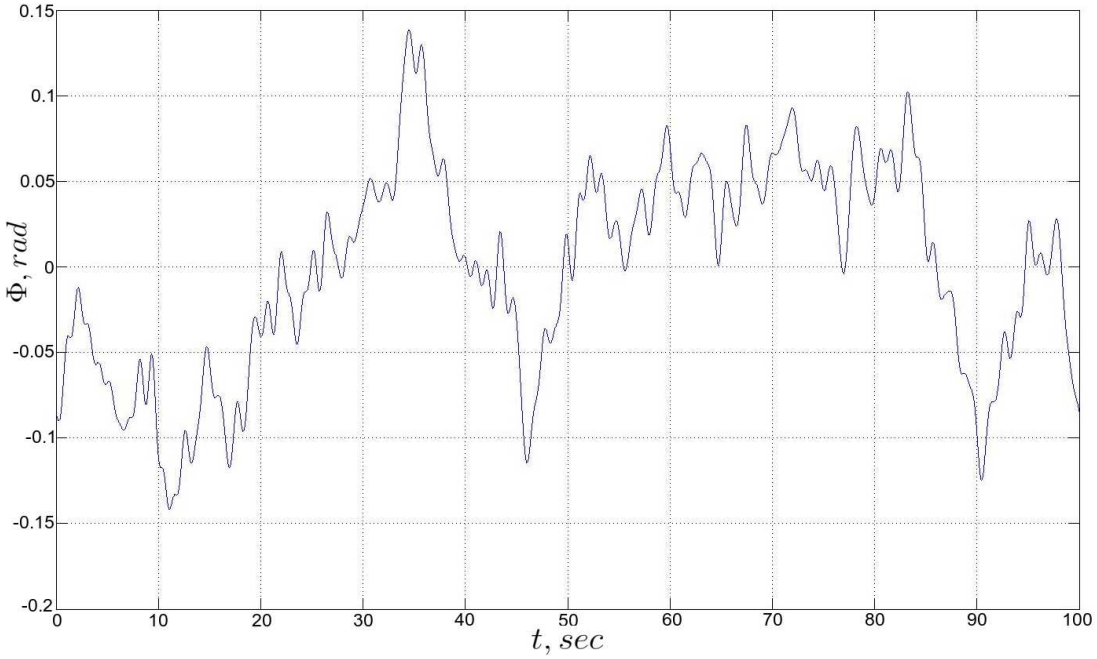

Figure 2.5: Φ (phase of the motional resistance signal and the output signal) fluctuations for some fluctuations of L_x and C_x

2.1.4 Numerical Simulation

Let us suppose that power spectral densities of parameter fluctuations are known, then the numerical method of finding the PSD of generated phase noise can be represented with the following steps:

1. generating a set of signals (fluctuations) in the time domain with a PSD corresponding to the known PSD of parameter fluctuations (several signals with the same PSD are needed to verify if the solution is the same for the whole class of fluctuations, in other words, it does not depend on the exact form of these fluctuations);
2. substitution of each signal into system (2.14);
3. solving system (2.14) for M and Φ for each signal from the set;
4. finding the PSD for time-domain signals obtained in the previous steps and averaging of results for the given set. If all signals from the set produce the same result, then this result is considered as correct. Finding the confidence range.

For the purposes of signal generation with the given PSD, the following well known formula is used:

$$S_x(f) = \lim_{T\to\infty} \frac{1}{T}\mathbb{E}\Big[|X_T(f)|^2\Big], \tag{2.16}$$

where $X_T[f]$ is the Fourier Transform of a continuous-time stochastic process $x(t)$, and $S_x(f)$ is its PSD.

To generate random fluctuations (random phase for each Fourier frequency) for the given PSD the following algorithm can be used:

1. to take the square root of the absolute value of the given PSD for each data point to get a magnitude spectral density: $|X(f)| = \sqrt{S_x(f)}$;
2. to generate random (uniform probability density) phase in frequency domain: $\Psi(f) = 2\pi n(f)$, where $n(f)$ is a random number generated for each frequency f;
3. to take the Inverse Fourier Transform of the random spectrum: $\Delta L_x(t) = \mathcal{F}^{-1}(|X(f)|\cdot exp(j\Psi(f)))$, where $\mathcal{F}^{-1}(\cdot)$ is the Inverse Fourier Transform.

Numerical simulations show that in order to obtain a result in accordance with experimental observations (i.e. f^{-1} and f^{-3} regions) the original PSD of L_x and C_x fluctuations must follow f^{-1} law.

Note should be taken that if the PSD of the phase fluctuations is limited by the frequency which is less than the sampling frequency of the system, then the generated signal

is differentiable. And differentiability is a mandatory requirement for the fluctuations of system parameters.

Calculations have been made (see Fig. 2.6) for a high quality quartz crystal (BVA-type, SC-cut) with the following parameters: resonance frequency $f_0 = 9999763.078$ Hz (C mode, 3rd overtone), motional resistance $R_x = 90$ Ohm, average motional inductance $L_x = 1.8$ H, average motional capacitance $C_x = 140$ aF. So, for this crystal resonator the unloaded Q is approximately $1.25 \cdot 10^6$.

As expected, if fluctuations of the equivalent inductance is a random ergodic process with a f^{-1} power spectral density, then the resulting PSD of average phase fluctuations has two regions where the power spectrum is proportional to f^{-1} and f^{-3} (see Fig. 2.6). Fig. 2.6 shows three PSD curves for three different levels of L_x fluctuations: -45 dBc/Hz (curve 1), -50 dBc/Hz (curve 2), -55 dBc/Hz (curve 3) at 1 Hz. This result is obtained for all generated signals of parameter fluctuations from the initial set. The inductance fluctuations $\Delta L_x(t)$ also result in fluctuations of the system natural frequency, as it was stated earlier.

The Leeson frequency of the resonator under study is a half of its bandwidth and can be found as follows:

$$f_L \approx \frac{f_0}{2Q_L} \approx 3.9 \text{ Hz}. \tag{2.17}$$

This formula cannot be regarded as precise, because a loaded quality factor Q_L is a function of time according to expression (2.7). However, Figure 2.6 shows approximately the same result as a border frequency between f^{-1} and f^{-3} regions.

It can be seen from Fig. 2.6 that for smaller values of input fluctuations the resulting PSD curves have more distortions, thus, the slope f^{-3} may be mistakenly regarded as f^{-2}. This fact is a result of numerical limitations of the used algorithm for direct and inverse Fourier Transforms (limitation of data types). But it is evaluated that in order to achieve the level of about -135 dBc/Hz at 1 Hz, the level of L_x fluctuations has to be approximately -56dBc/Hz at the same frequency.

Also it has to be mentioned that for other spectral laws of input parameter fluctuations (f^0, f^{-2} or any other) the output fluctuations have different (from those shown in Fig. 2.6) PSD configurations.

2.1.5 Influence of the Equivalent Resistance Noise

The model described above does not take into account flicker and thermal noise of the equivalent series and load resistances. These types of noises can be easily introduced into the model. In fact, the result system (2.14) remains valid even in this case, but parameters

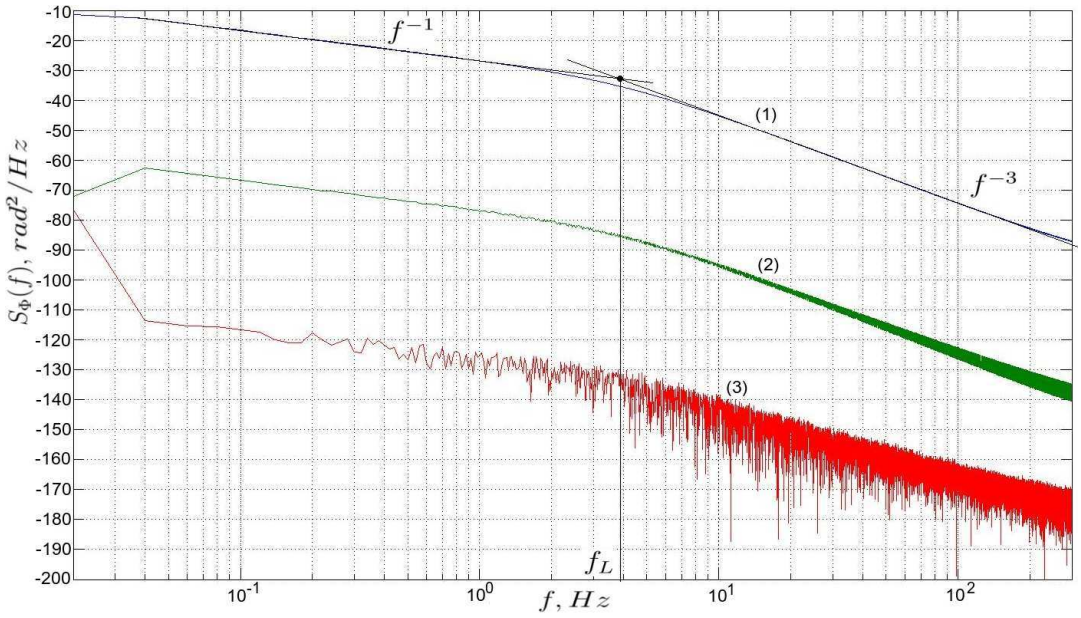

Figure 2.6: Power Spectral Densities ($S_\Phi(f) = 2\mathscr{L}(f)$) of average phase fluctuations generated by $L_x(t)$ fluctuations with a f^{-1} power spectral densities with levels of -45 dBc/Hz (1), -50 dBc/Hz (2), -55 dBc/Hz (3) at 1 Hz

ω_0^2, δ and K have to be extended:

$$\omega_0^2 = \frac{1}{C_x L_x} - \frac{2\dot{R}}{R}\left[\frac{\dot{L}_x}{L_x} - \frac{\dot{R}}{R}\right] - \left[\frac{\ddot{R}}{R} - \frac{\ddot{L}_x}{L_x}\right],\ \delta = \frac{2\dot{L}_x + R}{2L_x} - \frac{\dot{R}}{2R},\ K = \frac{R}{2L_x}. \quad (2.18)$$

where $R = R_L + R_x$. These three parameters represent system noise sources, amongst which ω_0^2 is dominant for a considered frequency interval. This parameter represent a squared natural frequency of a resonator and its fluctuations are equivalent to frequency fluctuations of the input signal.

System parameter ω_0^2 consists of three terms. The first term $-\frac{1}{C_x L_x}$ has a spectrum slope f^{-1} (when C_x and L_x fluctuate according to f^{-1} PSD) and produces clear pattern of f^{-1} and f^{-3} noise PSDs slopes at the resonator output. The second term has a PSD slope of f^0 for all frequencies of the spectrum, if R noise has also flicker spectrum. By, applying the same rule as to the first term, the resulting PSD of the system, when only this term is present, consists of f^0 and f^{-2}. The third term also results in white noise of the equivalent resonance frequency ω_0, and so produces f^0 and f^{-2} spectral laws.

Fig. 2.7 presents three PSDs, generated separately by the first (curve (1)), second (curve (2)) and third terms (curve (3)) of ω_0^2. As it is shown in this figure, f^{-2} can be seen instead of f^{-3} for some resonators, if phase noise generated by the second and third terms of ω_0^2 dominate in this region. Thus, this effect depends on resonator parameter (static values of C_x, L_x and R), as well as noise levels of these parameters. So, it is not surprising that this effect is present for some types of crystal resonators.

2.1.6 Link between the Phase Plane Model and the Present Approach

System (2.14) shows a dynamical link between fluctuations of the output signal in form of amplitude M and phase Φ, and fluctuations of the model parameters (equivalent inductance L_x and equivalent capacitance C_x). Such a system represents time-varying system where excitation is introduced with parameter fluctuations. A similar relationship may be written for a case of time-invariant additive model of the resonator phase noise, when excitation is introduced with a phase noise of the input signal:

$$u_i(t) = u_a \cos(\omega t + \theta(t)),$$

where θ is an additive phase noise. When a signal with an additive phase noise is applied to the π-network, it is filtrated in the phase plane. Following the same procedure as in the case of the parametric model, another system in terms of output averaged amplitude and phase (M, Φ) may be derived (2.19):

$$\begin{cases} \dot{M} = -\delta M + k u_a \frac{(\omega+\dot{\Theta})}{\omega} \cos(\Phi - \Theta), \\ \dot{\Phi} = \Omega - k \frac{u_a}{M} \frac{(\omega+\dot{\Theta})}{\omega} \sin(\Phi - \Theta), \end{cases} \tag{2.19}$$

where Θ is the average (for one period of the input signal) value of input phase fluctuations $\theta(t)$, and Ω, δ and k are time-invariant parameters.

If the power spectral density of the input phase noise follows f^{-1} law, then simulation of this system with the method described above showed the same results as simulation

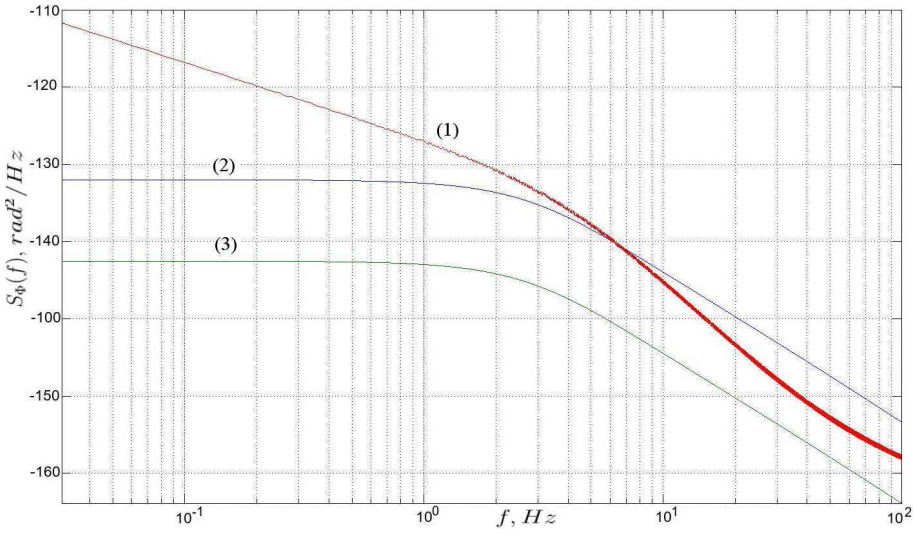

Figure 2.7: Resulting Power Spectral Densities of average phase fluctuations generated by first (curve (1)), second (curve (2)) and third terms (curve (3)) of fluctuating parameter ω_0^2 (2.18), when L_x, C_x and R_x disturbances has flicker noise PSD. The levels of applied noise are arbitrary.

of system (2.14), i.e. the output phase noise PSD has f^{-1} and f^{-2} regions with Leeson frequency of about 3.9 Hz. This fact proves that a quartz crystal inside the π-network acts as a first order filter in the phase plane. In fact, both systems ((2.14) and (2.19)) represent the same nonlinear dynamics, but with different inputs of excitation.

Assuming the following simplifications:

$$1 + \frac{\dot{\Theta}}{\omega} \approx 1, \quad \frac{\omega^2 - \omega_0^2}{2\omega} \approx \omega - \omega_0 = -\Omega, \tag{2.20}$$

the same system of equations may be used to find the resonator transfer functions in the the phase space:

$$\mathscr{H}(s) = \frac{\Phi(s)}{\Theta(s)} = \frac{\delta s + \delta^2 + \Omega^2}{s^2 + 2\delta s + \delta^2 + \Omega^2}. \tag{2.21}$$

The transfer function corresponds to the phase plane model obtained with another heuristic approach [26, 2]. In fact, the latter is a special case of the present model with the following main simplifications: 1) fluctuations of δ and k are discarded (see (2.14)); 2) simplifications described in (2.20) are used; 3) the second and third terms of parameter ω_0^2 (see (2.18)) are excluded.

Moreover, if both input amplitude and phase noise and inner parametric noise are of interest for some reasons the model may be extended:

$$\begin{cases} \dot{M} = -\delta(t)M + K(t)\Big[-\frac{\dot{u}_a}{\omega}\sin(\Phi - \Theta) + u_a\big(1 + \frac{\dot{\Theta}}{\omega}\big)\cos(\Phi - \Theta)\Big], \\ \dot{\Phi} = \Omega(t) + K(t)\frac{1}{M}\Big[-\frac{\dot{u}_a}{\omega}\cos(\Phi - \Theta) - u_a\big(1 + \frac{\dot{\Theta}}{\omega}\big)\sin(\Phi - \Theta)\Big]. \end{cases} \tag{2.22}$$

This system of differential equations represents a Multiple Input Multiple Output (MIMO) time-varying transfer function for amplitude and phase noises, which is the most general case of resonator representation in the amplitude-phase space. A mathematical description of a linearized MIMO model for the BAW resonator is given in Appendix A.

2.1.7 Comparison of the Noise Conversion Model and the Present Approach

Here we distinguish two cases: within and beyond half bandwidth, which are separated with Leeson's frequency f_L.

Within half bandwidth both models are in full correspondence. The shape of the PSD is determined by the effect of motional inductance and capacitance flicker noise. Furthermore, according to all three approaches, the level of the resulting flicker noise is proportional to the squared loaded quality factor (Q_L^2), in terms of $S_\Phi(f) = 2\mathscr{L}(f)$.

Beyond the half bandwidth, models are in contrast to each other. First, let's consider results predicted by the noise conversion method. According to the results obtained in [28]

the PSD of the resonator phase noise may be formed by the following noise sources: motional inductance and capacitance flicker noise (f^{-5}), resonator additive thermal noise (f^{-2}), motional resistance flicker noise (f^{-3}), load noise (f^{0}). So, as it has been concluded in this paper: the PSD slope beyond the half bandwidth can vary from f^{-3} to f^{-2} as a result of losses additive thermal and flicker noises. For more information see [28].

Let's consider contradictory points of the present model and the noise conversion method:

1. motional resistance flicker noise according to the simulations presented here may produce f^{-2} for certain resonators, but not f^{-3} as in [28];
2. as it has been shown both analytically and numerically, the motional inductance and capacitance flicker noise results in f^{-3} phase noise slope at the output (but not f^{-5}), which is confirmed by experiments in 90% of all cases. Also, L_x and C_x are the only sources of f^{-3} noise according to the previous point;
3. the motional resistance additive thermal noise cannot be considered as a noise source for f^{-2} phase noise. Indeed, in accordance with [28] the level of the noise at the output can be calculated as follows:

$$\mathscr{L}(f) = \frac{2kT}{P}\frac{f_L^2}{f^2}, \tag{2.23}$$

   where k is Boltzmann's constant, $T = 350$ K, $P = 20$ μW is the carrier power, and $f_L \approx 4.5$ Hz for the case shown in Fig. 2.2. With this data one may obtain with (2.23) -153 dBc/Hz at $f = f_L$, which is about the same level as the measurement bench noise. And, the actual measured f^{-2} noise is about 25 dBc/Hz higher.
4. f^{0} slope of the resulting PSD has been discarded, since it cannot be seen with the present measurement equipment, which is the main source of f^{0} noise in Fig. 2.1 and 2.2.

Since the results of two approaches contradict each other, further scientific discussions and measurements are badly needed for finding the actual sources of the resonator noise.

2.1.8 Conclusion

It can be concluded from the results of the previous numerical experiments, that most common patterns of the phase noise at the output of the quartz resonator (See Fig. 2.1 and 2.2) can be regarded as a result of its dynamics L_x (as well as, C_x and R_x) fluctuations with f^{-1} spectrum. Inside the resonator half bandwidth the resulting flicker phase noise is determined by f^{-1} fluctuations of L_x and C_x. Outside the half bandwidth the phase noise can be formed by pairs C_x-L_x with the result of f^{-3} or L_x-R_x with the result of f^{-2}.

The first case is observed experimentally in 90% of measurements. And the remaining 10% have been observed just on one type of resonators.

The simulation results testify to the validity of the proposed way of resonator phase noise modeling. Contrary to ordinary phase space method the approach proposed in this paper is based on consideration of the true phase noise origin, but not a virtual additive phase noise. This origin lies in parameter fluctuations of the quartz crystal due to fluctuations of temperature, pressure, etc. So, the proposed method confirms with simulation a guess that phase noise generated by a quartz crystal is a result of natural frequency fluctuations. The presented model is more general and incorporates link between magnitude and phase noises in the cases of parametric noise, input additive noise and both (2.22). Nevertheless, the main difficulty is connected with the fact that the presented approach has not been reduced to simple engineering solutions. Instead one can use the ordinary phase space model as a simplified solution.

In the same time the results obtained with this approach contradict the results of noise conversion method for the phase noise beyond the half bandwidth. This leads us to further discussions on BAW resonator phase noise origins.

Another question is the source of the parameter flicker noise. A possible answer is obtained with a series of experiments with the phase noise measurements of quartz resonators at cryogenic conditions (see subsection 6.5.4). Also, sources of the flicker noise could be possibly found in fractional order dynamic properties (more precisely, the dynamics of the $\frac{1}{2}$-order) of the BAW resonators. The possibility of existence of such properties is analyzed using a resonator distributed parameter model (see section 2.4).

2.2 Phase Noise in Nonlinear Resonator

This section considers some properties of BAW resonators in the presence of nonlinearities. The distinctive features of such systems are figured out and discussed.

2.2.1 Resonator Phase Noise Filtering Properties in Nonlinear Regime

Like the previous section, the present one considers a crystal resonator working in classical π-network (see Fig. 2.3). For simplicity it is also taken that this resonator has no spurious modes and shunt capacitance is negligible ($C_0 \to 0$). So, a simple π-network is driven by a sinusoid signal, which contains phase fluctuations around its average value. The resonator consists of a motional resistance R_x, capacitance C_x and inductance L_x and is loaded with a resistance R_L. In this section all the parameters are considered as constant

and the disturbance is introduced in the system with variable phase $\theta(t)$ of the input signal (see equation (2.1.6)). But contrary to the previous section some of the parameters are said to be dependent on the level of the applied signal, so that the device becomes nonlinear. The section answers the question about the influence of the nonlinearities on the resonator transfer function in domain of signal phases.

As it is usually suggested [11, 12], the crystal resonator nonlinear capacitance and resistance have the following dependences on the applied currents:

$$R_x(i) = R_{x0}\big(1 + k_1 i^2\big), \quad C_x(i)^{-1} = C_{x0}^{-1}\big(1 + k_2 i^2\big), \tag{2.24}$$

where i is the current through these nonlinear elements. In this case, according to the well-known physical laws, the system governing equation can be written as follows:

$$u_i = L_x \frac{di}{dt} + \int_{-\infty}^{t} \frac{i(\tau) + k_2 i(\tau)^3}{C_{x0}} d\tau + R_{x0}\big(1 + k_1 i^2\big) i + R_L i. \tag{2.25}$$

This initial equation can be transformed into another compact form, written for the system current:

$$\frac{d^2 i}{dt^2} + 2\delta(1 + \rho_1 i^2)\frac{di}{dt} + \omega_0^2(1 + \rho_2 i^2) i = k\frac{du_i}{dt}, \tag{2.26}$$

where

$$\delta = \frac{R_{x0} + R_L}{2L_x}, \quad \rho_1 = \frac{3k_1 R_{x0}}{R_{x0} + R_L}, \quad \omega_0^2 = \frac{1}{C_{x0} L_x}, \quad \rho_2 = k_2, \quad k = \frac{1}{L_x}. \tag{2.27}$$

As it is made in the previous section, the second order differential equation (2.26) can be easily transformed into a system of differential equations in the Cauchy form for generic variables with the variable change $i = x$:

$$\begin{cases} \dot{x} = y, \\ \dot{y} = -2\delta\big(1 + \rho_1 x^2\big) y - \omega_0^2\big(1 + \rho_2 x^2\big) x + k\frac{du_i}{dt}, \end{cases} \tag{2.28}$$

Once again, even though system (2.28) can be solved numerically, it is more efficient to apply the method of averaging same as in the previous section.

System (2.28) is written in Cartesian or rectangular coordinates (voltage and velocity of its change). The same system may be also transformed into the polar coordinates notation (magnitude and phase), using the change of variables similar to (2.10):

$$x(t) = m(t)\cos(\omega t + \phi(t)) = m(t)\cos(\psi(t)), \qquad y(t) = \frac{dx(t)}{dt} \approx -m(t)\omega\sin(\psi(t)). \tag{2.29}$$

The coordinate $x(t)$ is found for the case when the magnitude $m(t)$ and the phase fluctuation $\phi(t)$ change much slower than the fast term ωt. In this case $m(t)$ and $\phi(t)$ change with the rate of input phase $\varphi(t)$, and the phase ωt changes with the rate of the input signal (for example, from typically 1 MHz to 100 MHz in the case of quartz resonators).

On the next step, expressions (2.29) have to be substituted into system (2.28). The result can be reduced to the Cauchy form after a series of equivalent reorganizations (multiplication by $cos\psi$ and $sin\psi$ and summation). And, finally, this system has to be integrated over 2π for the variable ψ, which represents full phase of the input signal (see eq. (2.29)). It has to be assumed that the input phase fluctuations as well as m and ϕ does not change significantly during one period of the input signal $T = \frac{2\pi}{\omega}$. So, this procedure gives a second order system for the averaged values (averaged over one period of the input signal T) of magnitude M and phase Φ:

$$\begin{cases} \dot{M} = -\delta M - \lambda_1 M^3 + \alpha\cos(\Phi - \Theta), \\ \dot{\Phi} = \Omega + \lambda_2 M^2 - \dfrac{\alpha}{M}\sin(\Phi - \Theta), \end{cases} \tag{2.30}$$

where

$$\Omega = \frac{\omega_0^2 - \omega^2}{2\omega}, \quad \lambda_1 = \frac{1}{4}\rho_1\delta, \quad \lambda_2 = \frac{3\omega_0^2\rho_2}{8\omega}, \quad \alpha = \frac{ku_a}{2}. \tag{2.31}$$

Ω is a detuning frequency.

It has to be noted that according to (2.30) for rather high values of the magnitude M even in the absence of detuning frequency Ω there is a constant phase shift between input Θ and output Φ phases.

Due to the fact that the input phase fluctuations are rather small, system (2.30) can be linearized near the operating point in order to find out the resonator phase noise filtrating properties. To do this, the magnitude and the phase have to be represented as sums of constant (correspondingly, $\overline{M}$ and $\overline{\Phi}$) and small variable (correspondingly, $\widetilde{M}$ and $\widetilde{\Phi}$) parts. The constant parts characterize the operating point of the system. And the variable parts represent small fluctuations around this point. Also, it has to be noted that further development is made for the case (without lack of generality), when the input phase has only variable part.

The made decomposition of the solution leads to the separation of the initial system into two dependent systems. The first one is written for the operating point, and another describes small variations around this point. The first system may be represented in the following way:

$$\begin{cases} \delta\overline{M} + \lambda_1\overline{M}^3 = \alpha\cos\overline{\Phi}, \\ \Omega\overline{M} + \lambda_2\overline{M}^3 = \alpha\sin\overline{\Phi}, \end{cases} \tag{2.32}$$

which is equivalent to the sixth order equation in terms of $\overline{M}$. For the sake of simplicity, let further $\overline{M}$ and $\overline{\Phi}$ are physical grounded solutions of system (2.32).

The second equation of system (2.32) suggest an important fact: even in the case of the zero detuning frequency Ω, nonlinearity gives a constant phase shift between the input and output signal. In other words this phase shift depends on the excitation level α. This means that zero phase shift between the input and the output corresponds to some non-zero value of the detuning frequency Ω. This may lead to a serious mistake

if the resonance frequency is found as a frequency with the zero phase shift for the very low excitation level, and then it is taken as that for higher driving forces. The resonance frequency in the nonlinear case is found from the following condition:

$$\omega^2 \approx \omega_0^2\big(1+\frac{3}{4}\rho_2\overline{M}^2\big). \tag{2.33}$$

and not simply $\omega_0 = \omega$. And the magnitude of the solution in the case of the resonance is found from the equation:

$$\lambda_1\overline{M}^3 + \delta\overline{M} - \alpha = 0. \tag{2.34}$$

Another point here is the dependence of the resonance frequency shift between linear and nonlinear cases on the quality factor of the resonator in a linear regime. If the first nonlinearity in equation (2.26) is neglected ($\rho_1 \approx 0$), then system (2.32) can give the following approximation based on the resonance condition:

$$\Delta\omega \approx -\frac{3}{2}\frac{Q^2}{\omega_0}\alpha^2\rho_2. \tag{2.35}$$

The important conclusions are 1) the frequency shift is proportional to the power of the input signal (represented here by α^2), 2) the frequency shift is higher for the resonators with the higher quality factor (the relation depends on the nonlinearity type), 3) it is lower for higher resonance frequencies. These conclusions are useful to explain experimental results presented in Subsections 4.2.4 and 4.2.5.

In order to find linear transfer functions between input and output phases and magnitudes, it is needed to consider small variations around the steady-state solution, i.e. the system for $\widetilde{M}$ and $\widetilde{\Phi}$ with known $\overline{M}$ and $\overline{\Phi}$ (found from (2.32)).

$$\begin{cases} \dot{\widetilde{M}} = -\delta\widetilde{M} - 3\lambda_1\overline{M}^2\widetilde{M} - \alpha\sin\overline{\Phi}\big(\widetilde{\Phi}-\Theta\big), \\ \overline{M}\dot{\widetilde{\Phi}} = \Omega\widetilde{M} + 3\lambda_2\overline{M}^2\widetilde{M} - \alpha\cos\overline{\Phi}\big(\widetilde{\Phi}-\Theta\big). \end{cases} \tag{2.36}$$

Transforming system (2.36), a linear transfer function in the domain of phase may be derived:

$$\mathscr{H}(s) = \frac{\widetilde{\Phi}}{\Theta} = \frac{\delta' s + \delta'\delta'' + \Omega'\Omega''}{s^2 + (\delta'+\delta'')s + \delta'\delta'' + \Omega'\Omega''}, \tag{2.37}$$

where

$$\delta' = \delta + \lambda_1\overline{M}^2, \quad \delta'' = \delta + 3\lambda_1\overline{M}^2, \quad \Omega' = \Omega + \lambda_2\overline{M}^2, \quad \Omega'' = \Omega + 3\lambda_2\overline{M}^2. \tag{2.38}$$

For the marginal case $\lambda_1 = \lambda_2 = 0$ system (2.37) corresponds to one of the linear case derived with another method for the linear case [1].

So, like in the linear case, the crystal resonator with considered nonlinearities represents a low-pass filter in the phase plane. The pole and zero critical (break) frequencies

of this filter are found as follows (underdamped case, that is relevant for high Q crystal resonators):

$$\omega_{p12} = \sqrt{\delta'\delta'' + \Omega'\Omega''} \quad \omega_z = \frac{\delta'\delta'' + \Omega'\Omega''}{\delta'}. \tag{2.39}$$

These two frequencies define the system bandwidth. Moreover, since they are close to each other for relatively small detuning frequencies and amplitudes, it is sufficient to consider just one pole critical frequency for understanding the dynamical properties of the filter.

Analyzing formulae (2.38) and (2.39), a difference between linear and nonlinear resonator in the phase domain can be observed. For the linear system, it is never possible to decrease the pole break frequency by changing the detuning frequency since it is proportional to the square root of the frequency. This directly means that the phase noise filtering properties of the resonator could not be improved by changing Ω. This is not true for the nonlinear resonator. Indeed, the square of the pole break frequency is

$$\omega_{p12}^2 = \Omega^2 + 4\lambda_2\overline{M}^2\Omega + 3\lambda_1^2\overline{M}^4 + 4\delta\lambda_1\overline{M}^2 + 3\lambda_2^2\overline{M}^4 + \delta^2. \tag{2.40}$$

So, the bandwidth of the nonlinear resonator is shorter than that of the linear one with the same damping (or the same resonator in the linear mode) if

$$\omega_{p12}^2 - \delta^2 = \Omega^2 + 4\lambda_2\overline{M}^2\Omega + 3\lambda_1^2\overline{M}^4 + 4\delta\lambda_1\overline{M}^2 + 3\lambda_2^2\overline{M}^4 < 0, \tag{2.41}$$

because δ is the shortest bandwidth of the linear system for all Ω. Since the right-hand side of inequality (2.41) contains a term with an odd power of Ω, there exists a region in the $(\Omega, \overline{M})$-plane for some values of λ_1, λ_2 and δ where this inequality holds true. In other words, the nonlinearity decreases the phase filtering bandwidth for the detuning frequency in the range:

$$-2\lambda_2\overline{M}^2 - \sqrt{\lambda_2^2\overline{M}^4 - \lambda_1^2\overline{M}^4 - 4\delta\lambda_1\overline{M}^2} < \Omega < -2\lambda_2\overline{M}^2 + \sqrt{\lambda_2^2\overline{M}^4 - \lambda_1^2\overline{M}^4 - 4\delta\lambda_1\overline{M}^2}, \tag{2.42}$$

where dependance of ω on λ_2 is neglected. Also, it can be noted that for high quality resonators $\lambda_2 \gg \lambda_1$. Range (2.42) exists if the square root gives a real value, so the amplitude condition is fulfilled:

$$\overline{M}^2 > \frac{4\delta\lambda_1}{\lambda_2^2 - \lambda_1^2}, \quad \text{or} \quad \overline{M}^2 > \frac{16\rho_1}{9\rho_2^2 Q - \rho_1^2} \tag{2.43}$$

where $Q = \frac{\omega_0}{2\delta}$.

The analysis made above is simplified. It takes into account only one critical frequency. So, in order to demonstrate the ability of the nonlinearity to decrease the system bandwidth, the magnitude plot is calculated for one illustrative example (see Fig. 2.8). As a reference, the case of the corresponding linear regime is calculated (crosses). Two cases with Ω fulfilling conditions (2.42) and (2.43) demonstrate the narrower bandwidth than the beast possible linear case (curve (2) and (3)). The case, when the conditions are not respected, demonstrate the increase of the system bandwidth (curve (4)).

The conclusion is that if a resonator with a damping δ and nonlinearities characterized by parameters λ_1 and λ_2 could have a narrower bandwidth in the plane of phases (and thus batter phase noise filtering properties) than a similar resonator without nonlinearities or the same resonator in the linear mode if the amplitude of the signal obeys relation (2.43) and the detuning frequency is in the range defined by (2.42). In other cases, the nonlinearity degrades the resonator properties.

2.2.2 Amplitude-to-Phase Conversion in Nonlinear Resonator

Another distinctive feature of a nonlinear resonator is its ability to convert amplitude noise into the phase noise. Indeed, from the MIMO model of the linear resonator (see Appendix A) it follows that the transfer function from the input signal amplitude to the output phase is given as

$$\mathscr{H}_{u\Phi}(s) = \frac{\widetilde{\Phi}}{\widetilde{u}_a} = -\frac{\overline{\Omega}}{\overline{u}_a} \frac{s}{s^2 + 2\overline{\delta}s + \overline{\delta}^2 + \overline{\Omega}^2} \tag{2.44}$$

This transfer function is a derivative for angular offset frequencies $\omega < \sqrt{\overline{\delta}^2 + \overline{\Omega}^2}$. So, up to this frequency the corresponding magnitude plot has a slope of +20 dB/dec. That means that the conversion of the amplitude noise to the phase noise decreases with decreasing offset from the carrier. Moreover, the transfer function disappears if the frequency of the excitation signal equals the resonance frequency ($\Omega = 0$ case).

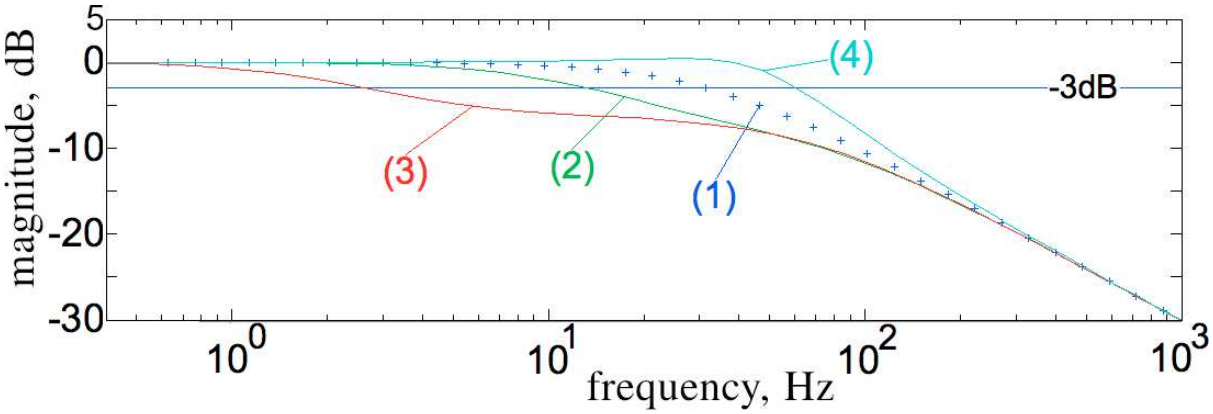

Figure 2.8: Magnitude plot of the transfer function $\mathscr{H}_{\Theta\Phi}(s)$ in the case of nonlinear resonator: (1) - the linear regime with $\Omega = 0$, (2) and (3) - Ω is in the range (2.42), (4) - Ω is out of the range (2.42)

For the nonlinear regime, the same transfer function is written as

$$\mathscr{H}_{u\Phi}(s) = -\frac{1}{\overline{u}_a}\frac{s\overline{\Omega}' + \overline{\Omega}'\overline{\delta}'' - \overline{\Omega}''\overline{\delta}'}{s^2 + (\overline{\delta}' + \overline{\delta}'')s + \overline{\delta}'\overline{\delta}'' + \overline{\Omega}'\overline{\Omega}''} = -\frac{1}{\overline{u}_a}\frac{s\overline{\Omega}' + 2\overline{M}^2(\overline{\Omega}\lambda_1 - \overline{\delta}\lambda_2)}{s^2 + (\overline{\delta}' + \overline{\delta}'')s + \overline{\delta}'\overline{\delta}'' + \overline{\Omega}'\overline{\Omega}''} \tag{2.45}$$

This transfer function is not a derivative for low Fourier frequencies. So, its magnitude plot has a zero slope with the constant gain of

$$g_{u\Phi}(\overline{M}) = -\frac{1}{\overline{u}_a}\frac{\overline{\Omega}'\overline{\delta}'' - \overline{\Omega}''\overline{\delta}'}{\overline{\delta}'\overline{\delta}'' + \overline{\Omega}'\overline{\Omega}''}, \tag{2.46}$$

that explicitly depends on $\overline{M}$. The extrema of this function are the physical based solutions of a eighth order polynomial equation which could be easily derived by differentiating (2.46). That means that the resonator performs a equal amplitude-to-phase conversion for all Fourier frequencies up to the first zero or the pole. Thus, the nonlinear regime has to be avoided, specially in oscillators, where amplitude-to-phase conversion is important.

The comparison of two transfer function states that nonlinear device transforms the amplitude noise into the phase noise for close-to-carrier Fourier frequencies. Thus, close-to-carrier noise of the resonator in a nonlinear regime could exceed that of in the linear one. This phenomenon has been experimentally observed in [14].

It has to be noted that the transfer functions from parameter fluctuations $\widetilde{k}$ to the output phase has absolutely the same dynamical properties. Thus, the conclusions has to be the same for this noise source.

So, the overall influence of the resonator nonlinearity on the signal frequency stability is negative. Indeed, even the effect of bandwidth decrease could not overcome the excess noise effect. The possible narrowing of the bandwidth is difficult to achieve in practice due to the shortness of the corresponding zone of detuning frequencies. Thus, nonlinear effects should be avoided in the further development of actual frequency sources.

2.3 Phase Noise in Oscillators

This section concerns the phase noise in harmonic oscillators from the point of view of the linear control system theory. The section revises the Leeson effect by the expansion of the theory on amplitude-phase relations in oscillators. The similar ideas have been considered by E. Rubiola and R. Brendel [34]. However, the present section goes further and considers the problem from another point of view. It systematically examines the relations between fluctuations of different oscillator parameters and the output phase. The section considers an oscillator which works out of the resonator resonance frequency. Since the amplitude noise is out of the scope of the present work, the corresponding

transfer functions are not given in this section. Though they are directly follow from the obtained results.

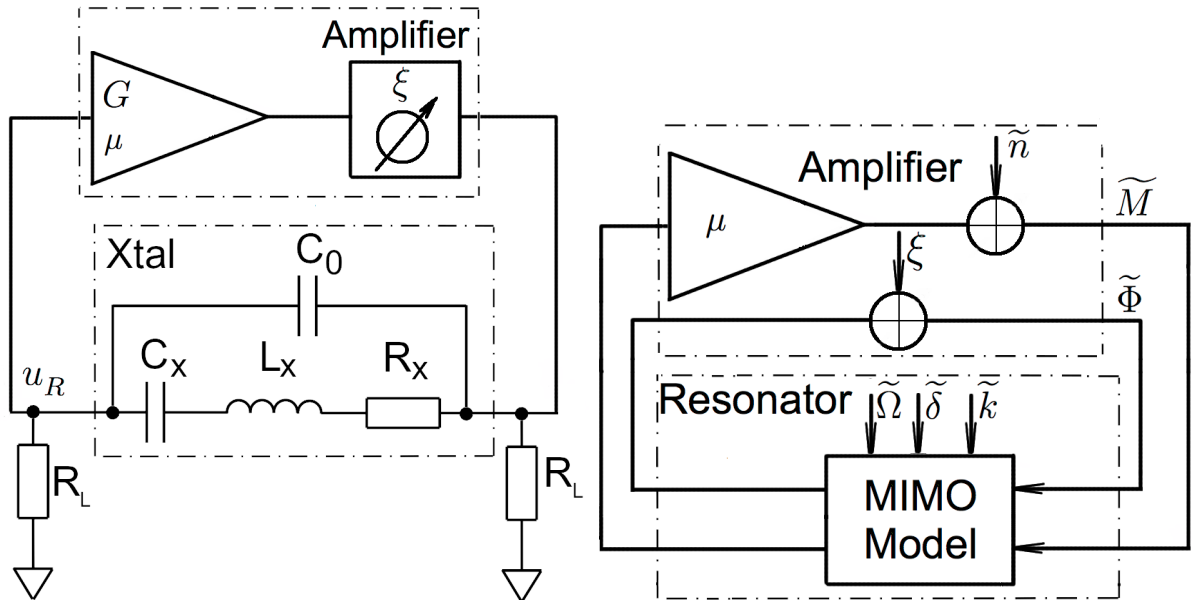

(a) General oscillator model (b) MIMO representation

Figure 2.9: Oscillator model for the phase noise analysis

The analyzed oscillator model is shown in Fig. 2.9. The system consists of a resonator inside a π-network and an amplifier. The resonator is represented with its linear MIMO model presented in Appendix A.

In order to simplify the analysis, the amplifier is considered to have an infinite input and output impedances, so the derived MIMO model is relevant. Moreover, the amplifier is modeled by a small signal gain μ and a phase sifter ξ. So, the amplifier transfer matrix in the domain of amplitude-phase fluctuations is

$$\mathbf{P} = \begin{pmatrix} \mu & 0 \\ 0 & 1 \end{pmatrix} \tag{2.47}$$

The phase shifter is introduced in order to model the typical situation when oscillator does not work exactly at the resonance frequency. In the same time, the phase shifter does not increase the order of the model, so it does not effect its complexity. Moreover, since the amplifier is a wide-band component (comparing to the resonator), the phase shifter is a good approximation of its dynamical properties. Decomposing ξ into constant $\overline{\xi}$ and variable $\widetilde{\xi}$ parts, the latter part may be considered as the amplifier phase noise. In addition to the small signal gain μ, it is needed to introduce an amplifier "large signal" gain G, as a ratio between steady state amplitudes at the amplifier output and input.

It is possible to represent the amplifier nonlinearity in the following form

$$v = a_1 u - a_3 u^3, \tag{2.48}$$

where v and u are respectively amplifier output and input signals and a_1 and a_3 are some positive constants. Linearizing this relation for zero ($\overline{v}$ and $\overline{u}$) and first order terms ($\widetilde{v}$ and $\widetilde{u}$), the following relations are obtained:

$$\mu = \frac{\widetilde{v}}{\widetilde{u}} = a_1 - \frac{9}{4}a_3\overline{u}^2, \quad G = \frac{\overline{v}}{\overline{u}} = a_1 - \frac{3}{4}a_3\overline{u}^2 \tag{2.49}$$

Also, for consistency

$$\nu = \frac{\mu}{G} = 1 - \frac{3}{2}\frac{a_3\overline{u}^2}{a_1 - \frac{3}{4}a_3\overline{u}^2}. \tag{2.50}$$

It is natural to suppose that $a_1 > a_3$, so $0 < \nu < 1$ for reasonable values of $\overline{u}$.

Scheme in Fig. 2.9(b) represent the oscillator in the amplitude-phase space with the state vector $\mathbf{Y} = \left[\widetilde{M}\ \widetilde{\Phi}\right]^T$. The system is disturbed by amplifier amplitude $\widetilde{n}$ and phase $\widetilde{\xi}$ noises as well as by resonator parameter fluctuations $\widetilde{\Omega}$, $\widetilde{\delta}$ and $\widetilde{\xi}$:

$$\mathbf{X}_a = \begin{pmatrix} \widetilde{n} \\ \widetilde{\xi} \end{pmatrix}, \mathbf{X}_r = \begin{pmatrix} \widetilde{\delta} \\ \widetilde{\Omega} \\ \widetilde{k} \end{pmatrix}.$$

So, the system governing equation may be written with the notation used in Appendix A:

$$\mathbf{Y} = \mathbf{P}(\mathbf{H}_r\mathbf{X}_r + \mathbf{H}_i\mathbf{Y}) + \mathbf{X}_a. \tag{2.51}$$

The solution of equation (2.51) is straightforward:

$$\mathbf{Y} = (\mathbf{I} - \mathbf{P}\mathbf{H}_i)^{-1}(\mathbf{P}\mathbf{H}_r\mathbf{X}_r + \mathbf{X}_a), \tag{2.52}$$

where $\mathbf{I}$ is the identity matrix. This equation gives the linear transfer functions from parameter small changes to generated signal amplitude and phase fluctuations. Let us consider some of these transfer functions.

The linear transfer function from the amplifier phase noise to the output phase is given as follows:

$$\mathscr{H}_{\xi\Phi}(s) = \frac{\widetilde{\Phi}}{\widetilde{\xi}} = 1 + \frac{\overline{\delta}}{s} + \frac{\overline{\Omega}^2}{s}\frac{1-\nu}{s + \overline{\delta}(1-\nu)} \tag{2.53}$$

The first two terms of transfer function (2.53) represents the well-known Leeson effect (see Chapter 1) with the Leeson frequency $f_L = \frac{1}{2\pi}\overline{\delta} = \frac{1}{2\pi}\frac{\overline{\omega}_0}{2Q_L}$. The third term is a correction due to the amplitude-phase relations in the resonator. Obviously this term disappears for the oscillator working exactly at the resonance frequency $\overline{\omega}_0$. In other cases, the additional term could slightly change the Leeson frequency.

The amplifier amplitude noise transforms to the oscillator phase noise as follows:

$$\mathscr{H}_{n\Phi}(s) = \frac{\widetilde{\Phi}}{\widetilde{n}} = -\frac{\overline{M}}{G}\frac{\overline{\Omega}}{s + \overline{\delta}(1-\nu)} \tag{2.54}$$

where $\overline{M}$ is a steady state amplitude of the oscillations. It can be found making assumption on amplifier nonlinearities. Transfer function (2.54) disappears for the oscillator working exactly at the resonance frequency $\overline{\omega}_0$. Unlike the previous case, it does not change the close-to-carrier slope of the PSD for the input fluctuations.

Fluctuations of the resonator damping $\widetilde{\delta}$ transforms to the oscillator phase noise according to the transfer function

$$\mathscr{H}_{\delta\Phi}(s) = \frac{\widetilde{\Phi}}{\widetilde{\delta}} = -\frac{\overline{\Omega}}{s}\frac{1-\nu}{s+\overline{\delta}(1-\nu)}. \tag{2.55}$$

As before, this transfer function vanishes for the case $\omega = \overline{\omega}_0$. But this time the slope of the close-to-carrier fluctuation PSD is multiplied by f^{-2}.

Fluctuations of the resonator resonance frequency $\widetilde{\omega}_0$ are approximately equivalent to the fluctuations of the dumping frequency $\widetilde{\Omega}$, so

$$\mathscr{H}_{\omega\Phi}(s) = \frac{\widetilde{\Phi}}{\widetilde{\omega}_0} \approx \frac{\widetilde{\Phi}}{\widetilde{\Omega}} = \frac{1}{s}. \tag{2.56}$$

This transfer function is pure integrative. This implies a multiplication of the spectral density by f^{-2} for the whole range of Fourier frequencies.

Finally, fluctuations of the scaling parameter transform to the phase noise according to the transfer function:

$$\mathscr{H}_{k\Phi}(s) = \frac{\widetilde{\Phi}}{\widetilde{k}} = -\frac{\overline{\Omega}}{\overline{k}}\frac{1}{s+\overline{\delta}(1-\nu)}. \tag{2.57}$$

This transfer function exists only for $\omega \neq \overline{\omega}_0$. Even in this case, the transfer function does not change the slope of the close-to-carrier PSD.

Transfer functions (2.53), (2.54), (2.55), (2.56) and (2.57) are an extension of the standard Leeson effect on oscillator parameter fluctuation in the presence of the amplitude-phase coupling. They show the impact of the corresponding noise source into the oscillator closed loop phase noise. In fact, all these transfer function could be classified into two kinds: 1) transfer functions that have a integrative denominator multiplier, and so they introduce the change of PSD slope near the carrier ($\mathscr{H}_{\xi\Phi}(s)$, $\mathscr{H}_{\delta\Phi}(s)$ and $\mathscr{H}_{\omega\Phi}(s)$); 2) transfer function that do not have an integrative multiplier and, thus, they do not change the PSD slope near the carrier ($\mathscr{H}_{n\Phi}(s)$, $\mathscr{H}_{k\Phi}(s)$).

The resulting phase noise is a superposition of all phase noise spectra multiplied by the corresponding squared transfer functions (supposing that all the noise sources are uncorrelated):

$$\begin{aligned} S_\varphi(f) = \mathscr{H}^2_{\xi\Phi}(f)S_\xi(f) + \mathscr{H}^2_{\delta\Phi}(f)S_\delta(f) + \mathscr{H}^2_{\omega\Phi}(f)S_\omega(f) + \\ + \mathscr{H}^2_{n\Phi}(f)S_n(f) + \mathscr{H}^2_{k\Phi}(f)S_k(f). \end{aligned} \tag{2.58}$$

It is usually considered that the transfer functions of the first type dominate. Moreover, only first two terms of transfer function (2.53) are considered. But, at least, from the theoretical point of view, it is possible that for some range of Fourier frequencies, noise source with the second type transfer functions become dominant. This situation can change the usual picture of the oscillator PSD (see section 1.3.3, Fig. 1.5).

Let us consider a usual case for the BAW oscillators $f_c > f_L = \frac{1}{2\pi}\overline{\delta}$. To simplify the discussion, it is supposed without lack of generalization that noise sources $\widetilde{\xi}$ and $\widetilde{k}$ (representing both transfer function types) are dominant over all the rest. Also, it is considered that $S_k(f)$ has a slope of f^{-2} for close-to-carrier Fourier frequencies (this could be a case of the random-walk due to the temperature). In the same time $S_\xi(f)$ is proportional to f^{-1} for frequencies less than the corner frequency f_c and f^0 for higher Fourier frequencies.

The impact of the transfer function $\mathscr{H}_{k\Phi}$ on $S_k(f)$ is twofold. First, the transfer function multiplies the spectra by

$$\beta = \frac{\overline{\Omega}}{\overline{k\delta}(1-\nu)} = \frac{2\overline{\Omega Q}_L}{\overline{k}\overline{\omega}_0(1-\nu)} \tag{2.59}$$

inside the transfer function bandwidth. This means that for resonators with higher Q_L (this is the case of cryogenic oscillators), the corresponding noise multiplication coefficient is higher. Consequently, the noise impact into the total noise is more significant. Second, for frequencies higher than a cut of value $\overline{\delta}(1-\mu) = 2\pi f_L(1-\mu)$, the spectrum is multiplied by f^{-2} (outside the transfer function bandwidth). These transformations are shown in Fig. 2.10, (A).

Transfer function $\mathscr{H}_{\xi\Phi}$ modifies the corresponding phase noise PSD according to the standard Leeson effect. Here, the third term in equation (2.53) is neglected for simplicity. This transformation is shown in Fig. 2.60, (B).

The resulting oscillator phase noise PSD is

$$S_{\varphi T}(f) = S_A(f) + S_B(f) = \mathscr{H}^2_{k\Phi}(f)S_k(f) + \mathscr{H}^2_{\xi\Phi}(f)S_\xi(f). \tag{2.60}$$

Let the resonator loaded quality factor is high enough. Then it is possible that the first term of equation (2.60) overlaps the second. Thus, for some range of frequencies $S_A(f)$ hides the standard Leeson effect ($S_B(f)$) introducing two additional spectrum slopes (f^{-2} and f^{-4}). This effect is presented in Fig. 2.10, (C). The resulting PSD is shown with a solid blue line. A dashed green line is due to $S_B(f)$, and a dashed red line is $S_A(f)$.

So, if Q_L is high enough, then for some range of frequencies f^{-2} and f^{-4} noises of $S_A(f)$ dominate over f^{-3}. This situation gives the following order of slopes starting from the carrier:

1. f^{-3} - the $\widetilde{\xi}$ flicker noise multiplied by f^{-2} ($\mathscr{H}^2_{\xi\Phi}(f)f^{-1}$ for $f < f_L$);

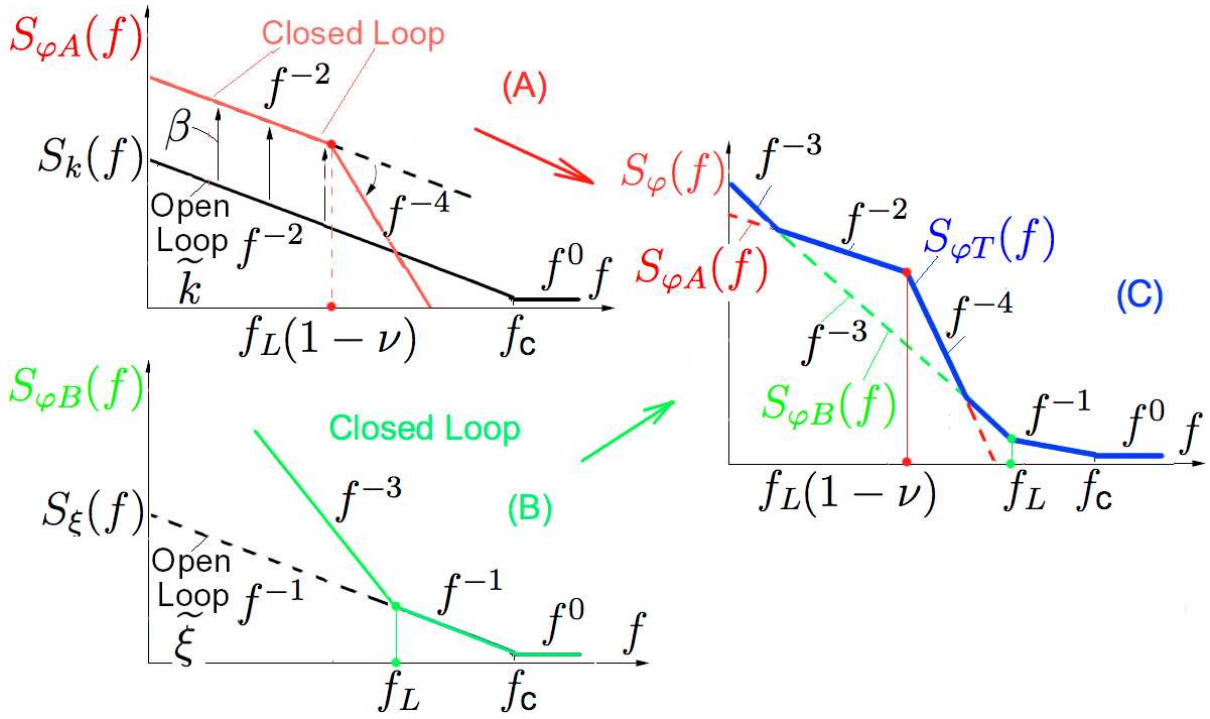

Figure 2.10: Predicted oscillator pass noise PSD for an oscillator with high Q: (A) the effect of the closed loop (transfer function $\mathscr{H}_{k\Phi}$) on $S_k(f)$, (A) the effect of the closed loop (transfer function $\mathscr{H}_{\xi\Phi}$) on $S_\xi(f)$, (C) - possible resulting PSD

2. f^{-2} - the $\widetilde{k}$ random walk multiplied by β ($\mathscr{H}^2_{k\Phi}(f)f^{-2}$ for $f < f_L(1-\mu)$);

3. f^{-4} - the $\widetilde{k}$ random walk multiplied by βf^{-2} ($\mathscr{H}^2_{k\Phi}(f)f^{-2}$ for $f > f_L(1-\mu)$);

4. f^{-1} - the $\widetilde{\xi}$ flicker noise ($\mathscr{H}^2_{\xi\Phi}(f)f^{-1}$ for $f_L < f < f_c$);

5. f^0 - the $\widetilde{\xi}$ white ($\mathscr{H}^2_{\xi\Phi}(f)f^{-1}$ for $f > f_c$).

Also, a short range of the f^{-3} noise possibly could exists between f^{-4} and f^{-1} due to the $\widetilde{\xi}$ flicker noise multiplied by f^{-2}.

Concluding the section, it is needed to state that the output phase noise PSD of an oscillator could be different from that predicted by the standard Leeson relations (Fig. 1.5). This happens because standard formulation of the effect does not takes into account amplitude-phase relations and does not consider fluctuations of some important oscillator parameters. It is shown that even for feedback oscillators with usual topologies, a PSD could have additional spectrum slopes. This is the case of oscillators based on resonators with very high quality factors. Such high quality factors could be obtained in the liquid helium temperature range. An experimental example of this effect is shown in subsection 7.3.1 for a cryogenic MOSFET-based oscillator. This subsection demonstrates

a measured PSD with the effects that are shown in Fig. 2.10 for the close-to-carrier Fourier frequencies.

2.4 Some Observations on the Resonator KLM Model

This section presents how an advanced physical model of a BAW device could lead to the prediction of its fractional dynamical properties (properties of the $\frac{1}{2}$-order). These properties may be one of the possible explanations of the f^{-1} noise.

A conventional lumped equivalent circuit is used for modeling different types of BAW resonators in the sections above. This model consists of series connection of an inductor, a capacitor and a resistance. However, earlier works dedicated to BAW devices proposed another model based on distributed elements. It can be found in [35, 36, 37]. For the further analysis we use the further extension of this model known as a lineal model proposed by Krimtholz, Leedom, and Matthaei (KLM) [38]. Unfortunately, this model is never considered for the analysis of the noise in BAW resonators. Recently, this model was revised and used to account for the nonlinear effects occurring in acoustic devices [39, 40].

The equivalent circuit of the KLM model is shown in Fig. 2.11. This circuit includes a transmission line that is built based on equivalences between acoustic wave and electrical devices (voltage is equivalent to force and current to velocity). Two transmission line parameters, the line characteristic impedance Z_{ch} and phase velocity v_{ph}in this transmission line are found as:

$$Z_{ch} = \rho v_{ph} A, \quad v_{ph} = \sqrt{\frac{c^D}{\rho}}, \tag{2.61}$$

where A the area of the electrodes, c^D is the stiffened elasticity, and ρ is the density of the piezoelectric material, respectively. Other parameters of the equivalent circuit (Fig. 2.11) are [38, 39]:

$$\Phi = \frac{\omega Z_{ch}}{2h} \sin^{-1} \frac{\omega l}{2v_{ph}}, \quad C_0 = \varepsilon^S \frac{A}{l}, \quad X_1 = \frac{h^2}{\omega^2 Z_{ch}} \sin \frac{\omega l}{2v_{ph}}, \tag{2.62}$$

where h is a piezoelectric constant of the crystal, ε^S is a dielectric constant and l is its thickness.

Since we consider the case of high resonant frequencies, we neglect X_1 and C_0 for the further analysis. In fact, the same simplification is made in the previous subsections.

In addition to the original work, we introduce the losses mechanism which is modeled as series resistance in the equivalent circuit. Also, it is assumed that the distribution of transmission line parameters is not uniform, so that they depend on the distance from an input. Thus, the electrical equivalent model of the BAW resonator is a losser transmission

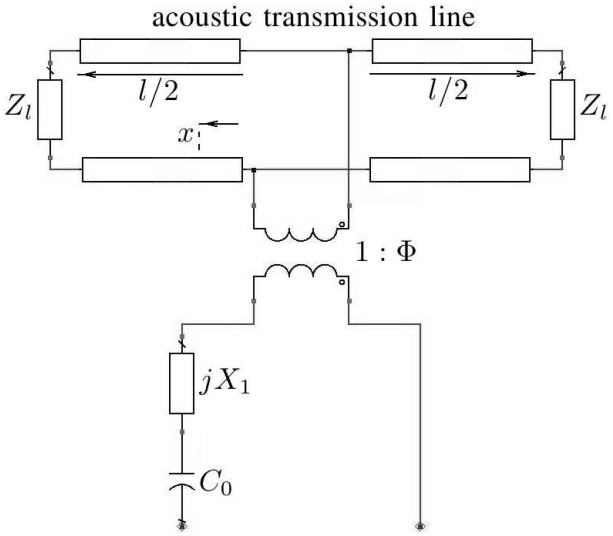

Figure 2.11: KLM model of a BAW resonator

line governed with a system of the partial differential equations (PDEs):

$$\begin{cases} \dfrac{\partial v(t,x)}{\partial x} = R(x)i(t,x) + \dfrac{\partial L(x)i(t,x)}{\partial t}, \\ \dfrac{\partial i(t,x)}{\partial x} = C(x)\dfrac{\partial v(t,x)}{\partial t}, \end{cases} \tag{2.63}$$

where $R(x)$, $L(x)$ and $C(x)$ are the equivalent specific series resistance, the specific series equivalent inductance and specific parallel equivalent capacitance respectively. These parameters correspond to equivalent R-L-C parameters in the lumped model.

First step is to apply the Laplace transform in the time domain:

$$\begin{cases} -\dfrac{dV(s,x)}{dx} = (R(x) + L(x)s)I(s,x) = Z(s,x)I(s,x), \\ -\dfrac{dI(s,x)}{dx} = (G(x) + C(x)s)V(s,x) = Y(s,x)V(s,x), \end{cases} \tag{2.64}$$

where $V(s,x)$ and $I(s,x)$ are a Laplace transforms of the voltage $v(t,x)$ and the current $i(t,x)$, and s is the Laplace variable in the time domain.

System (2.64) is a system of ordinary differential equations with respect to $V(s,x)$ and $I(s,x)$. For its approximate solution, the change of the independent variable x is introduced. The change of the variable is made according to the relation:

$$\frac{dh}{dx} = \sqrt{Z(s,x)Y(s,x)} = \gamma(s,x). \tag{2.65}$$

So, the system appears in the form (arguments of all parameters and variables are omitted

further):

$$\begin{cases} -\dfrac{dV}{dh} = \sqrt{\dfrac{Z}{Y}}I, \\ -\dfrac{dI}{dh} = \sqrt{\dfrac{Y}{Z}}V, \end{cases} \tag{2.66}$$

Substitution of the second equation into the first one gives

$$\frac{d^2I}{dh^2} + \rho\frac{dI}{dh} - I = 0, \tag{2.67}$$

where

$$\rho = \sqrt{\frac{Y}{Z}}\frac{d}{dh}\sqrt{\frac{Z}{Y}} = \frac{1}{2}\frac{d}{dh}\ln\frac{Z}{Y} \tag{2.68}$$

For further simplification, the following substation of I could be considered:

$$I(s,h) = \exp\Big(-\frac{1}{2}\int \rho dh\Big)\sigma(s,h) = \Big(\frac{Y}{Z}\Big)^{\frac{1}{4}}\sigma(s,h), \tag{2.69}$$

that gives

$$\frac{d^2\sigma}{dh} = \Big(1 + \frac{\rho^2}{4} + \frac{1}{2}\frac{d\rho}{dh}\Big)\sigma. \tag{2.70}$$

If parameter variations inside the resonator are smooth and small enough in comparison with their absolute values, it is possible to neglect both terms $\frac{d\rho}{dh}$ and ρ^2. So, the approximate solution of equation (2.70) is given simply as

$$\sigma(s,h) = \cosh(h)\sigma(s,0) + \sinh(h)\frac{d\sigma(s,0)}{dh}. \tag{2.71}$$

Taking into account both substations ((2.65) and (2.69)), the result could be written in the form:

$$\begin{aligned} &I(s,x)\Big(\frac{Z(s,x)}{Y(s,x)}\Big)^{\frac{1}{4}} = I(s,0)\Big(\frac{Z(s,0)}{Y(s,0)}\Big)^{\frac{1}{4}}\cosh\int\gamma(s,x)dx + \\ &+\frac{1}{\gamma(s,x)}\Big[I(s,0)\frac{d}{dx}\Big(\frac{Z(s,0)}{Y(s,0)}\Big)^{\frac{1}{4}} - \Big(\frac{Z(s,0)}{Y(s,0)}\Big)^{\frac{1}{4}}Y(s,0)V(s,0)\Big]\sinh\int\gamma(s,x)dx. \end{aligned} \tag{2.72}$$

or

$$\begin{aligned} I(s,x) = \Big[I(s,0)\Big(\cosh\int\gamma(s,x)dx + \frac{1}{4}\frac{d}{dx}\ln\frac{Z(s,0)}{Y(s,0)}\frac{1}{\gamma(s,x)}\sinh\int\gamma(s,x)dx\Big) - \\ -V(s,0)\frac{Y(s,0)}{\gamma(s,x)}\sinh\int\gamma(s,x)dx\Big]\Big(\frac{Y(s,x)Z(s,0)}{Z(s,x)Y(s,0)}\Big)^{\frac{1}{4}}. \end{aligned} \tag{2.73}$$

Applying the same procedure, it is possible to derive the similar expression for $V(s,x)$:

$$\begin{aligned} V(s,x) = \Big[V(s,0)\Big(\cosh\int\gamma(s,x)dx + \frac{1}{4}\frac{d}{dx}\ln\frac{Y(s,0)}{Z(s,0)}\frac{1}{\gamma(s,x)}\sinh\int\gamma(s,x)dx\Big) - \\ -I(s,0)\frac{Z(s,0)}{\gamma(s,x)}\sinh\int\gamma(s,x)dx\Big]\Big(\frac{Z(s,x)Y(s,0)}{Y(s,x)Z(s,0)}\Big)^{\frac{1}{4}}. \end{aligned} \tag{2.74}$$

So, the system input impedance in any point is

$$Z(s,x)=\Big(\frac{Z(s,x)Y(s,0)}{Y(s,x)Z(s,0)}\Big)^{\frac{1}{2}}\cdot \\ \frac{Z(s,0)\Big(\cosh\int\gamma(s,x)dx+\frac{1}{4}\frac{d}{dx}\ln\frac{Y(s,0)}{Z(s,0)}\frac{1}{\gamma(s,x)}\sinh\int\gamma(s,x)dx\Big)-\frac{Z(s,0)}{\gamma(s,x)}\sinh\int\gamma(s,x)dx}{\Big(\cosh\int\gamma(s,x)dx+\frac{1}{4}\frac{d}{dx}\ln\frac{Z(s,0)}{Y(s,0)}\frac{1}{\gamma(s,x)}\sinh\int\gamma(s,x)dx\Big)-Z(s,0)\frac{Y(s,0)}{\gamma(s,x)}\sinh\int\gamma(s,x)dx}. \tag{2.75}$$

where $Z(s,0)$ is the input impedance.

Impedance and conductance distributions could be represented as follows:

$$Z(s,x)=Z(s,0)(1+\chi_z(s,x)),\quad Y(s,x)=Y(s,0)(1+\chi_y(s,x)), \tag{2.76}$$

where $\chi_z(s,x)\ll 1$ and $\chi_y(s,x)\ll 1$. In this case, relations (2.73)-(2.75) have at least two multipliers that could be a source of fractional order dynamical relations. First, the coefficient

$$\Big(\frac{Z(s,x)Y(s,0)}{Y(s,x)Z(s,0)}\Big)^{\frac{1}{2}}=\sqrt{\frac{1+\chi_z(s,x)}{1+\chi_z(s,x)}}, \tag{2.77}$$

potentially could have fractional dynamic properties on the limited range of frequencies for certain distributions. For example, if the parameters are distributed linearly

$$\begin{array}{l} Z(s,x)=Z_0(s)+xZ_1(s)=R_0+sL_0+x(R_1+sL_1),\\ Y(s,x)=Y_0(s)+xY_1(s)=sC_0+x(G_1+sC_1). \end{array} \tag{2.78}$$

then

$$\sqrt{\frac{1+\chi_z(s,x)}{1+\chi_z(s,x)}}=\sqrt{\frac{1+\frac{Z_1}{Z_0}x}{1+\frac{Y_1}{Y_0}x}}=\sqrt{\frac{sC_0}{R_0+sL_0}\frac{s(L_0+L_1x)+R_1+R_0}{s(C_0+xC_1+xG_1)}} \tag{2.79}$$

has differentiation of the $\frac{1}{2}$-order for low frequencies.

Second, coefficient $\frac{1}{\gamma(s,x)}\sinh\int\gamma(s,x)dx$ could have the same properties. This fact is numerically demonstrated, for example, for the case of linear distribution of both $Z(s,x)$ and $Y(s,x)$ along the resonator length. Indeed, if relations (2.78) are valid then after the first order expansion of sinh:

$$\frac{1}{\gamma(s,x)}\sinh\int\gamma(s,x)dx\approx\frac{1}{\gamma(s,x)}\int\gamma(s,x)dx=\frac{Z_1Y_0+2Z_1Y_1x+Z_0Y_1}{4Z_1Y_1}- \\ +\frac{Y_0^2Z_1^2-2Z_1Z_0Y_1Y_0+Z_0^2Y_1^2}{8\sqrt{Z_1Y_1ZY}}\Big[\frac{\ln(2)}{Z_1Y_1}+\ln\Big(\sqrt{\frac{Z_1}{Y_1}}Y_0+2\sqrt{Z_1Y_1}+2\sqrt{ZY}\Big)\Big]. \tag{2.80}$$

The ability of this coefficients produce dynamical relations of the order $\frac{1}{2}$ can be shown numerically for some range of values.

For example, let some hypothetical noise source be a voltage noise source $u(s)$ located at the end of the transmission line of the length l. So, the voltage noise of this source is measured at its input terminals is given as

$$v(s) = 4\Big(\frac{Y(s,l)Z(s,0)}{Z(s,l)Y(s,0)}\Big)^{\frac{1}{4}} \frac{4\nu\lambda - \frac{d}{dx}\frac{Y(s,0)}{Z(s,0)}}{16\lambda^2\big(\nu^2 - Y(s,0)Z(s,0)\big) - \big(\frac{d}{dx}\frac{Y(s,0)}{Z(s,0)}\big)^2}\lambda u(s). \tag{2.81}$$

where

$$\lambda = \gamma(s,l)\sinh^{-1}\int\limits_0^l \gamma(s,x)dx, \quad \nu = \cosh\int\limits_0^l \gamma(s,x)dx \tag{2.82}$$

Thus, the spectral density of the resulting noise directly is proportional to the square root of coefficient (2.79) and inversely proportional to coefficient (2.80). As it is shown, both coefficients could produce the dynamical relations of the fractional order.

So, the present section considers the possibility of the KLM model to predict the fractional dynamical properties of the BAW resonators. It is shown that this distributed model alongside with an assumption on the nonuniform distribution of the resonator parameters give the dynamical relations of the fractional order. This phenomenon cannot be predicted by the standard analysis of the model with lumped parameters. However, noise and fluctuations in the considered model have to be analyzed further in more details.

Chapter 3

Overview of The Cryogenic Test-Bench

This chapter concerns a cryogenic test-bench as a base for all experiments of the present work. Special attention is devoted to main instabilities originated from the cryogenic system.

3.1 Components and General Description

Experimental difficulties at temperatures close to that of liquid helium (4.2K) have probably slowed down the development in low-temperature electronics in the second part of the XX century. Nowadays cryogenic tools are more sophisticated and efficient than their ancestors. Recent progress on cryogenic coolers have improved and simplified experimental conditions and gave burst to many cryogenic applications. Thus, cryostats can be substituted for cryogenic generators, more easy to use and not limited in experiment duration. Moreover, further progress is able to shift the area of cryogenics from the pure science to wide real-world applications.

An experimental bench is based on a two-stage pulse-tube cryocooler which can absorb up to 1 W at temperatures lower than 10K, typically 4.2K. The core of the experimental set up is a cold head, where a device under test (DUT) is mounted on and enclosed in a vacuum chamber. Fig. 3.1 presents a general view of the experimental set up.

The second stage acts like a pump of calories whereas the DUT is slightly warmed up by means of a resistor associated to a sensor whose temperature can be externally controlled. From the measurement of the sensor temperature, the external feedback can control the DUT temperature with an accuracy of $\pm$2mK by heating more or less. The DUT can be a resonator or any other electronic device as well as an electronic system embedded. The DUT is attached to or inserted into a piece of the oxygen-free copper.

Figure 3.1: General view of the cryogenerator system and measurement devices

Now, let us consider different parts of the cryogenic set up separately.

Helium Compressor This system is built on an F-70H helium compressor (see Fig. 3.2) from Sumitomo Heavy Industries (SHI) which is compatible with a cold head of the Gifford-McMahon cycle or, as in case of the present system, with a pulse tube. Produced helium pressure is approximately 16.5 Bar. Consumption of electrical power of this device varies from 6.7 to 7.2 kW. The compressor thermal emission is considerable, thus it requires permanent external refrigerating by a cold water (about 15°C) system. For more information about the F-70H helium compressor see [41].

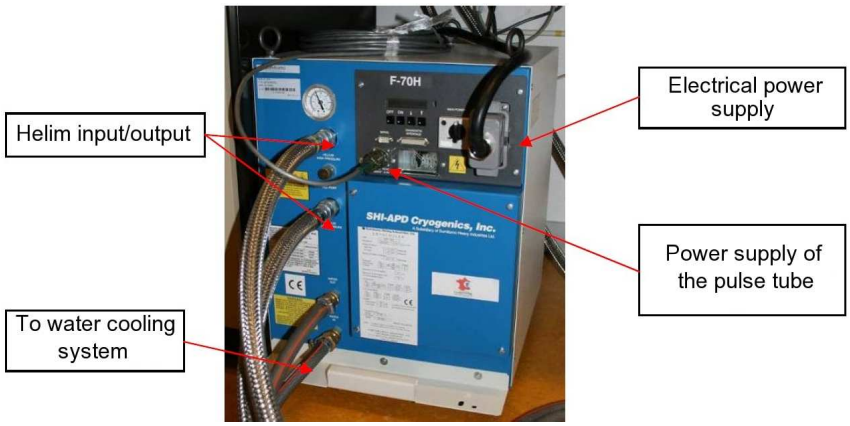

Figure 3.2: Helium compressor

Pulse Tube Cryocooler The cryocooler used in the present system is the helium pulse tube RP-082A from SHI [42, 43]. As it was mentioned above it consists of two stages: the first (higher-temperature) stage is able to absorb up to 40 W at 50K; the second stage takes up 1 W at 4.2K. The second stage temperature can go down to almost 3K if thermal losses are minimized (i.e. no cables and wires installed). The thermal losses

are mainly introduced with connecting cables needed for measurements and environmental control. As it is said abobe, the DUT is attached to a copper block which is temperature controlled. The maximum volume of the DUT attached at the second stage is about 1 dm^3. The cryocooler is shielded with two protection screens: a vacuum chamber and

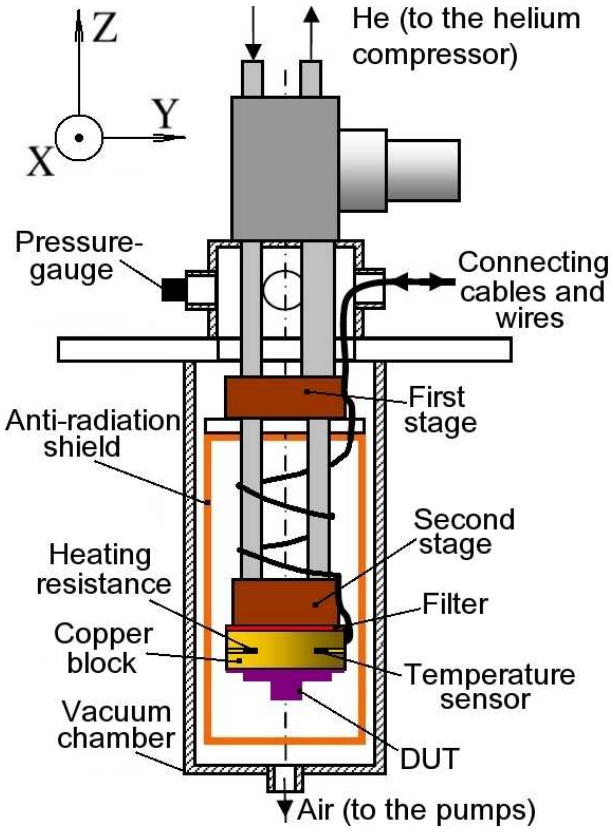

Figure 3.3: Schematic view of the experimental set up (pulse-tube cryocooler)

an anti-radiation shield. The former prevents the temperature losses due to the air heat conduction. Both primary and secondary pumps are cut off from the chamber during the whole measurement time. This shield has a room temperature and is made with light-reflecting material. The anti-radiation shield is attached to the first cryocooler stage with the temperature of about 50K. Its inner and outer surfaces are covered with the specially fabricated light-reflecting paper to reduce radiation losses of the second stage. Fig. 3.3 also shows different connecting cables and wires used for: 1) signals needed to control and measure the environment parameters such as a vacuum level and actual temperature, 2) RF signals from the DUT.

Pulse tube operation principles are close to that of the Stirling cycle [44] which engenders difference in the temperature with a help of the pressure variation and vice-versa. This cycle is a closed loop of the fluid and it consists of the following main parts: 1) a compressor which is needed to create pressure variation and gas charge, 2) the regenerator needed for thermal accumulation, 3) a tube and a dephasing system which permit to add

some pressure variation in a passive mode. In peculiar, the pulse tube is in a passive mode of the operation: usage of valves for the gaz movement optimization and the pressure in the regenerator opposite to a system of cold pistons. The helium pressure varies from 20 to 22 Bar inside the cold head. The operation principle is shown in Fig. 3.4.

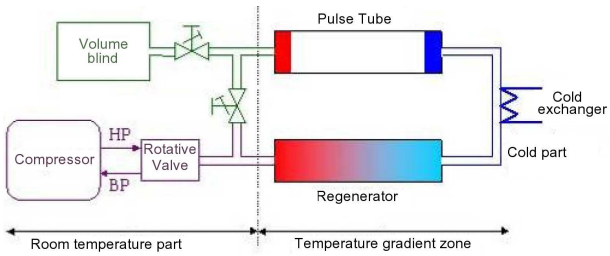

Figure 3.4: Closed cycle pulse tube operational principle

A Cold Water System is a system of the cold water generation for compressor refrigerating, which is build with Oreade9 cooler from Filtres Monnet (see Fig. 3.5(a)). Its power consumption is 8.8 kW.

Pump System A system of pumps (see Fig. 3.5(b)) consists of first and second stage pumps, first and second stage pressure measurement equipment and a security subsystem. This system creates a vacuum in an enclosure around the pulse tube in order to the reduce heat exchange by convection. The security subsystem is intended to separate the vacuum chamber from the ambient air in a case of the electricity cut-off. The vacuum level inside the chamber is about 10^{-7} mbar: both primary. Usually the pumps could be cut-off from the chamber and switched off the during measurements.

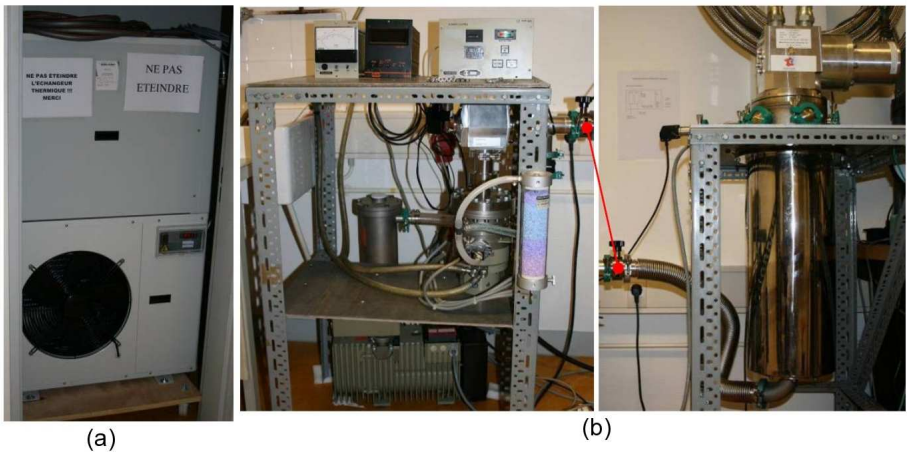

Figure 3.5: Cold water system (a) and pump system (b)

The block diagram of the whole cryogenic set up is shown in Fig. 3.6.

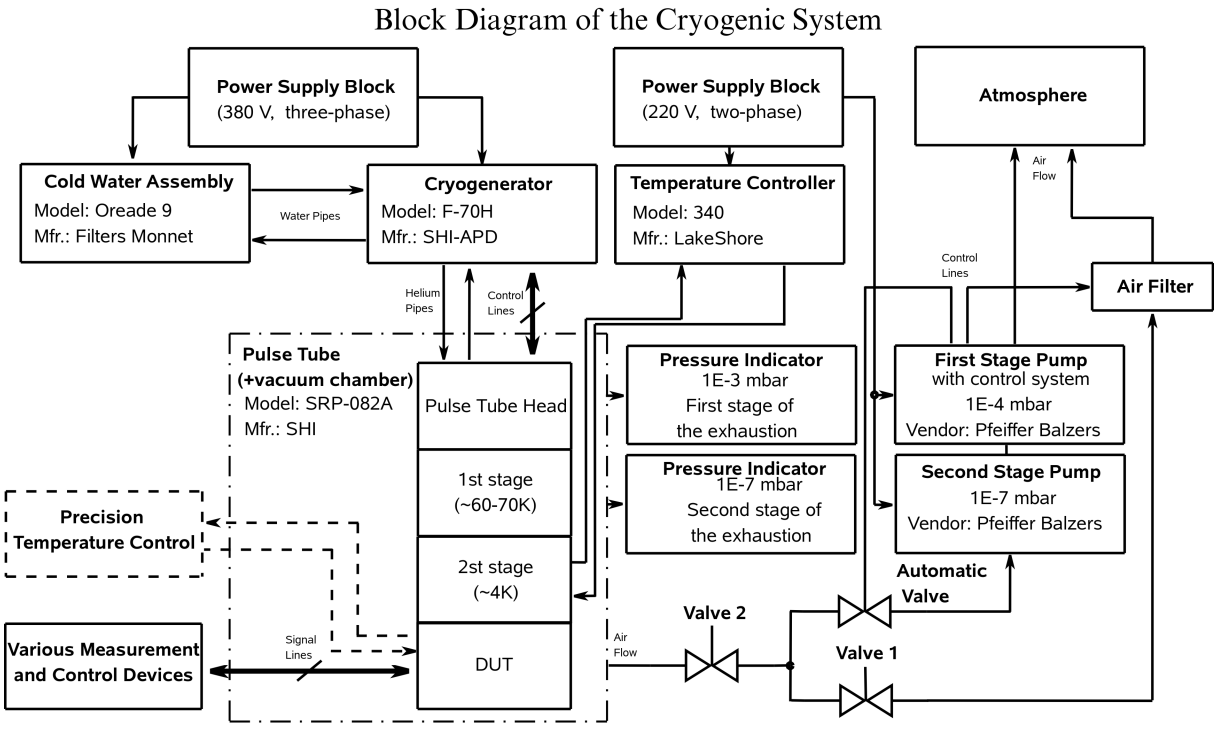

Figure 3.6: Block diagram of the cryogenic set-up

From the description of the cryogenic system it is clear that the DUT is a subject of external disturbances coming from the system itself. The main of these disturbances are temperature fluctuations and oscillations and vibrations. Both influences mainly come from the working principe of the cryogenic system which uses helium pulsations.

3.2 Temperature Fluctuations

The temperature of the DUT is monitored with a system based on LakeShore Model 332 Temperature Controller [45]. The system is equipped with two sensors: CERNOX (sensor B) and germanium (sensor A). The CERNOX sensor is calibrated to operate in the temperature range from 3K to 300K. In the same time, germanium sensor is only designed for operation under 80K (manually calibrated with the help of sensor A).

The periodical temperature fluctuations of the cryocooler second stage due to the helium pulsation are about 0.3K. The power spectral density (PSD) of temperature fluctuations of the second stage in the steady state consists of an f^{-2} region for frequencies less than about 10^{-2} Hz and an f^{0} region for higher frequencies. In addition, a clear spurious frequency of 1.7 Hz and its harmonics are present due to temperature pulsations.

In order to improve the thermal environment of the DUT, passive and active temperature stabilization methods are used. First, a thermal filter is introduced between the second stage and the copper block (see Fig. 3.3). The filter reduces the temperature pulsation down to 15mK, but increases an absolute temperature difference between these parts. This difference mainly depends on a number of cables connected to the DUT. Second, the active temperature regulation is implemented with a 332 Temperature Controller, the CERNOX sensor and a 20 Ohms heating resistor which is able to dissipate up to 25 W. The sensor and the actuator are installed inside the block of the oxygen-free copper directly under the filter. The control system eliminates the f^{-2} region in the temperature fluctuation spectrum (at least for frequencies higher than 10^{-3} Hz) and reduces the temperature pulsation down to 5mK. The power spectral densities of temperature fluctuations in both the second stage (unregulated and non-filtrated part) and the DUT (after filtering with active regulation) is shown in Fig. 3.7.

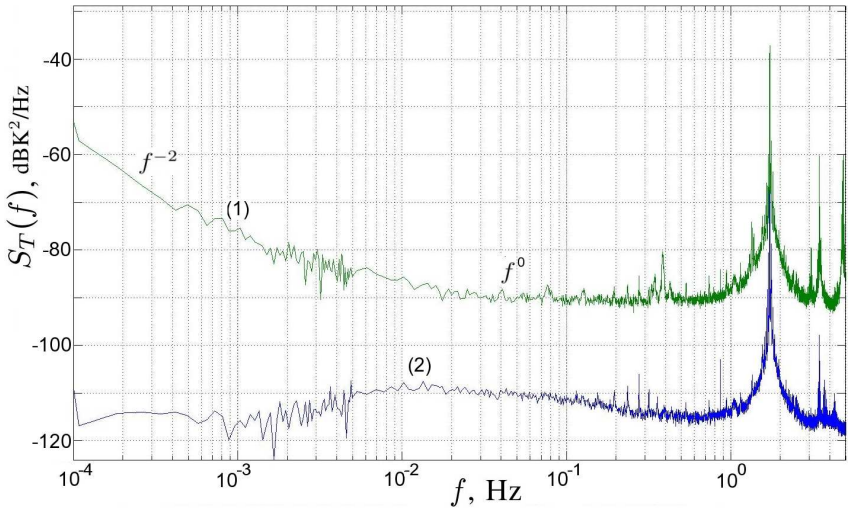

Figure 3.7: Power spectral density of temperature fluctuations: (1) - at the cryocooler second stage, (2) - at the DUT level

Fig. 3.7 shows that the remaining noise due to temperature instabilities at the DUT level (with no thermal load or cables installed) is almost a white noise in the frequency range of $10^{-3} - 10^{0}$ Hz.Although it has to be noted that the f^{-2} spectrum slope can still appear at this range of frequencies at the DUT level when measurements are performed during exponential transients in the whole thermo-mechanical system (cryogenerator, cables, DUT, etc.). This happens when the thermal load is high enough and connection cables thermally relate regulated and unregulated parts of the system. This point is discussed later.

Further improvement of the DUT temperature conditions may be made by the following means 1) materials with higher thermal capacitance (usually they have also lower thermal conductivity, and as a result the higher absolute temperature difference between the DUT and the second stage could be obtained); 2) second (more precise) temperature control directly near the DUT; 3) another anti-radiation shield at the level of the second

stage (it has to prevent DUT temperature fluctuations caused by the radiation heat exchange with the first shield; this shield, as well as the whole first stage, is not temperature regulated and, thus, it is not stable).

3.3 Vibration

Another type of cryocooler environmental disturbances is vibration. According to the cryocooler specification, the permanent pulsation of helium inside the pulse-tube causes DUT vibrations with an amplitude $A = 10$ μm and a frequency $f = 1.7$ Hz. This information is not enough for rigorous analysis of the environmental instabilities. So, some measurements of the cryocooler second stage acceleration are made.

A block diagram of a vibration measurement system is shown in Fig. 3.8. The cryocooler second stage acceleration is measured with a high sensitivity piezoelectric accelerometer A/600. The sensitivity of the accelerometer at cryogenic conditions is not known, so the measurement results are not graduated in this work. The accelerometer attached in different configurations to a second stage of the cryocooler. The measurement device connects to a home-made charge amplifier. The voltage at the output of the amplifier is acquired with a high performance real-time system ADwin-Pro II with an ADC module [46]. The data are transmitted to a personal computer with a fast Ethernet interface. The sampling frequency of all vibration measurements is 100 kHz (the high sampling frequency is used to reduce the spectral aliasing).

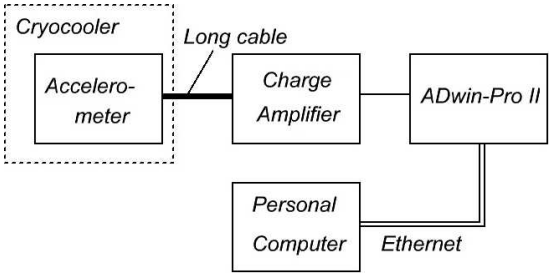

Figure 3.8: Vibration measurement system

The accelerometer was installed in three positions in order to measure second stage vibrations in three dimensions. The bottom view of these installations is shown in Fig. 1. In two horizontal variants the accelerometer is connected to the second stage with two blocks of aluminum and copper (Fig. 1(a), Appendix B and Fig. 1(b), Appendix B). The side view of these installations is presented in Fig. 2, Appendix B.

For each measurement the germanium temperature sensor is attached directly to the accelerometer. For the measurements with the horizontal orientation of the accelerometer, its temperature is about 8K. For the vertical orientation, accelerometer surface temperature is 6K. In both cases the second cryocooler stage is regulated at 3.8K. The temperature

difference is due to high thermal resistance of the aluminum block and the accelerometer itself.

The power spectral densities (PSDs) of the second cryocooler stage acceleration is shown in Fig. 3, Appendix B. The noise floor is the measurement system noise (see Fig. 3.8, Appendix B) acquired when the accelerometer is replaced with a constant capacitor (the cryocooler is turned on). This measurement is made with a sampling frequency of 1 kHz. The measurement results suggest that the DUT is a subject of f^{-1} instabilities in the frequency range of $10^{-2} - 10^{1}$ Hz due to vibration in the vertical axis.

Time domain measurement results are shown in Fig. 4, 5, 6 (all in Appendix B) in three considered axes (see also Fig. 3.3). The waveform shows the complexity of the vibration signal with time constants of very different magnitudes. The pulses (even that in one direction) are not identical (in other words, each pulse has its own shape). Furthermore, period of the pulsation varies with the time.

In order to reduce unwanted performance of the DUT due to external vibration, two means can be considered. Firstly, to minimize vibration influence on the vibration-sensitive DUT, one can choose the proper angle of a DUT orientation relatively to the main (vertical) axis of vibrations. This can be done, for example, in the case of BAW resonators. Secondly, an active vibration control of the main vibration mode (1.7 Hz) can be implemented.

Chapter 4

BAW Resonators at Cryogenic Temperatures

As it is mentioned in the Chapter 1 of the present work, one of the ways to increase the oscillator frequency stability is to increase the resonator quality factor. At the dawn of the cryogenic era, it was noted that quartz crystal resonators exhibit very high quality factors at low temperatures [47, 48, 49, 50]. This fact was confirmed a little bit later [4, 51]. And finally, recent and more accurate measurements made in FEMTO-ST Institute report even higher values of the Q at temperatures of the liquid helium [10, 8, 9]. The summary of all these investigations is given in Table 4.1. Main known operating conditions are also specified.

Table 4.1: Quartz crystal resonator at cryogenic temperatures (earlier studies)

Author, year	$Q \times f_0$ at 300K	$Q \times f_0$ at 4K
Warner, 1958 [47]		$5 \cdot 10^6 \times 10 \cdot 10^6$
Smagin, 1960 [48]	$6 \cdot 10^6 \times 1 \cdot 10^6$	$120 \cdot 10^6 \times 1 \cdot 10^6$ at 2K
Gagnepain, 1972 [49]	(5th OT)	$6.5 \cdot 10^6 \times 5 \cdot 10^6$
Mossuz, 1975 [50]	$2.13 \cdot 10^6 \times 5.0 \cdot 10^6$ (5th OT)	$7.95 \cdot 10^6 \times 5 \cdot 10^6$
Robichon, 1985 [4]	$2.4 \cdot 10^6 \times 5.0 \cdot 10^6$ (5th OT)	$91 \cdot 10^6 \times 5 \cdot 10^6$
El Habiti, 1993 [51]	$2.2 \cdot 10^6 \times 5.0 \cdot 10^6$ (3th OT)	$50 \cdot 10^6 \times 4.9 \cdot 10^6$
J. Imbaud, 2007 [10]	$1.2 \cdot 10^6 \times 10.0 \cdot 10^6$ (3th OT, Mode A)	$125 \cdot 10^6 \times 31 \cdot 10^6$ at 3.5K (5th OT, Mode C)

The dependence of the quartz crystal resonator quality factor on temperature when it decreases from the room value to cryogenics is quite well described in earlier studies at least down to about 10K. Going this direction the Q-factor (as well as the inverse to

acoustic losses in the material) first increases, then goes down in a first valley at about 50K, before increasing again with just a disturbance around 20K. The quality factor increase is essentially noticeable below this temperature.

In the area of 50K, the decrease in the resonator Q-factor is attributed to the relaxation phenomenon due to the presence of Na^+ impurities [52]. These ions are combined with Al^{3+} ions substituted to some silicon ions Si^{4+} in the lattice [53, 54]. Interactions of the acoustic wave with thermal phonons are responsible for the deterioration of the quality factor near 20K [49, 55, 56, 57]. Below 10K, the increase of the Q-factor sometimes becomes slower due to the presence to the amorphous layer of silica at the resonator surface [51, 58].

In 1988, J. J. Suter [59] showed that an electrodeless resonator of the BVA type exhibits a higher Q-factor than a conventional electrode-deposited resonator, at low temperature, especially below 5K. The fact that a metallised resonator has a lower Q-factor has also been mentioned by Fraser [54]. For this reason, only BVA-type resonators are considered further in this work.

As it can be seen from Table 4.1, the best results are achieved by Joël Imbaud in 2007-2008 in the FEMTO-ST Institute [10, 8, 9]. The present work is the further development of this research. The material presented in this chapter is closely related with some publications [60, 61]

This chapter is dedicated to the most important element of any frequency source, i.e. its resonator. To put it more precisely, the chapter considers different aspects of operation of BAW devices at the cryogenic temperatures. The discussion starts with the presentation of the measurement methods. Then main measurement results on 5 MHz quartz resonators are given and discussed from the point of view of corresponding physical theories. This section considers such characteristics as material losses, the amplitude-temperature effect and the frequency-temperature sensitivity. Finally, the last section concerns LGT resonators behavior at the broad range of low temperatures.

4.1 Measurement and Characterization Method

The resonator parameters are measured by a passive method using a 10-500 MHz network analyzer HP 4195A equipped with an implemented impedance test adapter, instead of inserting the resonator under test into a conventional π-network. The network analyzer is used both as a frequency source and a detector. This method of measurement is preferable in the cryogenic environment, because of the significant change of the resonator motional resistance with the temperature and other difficulties. This change leads to impedance mismatching of the usual π-network.

The measurement capability of the network analyzer is 800 samples over a minimum span of 0.1 Hz. Thus, a frequency resolution of better than 1mHz is available. The network analyzer also provides a phase resolution of 0.01 degree and a magnitude resolution of 0.01 dB. The system resolution is a crucial parameter of the present measurements, since higher values of Q correspond to narrower resonator bandwidths. The minimum power of the signal source is -50 dBm. A distinctive feature of the network analyzer method is a need for compensation of long connecting cables. Indeed, the resonators are connected to the analyzer with 1 m coaxial cables passing a temperature range from 4K to the ambient temperature. To compensate cable effects, three calibration references (the open circuit, the short cut and a 50 Ohms resistor) are put close to DUTs at the end of identical cables. Measurements are made with -40 dBm source power for 3rd and 5th overtones and -50 dBm for higher overtones.

Measurement system uses semi-rigid cables of 2.14 mm diameter, PTFE isolation and 0.51 mm inner conductor diameter for electrical connection of external measurement bench and the internal (cryogenic) DUT. The length of the internal part of all cables is about 1 m. It is worth to note that the cables gradually passes all between the room and the liquid helium temperature. So, the cables are the main thermal load for the second cryocooler stage. Thus, their number has to be limited. In all the experiments no more than 6 cables are used. Additionally, thin wires are sometimes used when DC voltages are needed.

The resonator measurement and characterization procedure is shown in Fig. 4.1. It starts with the searching for a resonance peak of the mode and overtone of interest. Usually this step makes some problems because exact resonance frequencies are not known *a priori*, but their bandwidths are extremely narrow. So, as a result it is required to scan broad ranges of frequencies with relatively small intervals.

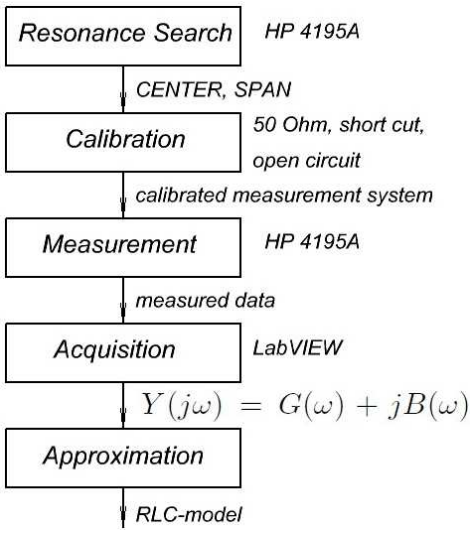

Figure 4.1: Measurement and model-extraction procedure

System calibration is carefully performed before each measurement, since, as it is mentioned above, the resonators under test are fed through rather long cables (see Fig. 3.3) whose effects must be compensated by the measurement system. To do so, the three calibration references are installed at the same place with the same cables as those connecting a resonator under test: the open circuit, the short cut and the 50 Ohms resistor. The resistance value of this special etalon does not change significantly between room and liquid helium temperatures. It varies from about 50.3 Ohms at room temperature to about 52 at 10K.

Once the calibration (under required cryogenic conditions and for a given frequency range, amplitude, number of points and sweep rate) is finished, the magnitude and phase of the resonator motional branch impedance are measured. These data are acquired with a help of the LabVIEW software through a GPIB connection and a personal computer. Resonator characteristic parameters are obtained with the help of the GB complex data representation. The GB-plot should be built for the vicinity of the resonance frequency of interest. The typical frequency GB-plot of the resonance is shown in Fig. 4.2.

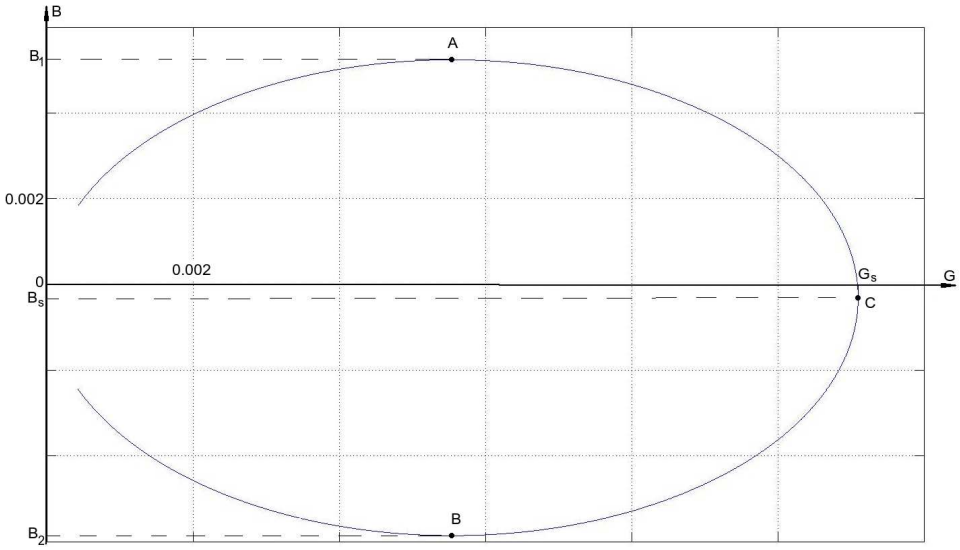

Figure 4.2: Typical GB-lpot of the resonance mode of a crystal resonator

The GB-plot is a graphical representation of the resonator admittance, i.e.

$$Y(j\omega) = G(\omega) + jB(\omega) = \frac{1}{Z(j\omega)} = \frac{1}{R(\omega) + jX(\omega)}, \tag{4.1}$$

where $Y(j\omega)$ is a complex admittance of the crystal, $G(\omega)$ and $B(\omega)$ are correspondingly real and imaginary parts of the complex admittance, $Z(j\omega)$ is a complex impedance, $R(\omega)$ and $X(\omega)$ are correspondingly real and imaginary parts of the complex impedance.

The graph, shown in Fig. 4.2, has three noticeable points: A, B, C. Frequencies at points A, B and C are f_1, f_2 and f_s. The latter is a frequency of the resonator series

resonance. The difference $\Delta f = f_2 - f_1$ is the device bandwidth. These data can be used to find the quality factor and the motional resistance as follows:

$$Q = \frac{f_s}{\Delta f}, \qquad R_x = \frac{1}{B_1 - B_2} = \frac{1}{G_s}. \tag{4.2}$$

In the same time, the shunt capacitance is defined as

$$C_0 = \frac{B_s}{\omega_s}. \tag{4.3}$$

This method is more accurate (accuracy is evaluated below) as well as well-founded than simple usage of the built-in parameter extraction methods of the measurement device. So, the used method can provide the parameters of the usual RLC model of the crystal resonator device. To do so, the model parameters are optimized to fit the measured curve. Such an approach provides the best available accuracy.

Let us evaluate an accuracy of Q-factor measurements for the case of the impedance analyzer resolution of $\delta = 1$ mHz and resonance frequency of 15.6 MHz (a 5 MHz (a room temperature C-mode) quartz resonator working at the fifth overtone of the A-mode at 4K). Thus, the accuracy of the bandwidth estimation can be estimated as $\pm 2\delta$. Comparing values of the resonance frequency and the bandwidth, the former is negligible. So, the maximum error of the Q-factor due to sampling can be estimated as

$$err = \frac{2\delta}{\Delta f \pm 2\delta} \tag{4.4}$$

Figure 4.3 shows the dependence of the maximum Q-factor measurements error due to sampling on the value of Q for the resonance frequency of 15.6 MHz. Note should be taken that only sampling error is taken into account. Thus, the frequency sampling error for Q-factor of $3.2494 \cdot 10^8$ is not less than 4%. The accuracy can be increased using interpolation and model fitting approaches.

4.2 5 MHz SC-cut Quartz Resonators at Cryogenic Temperatures

As a continuation of the research made by J. Imbaud, properties of SC-cut BVA-type 5 MHz quartz crystal resonators were investigated at cryogenic temperatures. Quartz BVA resonators are the subject of investigation of the present section, because it has been already shown that electrodeless resonators exhibit higher quality factors than electrode-deposited resonators [59]. More precisely the plano-convex SC-cut resonators optimized for room temperatures operation are chosen here as the most modern devices (active part diameter: 11 mm, thickness: 0.54 mm, curvature radius: 300 mm).

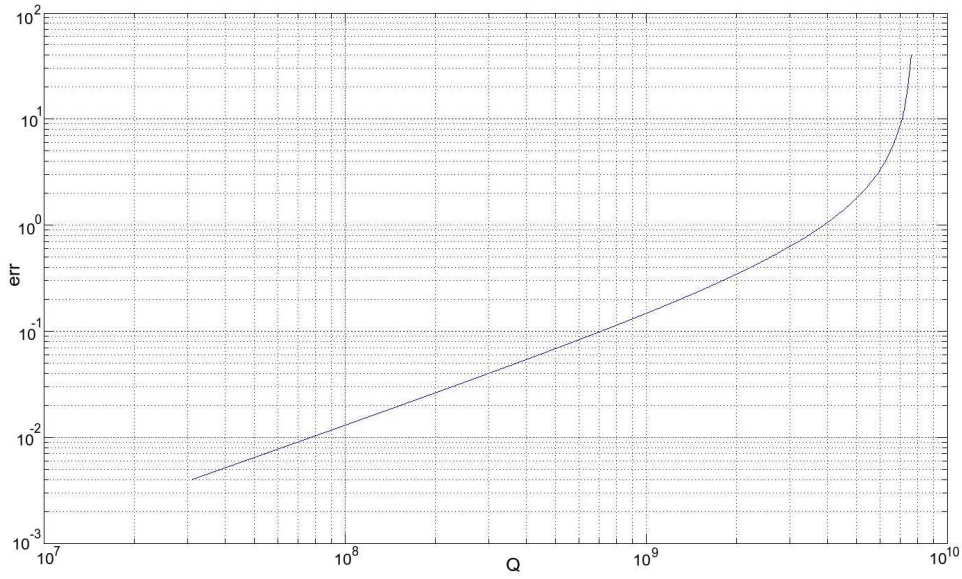

Figure 4.3: Maximum frequency sampling error versus the Q-factor for 15.597 MHz resonance frequency

4.2.1 Preliminary Measurements

This subsection considers two resonators of the suggested type. The shown results help to place these devices in comparison with that measured earlier, in particular, that of J. Imbaud.

Figure 4.4 shows a quality factor dependence on temperature for the fifth overtone of three vibration modes. The same dependence for the second resonator is plotted in Figure 4.5.

For the first resonator the $Q \cdot f$ product achieves $5.0683 \cdot 10^{15}$ Hz (the Q-factor of $3.2494 \cdot 10^{8}$ at about 15.9 MHz), which is even higher than the results obtained in the same conditions for similar 10 MHz: $3.875 \cdot 10^{15}$ (see Table 4.1 for J. Imaud and [10]). $Q \cdot f$ results for the second 5 MHz resonator are not so extraordinary ($3.96 \cdot 10^{15}$), but also exceed all earlier measurements. Another observation is that a kind of saturation is observed in $Q(T)$ dependence close to 4K for all modes. This effect also exists for 10 MHz devices and can be explained by mechanical damping of oscillations. In other words at these point it is mechanical construction which limits the device quality factor rather then material. Also, it can be noted that the sequence of the mode is the same as for 10 MHz resonators [10].

Figures 4.6 and 4.7 show the dependences of equivalent motional resistances of the resonators under study on temperature. These resistance change significantly in this short range of temperatures following the same trend as quality factors.

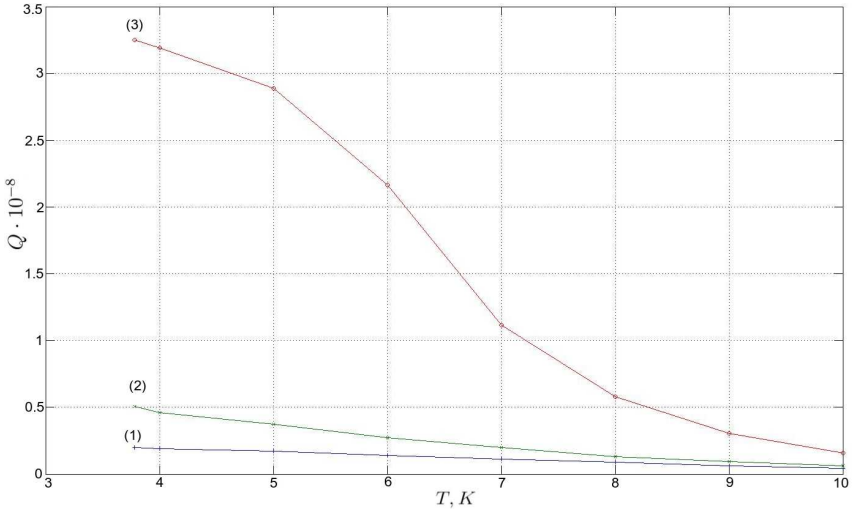

Figure 4.4: $Q(T)$ dependence for the first resonator: (1) - the C mode (5th OT), (2) - the B mode (5th OT), (3) - the A mode (5th OT)

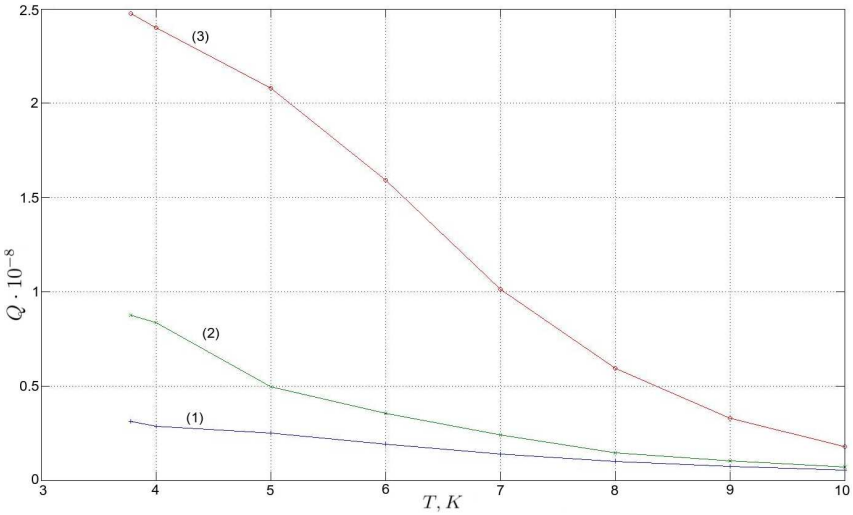

Figure 4.5: $Q(T)$ dependence for the second resonator: (1) - the C mode (5th OT), (2) - the B mode (5th OT), (3) - the A mode (5th OT)

Figures 4.8 shows the typical relative resonance frequency deviation from its value at 10K for the temperature range of $4 - 10$K. This deviation is found as follows:

$$y(T) = \frac{f(T) - f(10\text{K})}{f(10\text{K})}. \tag{4.5}$$

The measurement results states that for different modes resonant frequency can monotonically increase or decrease with the temperature.

As It is observed for this type of resonators (as well as measured earlier), the mo-

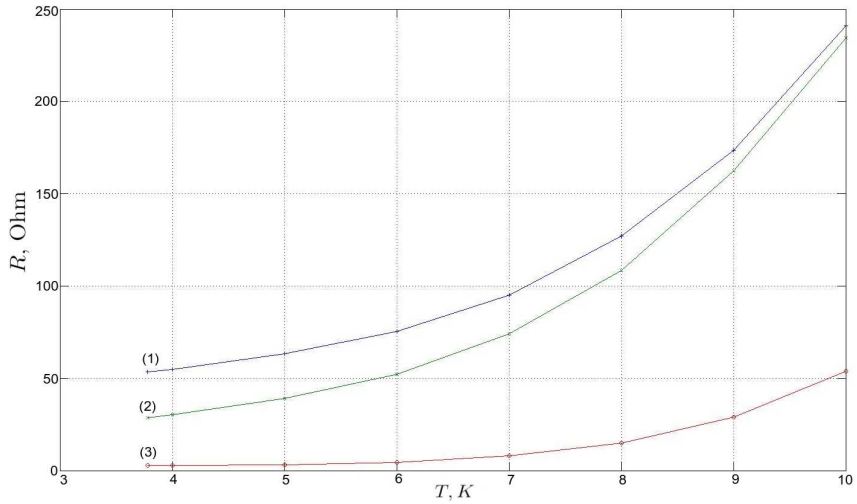

Figure 4.6: $R_x(T)$ dependence for the first resonator: (1) - the C mode (5th OT), (2) - the B mode (5th OT), (3) - the A mode (5th OT)

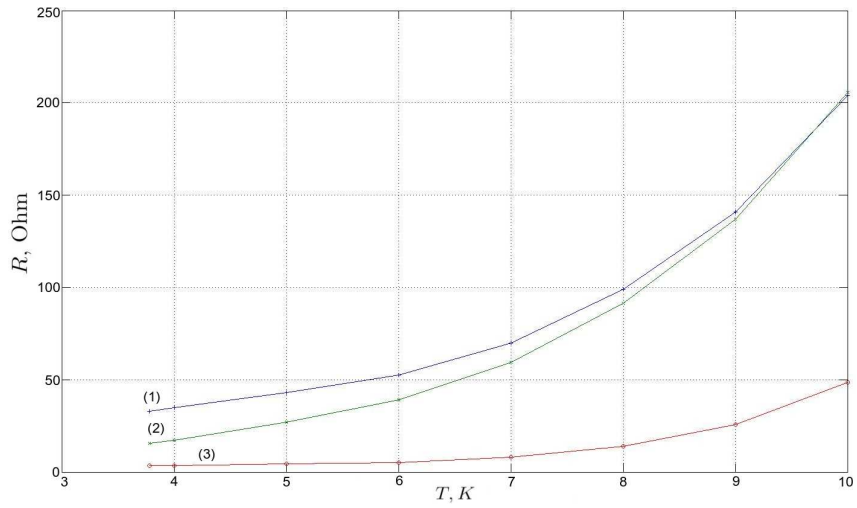

Figure 4.7: $R_x(T)$ dependence for the second resonator: (1) - the C mode (5th OT), (2) - the B mode (5th OT), (3) - the A mode (5th OT)

tional equivalent inductance as well as the motional capacitance are rather insensitive to the temperature, whereas the motional resistance decreases considerably with the temperature. The minimal value of the motional resistance for the first resonator (the fifth overtone of the A mode) is 2.8 Ohm for the first resonator and 3.5 Ohm for the second one. These values are less than those obtained for 10 MHz devices (approximately $5-6$ Ohm).

Tables 4.2 and 4.3 present results (calculated with GB-plot based on actual measurements) of the equivalent device parameters for these two quartz crystal resonators at 4 K. These parameters are calculated for 3rd and 5th overtones of A, B and C modes.

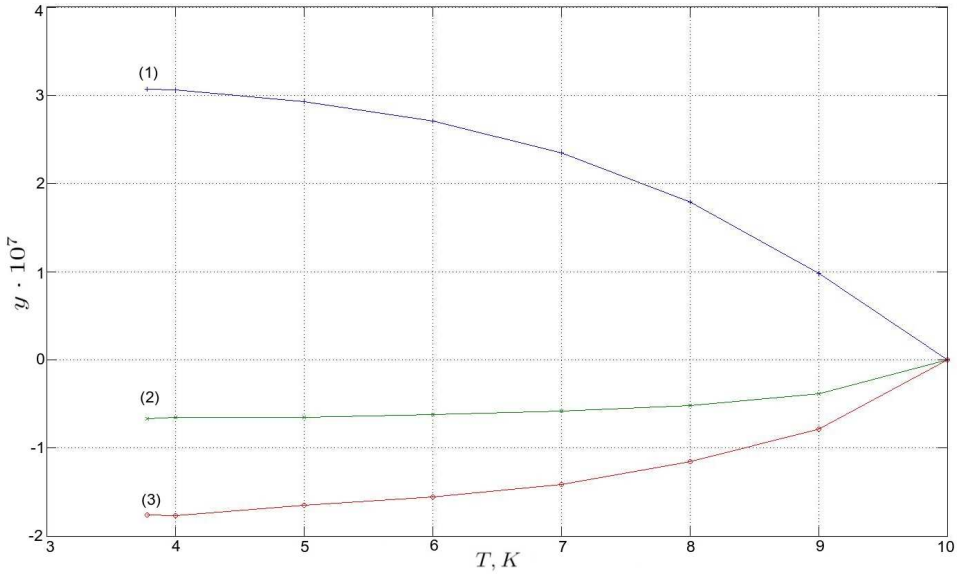

Figure 4.8: $y(T)$ dependence for the first resonator: (1) - the C mode (5th OT), (2) - the B mode (5th OT), (3) - the A mode (5th OT)

Table 4.2: Equivalent circuit parameter results for the first resonator at 4K

	3^{rd}OT, A	3^{rd}OT, B	3^{rd}OT, C	5^{th}OT, A	5^{th}OT, B	5^{th}OT, C
f_0, MHz	9.37368856	5.489693771	4.993002	15.59731894	9.197340241	8.395466
R_x, Ohm	2.1	6.5	19.3	3.5	32.7	158.5
L_x, H	18.2	5.6	3.8	11.6	28.8	69.1
C_x, aF	71.2	150.1	264.0	8.9	10.4	15.5
$Q \cdot 10^{-6}$	114	30	6	325	49	24

Table 4.3: Equivalent circuit parameter results for the second resonator at 4K

	3^{rd}OT, A	3^{rd}OT, B	3^{rd}OT, C	5^{th}OT, A	5^{th}OT, B	5^{th}OT, C
f_0, MHz	9.374325535	5.489795746	4.992999422	15.598415	9.197567973	8.395346675
R_x, Ohm	4.6	5.1	16.6	3.8	20.7	56.2
L_x, H	5.3	4.5	5.3	9.5	26.7	54.1
C_x, aF	56.1	188.4	192.0	11.0	11.2	6.6
$Q \cdot 10^{-6}$	68.5	30.0	9.9	243	75	51

Since $Q \cdot f$ product of considered 5 MHz SC-cut resonators at cryogenic temperatures are considerably higher than that for 10 MHz, than they are chosen for further deeper investigations as well as implemented frequency sources.

4.2.2 Resonator Losses at Cryogenic Temperatures

The main property of the devices of interest is the total losses that are inversely proportional to the device quality factor Q. The total losses (actually measured results) are a sum of all losses presented in the device, i.e. the material losses, mounting losses, electrical losses, etc.

$$\frac{1}{Q_{total}} = \frac{1}{Q_{wave-phonon}} + \frac{1}{Q_{thermoelastic}} + \frac{1}{Q_{phonon-electron}} + \frac{1}{Q_{mounting}} + ... \tag{4.6}$$

Concerning material part losses, this type of losses are represented in perfect material with three physical mechanisms [62, 55, 63, 64, 65]: acoustic wave-phonon dissipation (usually dominant intrinsic loss mechanism in insulators), thermoelastic dissipation (pronounced in plates or rods when the wavelength of flexural vibrations is larger than the thickness of the rod or the plate), phonon-electron dissipation (usually negligible in insulators). Since the first type of the listed material losses is dominant in the devices of interest, it is considered further.

Another material characteristic important for the sound attenuation characterization is the sound absorption coefficient given as follows:

$$\alpha(\omega) = \frac{1}{2}\frac{\text{Mean energy dissipated}}{\text{Energy flux in the wave}} = 2\pi\frac{\omega}{2QV_a}, \tag{4.7}$$

where V_a is the wave velocity and ω is an acoustic wave angular frequency.

The losses due to interaction of the acoustic wave and thermal phonons can be described with two distinct approaches. The first one, introduced by Akheiser [64], considers the interaction of a macroscopic strain wave in an insulator crystal with thermal phonons. Dependency of the phonon frequency on the strain leads to transport of the phonons between macroscopic regions of a crystal restoring the thermal equilibrium. This process is accompanied by acoustic wave energy loss. This approach is valid when the phonon life time is much smaller than a period of the acoustic wave, i.e. $\tau\omega \ll 1$, where τ is a thermal phonon life time and ω is an acoustic wave angular frequency. According to Akheiser approach the material $Q \cdot f$ product at high temperature is found as follows:

$$\alpha(\omega) = \frac{C_v T\gamma^2\tau}{2\rho V_a^3\big(1+(\omega\tau)^2\big)}\omega^2, \quad f \cdot Q = \frac{\rho V_a^2\big(1+(\omega\tau)^2\big)}{C_v T\gamma^2\tau}, \tag{4.8}$$

where $f = 2\pi\omega$, γ is the Grüneisen parameter, C_v the volumetric heat capacity, T the absolute temperature, ρ the density. The second approach, proposed by Landau and

Rumer [65], considers the acoustic wave as a parallel beam of interacting acoustic phonons. The interaction process involves acoustic quanta and individual thermal phonons. It is shown that the acoustic phonon attenuation is a result of three phonon interaction and is proportional to the angular frequency ω in the most studied case (also assuming that $\omega\tau \gg 1$ which is relevant at low temperature) [55]. So, the product of the quality factor and the resonance frequency is given by

$$\alpha(\omega) = \frac{\pi^5\gamma^2 k_B^4 T^4}{30\rho V_a^6 h^3}\omega, \quad f \cdot Q = \frac{15\rho V_a^5 h^3}{\pi^5\gamma^2\tau k_B^4 T^4}\omega, \tag{4.9}$$

where k_B is the Boltzmann constant and h is the Planck constant. According to this approach the material quality factor does not depend on the angular frequency ω.

It is clear that if the acoustic wave-thermal phonon attenuation is dominant for some range of temperatures, the dependence of the losses on temperature can show which regime is valid for the considered material in given conditions. To do so, for the first experiments, SC-cut BVA quartz resonators optimized for working on their C-mode (about 5 MHz at room temperature) are characterized between 3.8 and 20K. The results for 5th overtones of three different modes are shown in Fig. 4.9.

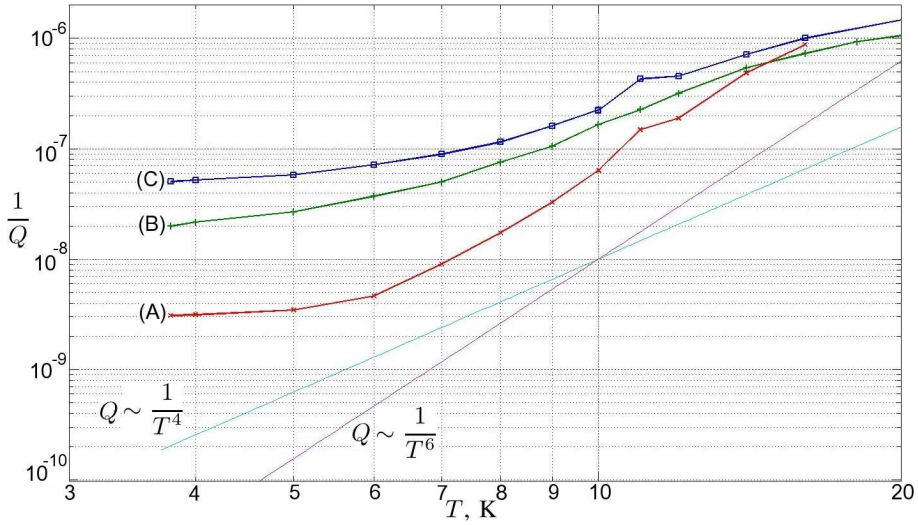

Figure 4.9: Measured device losses for 5th overtones of different modes in the temperature range $3.8 - 20$K: A-mode (quasi-longitudinal), B-mode (fast quasi-shear), C-mode (slow quasi-shear)

The dependence of the losses on temperature (Fig. 4.9) clearly shows three regions: a plateau for temperatures less than 6K (device losses are dominant, such as acoustic diffraction at the resonator surface or damping at the edge of the resonant disk), a linear region in the log-log scale (attributed to acoustic wave - phonon losses) and the second plateau for temperatures about 20K (region of the maximum absorption [51]). The medium region clearly shows the dependency of the type $Q^{-1} = aT^n + constant$, where n is close to 4 for quasi-shear modes and to 6 for a quasi-longitudinal mode. Though

for the latter mode, the dependence does not strictly confirms the slope predicted by the Landau-Rumer theory, the corresponding losses regime is actually dominant in quartz material at the liquid helium temperature. The increase of the power n has been already observed [63, 55].

The fact that the shear modes should exhibit higher losses than longitudinal modes has been predicted even in the original work of Landau and Rumer [65]. Indeed, for three-phonon processes the following conservation laws have to be respected:

$$\mathbf{k}_1 + \mathbf{k} = \mathbf{k}_2, \quad \omega_1 + \omega = \omega_2, \tag{4.10}$$

where $\mathbf{k}$ and ω are the wave vector and frequency of a sound phonon respectively. Also, the same notations with indexes 1 and 2 designate initial and resulting thermal phonons. It can be easily understood that these conditions cannot be fulfilled if sound and thermal phonons move with the same velocities. Indeed, the impulse conservation law implies

$$k \geq k_2 - k_1 \quad \Longrightarrow \quad \frac{\omega}{v'} \geq \frac{\omega_2}{v} - \frac{\omega_1}{v}, \tag{4.11}$$

where $\omega_i/k_i = v$ and $\omega/k = v'$ are thermal and sound phonon velocities respectively. Having in mind the energy conservation law, it can be concluded that $v' \leq v$. So, according to [66], only the following three-phonon processes are allowed:

$$\left.\begin{array}{l} S + S_1 \rightarrow S_2, \\ S + L_1 \rightarrow L_2, \end{array}\right\} \quad \text{shear modes,} \tag{4.12}$$

$$L + L_1 \rightarrow L_2\} \quad \text{longitudinal modes,} \tag{4.13}$$

where S and L stand for shear and longitudinal phonons. Indexes show initial and resulting thermal phonons. But collinear properties are forbidden since for collinear processes $v > v'$ [66]. Thus, only shear modes could exhibit three-phonon absorption on this level of approximation through the process $S + L_1 \rightarrow L_2$. Nevertheless, the collinear process also can become possible [67]. This could be shown if the finite time of thermal photon relaxation is taken into account. The appropriate calculations show that sound wave attenuation is also proportional to T^4 [55].

Some calculations [68] show that the sound wave attenuation in the case of a longitudinal wave is proportional to $T^2\tau^{-1}$. For this process, the power of the dependence of the relaxation time τ on the temperature could be up to 4. So, the resulting attenuation for the considered process is proportional to the temperature up to its 7th power.

The highest measured Q-values among 5th overtones of three modes are $325{\cdot}10^6$ for the A-mode, $50.5{\cdot}10^6$ for the B-mode, $2{\cdot}10^6$ for the C-mode. This sequence corresponds to the list of modes sorted out from the best trapped mode to the less trapped one according to the Stevens and Tiersten model [69]. Among all modes of 3rd and 5th overtones the best result is achieved for the 5th overtone of the A mode with $Q \cdot f$ product of about $5.1 \cdot 10^{15}$ which is the highest result in comparison with previous investigations [10, 8, 9]. But already starting at this stage, the problems of practical utilization arise. Since at cryogenic

temperatures the resonators have very low values of equivalent motional resistance (e.g. about 3 Ohms for the 5A mode), minimization of the active load is required in order to preserve the high quality factor. This considerably complicates the choice of signal sources and amplifiers.

4.2.3 Temperature Sensitivity

Another important characteristic of a resonator is its temperature sensitivity. Indeed, to minimize the influence of the environment on the frequency source, the sensitivity of the resonance element has to be minimized. Fig. 4.10 shows the fractional frequency temperature sensitivity for the three modes considered in the previous subsection.

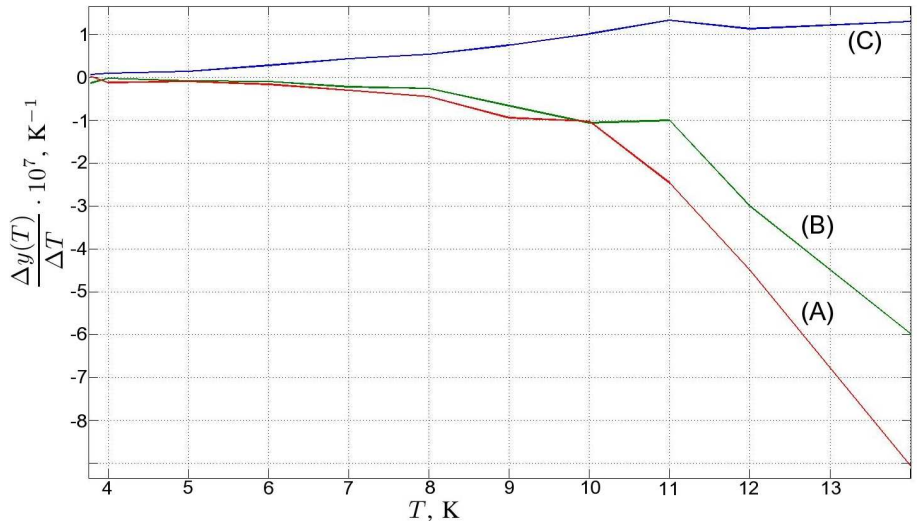

Figure 4.10: Fractional frequency temperature sensitivity: A, B and C-modes

As it is clearly seen from Fig. 4.10 the investigated modes does not have any turn-over point. The absence of a turn-over point poses serious problems in terms of crystal temperature stabilization. In general, the smaller sensitivity corresponds to lower temperatures for these devices. At 4K the sensitivities are $2 \cdot 10^{-9}$ K^{-1} for the A-mode, $3 \cdot 10^{-9}$ K^{-1} for the B-mode and $1 \cdot 10^{-8}$ K^{-1} for the C-mode. These results suggest that to obtain a desired fractional frequency stability of 10^{-13}, in best case, the temperature has to be controlled within 0.5mK.

4.2.4 Amplitude-Frequency Effect

BAW resonators are nonlinear devices in nature. Resonator properties can considerably depend on the power level of the excitation signal. This dependence becomes even more

pronounced with the increase of the quality factors, since the resonance frequency shift is depends on both the dissipated power and Q. To characterize this effect in cryogenic temperatures, the impedance of the resonator under test is measured with different levels of an excitation signal for the 5th overtone of the A-mode (that with the highest Q). The results are shown in Fig. 4.11. It could be noted that the resonator effective current decreases for the last curve. This fact is due to considerable increase of the device active resistance.

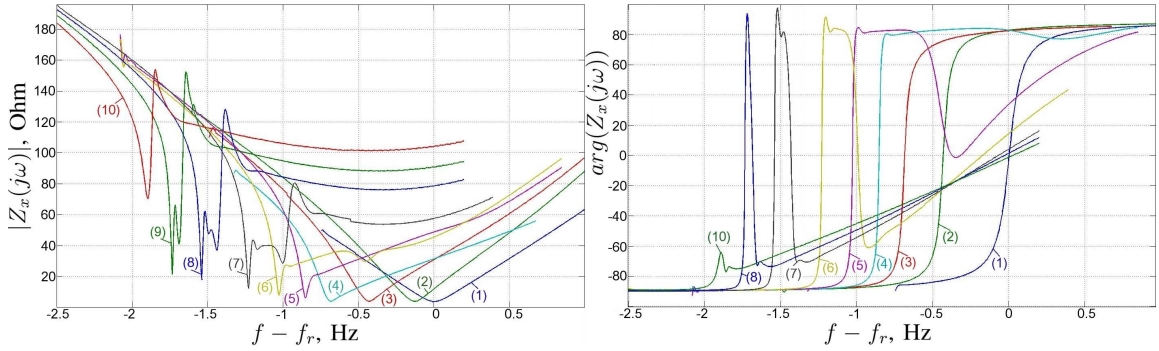

Figure 4.11: Impedance of the resonator near the 5th overtone of the the A-mode for different dissipation powers: (1) $P = 0.09\mu$W, $I = 0.154$mA, (2) $P = 0.22\mu$W, $I = 0.24$mA, (3) $P = 0.42\mu$W, $I = 0.32$mA, (4) $P = 0.64\mu$W, $I = 0.40$mA, (5) $P = 1.6\mu$W, $I = 0.48$mA, (6) $P = 2.26\mu$W, $I = 0.54$mA, (7) $P = 4.87\mu$W, $I = 0.62$mA, (8) $P = 9.20\mu$W, $I = 0.72$mA, (9) $P = 12.35\mu$W, $I = 0.76$mA, (10) $P = 17.20\mu$W, $I = 0.49$mA

Fig. 4.11 suggests that already for the dissipation power of $P = 0.22$ μW (Curve (2)) the impedance curve distortion exists. This amount of the power corresponds to the following energy stored by the resonator dissipating:

$$E = \frac{Q}{\omega_r} P = 0.72 \ \mu\text{J}, \tag{4.14}$$

where ω_r is the resonance angular frequency. Taking into account the resonator volume $V = 50$ mm^3, the energy density is about $E/V = 14.5$ J/m^3. As a reference value, it is possible to give the hysteresis limit for an AT-cut crystal resonator at the room temperature [70]: $E/V = 500$ J/m^3.

Next, for $P = 1.6$ μW the resonator self-heating effect becomes apparent. Also, it can be seen that for an increasing power P, the equivalent motional resistance also increases. These effects can even lead to temperature-amplitude oscillations. These oscillations are characterized by two states of low and high dissipation powers corresponding also to higher and lower values of motional resistance. In addition, the higher driving signal levels degrades resonator noise characteristics that is shown theoretically in Chapter 2 of this work and experimentally in [14].

The strong amplitude-frequency and self-heating effects arise another problem concerning effective utilization of cryogenic quartz crystal resonators in actual applications.

Indeed, in order to avoid this effect the driving signal has to be kept very low, but this fact degrades the system signal-to-noise ratio as well as it requires additional amplification stages. This problem is worsened by very low values of the resonator equivalent motional resistance. Thus, the motional resistances of several ohms require loads of less than one ohm in order to preserve the quality factor. And consequently small loads result in weaker voltages that can be further processed.

4.2.5 Amplitude-Frequency Effect in Cryogenic LD-cut Resonators

As it is shown in the previous subsection, the amplitude-frequency effect could be a serious problem for actual utilization of cryogenic SC-cut quartz resonators in frequency sources. An alternative to the investigated resonator type is a resonator of an LD-cut. The cut name means "low isochromism defect". It is claimed that such resonators exhibit the amplitude-frequency effect one hundred times lower than SC-cut devices [71]. Some characteristics of LD-cut resonators at liquid helium temperatures were previously considered in [10].

The amplitude-frequency effect of LD-cut resonators is characterized using a 10 MHz home made sample manufactured in a BVA "process". Similar to the case of SC-cut resonators the highest values of the quality factor are achieved for the fifth overtone of the A-mode. The tested sample exhibits the quality factor of $97.2 \cdot 10^6$ at the resonance frequency of 29.823 MHz with the active resistance of 8.5 Ohms at 4.1 K. The resonator impedance near this mode for different dissipation powers is sown in Fig. 4.12.

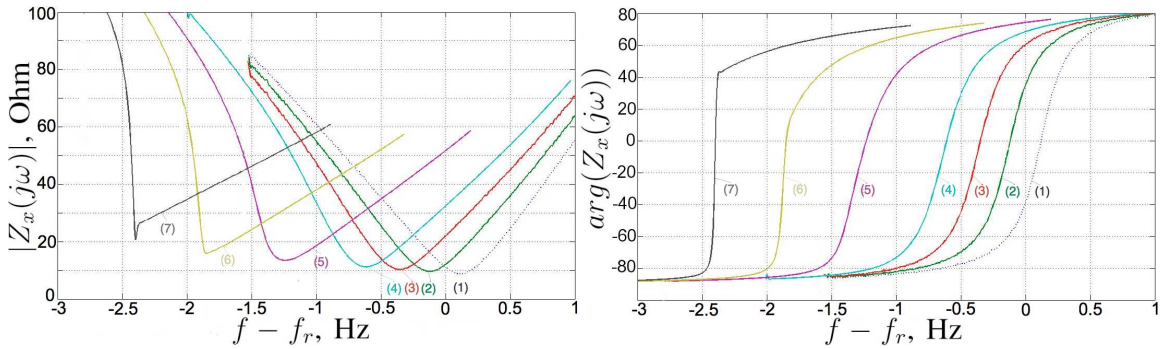

Figure 4.12: Impedance of the LD-cut resonator near the 3rd overtone of the the A-mode for different dissipation powers: (1) $P = 0.087\mu$W, $I = 0.1$mA, (2) $P = 1.27\mu$W, $I = 0.38$mA, (3) $P = 2.48\mu$W, $I = 0.5$mA, (4) $P = 4.1\mu$W, $I = 0.6$mA, (5) $P = 9.3\mu$W, $I = 0.83$mA, (6) $P = 14.8\mu$W, $I = 1.0$mA, (7) $P = 24.1\mu$W, $I = 1.1$mA

In addition to the 5th overtone, the experiment was repeated for the 3rd overtone of the same mode which exhibits the quality factor of $74.5 \cdot 10^6$ at the resonance frequency of 17.951 MHz with the active resistance of 9.2 Ohms at 4.1 K. Measured results are shown in Fig. 4.13.

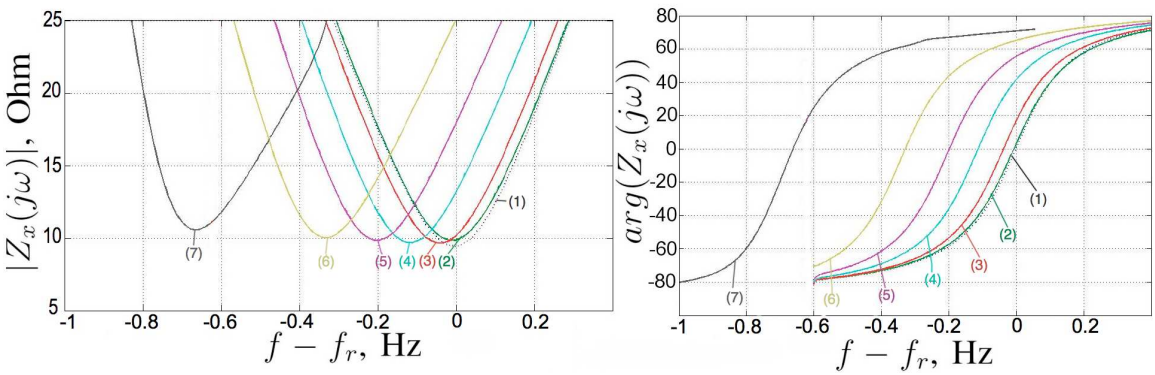

Figure 4.13: Impedance of the LD-cut resonator near the 3rd overtone of the the A-mode for different dissipation powers: (1) $P = 0.024\mu$W, $I = 0.05$mA, (2) $P = 1.1\mu$W, $I = 0.33$mA, (3) $P = 1.82\mu$W, $I = 0.44$mA, (4) $P = 3.5\mu$W, $I = 0.6$mA, (5) $P = 5.5\mu$W, $I = 0.75$mA, (6) $P = 8.5\mu$W, $I = 0.91$mA, (7) $P = 16.3\mu$W, $I = 1.24$mA

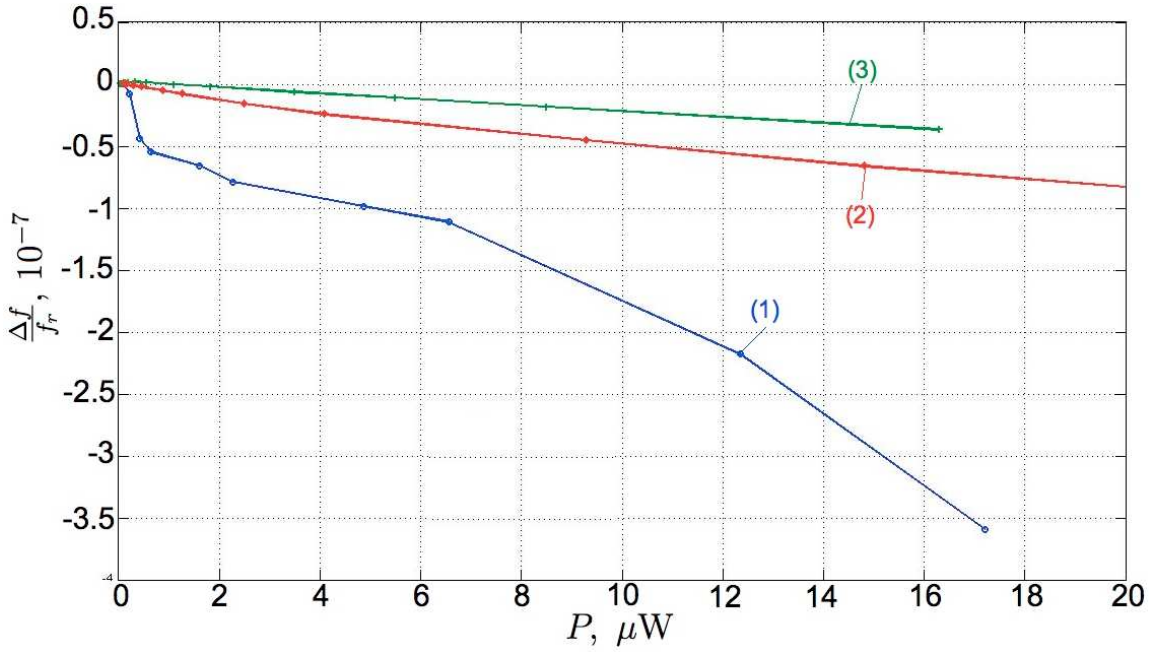

Figure 4.14: Relative resonance frequency shift as a function of the dissipation power: (1) - the 5th overtone of the the A-mode (SC-cut resonator), (2) - the 5th overtone of the the A-mode (LD-cut resonator), (3) - the 3rd overtone of the the A-mode (LD-cut resonator)

To compare the results for different modes and resonator cuts, a relative resonance frequency shift is plotted versus the dissipation power (see Fig. 4.14). Both characterized overtones for the LD-cut device demonstrate a linear dependence of the resonance frequency shift on the power in a range $2 - 17$ μW. These results correspond to theoretical findings presented in [72]:

$$\Delta f(P) = A \cdot P + B\sqrt{P}, \tag{4.15}$$

with $A \gg B$. Contrary to that the SC-cut resonator demonstrates an almost linear

dependence of the resonance frequency shift on the power only in a short range $1-7$ μW. However, for $P > 7$ μW the resonator self-heating effects become dominant over the isochromism defect which can be seen in Fig. 4.11.

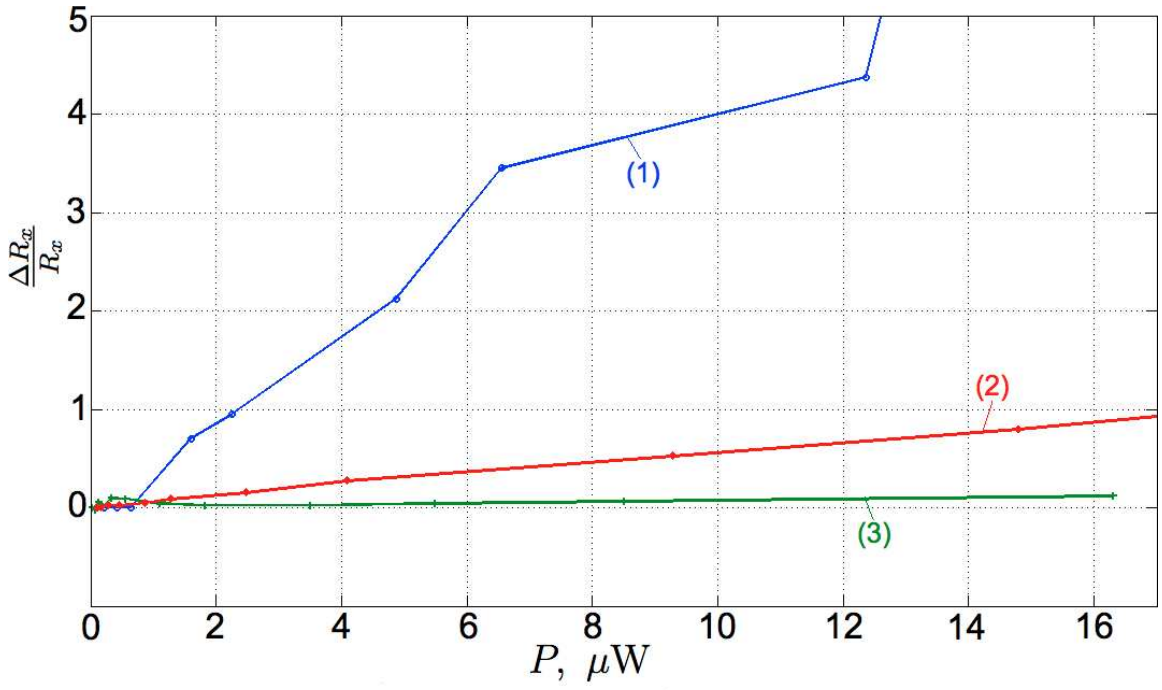

Figure 4.15: Relative active resistance change as a function of the dissipation power: (1) - the 5th overtone of the the A-mode (SC-cut resonator), (2) - the 5th overtone of the the A-mode (LD-cut resonator), (3) - the 3rd overtone of the the A-mode (LD-cut resonator)

The LD-cut device also has a linear dependence of the active resistance on the dissipation power. In the same time, relative active resistance for the SC-cut resonator chanties significantly and nonlinearly (see Fig. 4.15).

Concluding the subsection, it is worth to state that LD-cut resonator is indeed exhibits lower amplitude-frequency effect at liquid temperature than the SC-cut device. Though it has to be also noted that the former has 3.3 lower quality factor for the 5th overtone. So, the frequency shifts has to be compared only in strong connection with their Q-values as it is suggested in Section 2.2.

4.2.6 Higher Overtones

In order to deeply investigate the abilities of devices under tests, some higher resonator harmonics have been characterized at cryogenic temperatures. Thus, Fig. 4.16 demonstrates the presence of different anharmonics of the 11th overtone of the A-mode. The corresponding indexes for identifying the anharmonics are marked on the figure. The best

anharmonic mode has a quality factor of $417 \cdot 10^6$ at the frequency of 68823167 Hz with an equivalent resistance of 19 Ohms. The estimated $Q \cdot f$ product for this resonance equals to $2.87 \cdot 10^{16}$ Hz. Thus, the DUT working at this resonance at cryogenic temperatures has the highest reported quality factor ever measured on BAW resonators.

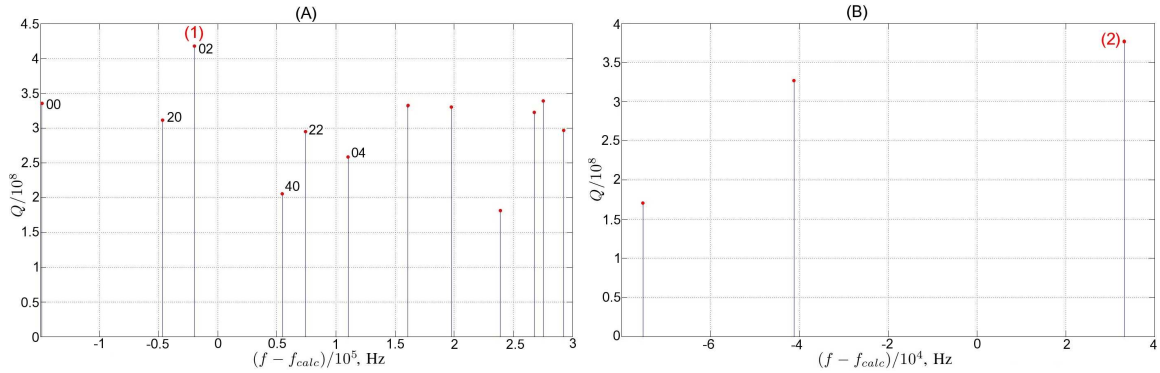

(a) Different anharmonics of the 11th overtone of the A mode ($f_{calc} = 68.842620$ MHz)

(b) Different anharmonics of the 13th overtone of the A mode ($f_{calc} = 81.392723$ MHz)

Figure 4.16: Anharmonics of the 11th and 13th overtones of the A mode

In the same way the 13th overtone of the A-mode is characterized. Here only three anharmonics are found. The best of them has a Q value of $377 \cdot 10^6$ at 81392723 Hz with an equivalent resistance of 30 Ohms. Thus, the highest $Q \cdot f$ measured on BAW resonators can reach $3.07 \cdot 10^{16}$ Hz.

So, these modes could be perspective for a practical utilization. But the issue of the selection or rejection of the undesired modes should be solved first in autonomous systems such as oscillators. Also, higher Q values result in a stronger amplitude-frequency effect [73].

4.3 LGT Resonators at Cryogenic Temperatures

The LGX material family is promising for designing BAW resonators with high quality factors. Among this materials the Lanthanum Gallium Tantalate (LGT) and Lanthanum Gallium Silicate (LGS) are the most commonly known. Nevertheless, their properties have not been yet investigated for temperatures lower than 80K. Our experiments show that though LGS resonators are capable of working at the liquid helium temperature, its quality factor for different modes vary about its value at room temperature. So, from the point of view of ultra-stable oscillator design these are of no interest and, thus, are not closely considered in the present work. Contrary to that LGT devices exhibit considerable increase in quality factor, which can be interested from the point of view of further resonator technology development. This is the first LGT resonator investigation in the temperature range between liquid helium and liquid nitrogen temperatures (previous measurements have been made just down to 130K).

In this section, investigation results on BVA-type plano-convex Y-cut LGT resonators (active part diameter: 10.2 mm, thickness: 0.65 mm, curvature radius: 100 mm) are presented. The attempts to characterize their LGS counterparts have been abandoned since they show a decrease of quality going from room to cryogenic temperatures.

4.3.1 LGT Resonator Losses

The characteristics of two LGT resonators of similar origin have been measured in the wide temperature range ($4 - 80$ K). The results for their quality factors are shown in Fig. 4.17. The maximum Q-factor is just about $7.2 \cdot 10^6$ that is only 5 times higher than its value at room temperature. Unlike in the case of quartz resonators, device losses dependence on temperature seem to be rather uniform. The only physical phenomenon clearly seen is the peak of losses at about 40 K. It can be attributed to relaxation processes due to the presence of impurities. In addition, a very important difference between two resonators is observed. These results suggest that the LGT resonator technology is far from being optimized in terms of different types of losses: device losses cover material losses. On the other hand, further technology development might lead to considerable increase of their quality factors in cryogenic conditions.

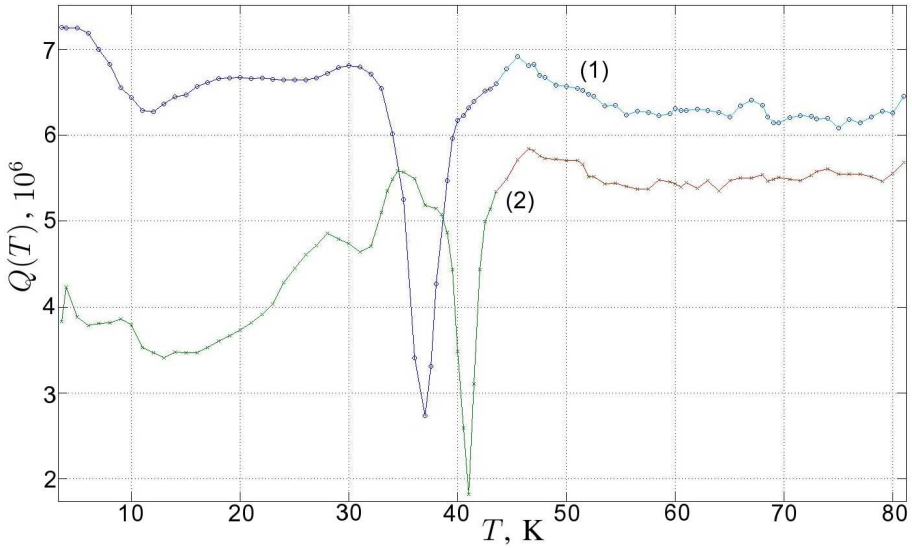

Figure 4.17: LGT resonator quality factor Q as a function of temperature T (two resonators)

Fig. 4.18 shows dependence of the resonator motional resistance on the temperature. In general this graph is inverse proportional to $Q(T)$ plot. Minimal obtained value is about 4.6 Ohm for the lowest accessible temperature. The highest values correspond to the $Q(T)$ drops in the vicinity of 40K.

To peaks clearly shown in Fig. 4.17 and 4.18 can be attributed to the presence of some material impurities. Though the difference in corresponding temperature is probably due

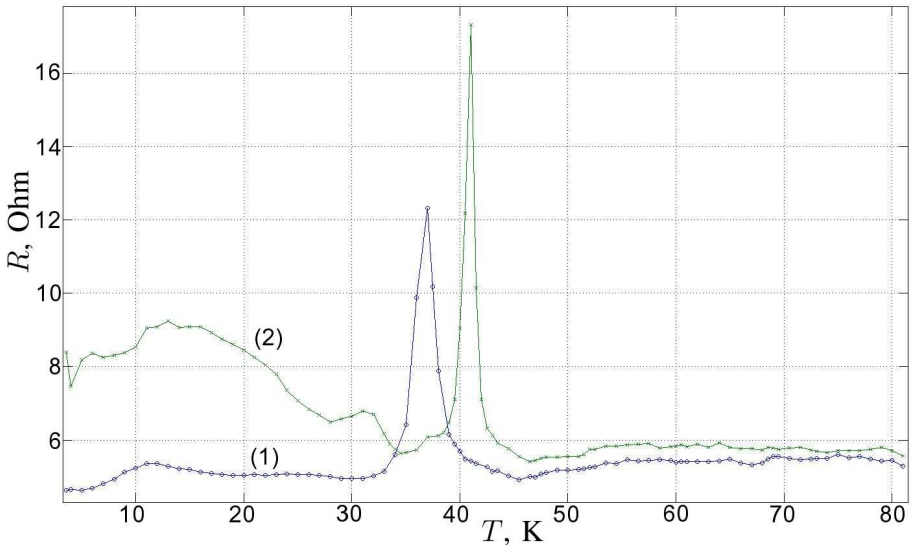

Figure 4.18: $R_x(T)$ dependence for the LGT resonators

to the fact the the resonators are made from the crystal blocks with slightly different characteristics. in any case, estimations show that these difference cannot be covered with the static thermal resistance of the copper block which is negligible at the liquid helium temperature.

The immaturity of LGT resonators is also confirmed by the high dispersion of the characteristics (see Fig. 4.17 and 4.18) measured for two sample devices of the similar origin.

4.3.2 LGT Resonator Temperature Sensitivity

The dependence of the fractional stability on the temperature is also examined for the LGT resonators (see Fig. 4.19). The relative frequency deviation is calculated with regard to the minimal accessible temperature of 3.6K:

$$y(T) = \frac{f(T) - f(3.6\text{K})}{f(3.6\text{K})}. \tag{4.16}$$

The behavior of both curves is not monotonic: resonators have a turn-over point of the parabolic type between 6 and 7 K. This phenomenon is advantageous for creating a highly efficient temperature stabilization system for the resonator.

Though LGT resonators exhibit higher values of quality factors at liquid helium temperatures and have a turn-over point in their frequency-temperature characteristics, their

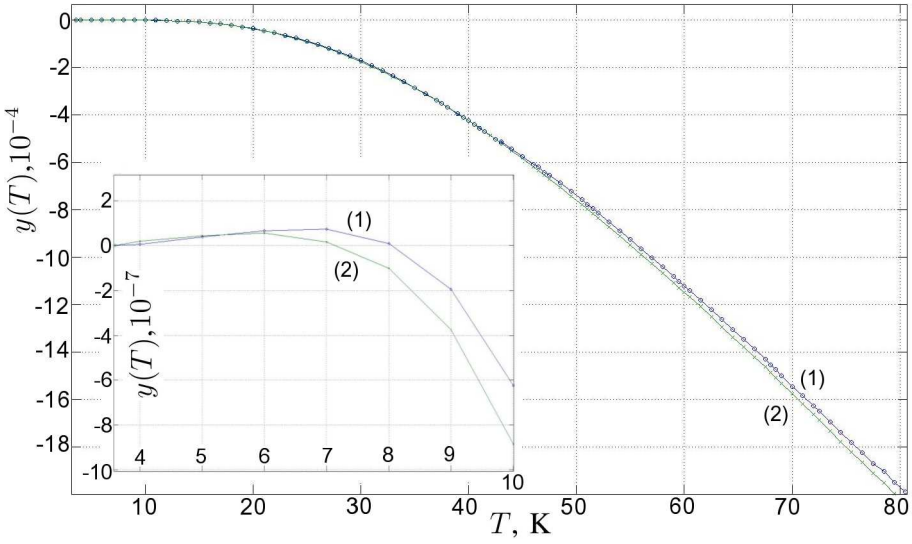

Figure 4.19: Fractional frequency y versus temperature T for two LGT resonators

utilization in ultra-stable frequency sources is not well-grounded, since quartz crystal resonators show much higher values of quality factors. This inferior characteristics are due two fact that LGT resonators are not well structurally optimized. So, their devices losses overwhelm material losses. These drawbacks could be attributed to the much shorter history of perfection than that of the quartz resonator technology.

Chapter 5

Components of Cryogenic Oscillators

This chapter is dedicated to different elements of cryogenic electronic systems, starting from the behavior of basic passive elements and up to measurements and modeling of active devices at very low temperatures. So, the first section describes common passive components, such as inductors, capacitors and resistances at low temperatures. The optimal choice of these devices for liquid helium electronic systems is made. Second section considers active components which are necessary blocks for all amplifiers and oscillators. This section starts with a short description of possible solution and deeply considers three possible variants. Then it passes to consideration of three main possible choices. Original characterization and modeling approaches are described. Actual liquid-helium amplifier designs are shown.

5.1 Passive Devices at Cryogenic Temperatures

Passive devices like capacitors, inductors and resistors are compulsory components of any electronic device. The availability of these devices for cryogenic electronics mainly defines a design of a resulting device. The problem of component choice is quite well solved for room temperature electronics. It also has some sufficient answers for liquid nitrogen systems. But, for liquid helium design, the problem remains to be unsolved. So, this short section is dedicated to performance and optimal choices of the most basic components at the liquid helium temperatures.

Standard electronic components have very limited range of operation (at best -55°C - $+125$°C for military devices). Though its not a secret that some of these devices are able to operate outside this range, though with possibly completely different parameters. For example, it is known for long time since the dawn of cryogenic era, that resistors and attenuators using nichrome (NiCr) thin films could be used in cryogenic systems. However, tantalum-nitride (TaN) has largely replaced nichrome for use in commercial

resistive thin-film microwave components [74]. Though it was found that TaN resistors depending on a manufacturer and technology may become superconductors with critical temperatures in the range 4.4-14K. So, the additional tests of available resistors were required.

Two types of 1%-accuracy resistors available at the laboratory were tested at cryogenic temperatures:

1. *thick film process resistors* from YAGEO (PHYCOMP) - RC0805JR-SKE24L (SMD Resistors 0805, 1%, 150 V, 100 ppm/C, power dissipation 0.125 W).
2. *metal film resistors* from Basic Kit LMA-24-SBR02 (MINI-MELF 0204-50, 1%, 50 ppm/K, rated power dissipation 0.25 W);

These two types of 1%-accuracy chip resistors have been tested with no superconductive properties found. Contrary to that, some of the verified resistors types demonstrated growth of their values. The following general rule has been observed: the higher room temperature resistance value, the higher increase of this value at liquid helium temperatures.

Tested thick film resistors (for more data see Tables 1 and 2, Appendix C) up to 10 Ohm demonstrate no considerable growth (less than 1%). Values of resistances higher than 1 kOhm may be shifted by more than a couple of dozens of percent. And resistors of hundreds of kOhms demonstrate enormous increase in the considered parameter (more than 100%). This unpleasant property may be overcame by simply taking into account of these changes of resistance value *a priori*. But this approach is complicated by the high dispersion of values. So, sufficient accuracy of the devices cannot be achieved. Moreover, the resistance values change significantly in the working temperature range 3.6-5K: tens of percents for the resistors of hundreds of kOhms. This fact makes these devices inapplicable for systems where low temperature sensitivity (such as ultra stable reference sources) is important. Though they may find an application as cheap temperature sensors with rather good choice of resistance values (see Table 3, Appendix C).

Metal film resistors (for more data see Table 4, Appendix C) demonstrate the same pattern of resistance change, but with much less deviations (for example, less than 2% for resistors of hundreds of kOhms). In the temperature range 3.2-5K the deviation does not exceed 1% for resistors less than 700 kOhms. So, this type is preferable for low temperature sensitive applications.

Values of all capacitors also change in cryogenic temperatures. Capacitors with two common types of ceramic dielectric materials were tested (from different manufacturers):

1. *EIA Class 2 dielectric*, in particular X7R, that is designed for capacitors with typically good non-critical coupling, filtering, transient voltage suppression, and timing applications;

2. *EIA Class 1 dielectric*, in particular C0G (EIA) or NP0 (industry spec), that is the material with the lowest capacitance/temperature dependence (Negative-Positive zero). C0G/NP0 dielectrics have the lowest losses.

All samples of X7R capacitors exhibit an almost tenfold decrease in capacitance going from room to liquid helium temperatures. For example, capacitance of the MLT030227 CMS1206 device changes from 3.3 nF to 268 pF. Moreover, starting approximately at 500 pF and lower, capacitors of this type turn to the inductive behavior at considered cryogenic conditions.

C0G capacitors demonstrate no considerable change of values between room and liquid helium temperatures as well as within $3.8 - 5$K temperature range. For example, the capacitors (from VISHAY, CMS0805, $\pm 5\%$) with the nominal value of 22 pF and measured 25 pF exhibit 24 pF at 4 K. For 100 pF nominal capacitors, these values are 106 pF and 103 pF respectively. And for 150 pF samples, 156 pF is measured at room temperature, and 153 pF are obtained for 4K.

Comparing these two solutions of dielectric choice, C0G capacitors are preferable since they do not require any value correction or compensation in the course of the system design.

Ordinary electrolytic capacitors, which in considered applications are usually used for voltage stabilization and do not require extraordinary accuracy, do not show a considerable value shift, which has to be corrected.

In addition to that, inductor investigations show little shifts in inductance values, which may be corrected when precision is the case. In the same time equivalent resistance of all inductors decreases between room and liquid helium temperature by several percents. Nevertheless, it is recommended to test each sample before usage.

Another important question for low noise applications is a level of generated thermal noise. This may be another way of increase in the source frequency stability. The power spectral density, or the voltage variance (mean square) per hertz of the bandwidth, is given by [75]:

$$d < V_R^2(f) >= 4k_B T R \tag{5.1}$$

were k_B is Boltzmann's constant in joules per kelvin, T is the resistor absolute temperature in kelvins, and R is the resistor value in ohms. According to 5.1 a ratio of voltage variances at different temperature equals to the ration of these temperatures. So, for liquid helium $T_1 \approx 4K$ and room $T_2 = 295$K temperatures this ratio is:

$$\frac{d < V_{R2}^2(f) >}{d < V_{R1}^2(f) >} = \frac{T_2}{T_1} = 73.75 \tag{5.2}$$

This means that the level of thermal noise in cryogenic electronic devices is 74 times lower than than at room temperatures. This is another advantage of cryogenic systems.

5.2 Active Components at Liquid Helium Temperatures

Nowadays scientists and engineers are confronted with applications of electronic systems in cryogenic environments. One may conventionally sort these applications according to the temperature [76]: liquid nitrogen range of temperatures (about 77K), liquid helium range (4.2K), deep cryogenic temperatures (down to some mK). Another division of cryogenic electronics is made according to the reasons of working at extremely low temperatures. In other words, according to the response to a question: why this electronic device works at cryogenic temperature. Firstly, some electronic devices are intended to work at low temperatures (for example, electronics for space missions). In this case, low temperature is an obstacle for engineers. Secondly, in some cases electronics is intentionally put into such extreme conditions in order to achieve some desirable features, such as low noise or high quality factors of some devices. In spite of the reason of working at cryogenic temperatures, developers have to solve the same problems concerning properties of electronic components under the working conditions, where a special attention has to be paid to active devices. Like for room temperature applications the active device selection is determined by requirements to the whole system, but the number of possibilities is much lower in cryogenics. Even though the active device has been chosen and its capability of working at given temperature is proven, additional problems are posed by simulation difficulties (which is a crucial step in modern circuit design), high dispersion of device characteristics and undesirable phenomena. This section describes the methodology of working on low-noise electronic devices within the liquid-helium temperature range which resolves some of stated above problems. This investigation may be particularly valuable, since this temperature range is much less investigated in comparison with liquid nitrogen temperatures.

The section is organized as follows. The first part deals with the short discussion of different transistor types which can be used for liquid helium electronic systems. The choice is made according to given engineering criteria. The second subsection presents a method for measurement and modeling of transistors static characteristics based on one of chosen transistor types. These two subsection represent the material published in [77]. The third and forth parts give experimental results two other types. And final decision is made based on these actual measurement results.

5.2.1 Selection of a Transistor for Liquid Helium Temperature Operation

Electronic applications for the liquid helium temperature range are not so numerous as those within the liquid nitrogen range. Thus, number of available papers dedicated to this area is rather limited. Nevertheless, it is possible to find some results of experimental investigation of different transistor types at liquid helium temperature. A transistor of a particular type has to have amplification features down to 4.0 K, low noise (particularly

phase noise), minimum of low temperature anomalies, low dissipation power, available commercial references and reasonable price. Moreover, for low noise oscillators and many other applications it has to be a packaged discrete device.

Based on available literature sources we have singled out the following groups of transistors, which are able to work at liquid helium temperature: silicon junction field effect transistor [78], silicon metal-oxide semiconductor field-effect transistor [79, 80], germanium junction field effect transistor [81], gallium arsenide metal semiconductor field-effect transistor [82], gallium arsenide junction field effect transistor [83], high electron mobility transistor [84, 85, 86], single-electron transistor, and silicon-germanium heterojunction bipolar transistor [87, 88, 89, 90, 91, 92, 93]. Some trends of evolution of cryogenic FET and HFET devices are described in [94].

Let us briefly consider advantages and drawbacks of each transistor type listed above. The first type is a silicon junction field effect transistor (Si JFET). This type of transistors has tolerable characteristics at temperatures higher than 30 K. Below 30 K their operation is a subject of the freeze-out effect, which can result in noise increase, different anomalies and, finally, loss of amplification properties. Although some successful applications of Si JFET at temperatures below 30 K have been reported [78], such solutions are usually impractical, since they require temperature isolation and additional heating.

Silicon MOSFETs are able to work at temperatures of the liquid helium. Moreover, since this type of transistors is widespread, a lot of commercial references are available. But the main disadvantage of this transistor type is that Si MOSFETs are characterized with high level of noise and anomalies of static characteristics below freeze-out temperature [79, 80]. These disadvantages can be overcame with optimizing the transistor structure for low temperature operation. But such transistors are not produced as commercial devices and, thus, are not available.

Germanium JFETs have much lower freeze-out temperature (usually it is taken equal to 20K) than a silicon device of the same type. So, this type of transistors is also a subject to high noise and static anomalies at 4.2 K [81].

GaAs MESFET devices working at low temperatures have a pronounced hysteresis when curves obtained with increasing voltage do not correspond to curves measured with decreasing voltage. In addition to this, some devices have “turn-on“ thresholds and inverse curvature of output characteristics [82]. In the same time foundry devices of this types lack such anomalies, but, as usual, are difficult of access. In addition to this all the GaAs MESFET devices have rather high noise levels.

GaAs JFETs have much less static anomalies than silicon and germanium devices of the same type. The only deviation from ideal operation is the apparent kink of the characteristics which has been explained with oscillation of the FET, because of a feedback between the leads [83]. But, nevertheless, these devices can be regarded as promising solutions because of the considerable noise level. Optimizing the device structure may

lead to noise decrease down to the level of silicon and germanium devises without the freeze-out effect [83].

A special group of active devices is formed with high electron mobility and single-electron transistors [84, 85, 86] widely used for SQUID (Superconducting Quantum Interference Devices) applications. Even though some practical applications are reported, it is difficult to find specific information on the characteristics and noise levels of these devices. It is simply reported [86] about high charge sensitivity, wide passband, low dissipation power, etc. Also, technologies of these devices are not well established and devises are not widely spread.

The majority of these types of devices have the same disadvantages, such as considerable noise levels, different types of unwanted low-temperature anomalies and/or unavailability. Even though there are some devices optimized specially for cryogenic operation, their commercial variants do not exist (just prototypes are available). Comparing results of previous investigations of all active devices listed above, we have chosen silicon-germanium heterojunction transistors as a subject for further research. Indeed, the best candidate for low-noise engineering applications (hyper stable frequency sources, in particular) seems to be a silicon-germanium heterojunction bipolar transistor (SiGe HBT), which have become a subject of interest for many scientists and engineers. These devices have low noise levels, moderate number of low-temperature anomalies and availability of commercial references. In addition to this, bipolar transistors rather than different types of field-effect transistors are the most usual active devices for hyper stable acoustic oscillators. Commercial references of SiGe HBTs are available from Infineon Technologies, IBM and NXP Semiconductors as packaged and on-wafer devices. The main disadvantage of this transistor type is that different references may have (or may not have) different cryogenic anomalies such as hysteresis, “turn-on“ thresholds, negative resistance, etc.

Next section considers and measurements and modeling methods for cryogenic transistors. The presentation uses packaged discrete transistors of the type BFP650 from Infineon Technologies as a demonstration example. This transistor reference is chosen, since its operation at liquid helium temperatures had already been proven [87]. Some other SiGe HBT devices from Infineon and NXP have been tested, but these pieces do not operate in the appropriate way at the considered temperature. The BFP650 reference is a SiGe technology device, which has a break-down voltage collector-to-emitter with base open (BVCEO) equal to 4 V, and collector current of about 100 mA for maximum transition frequency of 37.5 GHz and collector-emitter voltage of 3 V for normal room-temperature operation [95]. This device has been recommended in low-noise oscillator applications by the supplier.

5.2.2 Measurements and modeling of SiGe HBTs

For transistor testing at liquid helium temperature the same cryogenic system is used. As for quartz resonators the temperature of the second stage and, thus, the DUT is controlled with an additional commercial cryogenic temperature controller from LakeShore Cryotronics, Inc. The temperature control loop is closed with a heating resistance and a calibrated germanium sensor. The precision of the temperature control has been evaluated from the recorded power spectral density of the temperature fluctuations.

In the case of the described measurements, the DUT is a SiGe transistor in a SOT343 package. In order to improve thermal connection between the body of the transistor and the cold head and avoid electrical connection between the circuit and the cryocooler, the device is soldered up side down in such a way, that the package is put inside the slot. So, the upper surface of the transistor has a mechanical connection with the cold head (see Fig. 5.1) to improve heat exchange. A conductive layer and other electronic components which are on the upper side of the plate have no connection to the cold head.

The measurement bench is shown in Fig. 5.2. Base and collector currents of the transistor are measured with shunt resistors $R1$ and $R2$ respectively. Diode $VD1$, capacitor $C1$ and resistor $R4$ are used to avoid undesirable effects of long cables used to connect the transistor inside the cryogenerator and the external measurement circuit. This measurement bench is used to find currents and voltages of all transistor nodes.

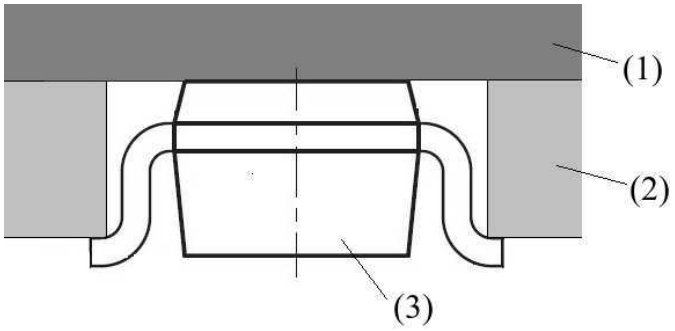

Figure 5.1: Transistor mount: cold head - (1), circuit board (conductive lay-out down) - (2), tranistor package - (3)

In such a design all components except for the transistors themselves are situated outside the cryogenerator. This solution minimizes the number of cables needed to connect to the “cold“ part of the bench.

All the measurements are automated with control software written in the LabVIEW graphical programming environment. Due to a non-standard approach to device modeling, which is described in section below, the measured data are not intended to be organized in the form of curves for some constant values. For example, measured points of output characteristics may be spread rather randomly and uniformly in a certain area (which

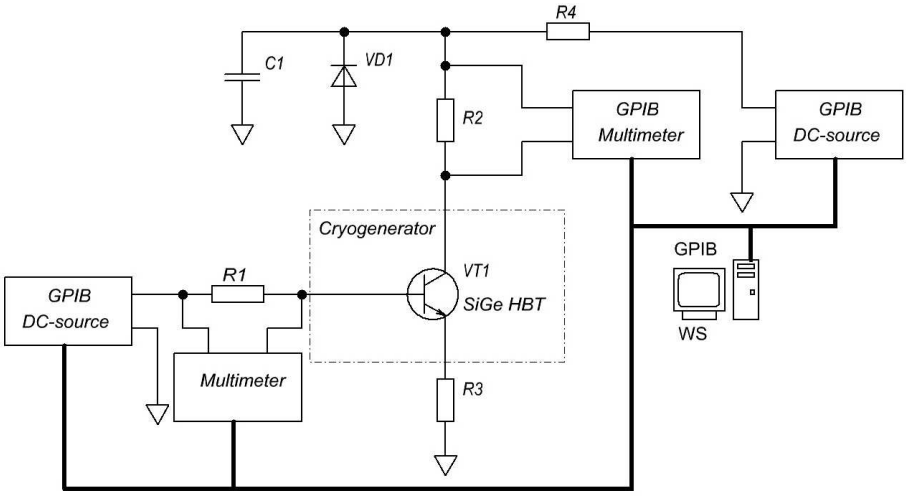

Figure 5.2: Experimental test bench used for measurement of output characteristics

is interesting for device simulation), but not in the form of a dependence curve of a collector-emitter voltage for certain constant values of a base current. This fact simplifies the measurement task, since no techniques are needed to stabilize the base current. The measured data are obtained by sweeping two voltage sources, when for a fixed value of the base voltage source, the collector voltage source sweeps all values in two directions.

Measurements Results Fig. 5.3 shows output characteristics of the transistor BFP650 at room temperature with the measurement bench described above. These data are measured for increasing and decreasing collector-emitter voltage (V_{CE}). Such a result correspond to the device specifications and demonstrates the aptitude of the measurement system.

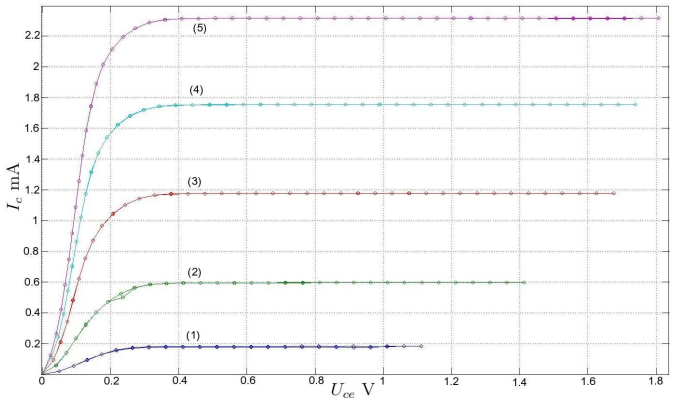

Figure 5.3: BFP650 output characteristics at room temperature: (1) $I_b = 0.59$ uA, (2) $I_b = 2$ uA, (3) $I_b = 4$ uA, (4) $I_b = 6$ uA, (5) $I_b = 8$ uA, (6) $I_b = 10$ uA

The results of measurements at the temperature of the liquid helium for the sake

of modeling are presented in the form of two surfaces. The first surface represents the dependence of the base current (I_B) versus base-emitter and collector-emitter voltages (V_{BE} and V_{CE} respectively). The second (output) surface is the dependence of the collector current (I_C) versus the same base current and collector-emitter voltage (I_B and V_{CE} consequently):

$$I_B = f(V_{BE}, V_{CE}), \quad I_C = g(I_B, V_{CE}). \tag{5.3}$$

These surfaces may be considered as input and output transistor characteristics. Typical examples of output surfaces for different transistors of the same reference BFP650 are shown in Fig. 5.4, 5.5, 5.6. It has to be pointed out that these results are measured as surfaces, but not as traditional curves like that in Fig. 5.3, where I_B is constant for each curve.

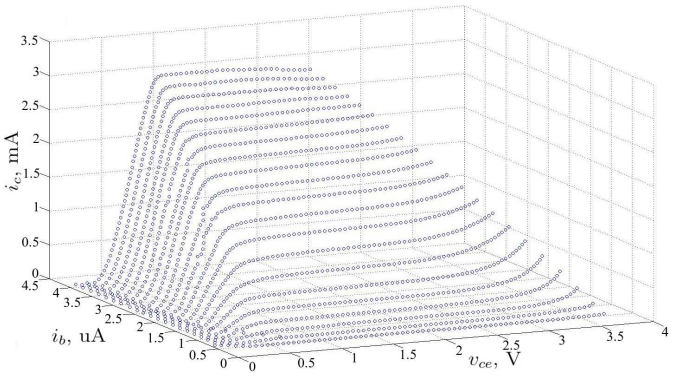

Figure 5.4: i_c as a function of i_b and v_{ce} for a transistor of the first type

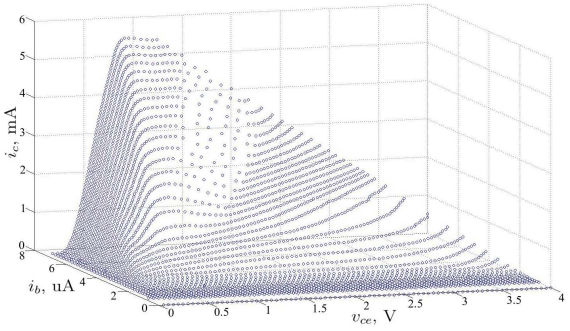

Figure 5.5: i_c as a function of i_b and v_{ce} for a transistor of the second type

Comparing these measurement results, one can observe the large characteristics dispersion between all transistors of the same type. Transistors exhibit different low temperature phenomena:

1. turn-off V_{CE} threshold (present in all transistors of this type);
2. cut-off V_{BE} area, which is not less than 1.1 V (present in all transistors of this type);

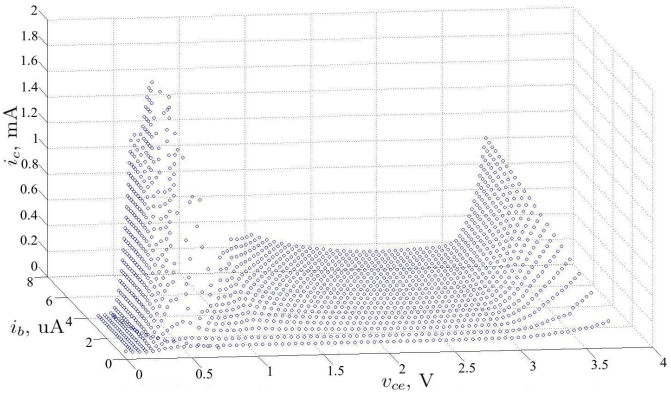

Figure 5.6: i_c as a function of i_b and v_{ce} for a transistor of the third type

3. area of negative differential resistance;
4. strong Early effect;
5. discontinuity and hysteresis behavior of $I_C(V_{CE})$ curves (this discontinuity occurs at different values of V_{BE} for different sweep directions) for rather high I_B currents.

It has to be mentioned that all the transistors exhibit the last phenomenon, but for the majority of them it is present for high I_C currents (greater than $5 - 6$ mA). This effect has been observed and explained for 300 GHz HBTs in the vicinity of the liquid-nitrogen temperature [92]. In the same way, the physical origins of the effect of negative differential resistance for SiGe transistors and the same temperature range is studied in [96]. The physical explanations of these effects observed for 40 GHz HBTs at liquid helium temperatures is a matter of further physical discussions. In any case these effects can be useful from the practical point of view. For example, negative differential resistance and discontinuity may be used in relaxation type oscillators.

According to the presence of these phenomena all transistors can be sorted into the following groups:

1. transistors without low-temperature phenomena except for the first and second types (see Fig. 5.4 for output characteristics);
2. transistors with considerable presence of third or fourth phenomena in addition to the phenomena of the first and second types (see Fig. 5.5 for output characteristics);
3. transistors with phenomena of fifth type for rather low I_C currents of about $0.4 - 1.5$ mA (see Fig. 5.6 for output characteristics).

Transistors of the second type are the most widespread (five out of ten). But the most desirable for real cryogenic applications are transistors of the first type (two out of ten) since

they have the minimum of undesirable phenomena. Unique low-temperature phenomena of the third group of transistors (two out of ten) may be used for such applications as frequency multipliers, various chaotic circuits, multi-valued digital logic circuits, etc. A special group of transistors is formed with devices which do not operate at liquid helium temperature (one out of ten).

Modeling of SiGe HBTs at Cryogenic Temperatures Precision electrical models are a necessity for modern electronic design. This fact holds true for designing electronic circuits for low-temperature applications. But it is known [97] that for extreme temperatures, standard compact models, even such sophisticated as VBIC and Mextram, fail to represent all physical phenomena. Another difficulty connected with cryogenic transistor modeling is the parameter extraction. The model difficulty and large number of parameters require special measurement strategies and commercial parameter extracting software (such as IC-CAP, UTMOST, etc.). Furthermore, in this case special measurements and extracting procedures have to be conducted for each single transistor, since, as it has been shown above, all transistors behave very differently at cryogenic temperatures.

In order to resolve these problems a simple neural network model has been proposed for transistor modeling. Such a model can be easily implemented in Advanced Design System (ADS) from Agilent Technologies.

According to the suggested model, a transistor is considered as a nonlinear two-port black-box. This system is modeled with two nonlinear implicit algebraic equations for the static device model:

$$\begin{cases} I_B - F(U_{BE}, U_{CE}, I_C) = 0, \\ I_C - G(I_B, U_{CE}) = 0. \end{cases} \tag{5.4}$$

Functions $F(\cdot)$ and $G(\cdot)$ are approximated with artificial feedforward neural networks based on the measurement results. As it is well-known, artificial neural networks (ANN) are universal nonlinear approximating and modeling tools based on a connectionist approach to computation. ANNs, see [98], consist of an interconnected group of artificial neurons, which simulate the structure and functional aspects of biological neural networks. In the present case two neural networks are trained to approximate functional relationships $F(\cdot)$ and $G(\cdot)$. Since the training algorithm is fully automatic, no special measurement strategy is needed. That is the reason why input and output characteristics are formed as surfaces, but not curves. In the same time, when the procedure is well established, the model building for each transistor is an easy and fast process and does not require special knowledge of the semiconductor physics at cryogenic temperatures.

Approximation is made with the help of MATLAB Neural Network Toolbox, which in case of inaccessibility may be successfully replaced with home-made software. Real unsorted measurement data are used for network training. The network for each function (F and G) consists of three layers of 4, 2 and 1 sigmoid neurons respectively. The total mean squared error performance for each surface is better than 10^{-4} and may be significantly decreased by increasing the number of inner neurons.

Such an approximation can be made only for transistors of the first and second type which are more interesting for conventional electronic applications, because sigmoid activation functions are not able to model discontinuities.

ADS implementation of the suggested model is made with a two-port symbolically-defined device (SDD) which can mathematically connect voltages and currents of its ports with implicit or explicit nonlinear equations. Fig. 5.7 shows an ADS design for measuring input and output curves of the suggested transistor model. In Fig. 5.8 and 5.9, the characteristics simulated with ADS for the models of the first and second transistor types respectively are compared to measured data (circles).

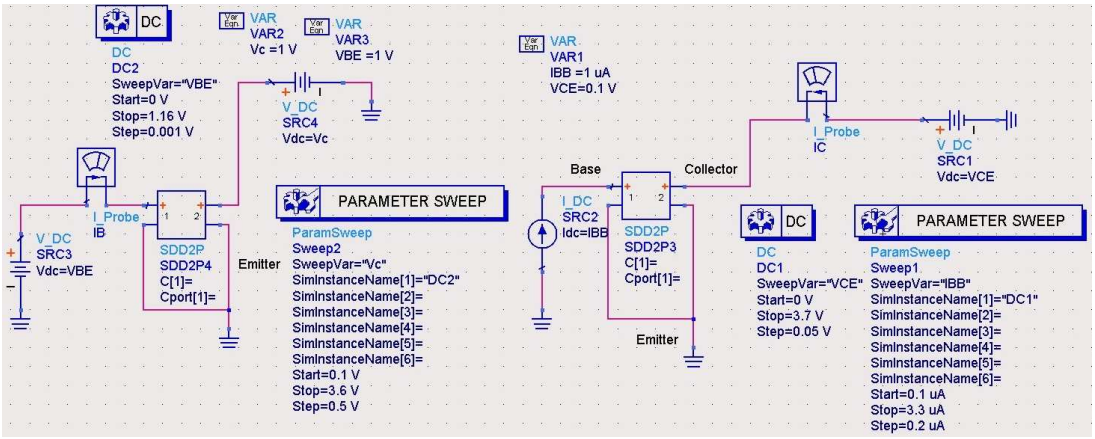

Figure 5.7: ADS design for measuring input and output characteristics of the transistor model

It is seen from Fig. 5.8 and 5.9 that the suggested model successfully approximate characteristics of SiGe HBTs of both the first and the second type at cryogenic temperatures. So, the suggested model can be successfully used for all types of designs available in ADS, in particular Harmonic Balance (HB), Transient Analysis, DC and AC Analyses.

In order to add dynamic features of the real transistor, this model may be expanded with base-emitter and collector-base capacitors of both linear or bias-dependent type without any revision of the model nature. The reactive features of the transistor can be directly measured or taken from a datasheet, since it has been found [99], that the reactive elements of such devices do not change considerably in the wide range of temperatures. This confirms that cryogenic DC measurements in addition to the ambient temperature reactive model are sufficient for many cryogenic designs of relatively low frequencies at cryogenic temperatures.

The disadvantages of this model are, first, the impossibility to extrapolate measurement data (one model is built for one value of temperature and for a given range of input values) and, second, the possible inaccuracy for high-frequency signals.

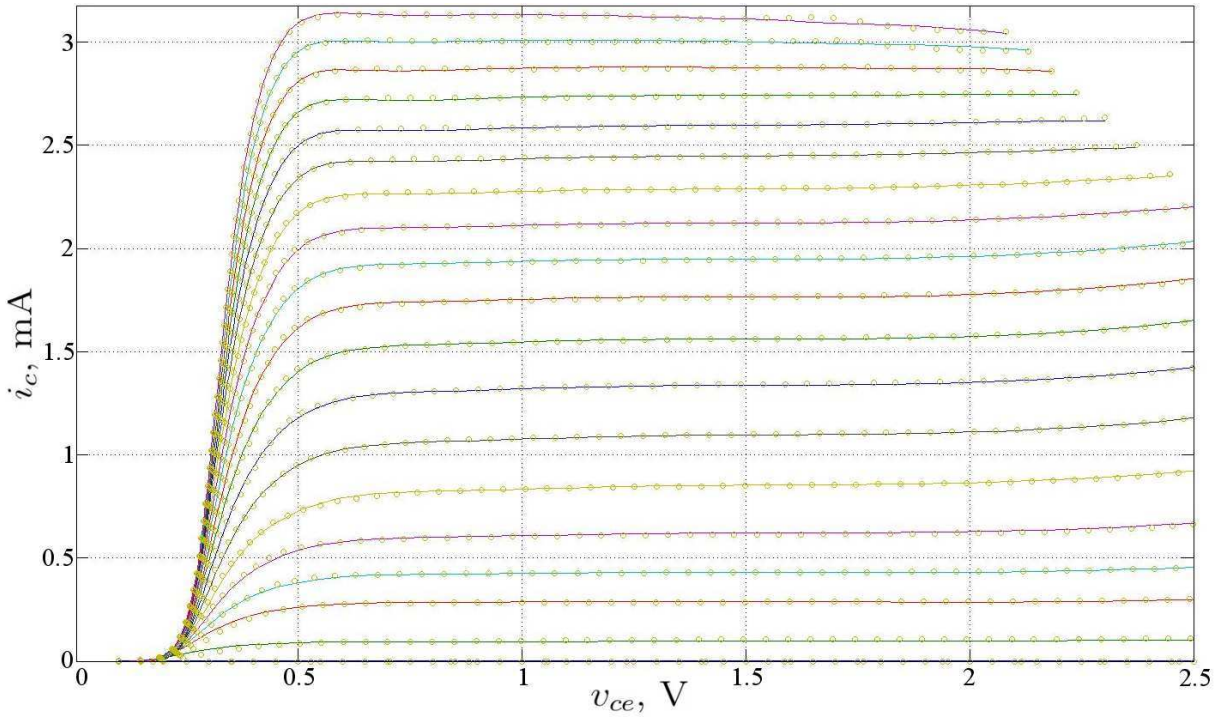

Figure 5.8: Measured (circles) and modeled with ADS (solid lines) output curves for a transistor of the first type

The advantages of this model are, first, the simplicity and rapidity of creation for any transistor of the first and the second type; second, the simplicity of integration into ADS; third, the high accuracy of approximation of DC measurements (all continuous types of low-temperature phenomena); forth, the possibility of usage in all types of design.

Example of an Amplifier Design The proposed transistor model of the first type has been used for designing a simple cryogenic common-emitter amplifier. This simple device can be used as a "cold" preamplifier of a frequency stabilization system based on the passive quartz resonator or as a part of an oscillating loop.

The ADS schematics of this electronic circuit is shown in Fig. 5.10. The resistors are shown with their actual measured low-temperature values. AC and DC analyses are performed for this type of an electronic circuit. DC analysis is needed for all types of simulation to check if the transistors work within measured data since the model is not capable to make extrapolation. For this design the collector current is about 1 mA.

The measurements of the amplifier transfer function are made with an Agilent Spectrum/Network/Impedance Analyzer 4395A. The effect of the long coaxial cables (about 0.9 m of internal cryogenerator cables and 0.5 m of external cable, which form input and output signal paths) is compensated with calibration. For this purpose two identical cables are soldered inside the cryogenerator near the DUT.

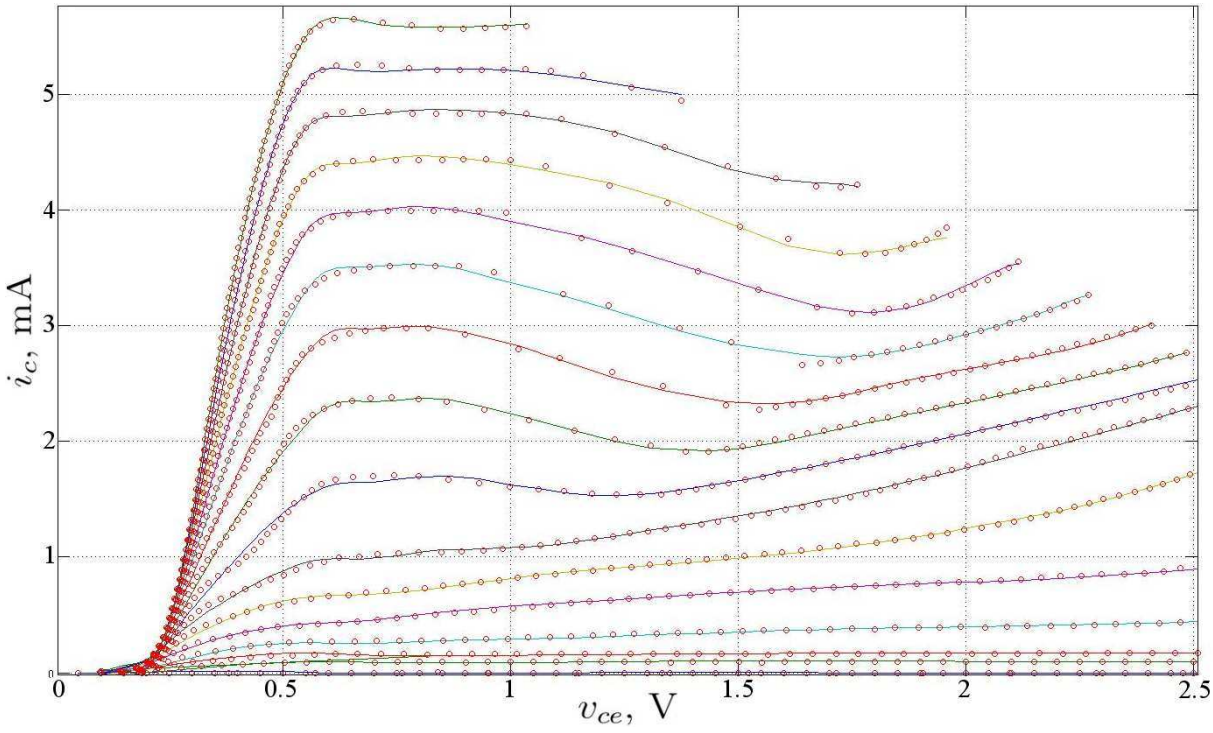

Figure 5.9: Measured (circles) and modeled with ADS (solid lines) output curves for a transistor of the second type

Fig. 5.10 shows the magnitude of the designed amplifier transfer function $H(j\omega) = V_{out}/V_{in}$ (where $\omega = 2\pi f$ is an angular frequency, *in* and *out* are shown in Fig. 5.11) as a result of measurements (solid curve) and simulation (dashed cure). The simulation results are in good agreement with measurements. This fact confirms the adequacy of the proposed methodology and modeling.

The presented amplifier provides a gain of about 9.7 dB for the typical frequency band of hyper-stable oscillators ($1 - 50$ MHz).

In this section we have considered several steps of electronic design procedure for the liquid-helium temperature range. At the first stage, an appropriate active device (SiGe HBT) has been chosen based on a list of requirements. This transistor type is a good candidate for utilization in low-noise electronic applications at liquid-helium temperatures. In this paper one commercially available reference of SiGe HBTs has been investigated. It turned out that the considerable dispersion of characteristics with manifest low temperature phenomena exists. In the same time some samples have very good characteristics with just the turn-off V_{CE} threshold and the increased cut-off V_{BE} area. Other samples are subject to considerable cryogenic phenomena, which, on the other hand, may be used for special purposes. At the second stage, an accurate and simple-to-use neural network model has been proposed for devices with continuous static characteristics. This model is suited for any type of circuit analyses, available in Agilent ADS. At the final stage, a

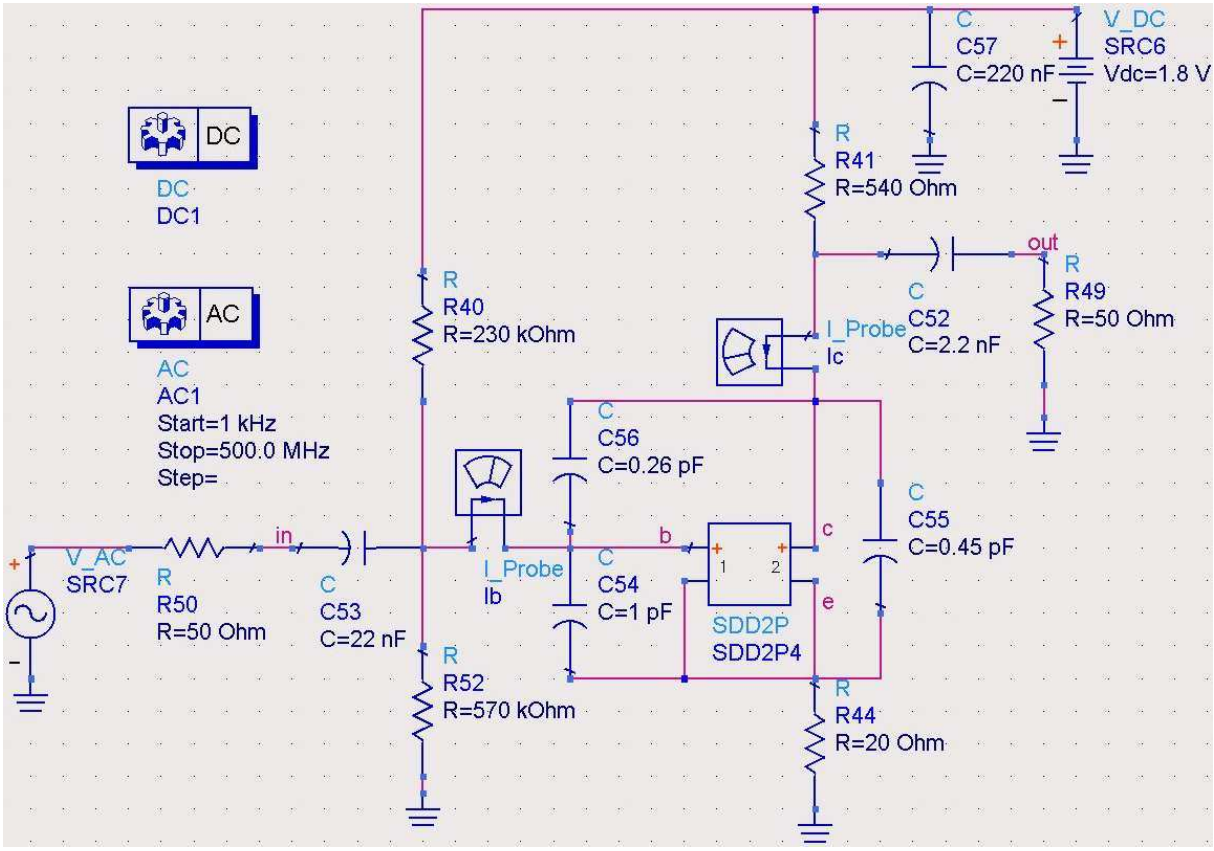

Figure 5.10: ADS Design of a simple cryogenic amplifier

simple cryogenic amplifier has been designed. The results of measurements are compared to simulation. Though this amplifier is rather simple it can be used further in frequency stabilization loops or hyper-stable oscillators. So, the whole modeling procedure and measured results provide useful information for scientists and engineers interested in low-noise electronics of liquid-helium temperature range.

5.2.3 N-Channel JFET

As it is shown in the previous subsection, SiGe HBTs are good candidates for actual applications as active devices in liquid helium electronics. But they have one severe disadvantage: after some cycles of cooling and heating, they fail (lose active properties). This happens probably due to the mechanical stress originating from different contraction temperature coefficient of the transistor body and package. So, the reliability of these devices leaves much to be desired.

Contrary to the statement made in the first subsection of the present section, the possibility of operation of JFET transistors is reported [10]. Among tested references

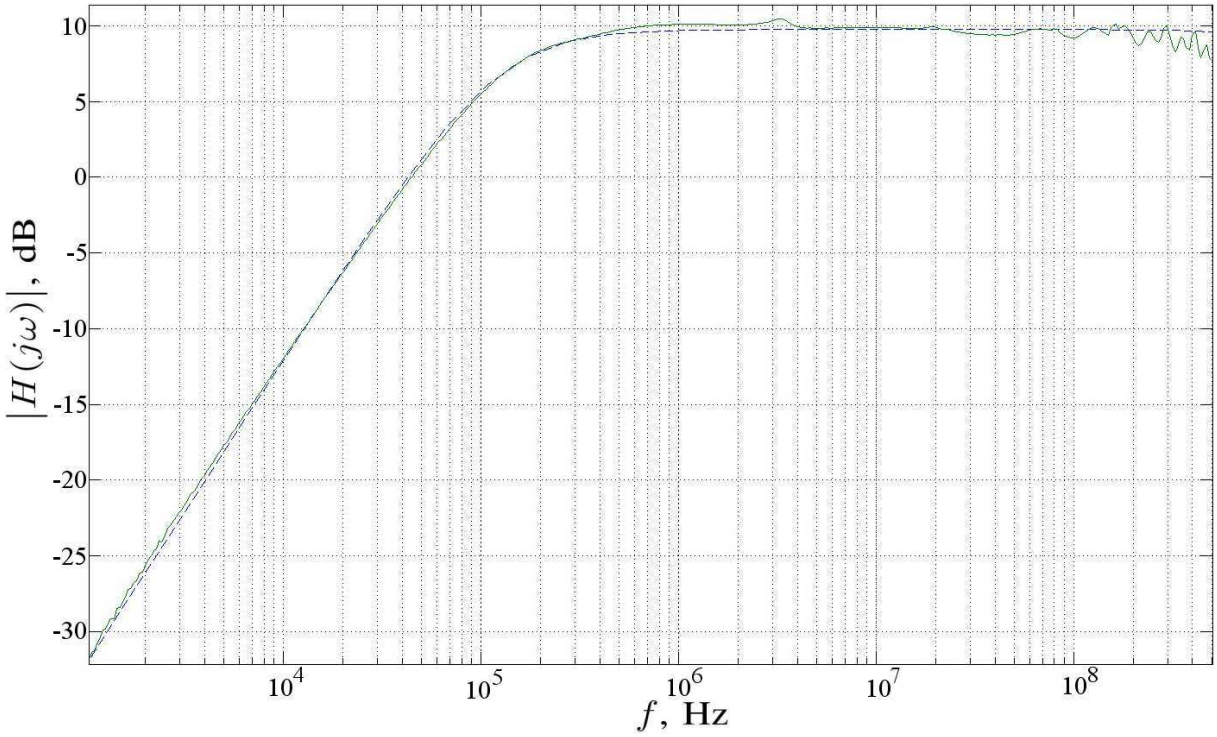

Figure 5.11: Comparison of the measured (solid curve) and simulated (dashed curve) magnitudes of the cryogenic amplifier transfer function

(2N3819, 2N4223, 2N4416, BFR30LT1, J201, J310, SST201) only 2N4223 transistors are said to be able to operate below 30K. The advantage of this transistor reference is that it has a metal package, known as TO-72. This fact, probably, solves the problem of package contraction and expansion with temperature. This subsection clarifies the possibility of utilization of this reference in actual liquid helium applications.

2N4223 transistors were tested in the similar way as BFP650 taking into account that the former are field-effect devices. So, the drain current I_D is measured and represented as a function of the gate-source and drain-source voltages (V_{GS} and V_{DS}, correspondingly) with the gate current I_G neglected:

$$I_D = F(V_{GS}, V_{DS}), \quad I_G \approx 0. \tag{5.5}$$

When transistors are in good thermal contact with the cold head (with the mounting similar to that in Fig. 5.1), tests of all the reference samples show absence of the drain current for all values of V_{GS} and V_{DS} voltages. But when transistors have no connection with the cold head (no any mechanical touch), about 50% of devices exhibit some dependence of the drain current on the node voltages. The typical characteristics of such devices are shown in Fig. 5.12. The device behavior is explained by the self-heating effect (see Fig. 5.12(b)) which is related to the measurement procedure. The first measurement curve (that for the first constant value of U_{GS}, curve (1)) makes the transistor to conduct

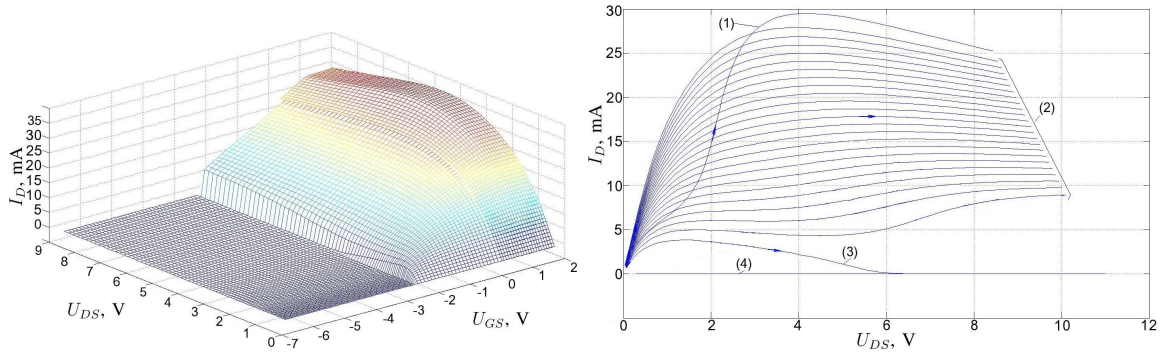

(a) Typical characteristic surface

(b) Measurment curves: (1) - heating chain of measurements, (2) - self-heated characteristics, (3) - transistor cooling chain, (4) - cold transistor measurements

Figure 5.12: Typical measured characteristic of about 50% of 2N4223 transistors

some current I_D. This current heats the device up. The increased temperature leads to increase in conducting current and so. This process may be thought as a kind of a positive feedback system in current-temperature relations. Evidently, the process ceases when transistor and the cold head achieve a thermal equilibrium state. In this state, transistor temperature is significantly higher than 4K. Following measurement curve are acquired for the transistor in self-heated mode (a group of curves (2), Fig. 5.12(b)). Next, when the drain current is rather weak, the system comes to a threshold: the current is not able to keep up the transistor temperature. So, both parameters rapidly decrease, since current decrease leads to decrease in temperature (curve (3)). All the following measurements are made for the "cold" transistor where the drain current is negligible.

Fig. 5.12 demonstrates the fact that the device under study is capable of working at the liquid helium environment (but not at liquid helium temperatures). Using this transistor, a cryogenic RF amplifier was designed. Its passive electronic components have the temperature of the cold head, and the transistor is placed inside a cavity in a copper block without mechanical contact. Unfortunately, this amplifier demonstrates very poor characteristics and has several disadvantages, such as necessity of manual transition into the self-heating mode (by applying higher bias and supply voltages), dependence on a circuit design and transistor position. In addition, the amplifier demonstrates very poor reliability and repeatability (high dependence on the environment). So, these inconveniences suggested the necessity of the transition to another type of transistors which is deeply investigated in the following subsection.

5.2.4 N-Channel Dual Gate MOSFET

As the first subsection states silicon MOSFET devices are able to work at liquid helium temperatures. This fact is confirmed by several preliminary investigations [10, 51, 50].

These works report good performance of BF988 transistors from Intersil though some other references (in particular, BF996 BF996S, BF998, BS170, VN10LP, ZVN3306A) were also tested. Though BF988 demonstrates the desired properties, others show the incapability of working at liquid helium temperatures. All the following measurements and test of transistors themselves and devices based on them are made for the case of good thermal contact between the package and the cold head (installation solution similar to that shown in Fig. 5.1).

The typical measurement results for BF988 transistors are shown in Fig. 5.13. Though characteristics at 4K have significant dispersion for different device samples, their type of the form mainly remains the same contrary to the case of SiGe HBTs where three different types of curves were figured out (see Subsection 5.2.2). And, unlike an N-Channel JFET, the operation of these devices is possible when the package directly adjoins the cold head. So, operation of BF988 transistors is not due to the self-heating effect that allows to avoid the reliability issues. It also has to be noted that some of the samples are "freezed out", so they do not conduct any current at liquid helium temperatures. But the rate of such sample, which cannot be used at 4K, is estimated to be less than 20%.

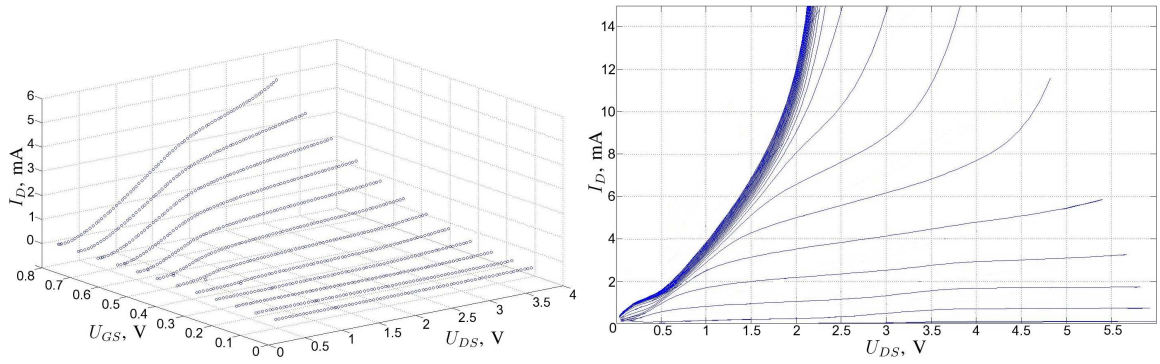

(a) Typical characteristic surface (b) Measured characteristic curves

Figure 5.13: Typical measured characteristic of BF988 transistors (with the second gate voltage $V_{G2S} = 4$ V)

Fig. 5.13 demonstrates that BF988 transistors are good candidates for implementation in liquid helium electronic systems. Following the procedure described in Subsection 5.2.2, transistor characteristics (Fig. 5.13) are approximated in the form 5.5 with the help of ANNs. The resulting model is fit for implementation in the ADS modeling software (for more details on the approach see Section 5.2.2). This implementation is used for further design of electronic device for liquid helium temperatures.

Cryogenic Amplifier Design and Implementation As a starting point two liquid-helium RF amplifiers were modeled and implemented. The circuit of these amplifiers is shown in Fig. 5.14. This system is a two-stage circuit: the first stage is a common-gate FET amplifier (based on transistor T1), and the second is an emitter follower (based on transistor T2) used to increase the load impedance of the first stage and to avoid influences of the connecting cables on the amplifying stage. The polarization of both transistors is

regulated individually in order to overcome the dispersion in their characteristics.

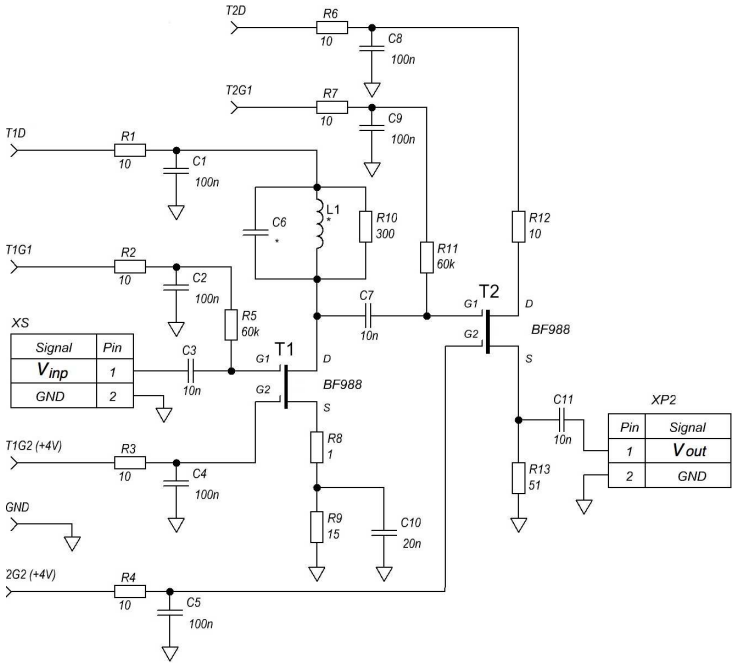

Figure 5.14: Schematic diagram of an amplifier based on BF988 transistors for liquid helium applications

The measurements of transfer functions of both amplifiers are made in the same way as in the case of SiGe HBTs. So, the network analyzer and with appropriate compensation of long cable effects is used (see Subsection 5.2.2 for more details). The magnitudes of the transfer functions measured for both cryogenic amplifiers (4.3K) based on BF988 transistors are shown in Fig. 5.15. For both amplifiers, polarization voltages of the first gate of the first transistor $V_{T1G1} = 0.8$ V, the first gate of the second transistor is biased with $V_{T2G1} = 1.26$ V, the second gates of the both have $V_{T1G2} = V_{T2G2} = 4$ V. Supply voltages are shown in Fig. 5.15. These values are chosen experimentally to achieve the maximum amplifier gain.

As Fig. 5.15 suggests, even though two amplifiers have identical circuits, they have slightly different characteristics. This fact is due to the considerable dispersion in transistor characteristics. The first device has an amplification of about 9 dB for 4.5 V supply voltage, 11 dB for 5.5 V and 13.3 dB for 6.5 V inside its bandwidth (approximately 450 kHz-110 MHz). Accordingly the second device has an amplification of about 10.7 dB for 4.5 V supply voltage, 15.8 dB for 5.5 V and 17.1 dB for 6.5 V inside its bandwidth (approximately 500 kHz-75 MHz). So, the second amplifier provides a higher gain with a shorter bandwidth.

The main disadvantage of both devices is relatively high dissipated power. This power increases the absolute temperature of the copper block under the thermal filter.

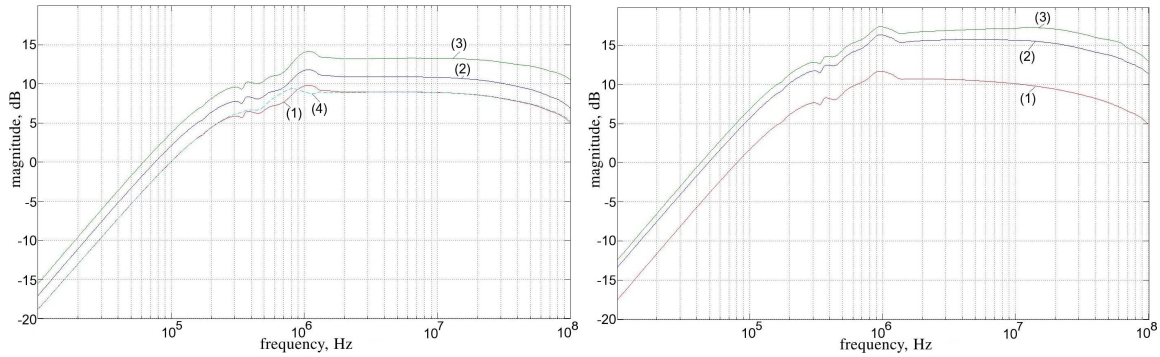

(a) First amplifier (b) Second amplifier

Figure 5.15: Transfer function magnitudes of two RF amplifiers working at 4.3K: (1) - $V_{2D} = V_{1D} = 4.5$ V, (2) - $V_{2D} = V_{1D} = 5.5$ V, (3) - $V_{2D} = V_{1D} = 6.5$ V, (4) - $V_{2D} = 4.5$ V, $V_{1D} = 5.5$ V

Cryogenic Amplifier Design Phase Noise Measurements Another important characteristic of an amplifier used in time and frequency applications is its phase noise. In order to estimate a phase noise of the designed amplifiers, three measurement schemes were implemented (see Fig. 5.16). Shown measurement system is represented with TSC5120A phase noise test set from Symmetricom [100] which uses a cross correlation technique. As a frequency source, the most available reference is used. It is a hydrogen maser with the carrier frequency of 5 MHz. All the amplifier noise measurements are made with the DUT temperature of 5K.

First, the phase noise of two amplifiers is measured (Fig. 5.16(a)). In this case, a signal from one source passes through the amplifiers and the one resulting signal is measured against another one. Such configuration means that a cross correlation algorithm of the measurement device eliminates the correlated noise. This correlated noise comes not only from the cables and the common signal source, but also from amplifier themselves since both amplifiers are subjects to the common vibration and temperature fluctuations. And, as a result, a sum of uncorrelated noises of two amplifiers is obtained (see Fig. 5.17(a)).

Second, the phase noise of one amplifier is measured by comparison of a signal amplified inside a cryogenerator and a signal passed directly through the cryogenerator connecting cables (Fig. 5.16(a)). In this case correlated cable noises are not seen on the resulting spectra due to their elimination by cross correlation technique. The result is shown in Fig. 5.17(a).

Third, connecting cable noise is measured using scheme 5.16(c). Here, a signal passed through cryogenerator is compared to the original reference. So, only uncorrelated, i.e. cable induced noise, is obtained (see Fig. 5.17(c)).

The uncorrelated noise of two amplifiers (Fig. 5.17(a)) shows two typical slopes of the phase noise spectrum. They are a white phase noise (f^0) and a flicker phase noise (f^{-1}). The latter has a value of about -134 dBc/Hz at 1 Hz from the carrier. And the

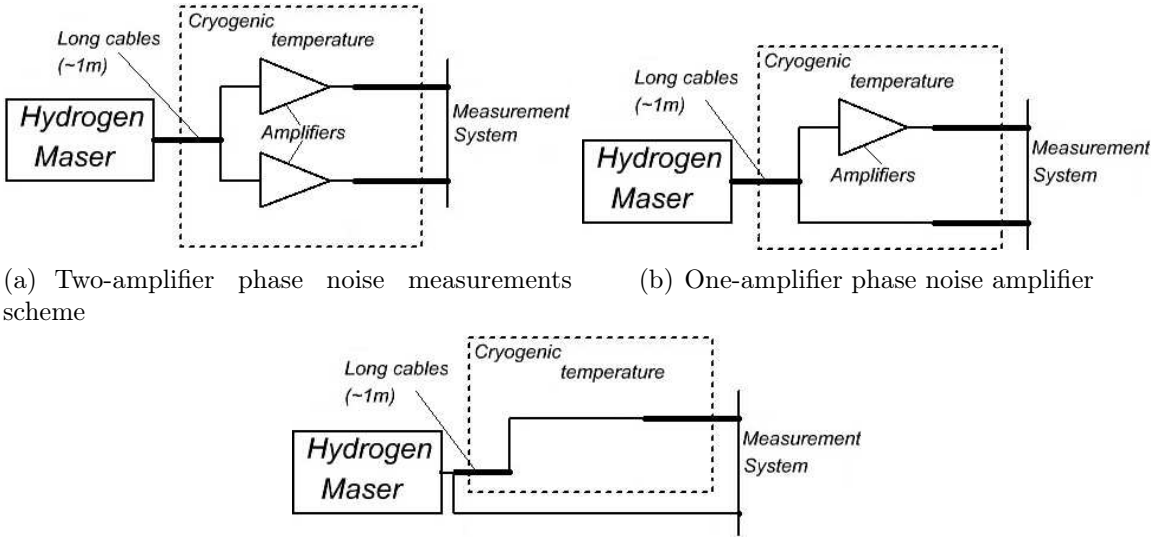

(a) Two-amplifier phase noise measurements scheme

(b) One-amplifier phase noise amplifier

(c) Cable phase noise amplifier

Figure 5.16: Phase noise measurement schemes

former is about at the level of -154 dBc/Hz. Concerning these two values, designed amplifiers outperform room-temperature commercial low-noise amplifiers (HVA-200M-40-B from FEMTO) which are used for room temperature parts of the closed reference systems in the following chapter (flicker of about -110 dBc/Hz at 1 Hz, and white noise at the level -139 dBc/Hz). Additionally, to these noise laws, a phase random walk (f^{-2}) is also observed for very low Fourier frequencies. This phenomenon is due to cable random walk which is not ideally compensated by two cables and due two differences in amplifiers themselves. Also, two spurious frequencies of 1.7 Hz and 3.4 Hz (obviously they correspond to the working cycle of the cryocooler) suggests existence of the difference in two measurement branches. Though to some extent these non-idealities could be neglected.

The present measurements may be used to evaluate an oscillator noise floor due to sustaining electronics. In this case, the main assumption states that the oscillator noise is dominated by the sustaining amplifier noise. For such an estimation, the measurement results can be taken as the open loop noise. So, estimate the one-sided power spectral density of random phase fluctuations at the Fourier frequency of 1 Hz:

$$S_\phi(1\text{Hz}) = \mathscr{L}(1\text{Hz}) + 3\text{dBc}) - 3\text{dBc} \approx -131\frac{\text{dBrd}^2}{\text{Hz}} = 10^{-13.1}\frac{\text{rd}^2}{\text{Hz}}, \tag{5.6}$$

Next, the one-sided PSD of fractional frequency fluctuations is calculated as follows, where loaded quality factor Q_l is taken to have a moderate value of $30 \cdot 10^6$:

$$S_y(1\text{Hz}) = \left(\frac{1}{2Q_l}\right)^2 S_\phi(1\text{Hz}) \approx 2.2 \cdot 10^{-29}\text{Hz}^{-1}. \tag{5.7}$$

So, the Allan deviation floor of such an oscillator can be estimated as

$$\sigma_y = \sqrt{2\ln(2)S_y} \approx 3.6 \cdot 10^{-15}. \tag{5.8}$$

This value is about two decades lower than that of actual room temperature quartz crystal oscillators.

The full phase noise of one amplifier (Fig. 5.17(b)) is dominated by the f^{-2} law in the vast frequency range starting from the carrier. This noise is a consequence of the temperature random-walk noise. As it is clearly seen, two spurious frequencies of 1.7 Hz and 3.4 Hz in this case are more important suggesting that this influence is simultaneously applied to both amplifiers in the previous measurement.

The cable phase noise in the close to the carrier region (Fig. 5.17(c)) is also a consequence of the temperature fluctuations with the f^{-2} spectral characteristic slope.

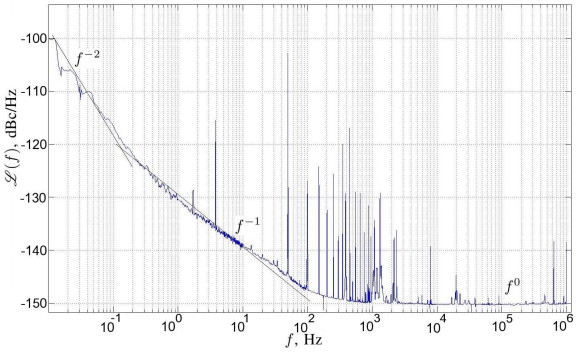

(a) Phase noise PSD of two amplifiers measured in parallel (Fig. 5.16(a))

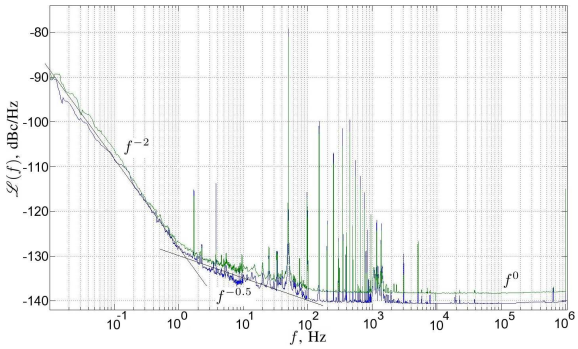

(b) Phase noise PSD of two amplifiers measured separately (Fig. 5.16(b))

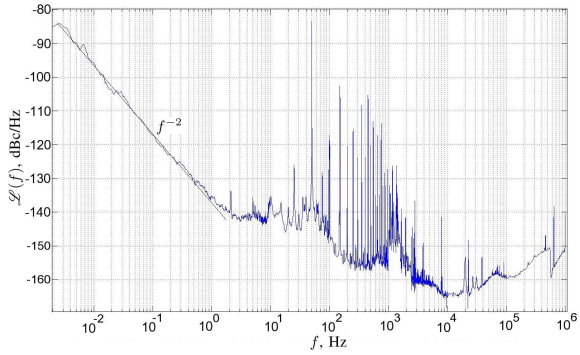

(c) Phase noise PSD of the connecting cables (Fig. 5.16(c))

Figure 5.17: Phase noise of cryogenic amplifiers and cables

Conclusion N-channel dual gate MOSFET transistor has a very important advantage over investigated SiGe HBT transistor reference. That is its reliability: all measured transistors showed no degradation with time, no unexpected fails after several circles of cooling and heating, no heightened sensibility to the environment. In other words, these devices are sufficiently robust. But, unfortunately, the measured reference could be referred as outdated. This fact could pose problems for future cryogenic projects. As for current projects, the solution is to make a stock. So, from this point of view the preference has to be given to the SiGe technology which is currently undergoing a phase

of fast development.

Chapter 6

Feedback Phase Noise Reduction

From the first years of electronic era, scientists and engineers have been looking for different ways of noise reduction. The statement is true for both non-autonomous and autonomous systems, such as frequency sources. For the latter systems, two main approaches may be separated. According to the first approach, a designer has to deepen inside his/her oscillator as a system of subsystems or simpler building blocks (resonators, amplifiers, transistors, whatever) improving its topology, noise characteristics, device sensitivity to external influences. Concerning the second approach the oscillator itself (with other components) is considered as a building block for a higher level super-system. Here, it is the upper level system which improves noise characteristics of the oscillator regardless of its physical nature, as well as internal features of other components. Also, it is worth to note that besides two approaches discussed above some intermediate solutions are possible [101]. This chapter is fully dedicated to the second approach or more precisely to a feedback noise reduction technique using an external cryogenic BAW device as a discriminator. This means that the oscillator remains a black-box frequency source, while external elements (including cryogenic) are called upon to increase the frequency stability of the whole super-system.

6.1 Idea Overview

Control system theory is an interdisciplinary field of mathematics and engineering, that investigates dynamical properties of different objects. These objects could be of any physical nature. For example, applications of the control system theory to electrical, electromechanical, hydraulic, chemical, etc objects and phenomena are widely known. In all these applications, the control task is usually to force one or several system variables to follow a reference over time. This could be an object position, rotor velocity, fluid level, DC voltage level, etc. In the same time, application of the control system approach to the frequency control is much less known to the general scientific public. Indeed, if a sinusoidal

signal is considered as an object of control, its frequency could be considered as a variable to be controlled. It is also worth to note that such an approach is not widely spread in the time and frequency scientific community, though it is gathering momentum ([2, 1]).

The classical approach to the different problems of the control engineering is to use a feedback. One or several system variables or outputs are measured and then used by a controller to force the object to follow the reference. Thus, for example, velocity or torque of a motor is measured with a sensor. This information is transformed into a voltage, which is used by a kind of electronic controller to affect motor processes. Very often this problem is complicated by a task to make the system insensitive to fluctuations inside an object or to some external unwanted excitations. For instance, the motor control system has to tolerate moderate changes in drive load. Another example is a cruise control where the vehicle speed has to be kept constant regardless the changes in road slope, wind, mass etc. In other words, the system has to be stabilized in terms of one of its variables. Other examples are a problem of idle speed fluctuation control in engines, control of fluctuations in isolated power systems such as wind farms, fluctuations in hot-melt pipe welding and so on. Exactly the same problem is in the nature of frequency control. The goal here is to keep the carrier frequency constant (in fact, this is an output object variable) or to minimize its fluctuations which arises due to internal processes, temperature, vibration, etc. To do so, the classical feedback approaches could be used.

Though frequency control and classical fields of control system theory applications have much in common, there is one important difference that distinguishes the former. This difference concerns the sensor problem, i.e. the problem to transform the output variable into a quantity which is easy to process (usually a voltage). In the majority of applications this could be done relatively easily due to the fact that the needed information is stored in the form of amplitude or DC signal. So, the task is just to transform one physical quantity into another. Contrary to this, to extract the information stored in the form of frequency fluctuations, a reference source with better frequency stability characteristics is required. Usually, the existence of such a source makes the problem ridiculous. So, this is a problem of fluctuation transformation from the domain of signal frequencies (or equivalently phases) to the voltage domain, that makes frequency control problems of special interest.

One of feedback noise reduction techniques is known as high-quality factor (high-Q) external discriminator [102]. In the considered case, the discriminator role is played by a π-network with a high quality quartz crystal resonator. Indeed, when using a crystal resonator in such a passive way, it is easier to reach a loaded quality-factor (Q-factor) close to 70% of its unloaded Q-factor. An abstract scheme of the feedback system is shown in Fig. 6.1. When the loop is locked, frequency disturbance of the VCO output signal is filtered with the quartz crystal π-network and then compared to the original signal with disturbance. Ideally, the mixer output voltage is proportional to the phase difference between original and filtered signals (i.e. to phase error). This phase error is used by a loop filter to suppress this disturbance at the output of the VCO. Here, a special role is devoted to a frequency synthesizer which changes the signal frequency up to

the resonance frequency of the passive quartz crystal. These frequencies have to coincide in order to achieve the best filtering features of the π-network (see Chapter 1 for noise filtering with the quartz resonator). In fact, here the VCO function is performed with a 10 MHz quartz-crystal ultra stable oscillator (USO) having a very limited frequency tuning range but coupled to a synthesizer to correct this lack of tunability. In a more conventional feedback loop, this assembling is replaced with a VCO whose frequency range includes the resonance frequency of the passive crystal.

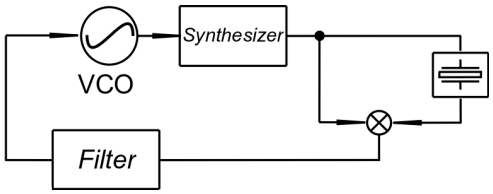

Figure 6.1: External frequency discriminator formed with the quartz crystal π-network and a phase detector

It is clear from the beginning (though this fact is proved and discussed in detail in the subsequent sections) that the system performance depends on the quality factor of the passive resonator. It is also shown that Q-factor is the only parameter (besides noise sources themselves) which influences the long term system performance. Nevertheless, in middle term the system requires optimization. So, in order to verify abilities of the loop under consideration to increase the frequency stability, a phase noise modeling is undertaken.

6.2 Modeling and Optimization Principles

In order to analyze the system from the point of view of the control system theory, its linearized frequency-domain model has been designed. Its corresponding block diagram is shown in Fig. 6.2, where each component of the loop is represented with a noiseless part, i.e. its transfer function, and a noise source added at its output (see Fig. 6.2 for the notations). The main goal of this model is to simulate the dependence of the phase noise at the system outputs, $out1$ or $out2$, versus a set of system loop parameters. It can be noticed that the first output can easily be measured against a reference frequency sources (Cesium clock or Hydrogen maser, for example, available in the laboratory) because of its nominal frequency at 10 MHz.

Assuming that the frequency control loop is locked, a linear mathematical model of the system can be developed. Behaviors of the loop elements (the VCO, the synthesizer, the quartz crystal, the filter and the phase detector) in a locked mode are described by their transfer functions $H_{vco}(s)$, $H_s(s)$, $H_r(s)$, $H_f(s)$, $H_{pdr}(s)$ and noise sources n_{vco}, n_s, n_r, n_f, n_{pd} correspondingly. Signal phases Θ_{vco}, Θ_s, Θ_r at the outputs of the VCO,

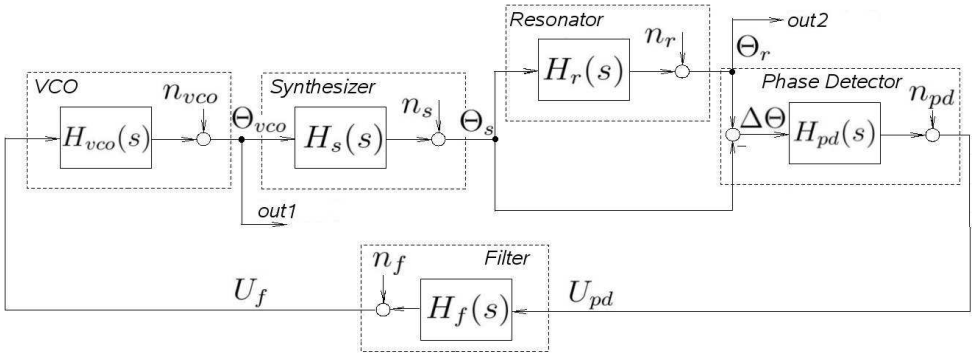

Figure 6.2: Block diagram of the linearized feedback system

the synthesizer, and the resonator respectively, and voltages U_{pd}, U_f (output voltages of the phase detector and the filter: see Fig. 6.2) are the control system variables. The inner variable of the phase detector $\Delta\Theta$ represents the difference between the original and filtered signals.

As shown in Fig. 6.2, there are five corresponding noise sources inside the loop. So, assuming without a lack of generality that these various noise sources are not correlated, the loop output phase noise is given by a linear combination of five terms ((6.1) and (6.2)). Each term consists of one of these noise sources multiplied by its corresponding weighting function, i.e the loop gain from its input node to the output node. These functions can easily be calculated with the help of Mason's rule:

$$\begin{aligned}\Theta_{out1}(f) = \Theta_{vco}(f) = H_{cl}(f)n_{vco} + H_{cl}(f)(H_r(f) - 1)\cdot \\ H_{pd}(s)H_{vco}(f)H_f(f)n_s + H_{cl}(f)H_{pd}(f)H_{vco}(f)H_f(f)n_r + \\ + H_{cl}(f)H_{vco}(s)H_f(f)n_{pd} + H_{cl}(f)H_{vco}(f)n_f. \end{aligned} \tag{6.1}$$

$$\begin{aligned}\Theta_{out2}(f) = \Theta_r(f) = H_{cl}(f)H_f(f)H_s(f)H_{vco}(f)H_r(f)n_{pd} + \\ H_{cl}(f)H_s(f)H_r(f)n_{vco} + H_{cl}(f)H_s(f)H_{vco}(f)H_r(f)n_f + H_{cl}(f)H_r(f)n_s + \\ + \Big(1 + \frac{H_{vco}(f)H_f(f)H_{pd}(f)H_s(f)H_r(f)}{1+H_{vco}(f)H_f(f)H_{pd}(f)H_s(f)-H_{vco}(f)H_f(f)H_{pd}(f)H_s(f)H_r(f)}\Big)n_r, \end{aligned} \tag{6.2}$$

where $H_{cl}(s)$ is a closed loop transfer function which could be expressed as follows:

$$H_{cl}(f) = \frac{1}{1 - (H_r(f) - 1)H_{pd}(f)H_{vco}(f)H_f(f)H_s(f)}.$$

The PSD of the phase deviation can be represented by the sum of the squared amplitude of each term in Equations (6.1) and (6.2) as follows:

$$\begin{aligned}S_{\phi 1}(f) = 2|\Theta_{out1}|^2 = 2|H_{cl}(f)|^2\Big(|n_{vco}|^2 + |n_{pd}|^2|H_f(f)|^2|H_{vco}(f)|^2 + \\ + |n_f|^2|H_{vco}(f)|^2 + |n_s|^2|H_r(f) - 1|^2|H_{pd}(f)|^2|H_f(f)|^2|H_{vco}(f)|^2 + \\ + |n_{res}|^2|H_{pd}(f)|^2|H_f(f)|^2|H_{vco}(f)|^2\Big) \end{aligned} \tag{6.3}$$

$$S_{\phi 2}(f) = 2|\Theta_{out2}|^2 = 2|H_{cl}(f)|^2\Big(|n_{vco}|^2|H_r(f)|^2|H_s(f)|^2 + |n_s|^2|H_r(f)|^2 + \\ + |n_{pd}|^2|H_f(f)|^2|H_{vco}(f)|^2|H_s(f)|^2|H_r(f)|^2 + |n_f|^2|H_s(f)|^2|H_r(f)|^2|H_{vco}(f)|^2\Big) + \\ + 2|n_{res}|^2\left|1 + \frac{H_{vco}(f)H_f(f)H_{pd}(f)H_s(f)H_r(f)}{1+H_{vco}(f)H_f(f)H_{pd}(f)H_s(f)-H_{vco}(f)H_r(f)H_f(f)H_{pd}(f)H_s(f)}\right|^2 \quad (6.4)$$

6.2.1 Element models

Let us consider transfer functions and noise components of all the loop elements. The corresponding noise PSDs are shown in Fig. 6.3.

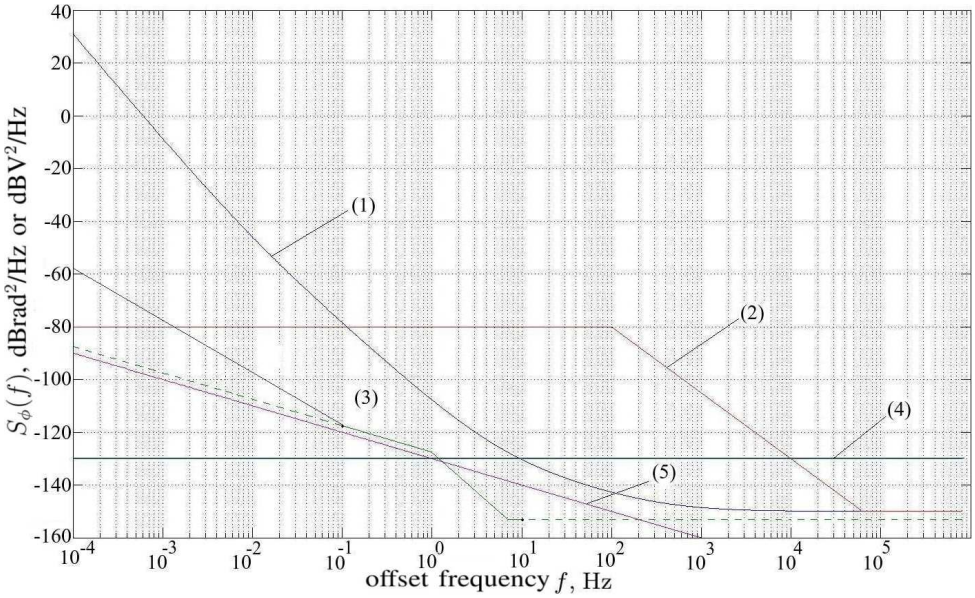

Figure 6.3: $S_\phi(f)$ of all noise sources: 1 - VCO, here a 10 MHz ovenized oscillator, 2 - Synthesizer, 3 - Resonator (just solid lines correspond to directly measured data), 4 - Phase Detector, 5 - Filter

1. By definition of the VCO, its phase fluctuations are the integral of frequency fluctuations around the nominal angular frequency ω_0:

$$\theta^*_{VCO}(t) = K_{VCO}\int_0^t U_c(\tau)d\tau,$$

where K_{VCO} is the VCO gain ($\frac{rad}{s \cdot V}$),and $\theta^*_{VCO}(t)$ is the noiseless output variable[1] of the VCO. So, the transfer function of the VCO (6.5) could be found by means of

[1]Here and further a variable with asterisk represents a noiseless part of the output, i.e. $\theta = \theta^* + n$

the Laplace transform:

$$H_{VCO}(s) = \frac{\theta^*_{VCO}(s)}{U_c(s)} = \frac{K_{VCO}}{s}. \tag{6.5}$$

The single-sided PSD of the VCO additive phase noise shown in Fig. 6.3 is obtained by direct measurements on a quite good 10 MHz oscillator (Curve (1) in Fig 6.3 is a typical result). It consists of four rather independent parts: white phase noise f^0, flicker phase noise f^{-1}, white frequency noise f^{-2}, flicker frequency noise f^{-3}, random walk frequency noise f^{-4}. Each noise component has its own physical nature. Thus, for example f^{-4} noise arises due to f^{-2} temperature variations inside the oscillator loop (this fact is discussed below). Also it has to be noted that both f^{-3} and f^{-2} noise components are almost absent in the spectrum of this specific oscillator.

2. The synthesizer (a HP 8643A in the following experiments) is used as an element which multiplies the frequency of the VCO. This component is used to change the signal frequency up to the resonance frequency of the passive quartz crystal ([103]). Usually the synthesizer is built on the base of a phase locked loop. A transfer function of the first order PLL in the phase plane (in locked regime) can be represented by the following expression (6.6).

$$H_s(s) = \frac{\theta^*_s(s)}{\theta_{VCO}(s)} = \frac{K_s}{T_s s + 1}. \tag{6.6}$$

In all the following numerical experiments, the dynamic features of the synthesizer are neglected since it is rather wide-band. The noise characteristic of this devise (Fig. 6.3, Curve (2)) are taken from the device data sheet ([104]).

3. The resonator can be represented as a first order phase filter in the phase domain (6.7) (see Chapter 2 of this work) which is the domain of signal phases. In absence of detuning frequency signal (it is driven to zero by the synthesizer), the resonator transfer function is

$$H_r(s) = \frac{\theta^*_r(s)}{\theta_s(s)} = \frac{1}{\tau s + 1}, \tag{6.7}$$

where τ is the resonator relaxation time $\tau = \frac{2Q_l}{\omega_0}$, Q_l being the loaded Q-factor of the resonator at the resonance angular frequency $\omega_0 = 2\pi\nu_0$. This system level representation of the resonator is not widely known and never used in circuit simulations. The power spectral density of the resonator phase noise is directly measured (Fig. 6.3, Curve (3), only solid lines) by [24, 3, 25]. As shown in Fig. 6.3, the PSD of a temperature-controlled resonator consists of f^{-3} and f^{-1} slopes which are results of natural frequency fluctuations. For frequencies typically lower than 10^{-2} Hz, the residual temperature fluctuations induce a f^{-2} noise ([105, 17, 14]), though this type of noise is not usually taken into consideration during simulation. The dashed line corresponding to high offset Fourier-frequencies is the noise floor of our measurement test bench. The resonator aging could also be added and approximated with a linear frequency drift rising as an additional f^{-4} slope for very low offset frequencies.

4. The simpler phase detector consists of an ideal multiplier, for which the double balanced mixer is a good approximation for RF and microwave frequencies. The output signal of the multiplier could be approximated by neglecting higher frequency terms:

$$U^*_{pd}(t) \approx \frac{V_r V_s}{2} \sin(\theta_r(t) - \theta_s(t)) = K_{pd} \sin(\Delta\theta(t)) \approx K_{pd}\Delta\theta(t),$$

where V_r and V_s are magnitudes of the output voltages of the resonator and synthesizer respectively. The linearization is relevant because of the very small phase error $\Delta\theta(t)$. Consequently the transfer function of the phase detector is approximated by an instantaneous element (Eq. 6.8) or a phase detector gain K_{pd} ($V\ rad^{-1}$).

$$H_{pd}(s) = \frac{U^*_{pd}(s)}{\Delta\theta(s)} = K_{pd}. \tag{6.8}$$

The phase detector phase noise is usually assumed to be proportional to the reference frequency ([106]), leading to curve (4) in Fig. 6.3 for a 10 MHz frequency carrier.

5. The last element of the closed loop is a filter (see Fig. 6.2). The structure and parameters of this element are subject of optimization. Since the ultimate practical realization of the filter is not known yet, its noise power spectral density was chosen generic, consisting of thermal noise and flicker noise regions (Fig. 6.3, Curve (5)). Exact values of their levels are not so important on this stage of optimization.

It can be noticed that the first branch with the resonator transfer function (see Fig.6.2), the second branch without any dynamic element, and the phase detector, act as a sensor, i.e. a resonator based frequency-to-voltage converter. This converter is a non-ideal differentiating element with a transfer function

$$H(s) = -\frac{\tau s}{\tau s + 1}. \tag{6.9}$$

Higher values of the quartz resonator quality factor make this element closer to ideal one. Also, it has to be said that this differentiation is compensated by the integration of the VCO transfer function. Thus, the system loop is not astatic (a dynamic system is astatic if it has an integration element in the loop, so the static (constant) error does not depend on the constant component of the disturbance) if an additional integration is not introduced into the filter transfer function.

6.2.2 Closed Loop Stability

The primary requirement to be satisfied by any control system including that in the field of frequency control is that it should be stable. The stability condition of the frequency

stabilization loop can be found using the Routh-Hurwitz stability criterion. For example assuming, the second order transfer function of the loop filter

$$H_f(s) = K_f \frac{b_2 s^2 + b_1 s + 1}{a_2 s^2 + a_1 s + 1}$$

the system stability is achieved if the following conditions are satisfied:

$$\begin{array}{l} a_2 > 0, \;\; \tau a_1 + a_2 + K b_2 > 0, \;\; \tau + a_1 + K b_1 > 0, \;\; K + 1 > 0 \\ (\tau a_1 + a_2 + K b_2)(\tau + a_1 + K b_1) > a_2 (K + 1) \end{array} \tag{6.10}$$

where $K = K_{pd} K_s K_{vco} K_f \tau$. Two important conclusions for the further system optimization can be made: an increase of the resonator quality factor (or equivalently a decrease of τ) and coefficient K generally makes conditions 6.10 less strict. Similar conditions could be found for a third order filter.

An important remark about the system stability has to be made at this point. The frequency-to-voltage conversation is made at the cost of introducing a derivative into the loop (see equation 6.9). The corresponding open-loop zero is canceled with the pole in $H_{vco}(s)$. This means that for some inputs and some outputs the system is critically stable (from inputs n_r, n_{pd} and n_f to both outputs).

6.2.3 Closed Loop Optimization and Experimental Measurements

As it is said in the introduction, the goal of the frequency control loop is the source frequency stabilization, which is commonly characterized by the notion of phase noise. This aim can be achieved by optimizing the loop filter in terms of minimization of the system Allan deviation $\sigma_y(\tau)$, for a selected integration time $\tau = \tau_0$, taking into account all noise sources in the closed loop:

$$\begin{array}{ll} \underset{\mathbf{x}}{\text{minimize}} & \sigma_y(\tau, \mathbf{x})|_{\tau=\tau_0} \\ \text{subject to} & (6.10). \end{array}$$

where $\mathbf{x} = [K_f, \; a_1, \; a_2 \ldots b_1, \; b_2 \ldots]^T$ is a vector of the loop filter parameters (see equation (6.2.2)). It is found that if τ_0 is sufficiently long, then the system performance is optimized for all the τ corresponding to the $\tau^{\frac{1}{2}}$ region, i.e. the long term stability is achieved.

To solve the optimization problem the value of $\sigma_y(\tau)_0$ has to be evaluated at each algorithm step for certain values of vector parameters $\mathbf{x}$. To do so, relationships (6.3) or (6.4), the given noise data (Fig. 6.3), the given loop parameters (τ, K_{vco}, etc.) and the loop filter parameters $\mathbf{x}$ of the present optimization step are used to calculate the system phase fluctuations spectrum $S_\phi(f)$. After that the spectrum is sampled in each decade, multiplied by the corresponding window function, and the result is numerically integrated

with the method of trapezoids between sufficiently small and sufficiently large frequencies. This estimated integral value is used to calculate $\sigma_y(\tau_0)$ according to its relationship with the PSD of phase fluctuations $S_\phi(f)$. The minimization problem is solved with one of the derivative-free methods ([107]), for example, the Nelder-Mead method.

According to the relationship of $\sigma_y(\tau)$ versus the PSD of phase fluctuations $S_\phi(f)$, the Allan deviation is simply calculated numerically from the method of trapezoids:

$$\sigma_y(\tau) \approx \sqrt{\frac{1}{(\pi\tau\nu_0)^2}\sum_{i=1}^{N}(S_\phi(f(i))\sin^4(\pi f(i)\tau) - S_\phi(f(i-1))\sin^4(\pi f(i-1)\tau))\Delta f}, \quad (6.11)$$

where $S_\phi(f(i))$ are the samples of the PSD of phase fluctuations, with $f(1) = 10^{-4}$, $f(N) = 10^5$ and $\lg(\Delta f) = a + \lg(f)b$.

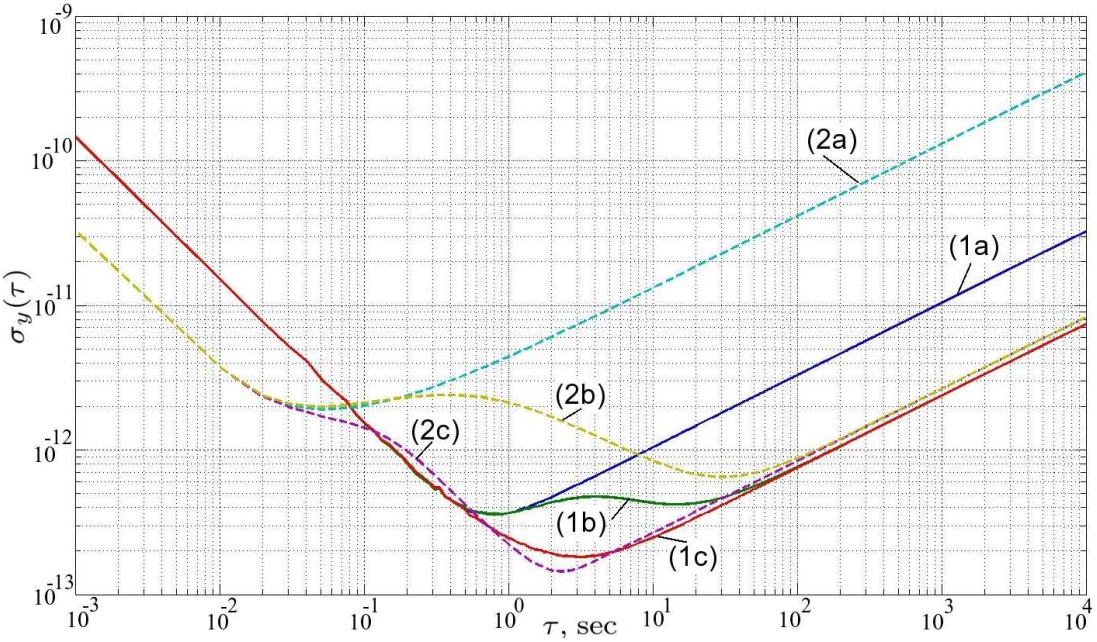

Figure 6.4: Phase noise modeling results ($\sigma_y(\tau)$): (1a) - 10 MHz VCO without a closed loop, (1b) - closed loop for 10 MHz VCO with random parameters of the filter whose transfer function is $H_f(s)$ (see Fig.6.2), (1c) - closed loop for 10 MHz VCO with optimized parameters of the filter. Dashed curves (2a), (2b), (2c): same simulations but with a high quality 100 MHz VCO, which exhibits better short-term performance

The results of the phase noise modeling and optimization in terms of Allan deviation are shown in Fig. 6.4. The expected feedback effect is clear: for medium and long terms integration times the improvement is obvious, while the frequency stability for short-term remains limited by the USO electronics. Depending on the aim, the 10 MHz USO could be replaced with a 100 MHz USO divided by 10 to provide the 10 MHz signal. Indeed, such a 100 MHz oscillator exhibits a better short term stability than a 10 MHz unit (in the frequency domain, its noise floor can be lower than -175 dBc/Hz at more than 100 kHz

from the carrier [108, 109], even if it is less good for the long term (i.e. close to the carrier the flicker noise is rather high) which is here compensated with the technique of the passive resonator feedback loop. Simulation results are also shown in Fig. 6.4 for this last case.

In order to confirm the optimization results, experimental tests have been performed with a 10 MHz USO, and a SC-cut quartz crystal working on the 3rd overtone of its C-mode (one of the thickness shear mode) as a passive component (i.e. the discriminator-resonator). The experimental bench is shown in Fig. 6.5. Low noise amplifiers are added between the mixer and both the π-network of the resonator and the phase shifter, first in order to preserve the Q-factor, and also to get mixer input signals of at least 7 dBm. The set of components {Phase-shifter (here an LC circuit), crystal π-network, amplifiers, mixer} is put inside an insulated box and roughly temperature-controlled at the turn-over temperature of the crystal resonator. As shown in Fig. 6.6, the experimental results are in very good agreement with the simulations (Fig. 6.4).

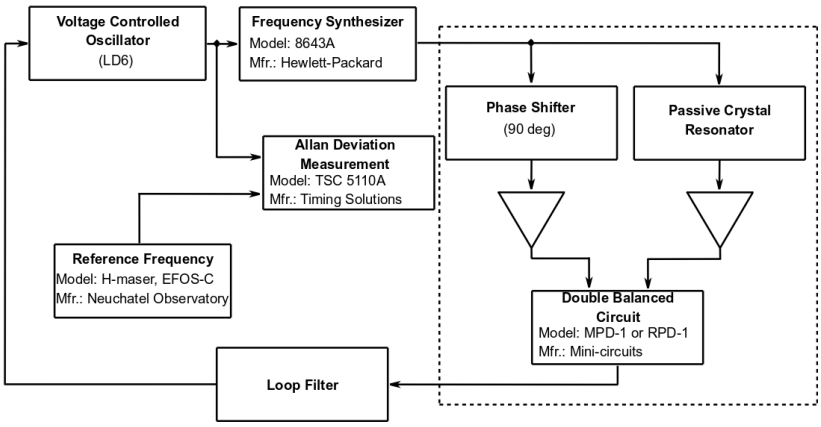

Figure 6.5: Experimental test bench of the passive resonator feedback loop

Theoretical and experimental results show that the best long term frequency stability results are obtained for high values of the gain coefficient K. As it is widely known such high-gain feedback makes the system robust to structural and parametric uncertainties of the component models. These uncertainties are mainly due to the existence of additional small time constants in the actual VCO, synthesizer and resonator, neglected during modeling. Though they have some influence on middle-term frequency stability, the long-terms stability tends to be robust to these model uncertainties. Contrary to that the closed frequency stabilization system performance appears to be sensitive to uncertainty in parameter τ of the resonator (or equivalently its quality factor). This dependence is explained in the next section.

6.3 Phase Noise Limits in Feedback System

The main goal of the feedback closed loop is to reduce the long-term instability of the system (Fig. 6.1 and Fig. 6.2). As a matter of fact, the near-carrier phase noise of the quartz crystal VCO has a PSD obeying the law $b_{-4}f^{-4}$ (random walk frequency) which corresponds to an Allan deviation part proportional to $\tau^{+\frac{1}{2}}$. This f^{-4} PSD behavior originates in the f^{-2} thermal behavior of its resonator (so transformed inside the oscillator loop according to the well-known Leeson's effect [110]). What is true for the VCO resonator also holds for the resonator used as the discriminator. At first sight, the long-term stability limitation of the closed-loop system (Fig. 6.1) could be attributed to the f^{-4} near-carrier PSD of the VCO and not to the f^{-2} PSD part of the discriminator-resonator. This is analyzed in the following section.

Let the loop filter has a first order transfer function:

$$H_f(s) = \frac{K_f}{\tau_f s + 1}. \tag{6.12}$$

In this case, $out1$ in Fig. 6.1 is sensitive to the VCO noise n_{vco}, according to the following loop transfer function:

$$H_1(s) = \frac{\Theta_{out1}}{n_{vco}} = \frac{(\tau s + 1)(\tau_f s + 1)}{\tau\tau_f s^2 + (\tau + \tau_f)s + 1 + K}, \tag{6.13}$$

where $K = K_{pd}K_sK_{vco}K_f\tau$. This equation shows that the static gain of the loop is in inverse proportion to $K + 1$, thus low-frequency noise can be reduced by changing the

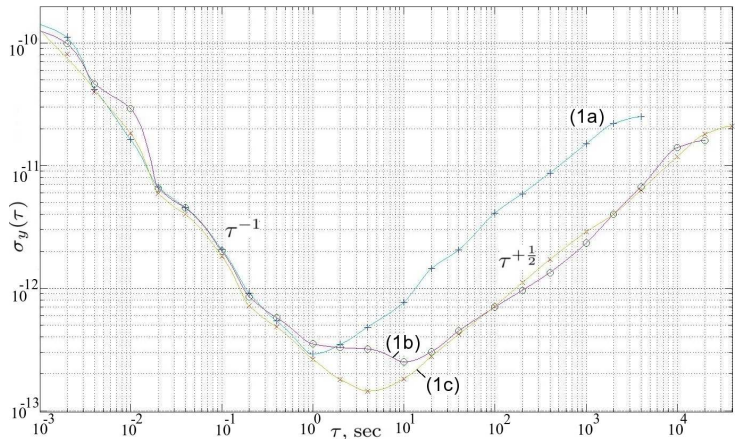

Figure 6.6: Phase noise measurement results ($\sigma_y(\tau)$): (1a) - 10 MHz USO without a closed loop, (1b) - closed loop with random parameters of the filter. The SC-cut resonator exhibits a motional resistance of $R_x = 90$Ohms and a Q-factor of $1.25 \cdot 10^6$. Once the resonator inserted inside the loop, the loaded-Q, Q_l, goes down to $1.17 \cdot 10^6$, (1c) - closed loop with optimized parameters of the filter

value of K_f. If an additional integrator is introduced into the transfer function of the filter, the loop has the following (astatic) transfer function:

$$H_{1A}(s) = \frac{\Theta_{out1}}{n_{vco}} = \frac{(\tau s + 1)(\tau_f s + 1)s}{\tau\tau_f s^3 + (\tau + \tau_f)s^2 + s + K}. \tag{6.14}$$

For both variants, the resulting PSD of a VCO f^{-4}-PSD behavior are respectively:

$$\begin{aligned} S_{out1}(f) &= |H_1(f)|^2 S_{nvco}(f) = \left|\tfrac{(\tau 2\pi fj+1)(\tau_f 2\pi fj+1)}{\tau\tau_f(2\pi fj)^2+(\tau+\tau_f j)(2\pi fj)+1+K}\right|^2 b_{-4} f^{-4}, \\ S_{out1A}(f) &= |H_{1A}(f)|^2 S_{nvco}(f) = \left|\tfrac{2\pi(\tau 2\pi fj+1)(\tau_f 2\pi fj+1)}{\tau\tau_f(2\pi fj)^3+(\tau+\tau_f j)(2\pi fj)^2+2\pi fj+K}\right|^2 b_{-4} f^{-2}, \end{aligned} \tag{6.15}$$

where j is the imaginary unit. The comparison of both formulas shows that, in principle, the astatic system is able to suppress the f^{-4} PSD component of the VCO (i.e. a $\tau^{+\frac{1}{2}}$-component of the Allan deviation of the system output), whereas without the astaticism there is just a reduction by $|1/(1+K)|^2$.

In the same way, when considering the influence of a discriminator-resonator noise n_r on the system output $out1$, both transfer functions for a static and astatic system become, respectively:

$$\begin{aligned} H_2(s) &= \tfrac{\Theta_{out1}}{n_r} = \tfrac{K_{pd}K_f K_{vco}(\tau s+1)}{s(\tau\tau_f s^2+(\tau+\tau_f)s+1+K)}, \\ H_{2A}(s) &= \tfrac{\Theta_{out1}}{n_r} = \tfrac{K_{pd}K_f K_{vco}(\tau s+1)}{s(\tau\tau_f s^3+(\tau+\tau_f)s^2+s+K)}. \end{aligned} \tag{6.16}$$

This time, the $a_{-2}f^{-2}$ PSD component of the discriminator-resonator results in:

$$\begin{aligned} S_{out1}(f) &= |H_2(f)|^2 S_{nr}(f) = \left|\tfrac{K_{pd}K_f K_{vco}(\tau 2\pi fj+1)}{2\pi(\tau\tau_f(2\pi fj)^2+(\tau+\tau_f)(2\pi fj)+1+K)}\right|^2 a_{-2} f^{-4}, \\ S_{out1A}(f) &= |H_{2A}(f)|^2 S_{nr}(f) = \left|\tfrac{K_{pd}K_f K_{vco}(\tau 2\pi fj+1)}{2\pi(\tau\tau_f(2\pi fj)^3+(\tau+\tau_f)(2\pi fj)^2+(2\pi fj)+K)}\right|^2 a_{-2} f^{-4}. \end{aligned} \tag{6.17}$$

This means that close to the carrier the f^{-4} noises of the corresponding static and astatic systems are respectively proportional to:

$$G_{f^{-2}} = \left|\frac{K_{pd}K_f K_{vco}}{2\pi(1 + K_{pd}K_s K_{vco}K_f\tau)}\right|^2, \qquad G_{f^{-2}A} = \left|\frac{K_{pd}K_f K_{vco}}{2\pi(K_{pd}K_s K_{vco}K_f\tau)}\right|^2. \tag{6.18}$$

from which it is clear that the increase of K_f or K_{vco} (K_s is fixed for a given quartz crystal) doesn't lead to the decrease of the output phase noise.

This result shows that the f^{-2} noise component introduced by the discriminator-resonator always produces f^{-4} components at the system output for both variants of the filter. And once again, this f^{-4} component reproduces a $\tau^{+\frac{1}{2}}$-slope of the Allan deviation at the output, even if the f^{-4}- noise component of the VCO phase noise is totally suppressed. Incorrect results may be obtained if this type of f^{-2} passive resonator noise is neglected as it is done in many cases. The second conclusion based on this result is that the output phase noise highly depends on the value of the crystal quality factor

(through its relaxation time τ): its close-to-carrier PSD is in inverse proportion of Q_l^2, and does not depend on the filter gain when it is sufficiently large.

The analysis made in this chapter describes noise processes in a closed loop system locked on a passive quartz crystal resonator. It is shown both analytically and experimentally that the system loop has a natural limit of optimization for a given value of the quality factor of the passive quartz resonator. This limit exists due to the f^{-2} noise component (which is even not always shown on measurement results of the quartz resonator noise and not considered during simulations) introduced into the loop by the residual temperature fluctuations on the passive resonator.

In fact, the only effective way to improve the system operation close to the carrier is the usage of a resonator exhibiting a higher value of the quality factor. And here the obvious solution is to use cryogenic quartz resonators. Let us take for example a 10MHz resonator which Q-factor reaches values of $1.25 \cdot 10^8$ at 3.3K for a frequency of 31 MHz. Fig. 6.7 shows the predicted Allan deviation of such a system with a cryogenic quartz crystal resonator whose loaded Q-factor is preserved at 79% of its unloaded Q-value and the same noise level. The long-term frequency stability would go down to some parts of 10^{-15} for averaging time between 10 and 100 seconds, which is a promising result for quartz crystal standards.

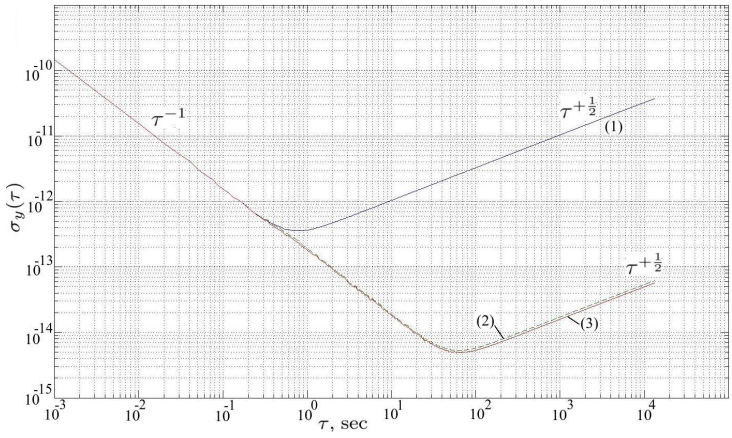

Figure 6.7: Allan deviation of the system with a cryogenic quartz crystal resonator: (1) - VCO without a closed loop, (2) - static closed loop, (3) - astatic closed loop system

6.4 Room-Temperature Practical Realization

The present section concerns the room temperature implementation of the closed loop frequency reference system. The goal is to introduce the requirements to this type of systems and to outline possible solutions to fulfill them. The obtained experience is useful for further design of the similar system at cryogenic temperatures. In fact, the

section is devoted to the electronic part that has to be designed in the laboratory. This part has to enclose a passive crystal resonator (a π-network), a phase shifter, a double balanced circuits, an optimized filter and amplifiers. This circuit has to meet the following requirements:

1. high loaded quality factor (Q_l), up to $70 - 75\%$ of the unloaded Q;
2. the lowest possible noise level of the whole circuit and high spectral purity of output signals;
3. low power dissipation of the crystal resonator.

The quality factor of the resonator depends on its total load resistance. In the case of the π-network with $\underline{Z}_1$ and $\underline{Z}_2$ equivalent shoulder impedances, the loaded Q-factor depends on the unloaded one according to relation 6.19.

$$Q_l = Q \cdot \frac{R_x}{R_x + Re(\underline{Z}_1) + Re(\underline{Z}_2)}, \tag{6.19}$$

where Q is an unloaded quality factor of the resonator, R_x is a motional resistance of the resonator. In accordance with the last equation, the load resistance has to be minimized. However, the values of resistances $Re(\underline{Z}_1)$ and $Re(\underline{Z}_2)$ can not be minimized to zero. In this case the power of the output signal also goes to zero. In fact the sum of $Re(\underline{Z}_1)$ and $Re(\underline{Z}_2)$ has to be relatively small comparing with the motional resistance of the resonator R_x. In the same time the π-network must be combined with a low input impedance amplifier.

The second requirement can be achieved by combination of several techniques in the course of design. One of them is the utilization of low noise components: transistors, ready-to-use commercial amplifiers, etc. In the same time, reduction of a number of active devices and utilization of linear amplification circuits guarantee fulfillment of this requirement.

According to the third requirement, the design must guarantee a necessary and sufficient drive level for the linear mode operation of the quartz crystal resonator. The minimum value of this parameter is derived from the quantity of the power needed for normal setting into operation of the quartz crystal. Its maximum value is determined by the upper linear operation border. High drive levels can lead to mechanical failures and a rapid aging.

For the practical realization of the system at room temperature, an SC-cut BVA-type quartz crystal resonator (Res. 5304) with following room-temperature parameters is chosen: 1) resonance frequency $f_r = 9999763$ Hz (the 5th overtone of the C Mode); 2) motional resistance $R_x = 90$ Ohm; 3) motional inductance $L_x = 1.79$ H; 4) motional capacitance $C_x = 141$ fF; 5) shunt (holder) capacitance $C_0 = 4.9463$ pF. These parameters

were directly measured with Agilent 4395A Network Analyzer equipped with Agilent 16092A Tool Kit. Further, the unloaded quality factor can be calculated from these data: $Q \approx 1.25 \cdot 10^6$.

To preserve the high quality factor of the resonator, a π-network can be used in combination with a low output impedance signal source and a low input impedance amplifier. In the first case, a signal source of the signal synthesizer (Hewlett-Packard 8643A) is used. This device has 50 Ohm inner output impedance and can provide up to +19 dBm magnitude of the output signal. To provide a low input impedance of the amplifier, a common-base BJT circuit is a suitable solution.

For the low noise implementation, an MPD-1+ device from Mini-Circuits is used as a phase detector. This double balanced mixer has $R_{DBM} = 50$ Ohm input resistance and requires +7 dBm magnitude of input signals (or 0.71 V in amplitude). This value represents a requirement for magnitudes of amplifier output signals in both signal paths. Utilization of the phase detector applies another restriction on the amplifier design concerning the spectral purity of applied signals.

A block diagram of two signal paths between the synthesizer and the double balanced mixer is shown in Fig. 6.8. As it is seen, two "arms" are equal except for the phase shifter and the resonator circuit. Since the quartz crystal resonator driven by its series resonant frequency behaves like a passive load R_x (inductive and capacitive active resistances compensate each other), the π-network gives zero phase shift at the resonant frequency. This means that needed phase shift of the phase shifter equals to $\pi/2$. An additional common-base amplifier are used to minimize the resonator load.

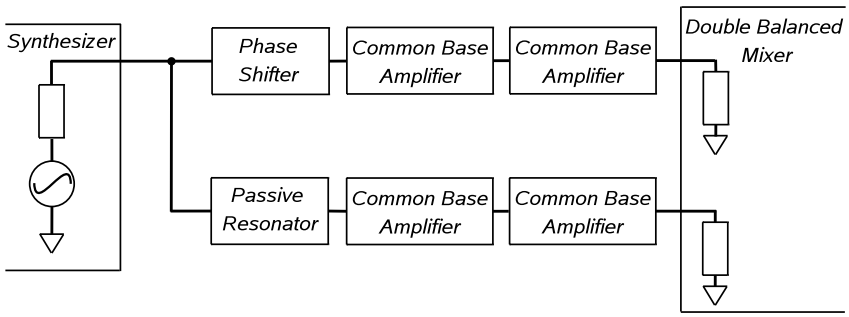

Figure 6.8: Block diagram of two discriminator signal paths

All the parts of the system shown in Fig. 6.8 are designed for the room-temperature operation. They are based on 2N2857 BJTs. The careful design of two consecutive amplifier stages provides a system with 7 Ohm input resistance, 30 dB amplification and low distortion for weak input signals.

Another considered element of the system shown in Fig. 6.8 is the π-network. The load resistance of the resonator crystal can be evaluated based on the following equation

$$R_{load} \approx Re(\underline{Z}_{in} + R_G||R_{synth}||R_G||(R_x + \underline{Z}_{in})) = 4.56 \text{ Ohms}, \quad \underline{Z}_{in} = (r_{in} + \frac{1}{j\omega C_1})||R_D \tag{6.20}$$

where r_{in} is the input resistance of the common-base amplifier without the right resistor of the π-network, R_G and R_D are values of the left and the right load resistors of the π-network respectively, (4 Ohms), R_{synth} is the output resistance of the synthesizer (50 Ohms). Eq. 6.20 gives an exact value in case of two utterly equal branches. In other cases it gives approximate value. But since the phase-shift (upper in Fig. 6.8) branch is adjusted to be equal to the second one, this estimation is rather accurate.

According to equation (6.19), the result of such a low value of the crystal load provides utilization of 95.2% of the unloaded quality factor for the system working at room temperatures.

The power dissipated in the quartz crystal resonator in case of the resonance can be evaluated with the following equation

$$P_x \approx \frac{V_x^2 R_x}{2(R_x + r_{in})^2} = 3.55\mu\text{W}$$

where V_x is a minimal needed amplitude of the signal at the input of the π-network (25.7 mV) to obtain +7 dBm at the inputs of the phase detector. The obtained value of dissipated power falls into the desired range.

Instead of the π-network, the upper branch (Fig. 6.8) has the phase shifter. As it was shown earlier, the phase shift of one signal at the input of the double balanced mixer has to be $\pi/2$ delayed relative to another. A simple circuit of the 90° passive phase shifter is shown in Fig. 6.9. The condition of $\pi/2$ phase shift is $|\underline{Z}_C| = |\underline{Z}_L|$, where $\underline{Z}_C = 1/(j\omega C)$ and $\underline{Z}_L = j\omega L$ for the operating frequency. The advantage of this circuit is that the value of the phase shift does not depend on the value of a load resistance.

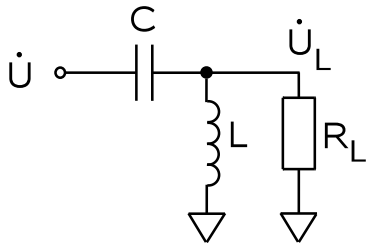

Figure 6.9: Simple passive phase shifter

Exact values of the inductance and capacitance of the circuit (Fig. 6.9) were adjusted in the course of simulation of the whole system. The best solution for the output signals

is obtained with $L = 1.2$ μH, $C = 200$ pF. This result is achieved by altering the value of the R_D resistor in the common-base amplifier (the upper branch only) with the 3.5 Ohms resistor R_{D2}.

Efficiency of the subsystem is verified with simulations. Fig. 6.10 shows simulated output signals in the time domain for the case of the resonance frequency. The signals of curves (3) and (4) are observed on the output resistances, which are inner resistances of the double balanced mixer. Curves (1) and (2) show the input signals of both common-base amplifiers (output signals of the phase shifter and the quartz crystal).

Also, it is needed to evaluate a shift of the resonance frequency originated from the circuit capacitances. The total series capacitance can be found using an imaginary part of the complex load resistance of the quartz resonator that gives $C_t \approx 29.6$ nF. So, the normalized frequency shift can be evaluated based on the following approximation:

$$\frac{\Delta f}{f_x} \approx \sqrt{1 + \frac{C_x}{2(C_0 + C_t)}} - 1 = 1.2094 \cdot 10^{-9}$$

Thus, the final phase shift of the resonance frequency is about 0.012 Hz. This value can be neglected.

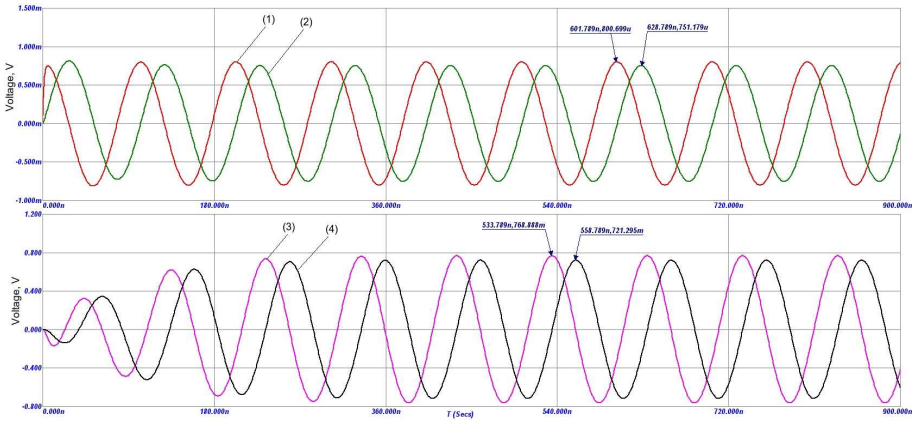

Figure 6.10: Simulation results: (1) - input signal of the upper branch amplifying stage, (2) - input signal of the bottom branch amplifying stage, (3) - output signal of the upper branch, (4) - output signal of the bottom branch

The AC analysis of the system is shown in Fig. 6.11. Both "arms" have approximately equal gain at crystal resonance frequency. The phase difference for this frequency is about $-88.4°$. To reduce calculation capacity, these plots are built for the system with the quartz crystal which has the unloaded quality factor $Q = 10^3$.

The developed system meets all requirements stated at the beginning of this section. For this design at room temperatures the loaded quality factor reaches more than 95% of the unloaded value or $1.168 \cdot 10^6$. In the same time the signals at the outputs are sufficient for the double balanced mixer. Also, low distortion is achieved using linear amplifiers.

The efficiency of the design is proved experimentally. The designed circuit works as required in the whole closed loop phase noise correction system (Fig. 6.5). For the first measurement attempt, the quartz resonator had a single oven. The home-made electronics (with the quartz crystal inside) is thermally isolated in order to minimize effects of the ambient temperature. The experimental results of measured loop frequency stability are shown in Fig. 6.6.

Some additional measurements are made to clarify some interesting points about the system (see Fig. 6.12). This figure shows the Allan deviation of the original VCO (Curve (1)), the closed loop with one stage temperature control of the passive resonator (Curve (2)), the VCO in the closed loop with two stage temperature control of the passive resonator and temperature controlled electronics (Curve (3)), frequency stability at the second output (see Fig. 6.2) of the loop with double temperature control (Curve (4)). As this can be easily seen from the presented figure, curve (3) is lower than curve (2) for high integration times τ. This experimental fact proves the conclusion of the previous section that quartz crystal temperature fluctuations (f^{-2}) limit the total system stability. Second output of the closed loop system has a much higher level of short term instabilities than the first one. This is mainly due to high phase noise of the frequency synthesizer.

6.5 Cryogenic Temperature Realization and Measurements

The previous chapter clearly shows the numerous difficulties associated with the circuit design for liquid helium temperatures. So, in order simplify the design of the reference system based on a cryogenic crystal resonator, it is decided to minimize the number of elements at the liquid helium temperatures. Such a solution increases system reliability

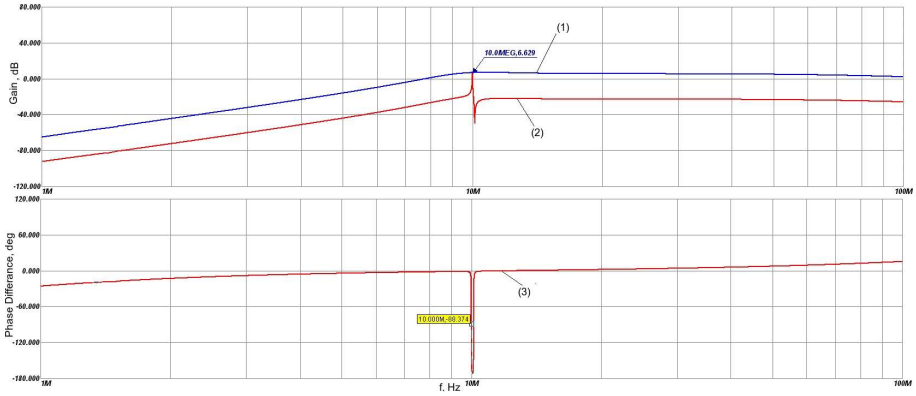

Figure 6.11: AC analysis. (1) - gain of the upper branch, (2) - gain of the bottom branch, (3) - phase difference of the output signals

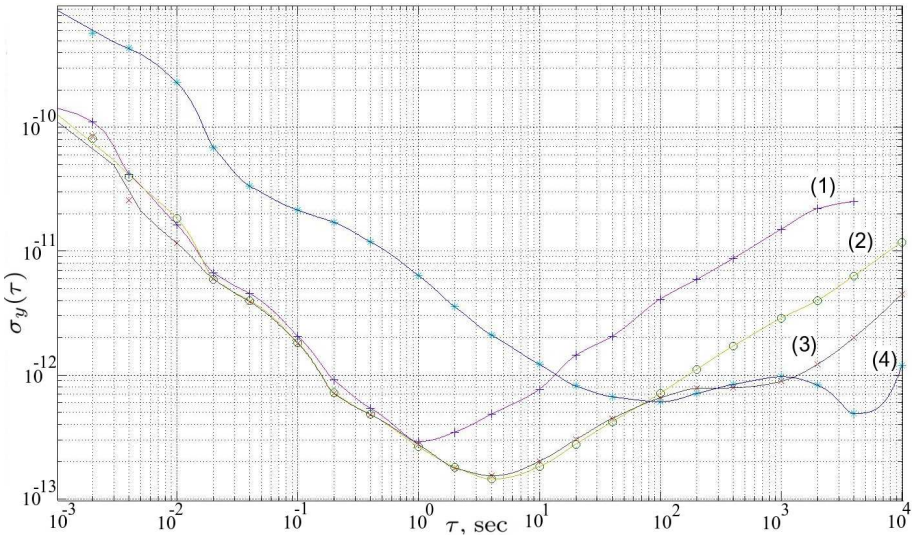

Figure 6.12: Additional measurements of the room-temperature closed phase-noise reduction system

and decreases development time. Besides that, this approach allows to minimize the number of connecting cables and wires and to reduce the dissipating power. This means that lower temperature could be accessible, that is better for resonator quality factor and frequency-temperature sensitivity.

The block diagram of the closed loop frequency reference system is shown in Fig. 6.13. Like in the case of the room temperature system, the carrier signal is produced by the VCO. The long-term frequency stability of this source is a quantity to be improved. Next, the frequency of the reference signal is multiplied by a signal synthesizer in order to much it to the resonance frequency of the crystal device. This signal is injected with one cable into a cryogenic resonator π-network and a phase shifter. The resulting signals pass identical cables and are amplified by room temperature low-noise amplifiers. These signals are down-converted to a DC voltage with a double balanced mixer. After that, the filtered DC signal is used to correct the VCO oscillating frequency by applying some command voltage to a regulation input.

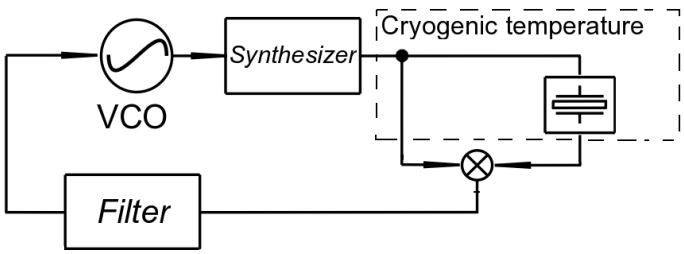

Figure 6.13: Block diagram of the closed loop frequency reference system based on a cryogenic quartz crystal resonator

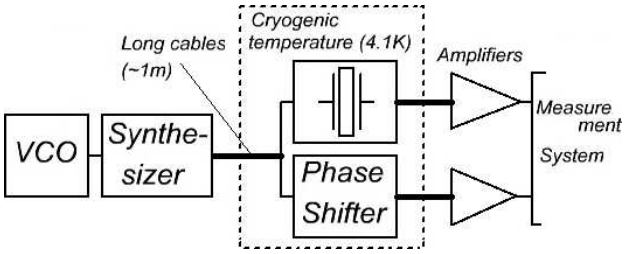

Figure 6.14: Open loop measurement scheme for cryogenic system instabilities

6.5.1 Open-Loop Measurements for Component Characterization

Usually, at room temperatures the phase noise of ultra stable quartz crystal resonators is measured with an interferometric measurement system [26]. The usual schemes use two almost identical resonators in two system branches. These resonators are chosen to have the closest characteristics (e.g. a resonance frequency, an equivalent motional resistance, a quality factor) possible in order to obtain almost identical transfer functions in the phase domain. Both resonators are driven with the same signal. The difference in resonance frequencies is covered with series capacitors. The main advantage of the scheme is an ability to cancel out the source phase noise, i.e. to measure the resonator noise even if it is below than that of the signal source. The disadvantage of the approach is inability to figure out a power spectral density of one resonator: a result is always an average spectral density of two devices.

Unfortunately, such a scheme is not possible for resonators working at cryogenic conditions. The reason is a significant dispersion of resonator parameters at low temperatures. Thus, for example, two 5 MHz resonators (obtained from a same batch) can exhibit a resonance frequency difference of 1.1 kHz in resonance frequencies, for the 5th overtone of the A-mode, at 4.2 K. For 10 MHz resonators, this difference is about 500 Hz. This phenomenon is due to small differences in crystal blank orientations [111]. This difference cannot be covered with trimming capacitors like in the case of room temperature measurements. So, to evaluate the resonator phase noise under cryocooler conditions, only an one-resonator scheme is available (see Fig. 6.14).

Another important remark concerns the orientation of a device in relation to cryogenerator axis. Indeed, the crystal resonator can be differently installed inside a copper block of the cryogenerator. The possible orientation of the crystal axes x_1, x_2, x_3 according to cryocooler axes X, Y,Z (see Fig. 3.3) shown in Fig. 6.15. Here, $\overrightarrow{g}$ and $\overrightarrow{a}$ are gravitational acceleration and cryocooler vibration vectors respectively. Indeed, the resonator plate can coincide with the X-Y plane or with the X-Z plane as shown in Fig. 6.15. All the measurements shown in the present subsection are made with orientation (1). The measurements are extended for another case in the further subsections.

The measurements are made step by step in order to figure out the origins of different instability phenomena. All the phase noise or frequency stability measurements are made

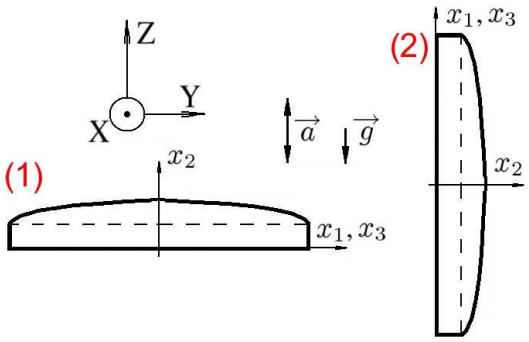

Figure 6.15: Possible orientations of the resonator disk with respect to cryocooler axes X, Y, Z

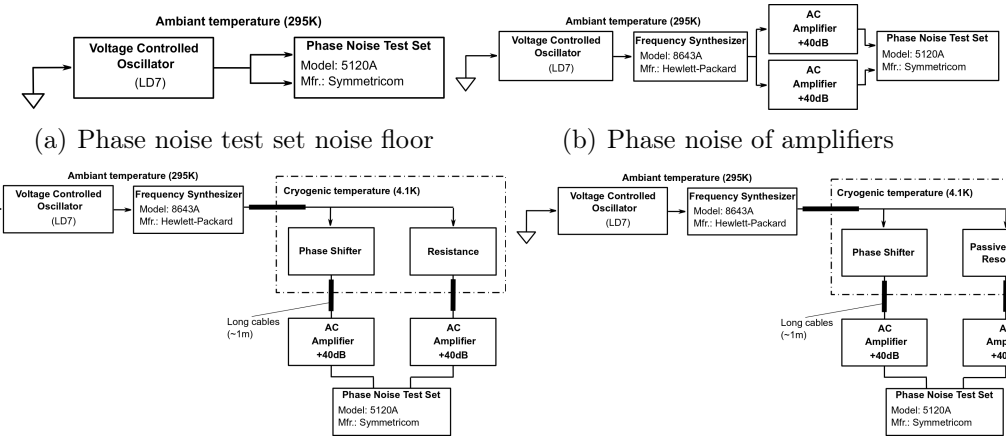

(a) Phase noise test set noise floor

(b) Phase noise of amplifiers

(c) Phase noise of the cryogenic part of the loop without a resonator

(d) Phase noise of the cryogenic part of the loop with a resonator

Figure 6.16: Phase noise measurement schemes for different elements of the frequency stabilization loop

with a TSC5120A phase noise test set from Symmetricom [100] with a VCO as a frequency source. Fig. 6.16 presents measurements schemes for different elements of the investigated system.

The first measurement is made to evaluate the noise floor of the phase noise test set itself. To do so, the source signal is split and used a the measured signal and as the reference (see Fig. 6.16(a)). Since frequency instabilities of both signals are fully identical, they are canceled out by the cross correlation technique. An obtained PSD gives an evaluation of the measurement noise floor. The results are shown in Fig. 6.18, curve (1).

On the second step, the phase noise of AC amplifiers (HVA-200M-40-B from FEMTO) is evaluated. Though these devices are specified to be low-noise, the manufacturer does not provide any figures concerning their phase noise. The measurement scheme is shown in Fig. 6.16(b). The figure shows that a signal from one source is split into two and

passed through two identical amplifiers. Next, frequency stability of one resulting signal is measured against another one. The correlated parts of the measured signal and the reference phase instabilities come from the voltage controlled oscillator (VCO) and the synthesizer and are canceled as before. Contrary to that, the uncorrelated parts are results of amplifier own noises (it is supposed that these noises are uncorrelated). In this way, the average phase noise of two identical amplifiers is measured. The results are shown in Fig. 6.18, curve (2). This is the phase noise of two amplifiers, so 3 dBm has to be subtracted in order to obtain a PSD for one device.

On the third step, the cryogenic part, except for the resonator, is added to the measurement scheme. The main goal here is to evaluate instabilities of the experimental equipment connected with cryogenic part and to compare them with the results on the following step (the same experiment, but with the resonator in the π-network). At the present step, the resonator is replaced with a resistance corresponding to its equivalent resistance at the cryogenic temperature. Fig. 6.16(c) shows the measurement scheme of the present step. A signal from one source comes to the cryogenic part through one cable. Next, it is split into to go through two branches with the π-network and the phase shifter. After that, the signals come out with two identical cables and pass through the AC amplifiers. After amplification, their frequency stability is measured one against another. In the same way as in the preceding steps, correlated fluctuations (coming from the signal source, cables, cryocooler, etc.) of the signals are compensated. The results are presented in Fig. 6.18, curve (3).

On the fourth step, measurement scheme repeats the same pattern as on the third step, but with the crystal resonator inside the π-network. An electrical circuit of the cryogenic part is shown in Fig. 6.17. It can be subdivided into two parts: a π-network (marked as "Passive Resonator") and a phase shifter. Note that both branches shift the signal phase by $+\pi/4$ and $-\pi/4$ in order to obtain the total $\pi/2$ phase difference at the input of the double balance mixer. This difference is achieved only when the crystal resonator is at its resonant mode or is replaced with an active resistance. So, a signal frequency at the output of the synthesizer has to be adjusted exactly to the resonant frequency of the crystal device at working temperature. In fact, the capacitance C1, resistances R1 and R2 and Xtal (or an equivalent resistance) form a filter, which has to be designed to obtain $\pi/4$ phase shift and sufficient amplitude at OUT1. Since the amplifier gain is limited to +40 dB, the cryogenic part has to be designed to provide minimum +7 dBm signals at the output of the amplifiers by providing the sufficient signal level at their input. The loaded quality factor of the resonator in this circuit is estimated as follows:

$$Q_L \approx Q\frac{R_x}{R_x + R1 + R2}, \tag{6.21}$$

where Q_L and Q are loaded and unloaded quality factors respectively and R_x is the resonator equivalent resistance. Resistance R3 and capacitors C2, C3, C4 are calculated to produce the inverse phase shift and the same amplitude at OUT2.

In Fig. 6.18, curve (4) shows the results of these measurements for the 5th overtone of the A-mode [61]. This mode has the highest value of the quality factor ($Q = 325 \cdot 10^6$ at

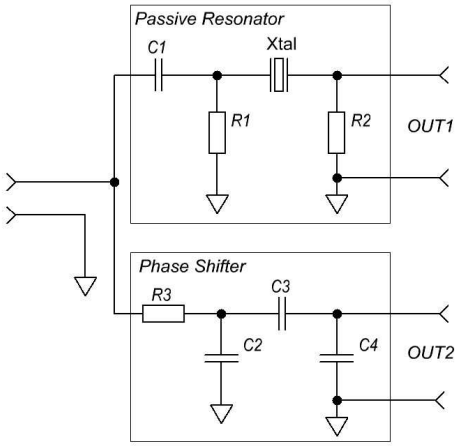

Figure 6.17: Electronic circuit of the cryogenic part of the experiment

15.6 MHz) in comparison with that of the third and fifth overtones. The highest possible Q is preferable for the closed loop frequency stabilization system (see section 6.3). So, it is the best candidate for further closed loop frequency measurements. In addition, the 5th overtone of the B mode ($Q = 50.5 \cdot 10^6$ at 9.2 MHz) and the 3rd overtone of the A mode ($Q = 114.6 \cdot 10^6$ at 9.4 MHz) are considered further.

The design of the cryogenic part of the measurement system implies several requirements. First, the resonator loaded quality factor has to be preserved. To do so, according to equation (6.21), the load has to be of the same order of magnitude as the resonator motional resistance. Unfortunately, the equivalent motional resistance of the resonator at these modes and overtones is very low (approximately 3.5 Ohms for the 5th overtone of the A-mode). Second, the influence of the connecting cables has to be minimized, in order to decrease the influence of the connecting cables (they are not thermally regulated). The specific capacity of the cables is about 95 pF/m. So, for used 1 m resistance R2 and capacitor C4 are short circuited with the impedance of 107 Ohm. This point also (as well as the first one) requires that the loading resistances (in particular, resistance R2) of the π-network has to be minimized. Third, the resonator nonlinear effects have to be avoided in order to prevent the excess noise [14]. Indeed, as it is shown in Chapter 4, a quartz crystal resonator at the cryogenic temperature is subject of strong amplitude-frequency effect [61]. This is mainly due to high values of the Q factor, since the frequency shift is proportional to the product of Q and the input signal power [73]. So, in order to limit such an effect, the resonator active power has to be kept low. This could be done by injecting lower power signals or by increasing the resonator load. The last approach contradicts the first and second requirements. And, forth, it is absolutely necessary that the π-network is able to provide at least +7 dBm at the output of the amplifiers, whose gain is limited. Indeed, in order to fulfill the magnitude requirement of the double balanced mixer with constant gain of two AC amplifiers, an output signal power of the cryogenic part has to be relatively high. This could be achieved by increasing the level of the excitation signal or by increasing the resonator load. As it is seen, all the four requirements are contradictory

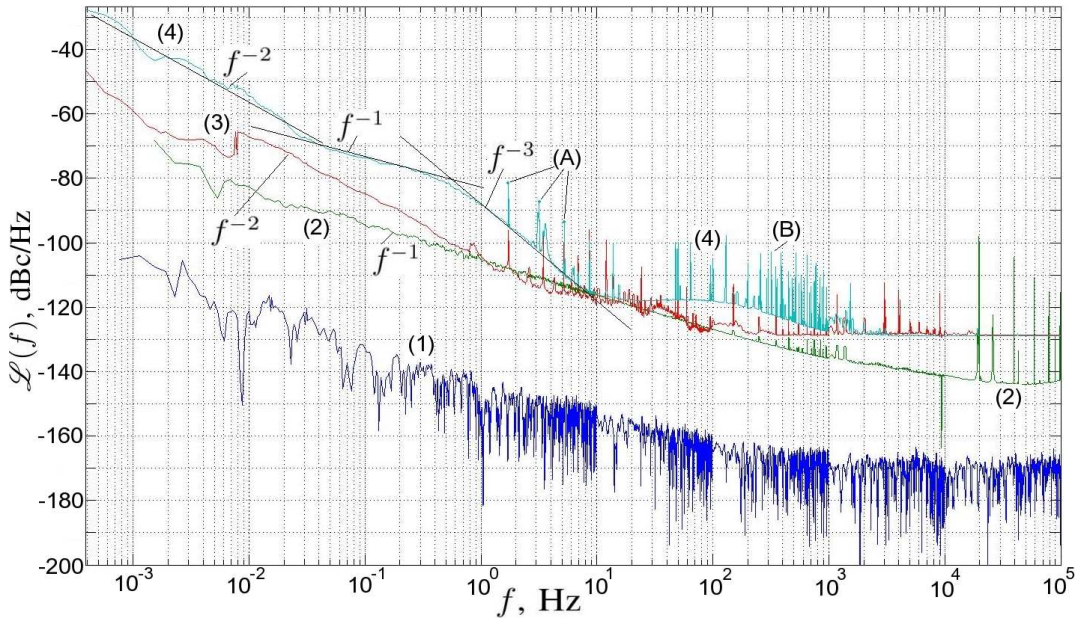

Figure 6.18: Phase noise spectral densities of different measurement experiments: (1) - measurement noise floor (Fig. 6.16(a)), (2) - amplifier phase noise (Fig. 6.16(b)), (3) - cryogenic (without a resonator) part phase noise (Fig. 6.16(c)), (4) - cryogenic (with a resonator) part phase noise (Fig. 6.16(d)). (A) - deterministic instabilities due to the cryogenerator (1.7Hz and its harmonics), (B) - synthesizer phase noise.

and difficult to accomplish together. Partially the situation is improves by the following approach. The gain of the utilized AC amplifiers is artificially increased by means of a higher load. For that, the output of each amplifier is connected to a home-made emitter follower. This device does not inject a considerable amount of the phase noise, but helps to increase the amplifier gain up to two times. But, even in this case, a kind of trade-off has to be achieved. This has been done by providing just about 12% of the unloaded quality factor in the best case (without accounting nonlinear effects).

Fig. 6.18 shows the phase noise spectral densities of the different measurement schemes shown in Fig. 6.16. The measurement noise floor clearly consists of white f^{-1} noises (curve (1)). Both noise types are much lower than the phase noise level of two amplifiers (curve (2)). This PSD also consists of the same noise slopes. Though amplifiers are specified to be low-noise devices, their phase noise is relatively high due to the fact that they are wide-band components. If one compares amplifier phase noise with that of the cryogenic part amplified with the same devices (curve (3)), another noise type appears. This is the random-walk phase noise, which appears for low Fourier frequencies. Its origin could be attributed to temperature fluctuations (it is known that temperature fluctuations are random walks whose spectral density is proportional to f^{-2} [105]) of the long cables utilized for connection of cryogenic and ambient temperature parts. As it is mentioned above, these cables are not temperature regulated and connect ambient temperature devices (at about 295K) and the cryogenic circuit (at 4.1K) with an intermediate connection at the first stage of the cryogenerator (at about 50K). This type of noise becomes important

mostly in the case when long thermal transients of the system are not over. Subsection 6.5.4 explains this fact.

When comparing measurements of the cryogenic part with and without the resonator (curves (4) and (5) respectively in Fig. 6.18), the two following comments could be made. First, inside the resonator bandwidth (Fourier frequencies lower than 0.5 Hz), the VCO and synthesizer phase noises are compensated because both branches are similar, due to the fact that the resonator works as a flywheel. So, in this first part of the spectrum one obtains the sum of phase noises of the amplifiers, cables and resonator. Since spectrum (4) in this region is considerably higher than spectrum (3) which does not contain the resonator phase noise, the difference can be attributed to the latter. f^{-2} and f^{-1} slopes are present in this part of the PSD. Second, outside the resonator bandwidth both oscillator and synthesizer noises are no more compensated, because in one of the branches the phase noise is filtered. So, here, the resulting phase noise includes noises from the amplifiers, cables, the oscillator, the synthesizer and the resonator. In the region between 0.5 Hz and 10 Hz the latter is dominant. An f^{-3} slope is clearly visible here. Between 10 Hz and 200 Hz (zone (B) in Fig. 6.18) the synthesizer phase noise is the highest one (these values correspond to the synthesizer documentation). After that, for Fourier frequencies higher than 200 Hz, the cryogenic part noise overlaps the others. Thus, between the lowest possible Fourier frequency and 10 Hz one obtains the resonator phase noise. It has to be noted that the presented measurements become possible, because this phase noise is relatively high.

The measured quartz crystal resonator working at cryogenic conditions has a PSD consisting of f^{-2}, f^{-1} and f^{-3} slopes. These results are similar to measurements made at the room temperatures [3]. In fact, the resonator can be considered as a low-pass filter in the phase domain. So, the resonator filtrates its own phase noise forming the f^{-1} slope inside its bandwidth and the f^{-3} slope outside, i.e. the output phase noise is the resonator flicker noise multiplied by a square of the resonator transfer function in the phase domain. The bandwidth of this filter corresponds to the corner frequency of the resonator phase noise PSD and is inversely proportional to the loaded quality factor. According to the measurement results, the bandwidth of the resonator in the phase domain working at 15597319 Hz is about 0.5 Hz that gives a loaded quality factor of about $15.6 \cdot 10^6$. In addition to stochastic instabilities of the resonator, deterministic fluctuations can be observed. These periodic fluctuations at a frequency of 1.7 Hz and its integer multiples (see peaks (A) in Fig. 6.18) are due to the cryogenerator working cycle that produces temperature changes and vibrations.

The proposed approach helped to find out the high level of the own resonator phase noise working at cryogenic conditions. In the same time, the origins of such a high phase noise are not clear from these measurements. Three possible reasons could be identified: (a) cryogenerator induced vibration, (b) temperature instability and (c) intrinsic resonator noise. These reasons are under scope in Section 6.5.4.

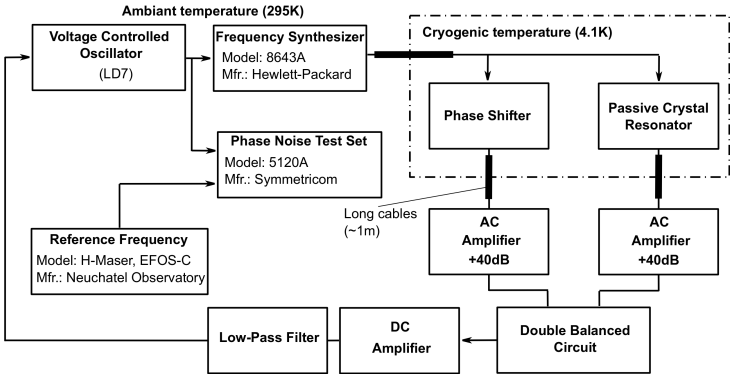

Figure 6.19: Block diagram of the closed loop frequency stabilization system based on a cryogenic quartz crystal resonator

6.5.2 Measurements of the Closed-Loop System Based on a Cryogenic SC-cut Resonator

This subsection presents some results of the frequency stability measurements of the closed-loop frequency stabilization system based on the cryogenic quartz resonator. The data is presented in the form of the Allan deviation. A hydrogen maser (EFOS-C from Neuchatel Observatory) is used as a frequency reference for these measurements. The resonator is installed in horizontal orientation, i.e. the crystal disk is normal to the Z-axes (see orientation (1) in Fig. 6.15).

Indeed, some more important informations on the long-term cryogenic resonator instabilities can also be deduced when the VCO (see Fig. 6.14) is locked on the cryogenic resonator frequency [61]. To do so, the output signals of both amplifiers are applied to a double balanced mixer for a down conversion to DC voltage. After a low frequency filtering, the DC signal is applied back to the VCO to lock the loop. So, the system Allan deviation for large averaging times is proportional to the resonator noise and inversely proportional to its quality factor. By analyzing this part, the resonator long term behavior can be estimated. This is difficult to make using the open loop approach.

First measurements are made for three different modes of resonator operation: the 5th overtone of the A-mode (see Fig. 6.20, curve(2)), the 3rd overtone of the A-mode (see Fig. 6.20, curve(3)) and the 5th overtone of the B-mode (see Fig. 6.20, curve(4)). The results are compared with the stand-alone voltage controlled oscillator (Fig. 6.20, curve(1)) used as a signal source in the loop. All three measurements show degradation of the frequency stability for small averaging times ($\tau < 0.1$ s) and improvement for large averaging times ($\tau > 10$ s). Also, in the latter region modes 3A and 5B demonstrate the same slope as the stand-alone oscillator, i.e. $\tau^{+1/2}$. This slope of the Allan deviation curve corresponds to the f^{-2} phase noise (phase random-walk). As opposed, the 5th overtone of the A-mode shows τ^{+1} law, which is a deterministic linear frequency drift. The frequency stability deterioration for small values of τ is due to the additional noise of the closed

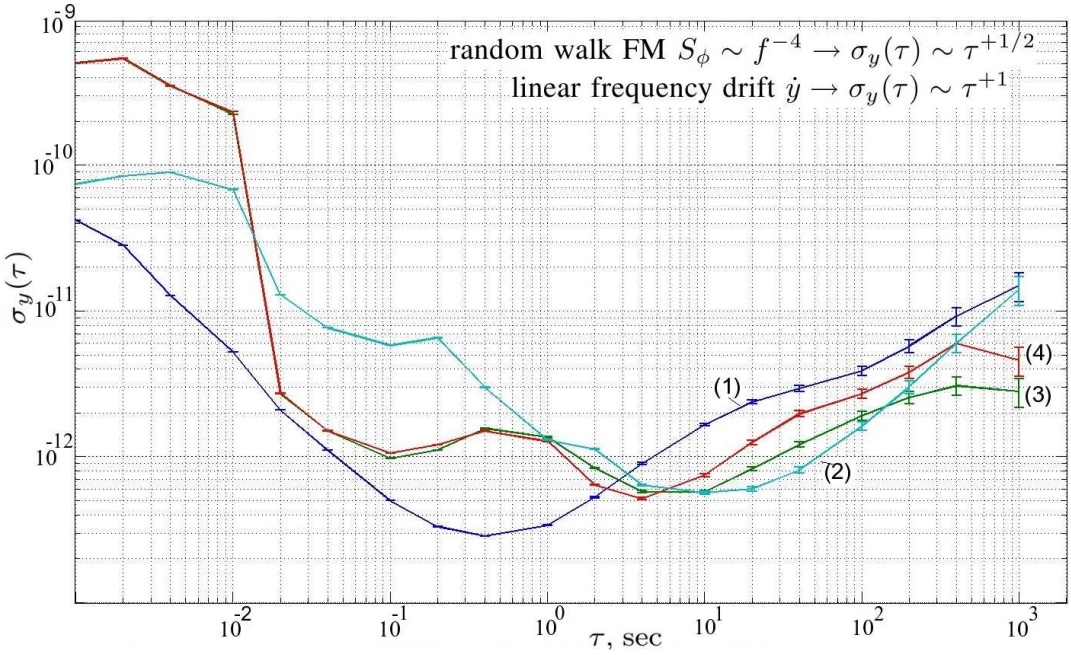

Figure 6.20: Allan deviation of the closed-loop frequency stabilization system locked at (2) - the 5th overtone of the A-mode, (3) - the 3rd overtone of the A-mode, (4) - the 5th overtone of the B-modeand a stand-alone oscillator (1)

loop electronic components as well as the short-term cryogenic resonator phase noise. The main difference between two cases is that the resonator working at the 5th overtone of the A-mode is in a nonlinear regime due to the amplitude-frequency effect (the Q-factor of this mode is much higher).

Stability measurements shown in Fig. 6.21 are for the closed-loop system locked on the 5th overtone of the A-mode. In these measurements, the frequency stability has been examined as a function of the amount of time of permanent operation of the resonator inside the cryocooler. So, Fig. 6.21 presents the Allan deviation measured during the first 12 hours (curve (2)) and after at least 60 hours of permanent operation (curve (3)). Both results can be compared with the stand-alone oscillator stability (curve (1)). As expected the closed loop degrades the system frequency stability for small averaging times τ, but improves it for large averaging times. In the same time, for large τ, curve (3) exhibits the same slope as the stand-alone oscillator, i.e. $\tau^{+1/2}$, which corresponds to the f^{-2} phase noise (phase random-walk). On the other hand, after just 12 hours of operation, the system shows a τ^{+1} law, that is a deterministic linear frequency drift. This drift is due to a rapid aging of a resonator in the first hours after the cooling process which changes its mechanical properties.

5th overtone of the A-mode. It is clearly seen that the system shows much better results for large averaging times measured after 60 hours of operation. Furthermore, the continuous linear frequency derivative is not seen, so the τ^{+1} law disappears.

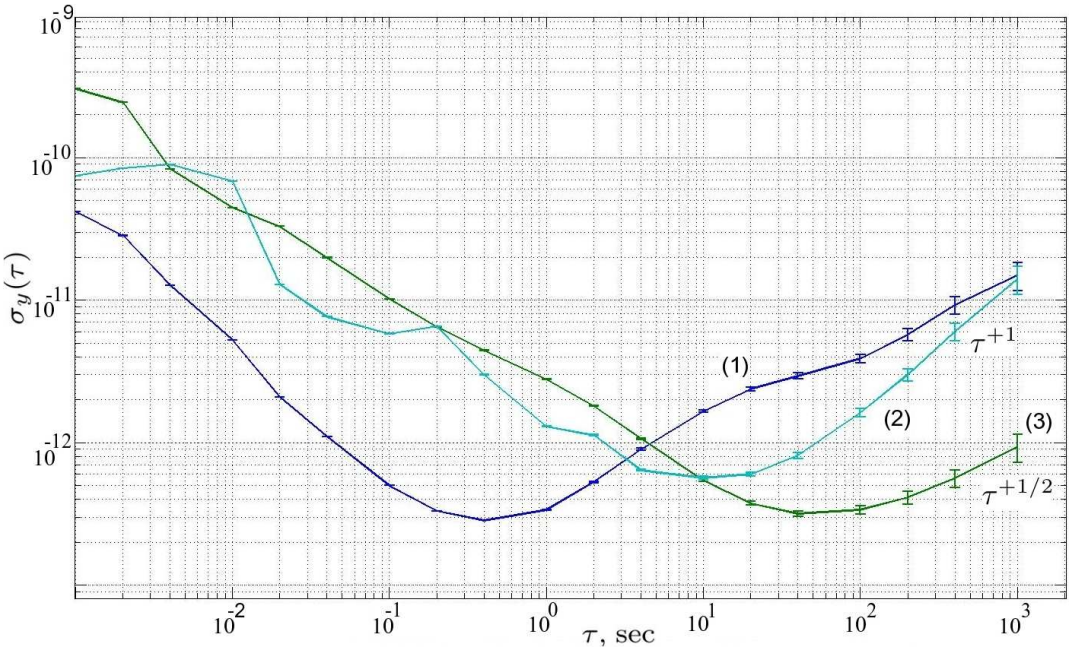

Figure 6.21: Allan deviation of the closed-loop frequency stabilization system locked on the A-mode of 5th overtone measured at (2) first 12 hours of resonator operation inside the cryocooler, (3) measured after at least 60 hours of resonator permanent operation in cryogenic environment and compared with the stand-alone oscillator (1), i.e. the VCO

6.5.3 Measurements of the Closed-Loop System Based on a Cryogenic LD-cut Resonator

The main problems of the design of the closed-loop system described in the previous subsection are high nonlinearity of the cryogenic SC-cut resonator and low sensitivity of a VCO. Indeed, as it is shown in subsection 4.2.4, SC-cut resonators exhibit the pronounced amplitude-frequency effect. One of the possible solutions is to replace an SC-cut device in the feedback with its LD-cut counterpart. Though the latter has a smaller value of the unloaded Q-factor, higher active resistance and lower sensitivity to a dissipation power (see subsection 4.2.4) allow to design a cryogenic part of the feedback system with a higher loaded quality factor. In addition, the system described in the previous subsection exhibited a problem with the VCO due to lack of its sensitivity. The problem was solved by replacing this controlled oscillator with another one with a higher sensitivity. Though this oscillator has much lower long-term stability, this could not be a problem since the system stability for long averaging times is determined by the cryogenic resonator and its own noise (see section 6.3).

Schematics of the cryogenic part of the system is the same as in the previous case (see Fig. 6.17). In the same time weaker nonlinear effects simplify the design procedure. Thus, the loaded quality factor for the implemented system achieved 34.6% of is unloaded value. This corresponds to $Q_L = 33.6 \cdot 10^6$. The resulting frequency stability in terms of

the Allan deviation is shown in Fig. 6.22. The corresponding phase noise power spectral densities are presented in Fig. 6.23.

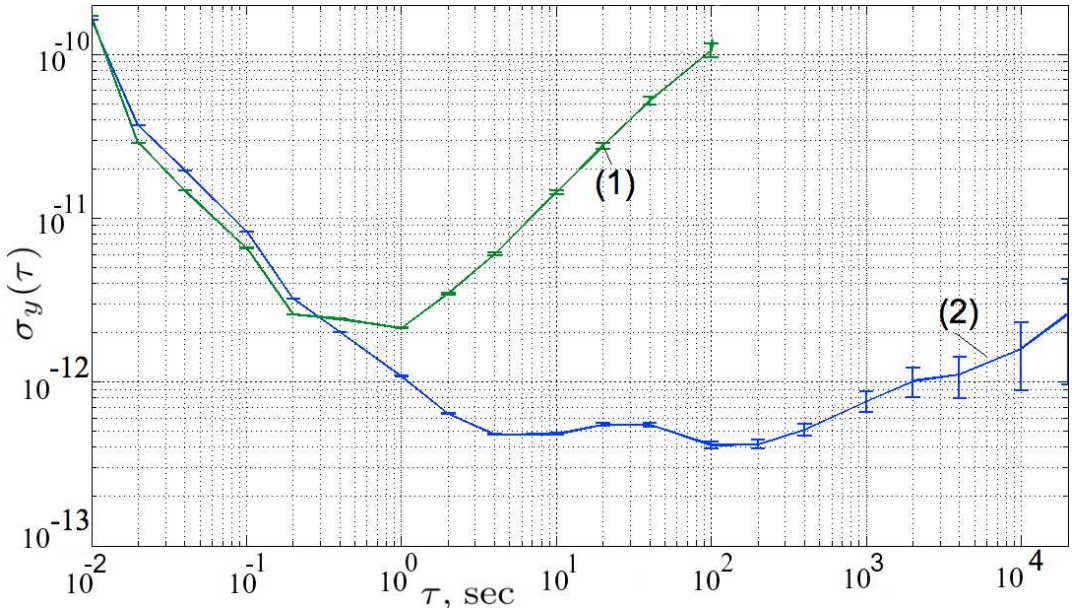

Figure 6.22: Allan deviation of the VCO (1) and the closed-loop frequency stabilization system locked on the A-mode of 5th overtone of the LD-cut resonator (2)

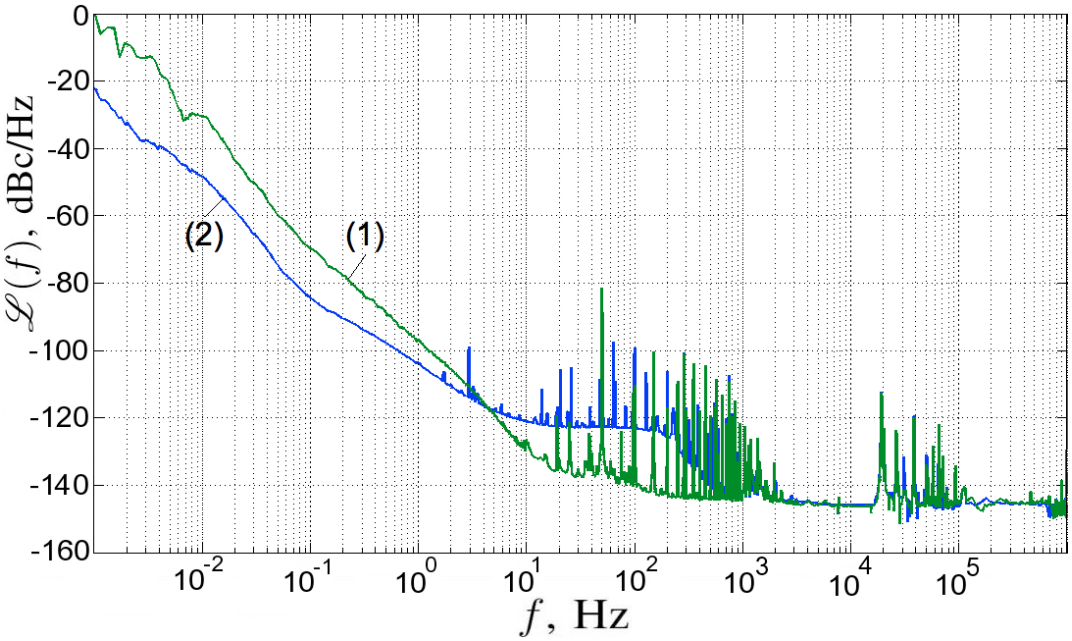

Figure 6.23: Phase noise PSD for the VCO (1) and the closed-loop frequency stabilization system locked on the A-mode of 5th overtone of the LD-cut resonator (2)

Though the LD-cut resonator exhibits the quality factor more than three times less than the SC-cut device, it can be more easily utilized for the frequency stabilization in

feedback systems. Thus, the tested feedback stabilization systems achieves frequency stability of $4 \cdot 10^{-13}$ at 100 seconds and has stability better than 10^{-12} between 1 and 2000 seconds.

6.5.4 Measurements Quartz Resonator Phase Noise at Cryogenic Temperatures

Section 6.5.1 explained the measurement techniques and gave phase noise measurement results for one possible system configuration. This approach makes possible measurements of the crystal resonator phase noise at cryogenic temperatures. In the present section these measurements are extended for different resonance modes, excitation levels, different amount of cryogenerator operation time and crystal orientations inside the cryocooler. The main difference in the measurement technique introduced in this section is that both branches of the cryogenic part are not designed for working in the system closed-loop. First, this implies that the system can work with a lower driving signal. Second, both branches are designed to be fully identical (see Fig. 6.17) except for the resonator in one and an equivalent active resistance in another. So, resistance R3 is replaced by capacitor C1, capacitor C2 and C4 are substitute for resistances R1 and R2 respectively, and capacitor C3 is replaced by a resistance equal to the active resistance of the cryogenic resonator. These improvements are made to minimize the influence of external disturbances on the cryogenic part and consequently to minimize the measurement noise floor.

First, one compares the results of the phase noise measured for different operating modes and overtones of the SC-cut resonator. Three modes are of the main interest here because of their relatively large quality factors: the 5th overtone of the A-mode (curve (2) in Fig. 6.24), the 3rd overtone of the A-mode (curve (3), Fig. 6.24), the 5th overtone of the B-mode (curve (4), Fig. 6.24). It is clear from the figure, that all the three modes have very similar close phase noise spectra. In the same time, a f^{-1} spectrum slope is almost absent for the 3rd overtone of the A-mode and the 5th overtone of the B-mode overtone. This fact may be a consequence of their high sensitivity to temperature fluctuations [61], and thus a rather high f^{-2} noise.

The next experiment compares phase noise spectra measured for the system with the resonator working at different excitation levels. Two measurements are made in this case. The first one is obtained with a level sufficient to provide +7 dBm at the inputs of the double balance mixer. Here, a +0.5 dBm level of the synthesizer output signal is used (see Fig. 6.25, curve (2)). Another experiment is made with a much lower level of the synthesizer signal, i.e. −4.5 dBm (see Fig. 6.25, curve (3)). The main difference in the obtained results is seen in the region of high Fourier frequencies. As expected, the white noise of the experiment is significantly lower for the higher excitation level, due to a better signal-noise ratio. In all other ways, the results follow the same trend: no significant change is found for the crystal flicker noise.

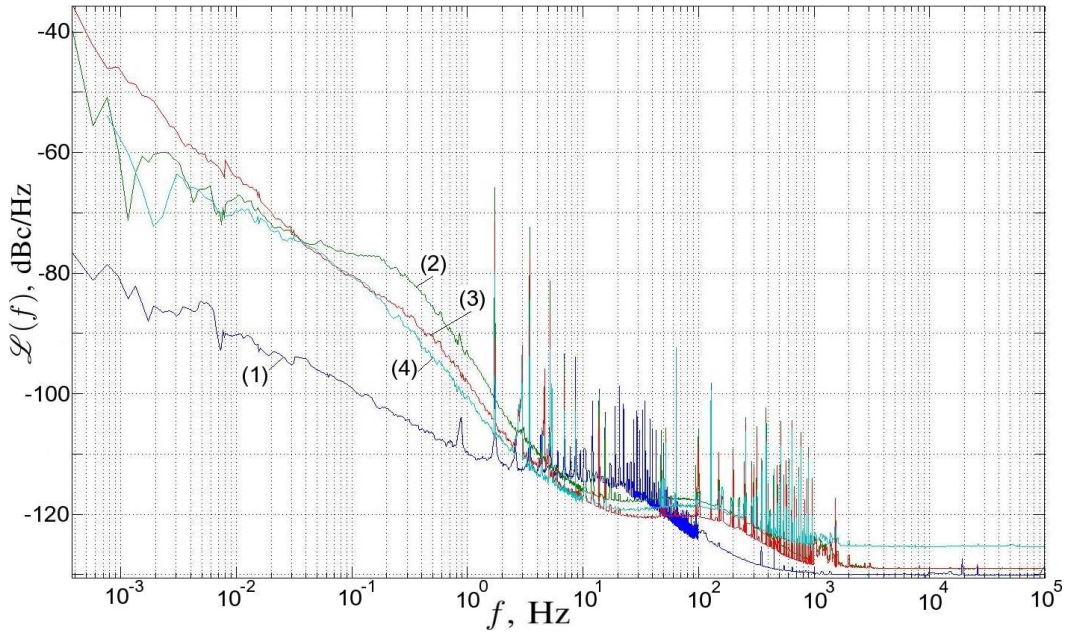

Figure 6.24: Phase noise PSDs: (1) - measurement phase noise floor, (2) - cryogenic part phase noise for the 5th overtone of the A-mode, (3) - cryogenic part phase noise for the 3rd overtone of the A-mode, (4) - cryogenic part phase noise for the 5th overtone of the B-mode

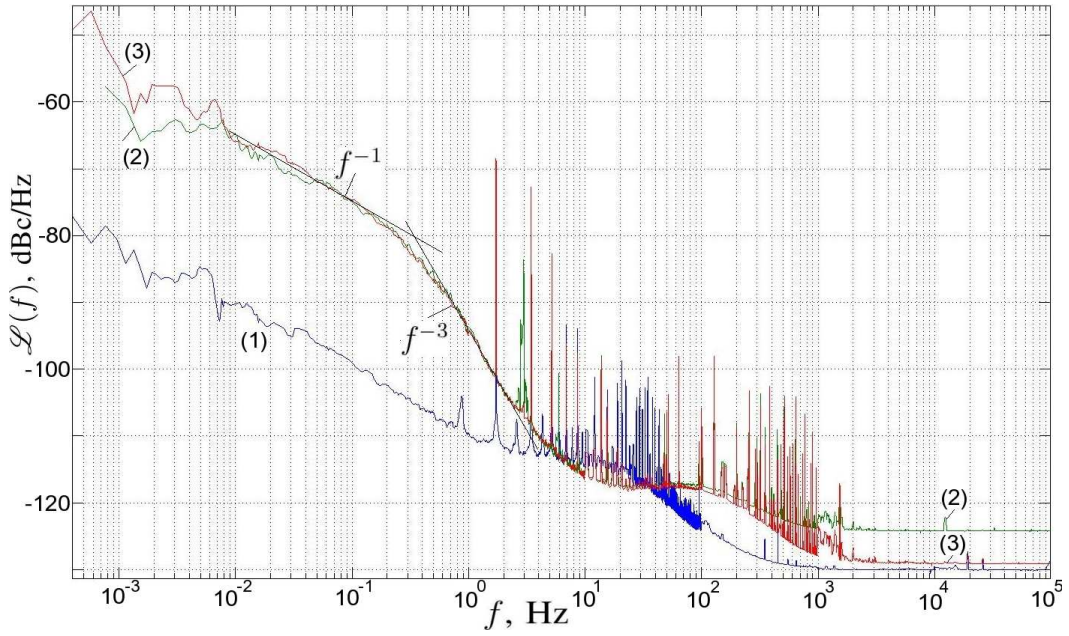

Figure 6.25: Phase noise PSDs: (1) - measurement phase noise floor, (2) - cryogenic part phase noise for the 5th overtone of the A-mode with -4.5 dBm synthesizer output signal, (3) - cryogenic part phase noise for the 5th overtone of the A-mode with $+0.5$ dBm synthesizer output signal

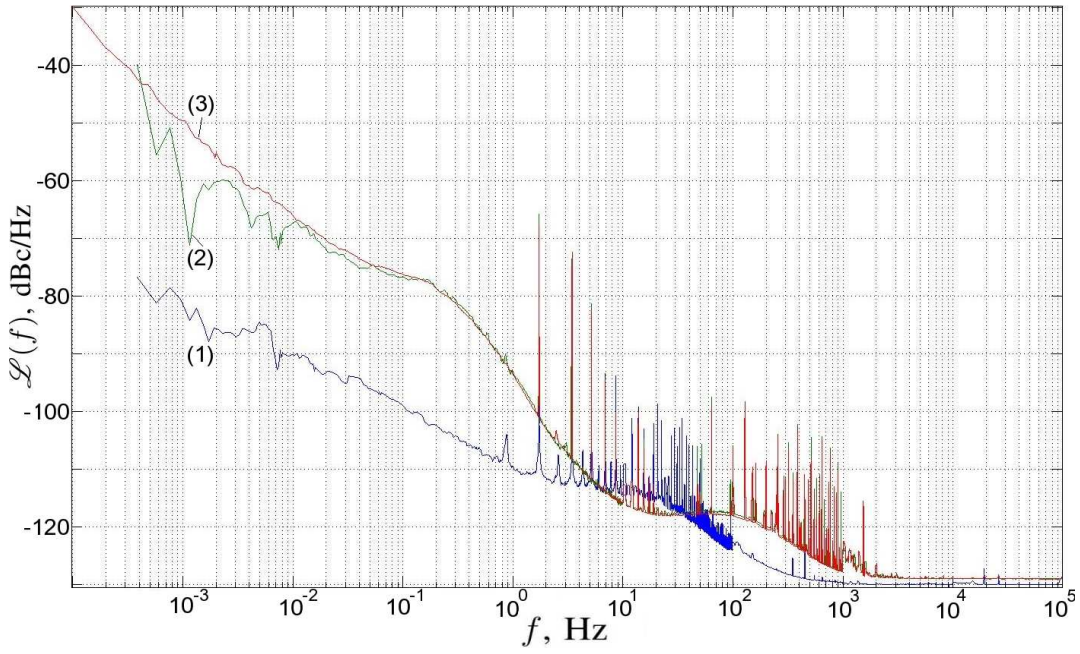

Figure 6.26: Phase noise PSDs: (1) - measurement phase noise floor, (2) - cryogenic part phase noise for the A-mode 5th overtone measured at first 12 hours of cryogenerator operation, (3) - cryogenic part phase noise for the A-mode 5th overtone after at least 24 hours of cryogenerator operation

Another experiment is made on the resonator working for different amounts of time in cryogenic conditions. As before, two cases are considered. The first measurement is made on the same day the cryocooler is turned on. This means that there is less than 12 hours between the time when the cryogenerator is turned on and the measurements themselves. Nevertheless, the steady state seems to be reached according to the measured temperature. The second measurement is made after at least 24 hours of cryogenerator permanent operation. The results are shown in Fig. 6.26 for the 5th overtone of the A-mode and in Fig. 6.27 for the 3rd overtone of the same mode.

As it is seen in Fig. 6.26, there is no clear difference between two measurements separated in time. Both spectra have close patterns and almost the same level.

For the time-separated measurements made for the 3rd overtone of the A-mode (see Fig. 6.27), a difference can be observed for low Fourier frequencies. One-day measurement has a very short region of f^{-1} slope, since f^{-2} noise is relatively high. Contrary to that, the second day measurement (Fig. 6.27, curve (3)) have a f^{-2} region much less important. Because this type of noise depends on the temperature fluctuations and the temperature sensitivity of the mode, it can be concluded that the whole thermo-mechanical system (cryogenerator, cables, DUT, etc.) has some remaining temperature transient processes with time constants greater than 12 hours. In the same time, flicker noise of all the modes and overtones does not change with the amount of time of cryogenerator operation.

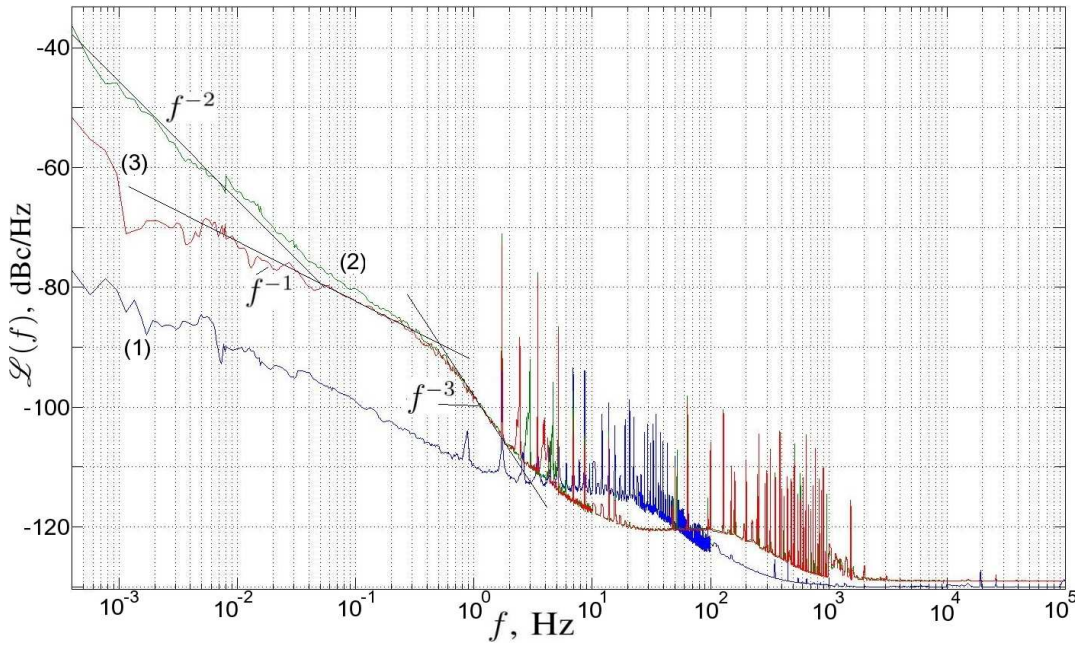

Figure 6.27: Phase noise PSDs: (1) - measurement phase noise floor, (2) - cryogenic part phase noise for the 3rd overtone the A-mode measured at first 12 hours of cryogenerator operation, (3) - cryogenic part phase noise for the 3rd overtone of the A-mode after at least 24 hours of cryogenerator operation

In order to separate the influences of temperature fluctuations from vibration-caused noise of the resonator, the phase noise is measured for two different crystal device orientations and different temperatures. Fig. 6.28 presents the resonator phase noise when the resonator plane coincides with the XY plane in Fig. 3.3 (i.e. the resonator disk is normal to the Y or X axes, according to Fig. 3.3), whereas in Fig. 6.29 the resonator is horizontal (resonator disk normal to the Z axis).

Taking into account the measured environmental disturbances (see sections 3.2 and 3.3), comparison of Fig. 6.28 and 6.29 suggests the following conclusions:

1. temperature instabilities and vibrations are the main causes of the resonator phase noise when the cryocooler is operating;

2. like at usual temperatures, the resonator phase noise is shaped with a low-pass transfer function in the phase domain [3, 2, 1] with f^0 and f^{-1} fluctuations at the input (see Fig. 6.30);

3. levels of f^0 and f^{-1} fluctuations depend on crystal orientation and temperature sensitivity at a given temperature;

4. vibrations of the crystal resonator with a f^{-1} PSD, result in its f^{-1} phase noise (in other words, resonator flicker phase noise is due to external vibrations);

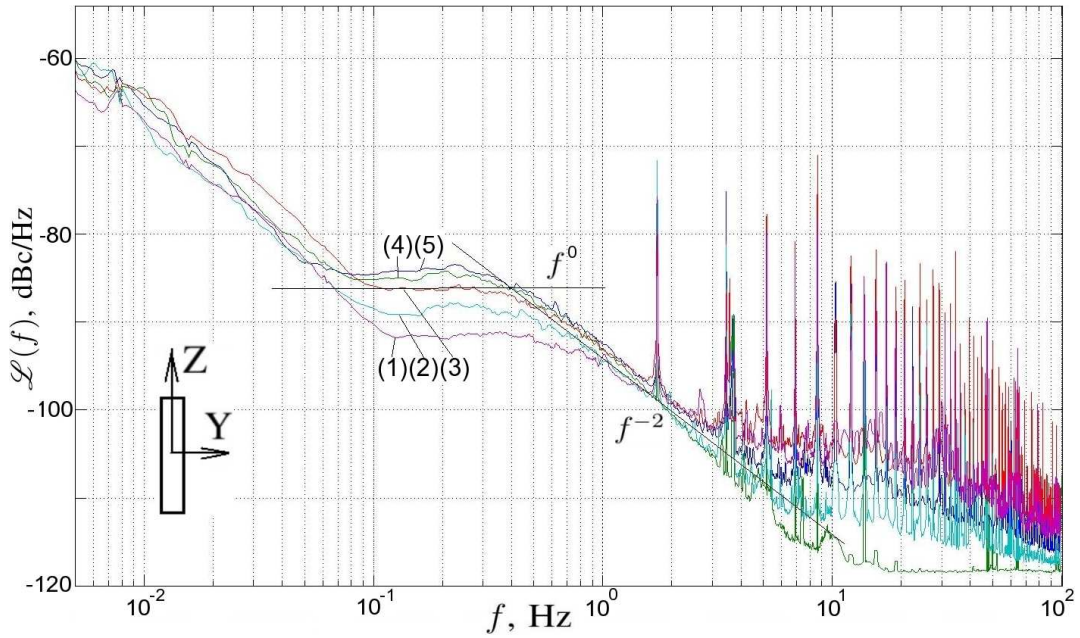

Figure 6.28: Phase noise PSDs of the resonator (the 5th overtone of the A mode) installed vertically at different operating temperatures: (1) - 5.3 K, (2) - 6 K, (3) - 7 K, (4) - 8 K, (5) - 9 K

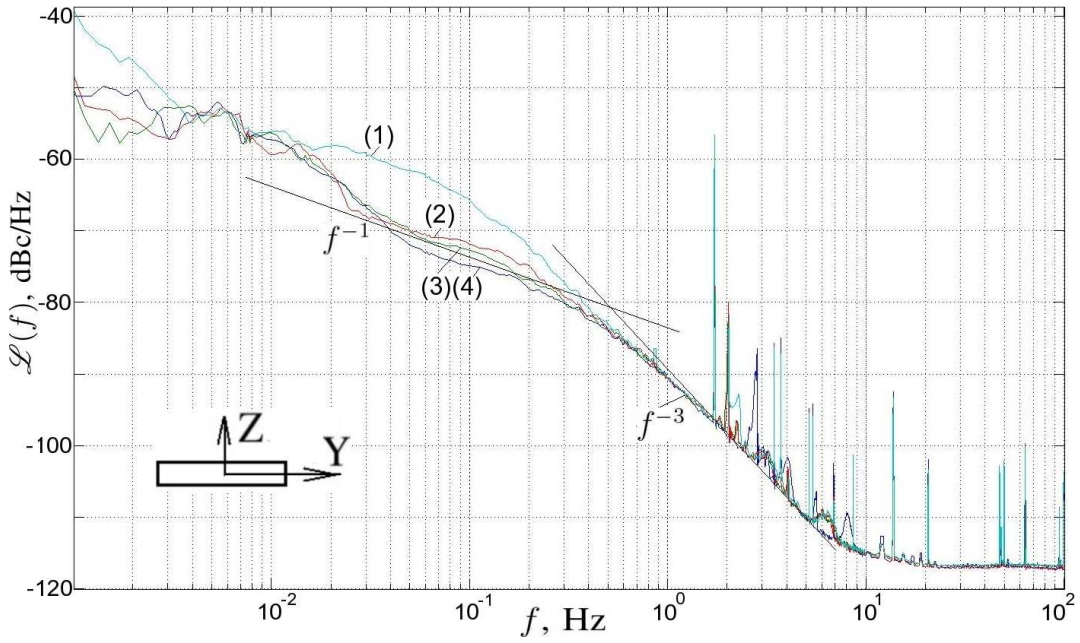

Figure 6.29: Phase noise PSDs of the resonator (the 5th overtone of the A mode) installed horizontally: (1) - 5.3 K, (2) - 6 K, (3) - 7 K, (4) - 8 K

5. the quartz crystal resonator is most sensitive to external vibration when the main vibration axis is normal to the resonator plate (this is an obvious mechanism, in fact);

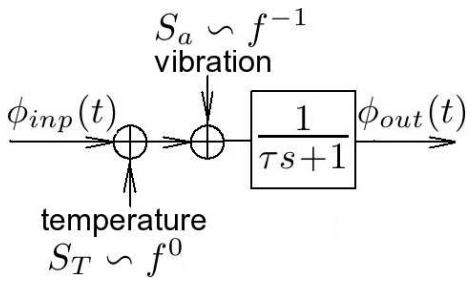

Figure 6.30: Model of the resonator phase noise at cryogenic temperatures. τ is the resonator relaxation time $\tau = \frac{2Q_l}{\omega_0}$. $\phi_{inp}(t)$, $\phi_{out}(t)$ are input and output phase fluctuations respectively

6. temperature instabilities of the crystal with a f^0 PSD result in a resonator f^0 phase noise;

7. temperature sensitivity of quartz crystal resonators decreases with temperature (this fact agrees with direct measurements of resonator characteristics [61]).

As a general conclusion to these points, it could be concluded that the influence of the vibration on resonator parameters and noise can be reduced simply by choosing the proper angle of resonator orientation relatively to the main (vertical) axis of vibration.

6.5.5 Resonator Self-Heating Effect

As it is shown in the previous chapters, nonlinearities of BAW devices is a very important issue for implementation of actual frequency sources. The measurements (see subsection 4.2.4, Fig. 4.11) show that already for dissipated power more than 0.1 μW, the cryogenic quartz resonator exhibits a shift of the resonant frequency, and, thus, some degradation of its quality factor (see section 2.2). Starting from the dissipated power of 1.2 μW (curve (5)), the device exhibits deformation of its characteristics due to the self-heating effect.

Some values of the driving signal power may lead to an effect of amplitude-temperature (or phase-temperature) oscillations. The signal with the high enough power induces the temperature rise of the quartz crystal resonator, which, further, shifts the resonance frequency according to the sign of the frequency-temperature characteristic [14]. If this shift is negative and large enough it may lead to a so-called down jump phenomenon, an abrupt change (decrease) of the amplitude and phase due to a transition in the hysteresis characteristic (see Fig. 6.31). Decreased amplitude results in much smaller dissipated power. Due to that temperature decreases causing a back frequency shift and an up jump phenomenon. These transitions give birth to steady oscillations of amplitude and phase of the signal passed through the resonator as well as its temperature.

Such oscillations were observed for the resonators under study at cryogenic temperatures during phase noise tests with high levels of the excitation signal. The measurement procedure is the same as in the previous sections. The results of the such measurements in terms of the phase noise PSD are represented in Fig. 6.32. As it can be seen from this figure, the spectrum obtains a considerable chain of spurious frequencies in the frequency range 0.1-1 Hz starting from 0.168 Hz. In the same time, the signal passed through the second branch does not have any spurious frequencies for this zone of the PSD. The observed spurs are harmonics of phase-temperature oscillations. The phase and amplitude oscillations exist only for the certain values of the driving frequency (close to the resonance frequency) and high enough driving levels. Evidently these fluctuations are not due to the operation of the cryogenerator, since the pulse tube works exactly at 1.7 Hz.

The demonstrated behavior of the thermo-mechanical system (the resonator, its environment and the driving signal) has to be avoided. For this purpose the resonator dissipated power has to be kept lower than 1 μW.

6.5.6 Comparison with Earlier Works

Three works give values of the flicker noise for resonators operating in cryostats [4, 111, 58]. These results are contradictory. It has to be noted that all three works present values of the fractional frequency fluctuations $S_y(f)$ just for one value of the Fourier frequency $f = 1$ Hz, and not over a wide Fourier frequency range like in Fig. 6.24-6.27. But, all authors attribute these single values to the resonator flicker noise without any discussion on the shape of the phase noise PSD. In fact, as it is seen from the experimental curves,

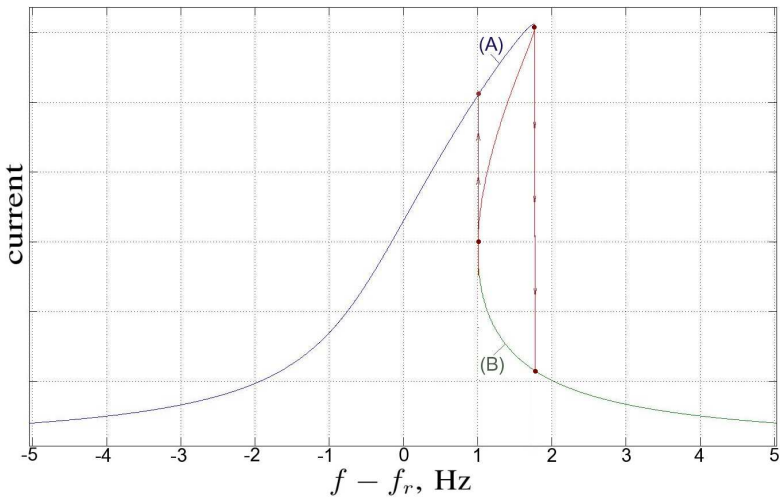

Figure 6.31: Magnitude characteristic of the resonator at high excitation level. Zone (A) corresponds to high levels of the dissipated power. Zone (B) corresponds to low levels of the dissipated power

this frequency always belongs to the f^{-3} spectrum region of the resonator noise. As it is seen this situation is typical for cryogenic conditions due to higher values of the quality factors and, thus, a much lower resonator bandwidth. So, for cryogenic conditions, the 1 Hz Fourier frequency is most likely situated outside the resonator bandwidth, and for the room temperature it is usually inside with the present day technology. This facts could lead to unjustified lower values of the resonator flicker noise. Moreover, depending on the quality of the temperature control (this is an issue for cryostats) and the actual resonator temperature sensitivity, this frequency range can be covered with f^{-2} phase noise slope, which is attributed to the random-walk temperature fluctuations. In this case, there is a risk to measure only temperature characteristics of the resonator-cryostat system, but not the resonator flicker noise.

G. Robichon *et al* [4] states more than one decade decrease in the phase noise, going from the room temperature ($S_y(1\text{Hz}) = 1.6 \cdot 10^{-24}$) to 4.2 K ($S_y(1\text{Hz}) = 1.4 \cdot 10^{-25}$) for an AT-cut crystal. The authors do not give any theoretical explanation of this phenomenon stating just correlation with the increase with the unloaded Q.

Similar results are given by J.J. Gagnepain *et al* [111]. This work attempts to relate the resonator $\frac{1}{f}$ noise and the quantum $\frac{1}{Q^4}$ law [112, 113], which is itself questionable [114, 115, 116]. The authors admit the deviation of the measurement results from the theoretical law and make a guess that this fact is attributed to the presence of different losses phenomena and the dependence of the resonator parameters on temperature.

These work of M. Planat *et al* [58] presents the dependence of the resonator fractional

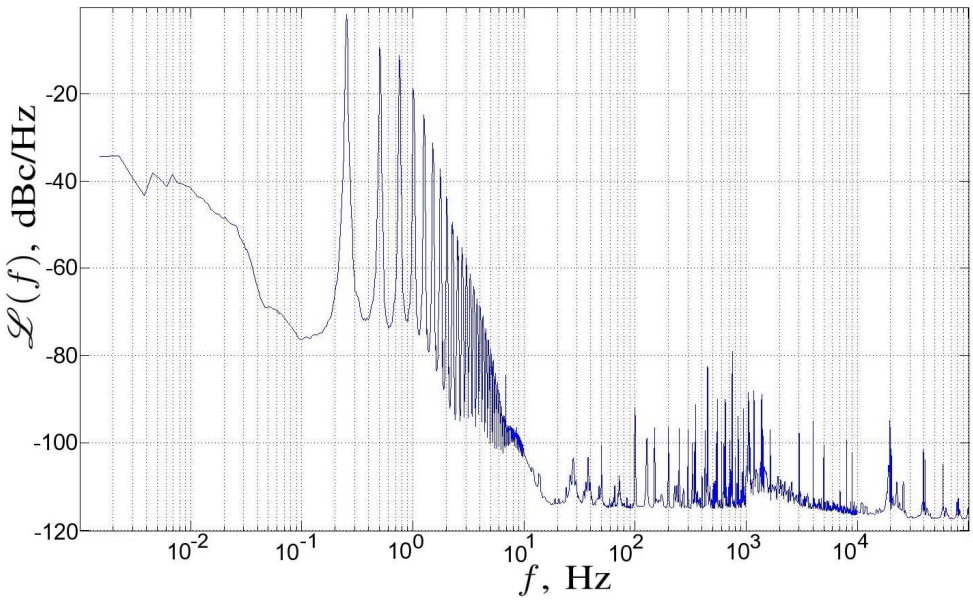

Figure 6.32: Phase noise spectral density of the output signal

s

frequency fluctuations S_y at 1 Hz on the temperature between 4 and 30 K. The work reports the strong correlation between acoustic wave attenuation around a phonon-phonon relaxation peak (20 K) and the $1/f$ noise. In fact, the results clearly show the absence of the connection between measured noise and the Q^{-4} law. The phase noise at 1 Hz from the carrier exhibits a considerable increase for the temperatures below 7 K. As it is said above, this may be attributed to difficulties with temperature regulation at very low temperatures. According to this work, S_y at 1 Hz equals about $1.5 \cdot 10^{-20}$ for the same type of 5 MHz AT-cut resonators. Thus, this result is almost 5 decades higher than that shown in [4, 111].

So, the previous works do not give an irrefutable answer on the question of the nature and even the value of the resonator flicker noise at liquid helium temperatures.

6.5.7 Discussion of the Measurement Results

It is interesting to get an idea of what could be the stability achievable by an oscillator built on such a resonator working at liquid-helium temperatures with the same loaded Q-factor as previously. It is still assumed that the resonator flicker noise dominates within the device bandwidth in comparison with the noise of sustaining electronics. So, the Allan deviation floor of such an oscillator can be estimated as

$$\sigma_y = \sqrt{2\ln(2)h_{-1}}, \tag{6.22}$$

where h_{-1} is the coefficient of the flicker power-low spectral density in terms of fractional frequency fluctuations (i.e. $S_y(f) = h_{-1}f^{-1}$) [1]. For the resonator, the relationship between phase and frequency spectra in its bandwidth is:

$$S_y(f) = \left(\frac{1}{2Q_l}\right)^2 \cdot S_\phi(f) = \left(\frac{1}{2Q_l}\right)^2 \cdot 2\mathscr{L}(f). \tag{6.23}$$

Thus, the power low coefficient h_{-1} can be estimated from the value of the f^{-1} asymptote line of $\mathscr{L}(f)$ at $f = 1$ Hz from curve (4) in Fig. 6.18. At 1 Hz this asymptote value is about -83 dB that gives $h_{-1} = 1 \cdot 10^{-23}$. Consequently, the Allan deviation floor of such an oscillator is $\sigma_y = 3.8 \cdot 10^{-12}$.

This value is more than ten times higher than that of actual state-of-the-art quartz crystal oscillators working at ambient temperatures.

Following the same procedure as in Section 6.5.1, an oscillator frequency stability floor can be estimated. This time it is supposed that the f^{-1}-like resonator noise is hidden by its f^0 noise caused by temperature in the 5.3K measurement case (Fig. 6.28, curve (1)). The maximum level of such a noise would have a power spectral density of $\mathscr{L}(f) \approx -102\ \frac{\text{dBc}}{\text{Hz}}$ in the worst case. This value gives an Allan deviation floor of the oscillator of $\sigma_y = 4.2 \cdot 10^{-13}$ for $Q_l = 15.6 \cdot 10^6$. Even in this case, the oscillator frequency stability is not better than that of the state-of-the-art room temperature quartz oscillators.

It can be noted the measurement capability of the presented approach is limited by the test bench flicker noise ($\mathscr{L}(f) = -110\ \frac{\text{dBc}}{\text{Hz}}$ at $f = 1$ Hz). So, the corresponding measurement noise floor of potential oscillators is also limited by $\sigma_y = 1.7 \cdot 10^{-13}$ for the same value of the loaded quality factor $Q_l = 15.6 \cdot 10^6$.

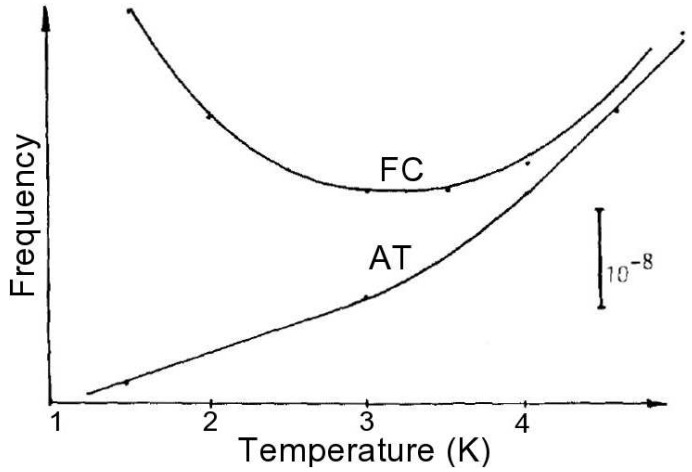

Figure 6.33: Comparison of frequency-temperature characteristics for AT and FC cut resonator (reprinted from [4])

These calculations show the best case noise floor of an oscillator based on such a cryogenic resonator. The best case means here that the device noise close-to-the-carrier is determined by the resonator proper noise and not by the noise of sustaining electronic components. This could be true when the latter noise is lower than that of the resonator. So, even in such a case, the oscillator performance could not outperform the state-of-the-art room temperature devices. The situation could be slightly improved by making the resonator environment more stable, i.e. by improving temperature control. This improvement can increase the oscillator frequency stability since it is clear that the limiting noise is due to temperature instabilities. Particularly, resonator temperature has to be controlled with sub-milikelvin precision. However, this approach could not be regarded as a panacea, since abilities of temperature and vibration control have their own reasonable limits. Some of these limits are introduced by the limitations of the cryogenic system itself. Another solution is to use the same principle as at room temperatures that make room temperature environmental control so effective, i.e. to benefit from a turn-over point in a resonance frequency-temperature characteristic. This approach significantly reduces frequency sensitivity to the temperature and, thus, pushes the limit of the oscillator performance. However, this idea requires systematic search for a crystal cut with a turn-over point for temperatures below 5K. One of the possible candidates is an FC-cut crystal resonator. The frequency-temperature characteristic of such a devise is shown in Fig. 6.33 (reprinted from [4]). But, unfortunately, the turn-over point is exhibited near 3K region which is inaccessible with the used cryogenic system. Moreover, the turn-over point is very sharp and cannot provide sensitivity better than $5 \cdot 10^{-9}$ K^{-1} in a 0.2K neighborhood. So, it is doubtful that this cut could provide any improvement to the oscillator stability due to device temperature insensitivity.

It worth to note that investigated SC-cut resonators exhibit a decrease in the temperature sensitivity with the decreasing temperature. So, it is possible that for sub-kelvin temperatures, these devices have sufficient temperature insensitivity to provide the satisfactory performance for cryogenic crystal frequency sources.

Chapter 7

Towards Cryogenic Quartz Crystal Oscillator

As it is stated at the beginning of the previous chapter, the phase noise reduction approaches may be divided into two big groups: the subsystem optimization and the supersystem compensation. The latter approach is considered in the previous chapter. The present part of the work is dedicated to the first group of methods. The mainstream idea is formulated in the first chapter of the present work: high values of the resonator quality factor provides narrower resonator bandwidth, which leads to a better closer-to-carrier noise performance. However, such unusually high values of quality factors lead to severe problems with oscillator modeling and optimization. Section 7.1 is an attempt to break through this obstacle. Another problem associated with cryogenic oscillator modeling is absence of any models for resonator noise for the harmonic balance analysis in conventional simulating tools. Such a model is proposed in Section 7.2 which presents the results previously published in [117]. The last section of the chapter is dedicated to the actual implementation of the liquid helium BAW oscillators.

7.1 Analytical Modeling of Oscillators with Extremely High Q

The objective of this section is to create analytical tools which may be successfully used for optimization of high-quality quartz crystal oscillators in terms of the phase noise. The material generally follows the presentation made in [118].

Nowadays electronic engineers widely use different computer-aided design (CAD) tools for electronic circuit modeling and optimization. These tools can help to significantly speed up the design process and to increase an accuracy. But sometimes they meet

some limits where these advantages are lost. A typical example is modeling of electronic oscillators based on quartz crystal resonators with outstanding high quality factors such as that obtained at liquid helium temperatures.

Usually, two common solutions of crystal oscillator modeling are used. The first solution is a combination of AC and Transient analyses provided by ordinary SPICE simulators. The AC analysis is used to find the oscillation frequency and the in-circuit quality factor. The transient analysis is used to check these results. However, on this step, the circuit Q is significantly reduced in order to decrease simulation time and/or even to achieve the simulation convergence towards a nontrivial solution. As a result, it is not possible to obtain trustful values of circuit currents and voltages (as well as such an important parameter as the crystal dissipation power). In addition to this, optimization of the system may pose additional problems, since it requires both AC and Transient analyses on each iteration step. So, this process can hardly be automated.

The second solution is known as a harmonic balance (HB) technique. This type of analysis is realized in some commercial RF-circuit simulators, such as ADS from Agilent and Harmonica (Serenade) from Ansoft. Nevertheless, such sophisticated and expensive simulators are capable of high-Q oscillator modeling, but this task is very time consuming and requires very good initial guess for an oscillation frequency (since there is now explicit source of frequency in the circuit). The last point requires an additional stage of the AC Analysis on each iteration step. So, even in this case, the automatic optimization is hardly possible.

Whatever the case, a convergence to the simulation algorithms is not guaranteed for oscillators with extraordinary values of quality factors. These facts make automatic optimization difficult and inefficient.

To overcome all the difficulties connected to high-Q oscillators modeling, another simple but effective technique could be proposed. The approach is more analytical than numerical and does not require any external SPICE or Harmonic Balance simulators. In rather simple circuits, all the concerning parameters may be calculated analytically or, in more elaborated cases, realized with simple home-made software. These parameters include the oscillating frequency, the amplitude of the first harmonic and the DC solution, the active power dissipated by the resonator and the oscillator, the in-circuit Q-factor.

In the following subsections different stages of the proposed technique are discussed. A Colpitts quartz crystal oscillator (see Fig. 7.1) is used for the explanation. However, this technique can be used for other types of oscillators with lumped components.

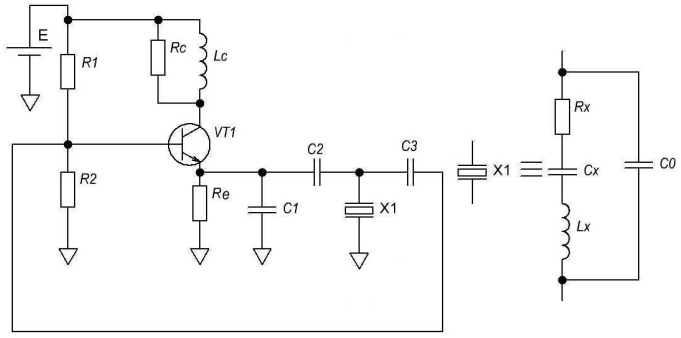

Figure 7.1: Colpitts quartz crystal oscillator

7.1.1 Oscillating Frequency and First Harmonic Amplitude

On this step of the present technique, one should transform an oscillator circuit into a closed loop system (similar to that which are widely used in the control system theory) with linear and nonlinear elements. The main idea here is to unite all linear dynamic components (inductors, capacitors and resistances), and process them as one linear block, which is connected in parallel with a nonlinear one. In our case, the nonlinear component is a BJT or HBT transistor. The crystal resonator is considered here as a linear network, which consists of a series motional branch (elements C_x, R_x and L_x) and parallel capacitance C_0.

From the oscillator circuit which is shown in Fig. 7.1 one may obtain its full equivalent circuit shown in Fig. 7.2 (a). To do this, it is needed to apply not only the rules of parallel and series connections of elements, but also the Y-Δ equivalent transforms. As a result, the oscillator consists of linear elements $Z_1(p)$, $Z_2(p)$, $Z_3(p)$, $Z_4(p)$ and $Z_5(p)$, where $p \equiv \frac{d}{dt}$.

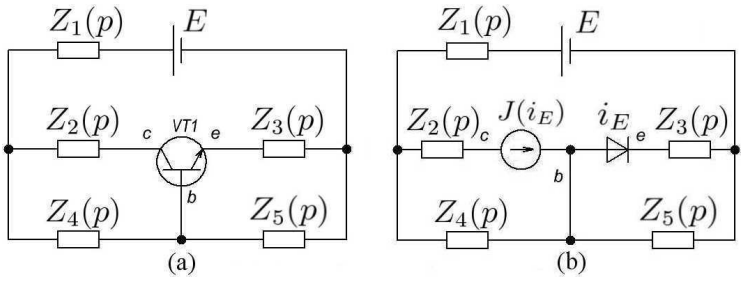

Figure 7.2: Steps of oscillator transformations

The BJT transistor must be represented with a nonlinear model. To simplify the model development, the straightforward choice is the Ebers-Moll model (see Fig. 7.2 (b)) consisting of a nonlinear element $i_E = I_f(u_{BE})$ and a linear current source $J = \alpha_f i_E$.

Next, following the same rules of transformation of the linear elements, one may obtain an one-loop oscillating circuit with one source of the bias (see Fig. 7.3 (a)), one linear and one nonlinear blocks. The dependent current source is transformed into a dependent voltage source and after that into a negative resistance. Finally, the system dynamics can be represented with a single formula:

$$E \cdot H_z(p) = u_{BE} + Z_l(p) \cdot I_f(u_{BE}), \tag{7.1}$$

where u_{BE} is a system variable (voltage between base and emitter of the transistor). The simple circuit, shown in Fig. 7.3 (a) and characterized with equation (7.1), may be considered as a closed loop in the nonlinear control theory (see Fig. 7.3 (a)). Such a loop has two main state variables: the emitter current i_E and the voltage base-emitter u_{BE}.

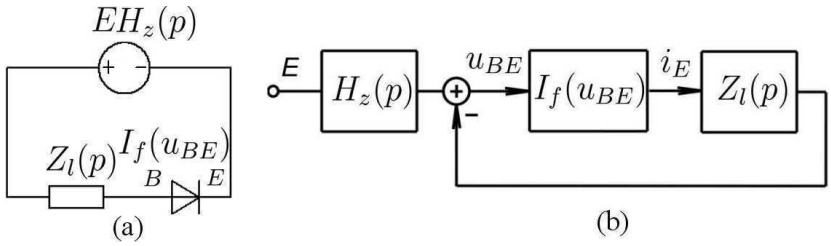

Figure 7.3: One loop oscillator representation: (a) - an equivalent circuit, (b) - a corresponding block-diagram, where $I_f(u_{BE})$ is a nonlinear part

The resulting circuit (Fig. 7.3) has the same mathematical sense as the initial one (Fig. 7.1), since no simplification (except for the model of the transistor) has been made. This means that such a loop can also be used for oscillator modeling, as well as the initial circuit. The fundamental difference between these two variants is that the former represents the lowest order of the entropy, and the latter is its variant with the highest entropy level (so it may correspond to a vast class of lumped oscillators).

The oscillator behavior can be represented with a block-diagram Fig. 7.3 (b), so that all investigation methods from the control theory (including investigation of oscillation conditions) can be used. Different methods have already been investigated to find amplitude and frequency of oscillations for this type of nonlinear systems. In this work we consider the method of describing functions. The describing function method (which is also sometimes called the Harmonic Balance method in the control theory) does not have a strict mathematical proof, though it is physically clear and correct. This method is very useful for high-order systems and helps to find oscillation conditions. The main criterion of the method application is so-called "filter hypothesis", which means that the linear part of the system has to filter the main harmonic and suppress others which arise at the output of the nonlinear element. This can be quantitatively expressed as follows:

$$\left|\frac{i_{Ek}}{i_{E1}}\right| \frac{Z_l(jk\omega)}{Z_l(j\omega)} \ll 1, \tag{7.2}$$

where i_{E1} and i_{Ek} are amplitudes of the first and kth harmonics of the emitter current respectively. It is clear that this condition is satisfied for such transfer functions which

have a helical gain-phase characteristic. Thus, a harmonic balance is reached in oscillating regime: high-order harmonics of emitter current produced by the nonlinear part are suppressed by the linear part, and the signal u_{BE} (which is closed to a sine signal, since harmonics are suppressed) is applied to the nonlinear part.

The presented method works as follows. Let us suppose that there is a sinusoidal signal at the input of the nonlinear element. So, at the output of this part of the system we obtain a signal of a more sophisticated form which has some high-order harmonics. Using a superposition property of the linear part of the system, we can regard that each of these harmonics acts independently from others. So, at the output of a nonlinear part, one obtains some harmonics with the same frequencies as at the input, but suppressed by $Z_f(jk\omega)$. If an amplitude of the first harmonic is much higher than others, the linear part is working as a low-pass filter, which suppress high-order harmonics produced by the nonlinearity.

To illustrate the method, a following example is considered: Fig. 7.4 shows Bode plot of oscillator linear parts ($Z_l(j\omega)$) for different values of quartz quality factor: 10^5, 10^6, 10^7 for the same values of the resonance frequency and the motional resistance. Numerical values (see Fig. 7.1) are $E = 5$ V, $R_c = 330$ Ohms, $L_c = 10$ uH, $R_1 = 10$ kOhms, $R_2 = 15$ kOhms, $R_e = 1.5$ kOhms, $C_1 = 150$ pF, $C_2 = 330$ pF, $C_3 = 1$ nF, $C_4 = 180$ pF, $\alpha_f = 0.99$, $r_0 = 1$ Ohm. The crystal resonator has the resonant frequency of $f_r = 10$ MHz, motional resistance of $R_x = 94$ Ohms and shunt capacitance $C_0 = 2$ pF.

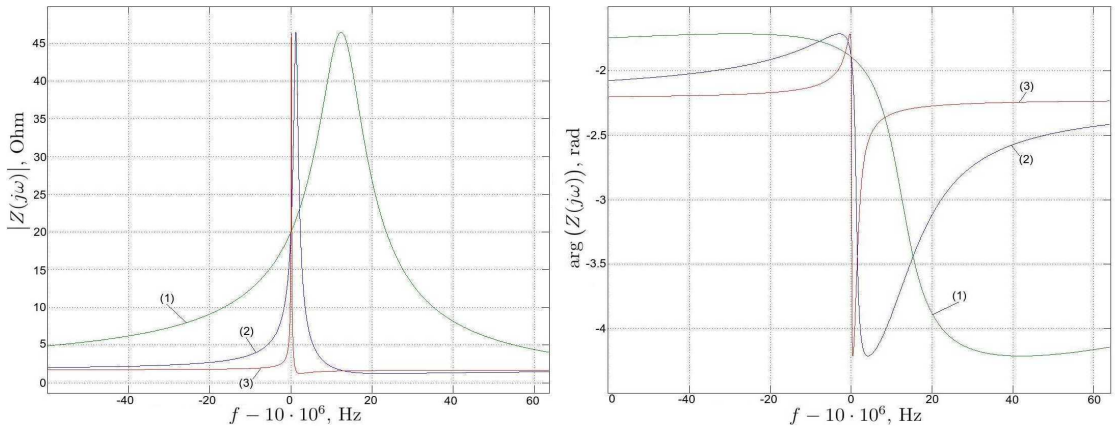

Figure 7.4: Bode plot of the linear part $Z_l(j\omega)$ for different values of the quartz crystal quality factor Q: (1) - 10^5, (2) - 10^6, (3) - 10^7 (with the same values of resonance frequency and motional resistance).

From Fig. 7.4 it is clear that the linear part of the loop works as a selective filter with a $-\pi$ phase shift at the oscillating frequency (another $-\pi$ phase shift to fulfill the Barkhausen conditions originates from the negative sign of the feedback). So, the linear transfer function $Z_l(j\omega)$ extracts one frequency or works as a discriminator. Thus, "filter hypothesis" holds true, so the describing function method can be applied for such a circuit.

To find the angular oscillating frequency $\omega_0 = 2\pi f_0$ one needs to solve equation $\Im\{Z_l(j\omega_0)\} = 0$ either analytically or numerically, since the nonlinear element is static.

Let a signal with the following form is applied to the nonlinear element:

$$V_{be}(t) = V_0 + a \cdot \sin(\omega t) = V_0 + a \cdot \sin(\psi). \tag{7.3}$$

Thus, a signal at the output of the nonlinear element can be expressed in the following form:

$$I_f(t) = I_0 + A_1 \cdot \sin\psi + B_1 \cdot \cos\psi + \sum HOH, \tag{7.4}$$

where Higher Order Harmonics are discriminated with a linear part, so that one can approximate:

$$I_f(t) \approx I_0 + A_1 \cdot \sin(\psi) + B_1 \cdot \cos(\psi), \tag{7.5}$$

where

$$A_1 = \frac{1}{\pi}\int_0^{2\pi} I_f(V_0 + a \cdot \sin(\psi))\sin\psi d\psi, \quad B_1 = \frac{1}{\pi}\int_0^{2\pi} I_f(V_0 + a \cdot \sin(\psi))\cos\psi d\psi \tag{7.6}$$

are Fourier coefficients.

Equation (7.3) can be differentiated and written in the operator form:

$$sV_{be} = a\omega\cos\psi. \tag{7.7}$$

Equations (7.3) and (7.7) allow us to express both sinus and cosinus of ψ:

$$\sin\psi = \frac{V_{be} - V_0}{a}, \quad \cos\psi = \frac{sV_{be}}{a\omega}. \tag{7.8}$$

So, substituting these two formulas into equation (7.5), one can rewrite the input-output relationship of the nonlinear part:

$$I_f = I_0 + A_1\frac{V_{be} - V_0}{a} + B_1\frac{sV_{be}}{a\omega} = I_0 - \frac{A_1}{a}V_0 + \Big(\frac{A_1}{a} + \frac{B_1 s}{a\omega}\Big)V_{be}. \tag{7.9}$$

The single-valued function (which we suppose $I_f(V_be)$ is) B_1 is always equals to zero, so the previous equation can be expressed in the following form:

$$I_f = I_0 + \frac{A_1}{a}(V_{be} - V_0) = I_0 + H_n(s, a, V_0)(V_{be} - V_0), \tag{7.10}$$

where $H_n(s, a, V_0)$ is a transfer function of a harmonically linearized nonlinear element.

$$Y_f(s, a, V_0) = H_n(s, a, V_0) = \frac{A_1(a, V_0)}{a}. \tag{7.11}$$

Using the transfer function of the harmonically linearized nonlinear element $H_n(s, a, V_0)$ (where s is the Laplace variable, a is the first harmonic amplitude, V_0 is a DC component), one can find parameters of system oscillations according to the Goldfarb and Kochenburger theory [119, 120]. According to this theory $H_n(s, a, V_0)$ acts as linear transfer function at the stability threshold. So, one can write an oscillation condition (for the first harmonic) taking into account that a bode characteristic of the closed loop has to pass through a point $(1, j \cdot 0)$, or $H_n(s, a, V_0)Z_l(s) = -1$.

In other words, to find the amplitude and frequency of the oscillation one needs to find an intersection point between $Z_l(j\omega)$ and $-1/H_n(j\omega, a, V_0)$ in the complex plane. In the considered case, the nonlinear characteristic is static, so it lies entirely on the real axis. Furthermore, the oscillating condition can be written as follows:

$$Z_f(j\omega_0) = -\frac{a}{A_1(a, V_0)}. \tag{7.12}$$

where ω_0 is an angular oscillation frequency.

Unfortunately, define integral (7.13) can not be calculated analytically.

$$A_1 = \frac{1}{\pi}\int_0^{2\pi} I_s \exp\Big(\frac{V_0 + a \cdot \sin(\psi)}{V_t} - 1\Big)\sin\psi d\psi. \tag{7.13}$$

So, the nonlinear function has to be approximated with a polynomial of the third order:

$$I_f = h_0 + h_1 \cdot u_{BE} + h_2 \cdot u_{BE}^2 + h_3 \cdot u_{BE}^3, \tag{7.14}$$

then the DC component of the base-emitter voltage (u_{BE_0}) can be found as a solution of the following equation:

$$k_3 u_{BE_0}^3 + k_2 u_{BE_0}^2 + k_1 u_{BE_0} + k_0 = 0, \tag{7.15}$$

where

$$k_3 = 2h_3, \quad k2 = (-12h_3 - 8h_2), \quad k_1 = \Big(-2h_1 - \frac{4}{Z_l(j\omega_0)} - 2h_2 - \frac{8}{3}\frac{h_2^2}{h_3} + \frac{1}{Z_l(0)}\Big)$$

$$k_0 = 2h_0 - \frac{4}{3}\frac{h_2 h_1}{h_3} - \frac{4}{3}\frac{h_2}{h_3 Z_l(j\omega_0)} - \frac{EH_z(0)}{Z_l(0)}.$$

And, the first harmonic amplitude is found as follows:

$$u_{be_1}^2 = -\frac{3h_3 u_{BE_0} + h_1 + 2h_2 u_{BE_0} + 1/Z_l(j\omega_0)}{\frac{3}{4}h_3}. \tag{7.16}$$

If more accurate solution is needed, the higher harmonics may be found [119]. Similar results may be obtained using more polynomial terms.

Then the right-hand expression of equation (7.12) can be found as follows

$$-\frac{a}{A_1(a,V_0)} = -\frac{a\pi}{\int\limits_0^{2\pi}\left(h_0 + h_1(V_0 + a\sin\psi) + h_2(V_0 + a\sin\psi)^2 + h_3(V_0 + a\sin\psi)^3\right)\sin\psi d\psi} = \tag{7.17}$$

$$= -\frac{1}{3h_3V_0^2 + \frac{3}{4}h_3a^2 + h_1 + 2h_2V_0}.$$

And, finally, the oscillation condition can be written in the follows form:

$$Z_f(j\omega_0) = -\frac{1}{3h_3V_0^2 + \frac{3}{4}h_3a^2 + h_1 + 2h_2V_0}. \tag{7.18}$$

It is clear that the necessary oscillation condition (but not sufficient!) is equality of the imaginary part of the $Z_f(j\omega_0)$ to zero. Thus, the frequency of oscillation (which though may not exist) can be found from the equation:

$$\Im\big(Z_f(j\omega_0)\big) = 0. \tag{7.19}$$

Oscillation frequency may be easily found graphically. This is illustrated in Fig. 7.5 which shows the Nyquist plot of the linear part $Z_f(j\omega)$ near the resonance frequency for the example under consideration ($Q = 10^6$). This graph shows that two possible solutions may exist (points (A) and (B)). But only one of them corresponds to stable oscillations. To verify this, both frequencies have to be investigated.

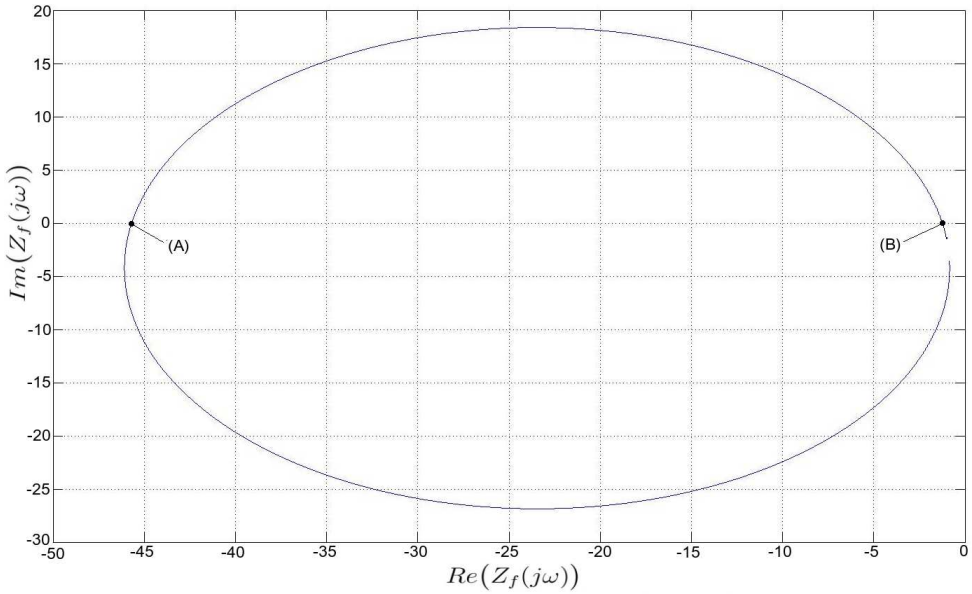

Figure 7.5: Nyquist plot of the linear part $Z_f(j\omega)$ for the given example with $Q = 10^6$

Nevertheless, further DC analysis is needed in order to prove existence of the oscillations and in order to find their amplitudes. An analytical expression similar to equa-

tion (7.18) can be written for the DC solution of the system:

$$Z_f(0) = -\frac{V_0 - K_z(0)E}{\int\limits_0^{2\pi} \big(h_0 + h_1(V_0 + a\sin\psi) + h_2(V_0 + a\sin\psi)^2 + h_3(V_0 + a\sin\psi)^3\big)d\psi} = \quad (7.20)$$

$$= -\frac{V_0 - K_z(0)E}{3h_3V_0a^2 + 2h_0 + 2h_2v_0^2 + 2h_1V_0 + h_2a^2 + 2h_3v_0^3}.$$

To find a solution it is possible to express a^2 from equation (7.18) and substitute it into equation (7.20). As a result of this operation, one obtains an algebraic equation of the 3rd order. Solution of the cubic equation (if one uses polynomial of higher order, a higher order result equation is obtained) provides a value of a DC shift of the solution V_0. After that, a first harmonic amplitude can be found using formula (7.18).

It has to be noted that even though some coefficients of cubic equation (7.15) have the term $Z_f(j\omega_0)$, all these coefficients are real numbers, since $Z_f(j\omega_0)$ (as well as $Z_f(0)$ and $K_z(0)$) is real (see condition (7.19)). Real coefficients of equation (7.15) mean that this equation always have at least one real root which means that a DC solution always exists. Contrary to that, oscillating solution has the following sufficient condition:

$$\frac{3h_3V_0 + h_1 + 2h_2V_0 + 1/Z_f(j\omega_0)}{\frac{3}{4}h_3} < 0, \quad (7.21)$$

where V_0 is a real solution of equation (7.15).

As we see from equation (7.15), both a and V_0 depend on parameters of the linear and nonlinear parts, though linear part provides only two real values $Z_f(j\omega_0)$ and $Z_f(0)$. In addition to this, parameters $K_z(0)$ and E are used.

Equation (7.15) can be solved analytically. To do so, two real coefficients have to be calculated:

$$p = -\frac{k_2^2}{3k_3^2} = \frac{k_1}{k_3}, \quad q = \frac{2k_2}{27k_3^3} - \frac{k_2k_1}{2k_3^2} - \frac{k_2k_1}{2k_3^2} + \frac{k_0}{k_3}. \quad (7.22)$$

Using the previous formulas, one can calculate a solution using a Cardano formula:

$$V_0 = \sqrt[3]{-\frac{q}{2} + \sqrt{\frac{q^2}{4} + \frac{p^3}{27}}} + \sqrt[3]{-\frac{q}{2} - \sqrt{\frac{q^2}{4} + \frac{p^3}{27}}}. \quad (7.23)$$

So, as it can be seen, all the calculations for a high-Q crystal oscillator may be performed in an analytical form. This approach helps to calculate the DC solution, first harmonic amplitude and oscillating frequency. Also some other well-known approaches from the control system theory may be applied here. The whole oscillator analysis does not require any simulator software, both simple SPICE or Harmonic Balance. The larger part of the effort is required for analytical transform of the original circuit, i.e. for the preprocessing stage. When it is done, the circuit simulation and optimization can be performed with no concern about time consumption or simulation algorithm convergence.

7.1.2 Power Dissipated in a Crystal Resonator

The power dissipated by a crystal resonator is a crucial parameter of the oscillator design. If the active power of the crystal is high enough, then it evinces nonlinear phenomena and a fast aging (see Chapter 1 for some details). For cryogenic crystal resonators this problem is more vital since the maximum possible level of dissipated power is much less at very low temperatures than at the room temperature (see Chapter 3). But, small excitation signals worsen the signal-to-noise ratio, and, thus, the short-term frequency stability. So, in the course of oscillator design and optimization, this parameter has to be taken into account.

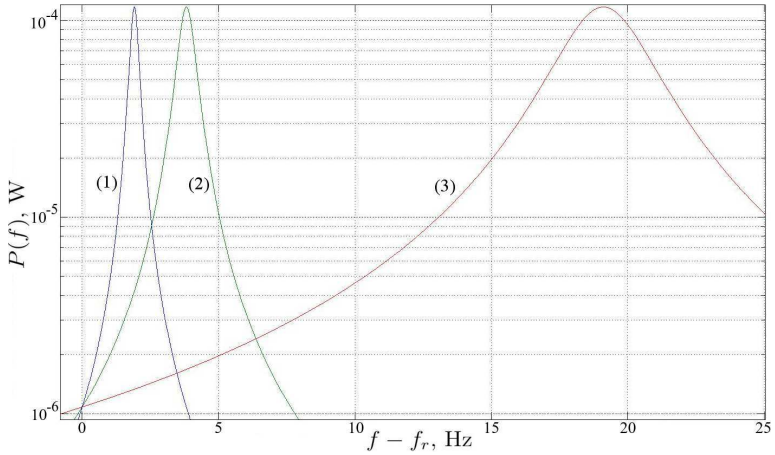

Figure 7.6: $P(f)$ around the resonance frequency for $I_i = 1\text{mA}$ and different values of the quartz crystal quality factor Q: (1) - 10^8, (2) - $5 \cdot 10^7$, (3) - 10^7

For a given solution of the system described above, one can find a current I_x and a voltage U_x of the quartz crystal (whose impedance is denoted by Z_x). In order to do that, an oscillator can be represented as a two-port linear network from the nonlinear element to the crystal resonator itself. The nonlinear element has to be substituted for a current source I_i which has a frequency and an amplitude of the first harmonic corresponding to the given solution. After that, a transfer function $H_i(j\omega)$ from the current I_i to the current I_x has to be found with a help of the linear network analysis. Here, the DC voltage source of the circuit has to be eliminated, since DC and first harmonic solutions are independent for linear networks and the crystal does not have a DC current component.

Fig. 7.7 (b) shows a modified oscillator circuit which can be easily calculated to find a transfer function from the input current I_i to the crystal resonator current I_x:

$$H_i(p) = \frac{I_x}{I_i} = \frac{\frac{Z_e}{Z_e+\frac{1}{pC_2}} - \frac{Z_a}{Z_a+\frac{1}{pC_3}} + \frac{Z_i}{Z_a+\frac{1}{pC_3}}}{\frac{Z_a+\frac{1}{pC_3}+Z_x+\frac{1}{pC_r}}{Z_a+\frac{1}{pC_3}} + \frac{Z_x+\frac{1}{pC_6}}{Z_e+\frac{1}{pC_2}}}, \tag{7.24}$$

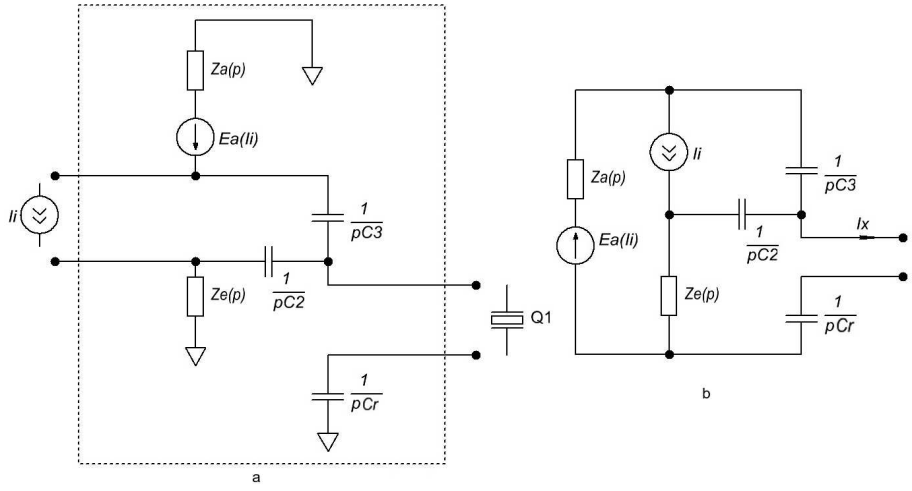

Figure 7.7: Simplified two-port system for resonator power calculation

where Z_x is a crystal resonator impedance.

So, the current through and the voltage drop on the crystal resonator for the given sinusoidal current I_i of the nonlinear element can be found as follows:

$$I_x(j\omega) = H_i(j\omega)I_i(j\omega), \quad U_x(j\omega) = Z_x((j\omega)H_i(j\omega)I_i(j\omega). \tag{7.25}$$

The active power dissipated by the crystal resonator can be expressed as:

$$P = Re(U_x(j\omega) \cdot I_x^*(j\omega)) = \left|H_i(j\omega)I_i(j\omega)\right|^2 Re(Z_x(j\omega)). \tag{7.26}$$

As an example Fig. 7.6 shows dependence $P(f)$ for a high-Q resonator (10^8) around a resonance frequency of about $f_r = 31.252$ MHz for the current of nonlinear element equal to 1 mA. Also, made numerical experiments have shown that for different values of Q and constant values of the resonance frequency, the active powers dissipated inside the crystal resonator are the same, but in the same time oscillation frequency changes significantly.

In the following numerical experiment crystal resonators with different quality factors but the same resonant frequencies and motional resistances are compared according to the active power dissipated by the first harmonic. Fig. 7.1.2 (a) shows that for all values of Q the active power is the same, but in the same time oscillation frequency f_o changes considerably (see Fig. 7.1.2 (b)).

7.1.3 Oscillator Quality Factor

The oscillator quality factor is the principal parameter which is used in the oscillator phase noise optimization. In order to achieve the highest possible frequency stability, this

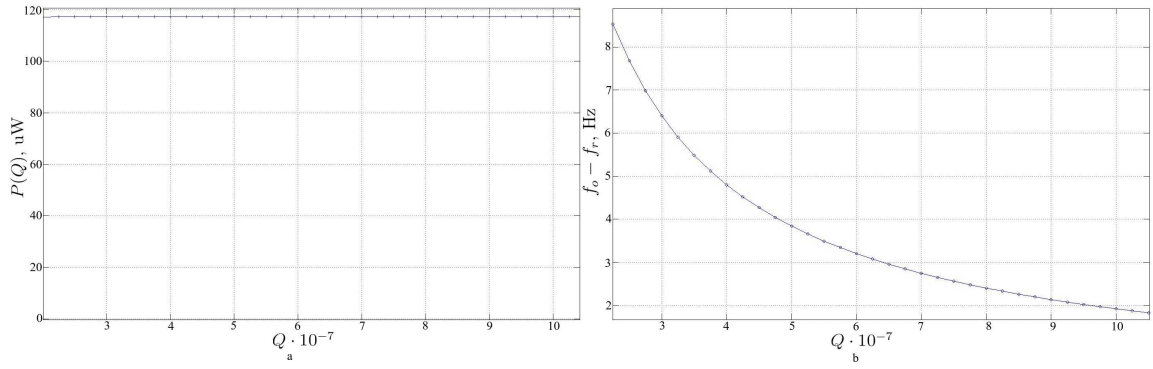

Figure 7.8: a. $P(Q)$ for constant values of I_i, R_x and f_r; b. $f_0 - f_r$ for constant values of I_i, R_x and f_r

parameter has to be maximized.

The oscillator quality factor can be calculated from transfer functions of the linearized oscillator open loop, i.e. its small signal model. In fact, these transfer functions can be found analytically. To do this, the oscillator loop is divided into two parts (see Fig. 7.9): a resonant network and an amplifier with transfer functions written for currents:

$$H_r(j\omega) = \frac{I_{o1}}{I_{i1}}, \quad H_a(j\omega) = \frac{I_{o2}}{I_{i2}}. \tag{7.27}$$

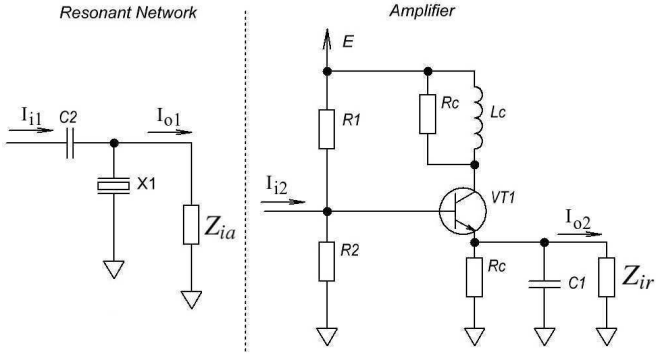

Figure 7.9: Resonant network and amplifier with their loads

In order to find the transfer functions $H_r(j\omega)$ and $H_a(j\omega)$, one needs to find load resistances Z_{ia} (amplifier input impedance) and Z_{ir} (resonator input impedance). For that, a closed oscillator loop can be represented (without lack of generality) as an infinite chain of sub-circuits: amplifiers and resonant networks (see Fig. 7.9). If the resonant circuit is the first block of the chain, then the input impedance of this chain corresponds to the amplifier load, and vice versa.

The input impedance of the infinite chain Z_{ia} (Fig. 7.10) can be easily found using a simple statement: if the first periodic unit of the infinite chain with the input impedance

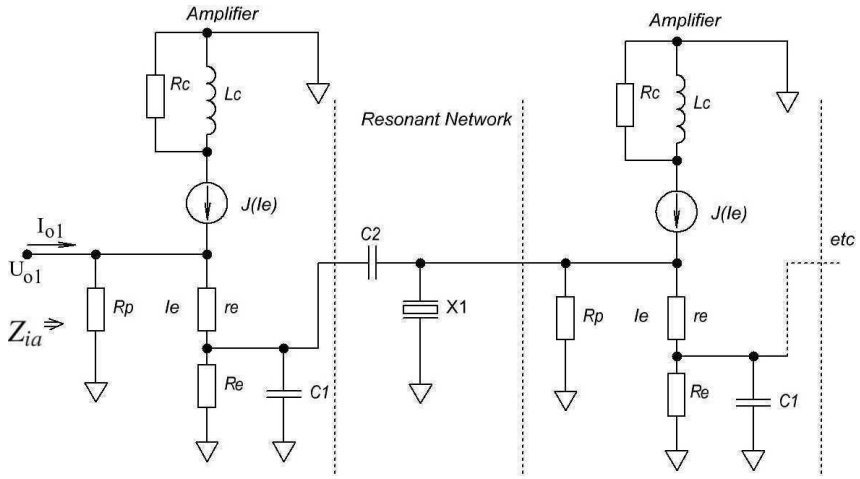

Figure 7.10: Equivalent circuit for the load impedance of the resonant network (Z_{ia})

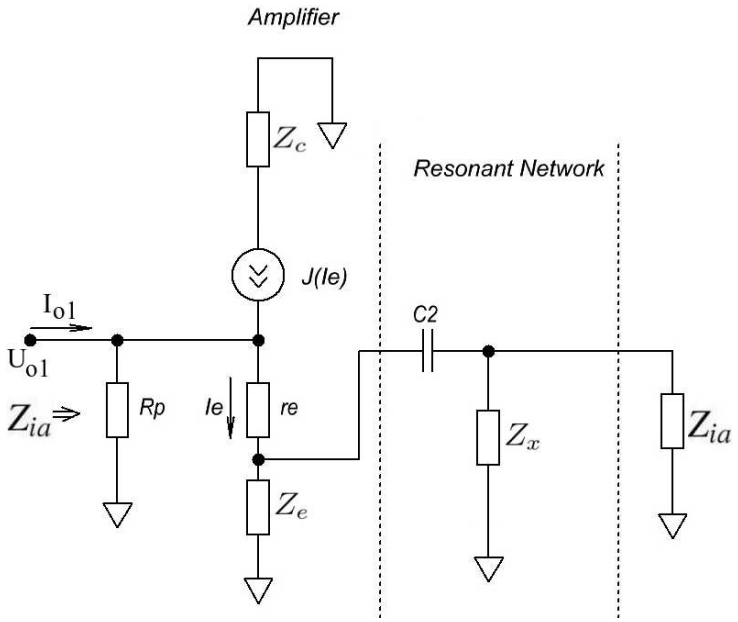

Figure 7.11: One periodic unit of the infinite chain for Z_{ia}

Z_{ia} is removed, then the rest of the chain has the same input impedance Z_{ia} (see Fig. 7.11). This statement is obviously clear from the physical nature of the periodic infinite circuit. Also, this statement means that the rest of the infinite circuit can be substituted for the impedance Z_{ia}. In other words, Z_{ia} is a function of Z_{ia}. This fact results in a second order algebraic equation of the following form:

$$AZ_{ia}^2 + BZ_{ia} + C = 0, \tag{7.28}$$

where A, B and C are parameters which depend on the circuit elements. An equation of the same type may be found analytically for the load impedance Z_{ir}. This leads to

analytical expressions of amplifier and resonant network transfer functions, which are expressed as follows for the present case:

$$H_r(j\omega) = \frac{Z_x}{Z_x + Z_{ia}}, \quad H_a(j\omega) = \frac{R_p Z_e}{\big((1-\alpha)R_p + r_e\big)(Z_{ir} + Z_e) + Z_e Z_{ir}}, \tag{7.29}$$

where Z_e is the impedance of the parallel connection of $C1$ and R_e, R_p is the resistance of resistances R_1 and R_2 connected in parallel, α and r_e are transistor linearized parameters.

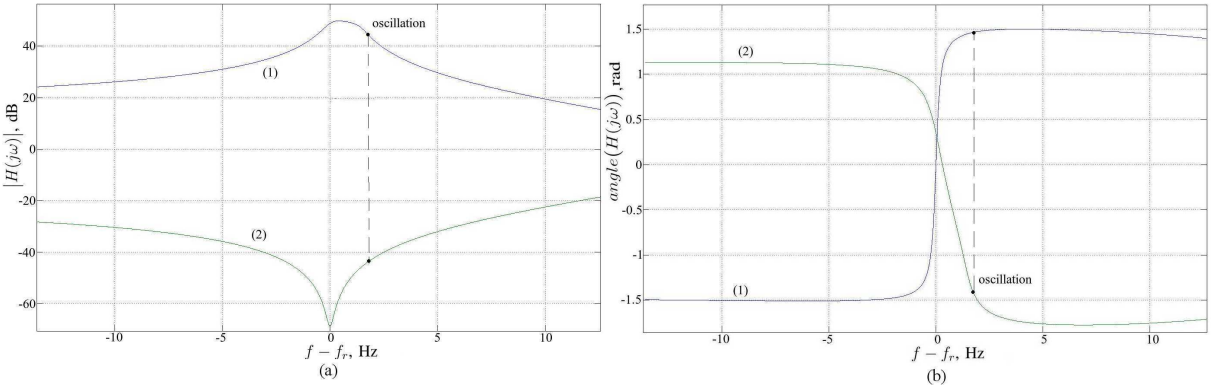

Figure 7.12: (a) Amplitudes $\big|H_a(j\omega)\big|$ (1) and $\big|H_r(j\omega)\big|$ (2); (b) Phases $arg\big(H_a(j\omega)\big)$ (1) and $arg\big(H_r(j\omega)\big)$ (2)

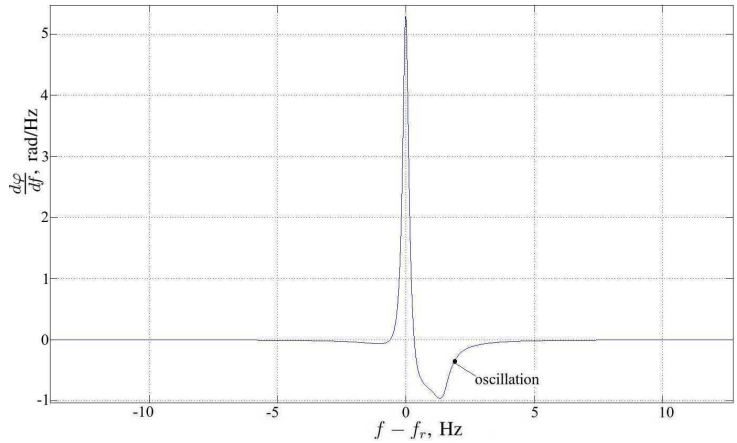

Figure 7.13: Dependence of $\frac{d\varphi}{df}$ on frequency

Fig. 7.12 shows amplitude-frequency (a) and phase-frequency (b) characteristics of the resonant network and the amplifier respectively. Fig. 7.13 shows the dependence of $\frac{d\varphi}{df}$ versus frequency, which is sufficient to find the oscillator quality factor:

$$Q = -\frac{f_o}{2}\frac{d}{df} arg\big(H_r(2\pi fj)H_a(2\pi fj)\big)\Big|_{f=f_o} = -\frac{f_o}{2}\frac{d\varphi}{df}\Big|_{f=f_o}. \tag{7.30}$$

This expression also can be found analytically. The calculated characteristics are in good agreement with approximate numerical results obtained with the SPICE AC analysis.

7.1.4 Oscillator Parametric Optimization

In the introduction to this section it is shown that optimization of very high-Q oscillators in the case of traditional simulation approaches is a manual tiring process. Attempts of automatic optimization [121] meet four types of problems: convergence problems (all types of analyses have to converge on each iteration step); optimization time problems (this process is extremely time-consuming); a requirement of different types of analyses on each iteration step; limitations of optimization algorithms posed by a simulating software. Contrary to that, the proposed approach has no all these drawbacks. First, analytical methods have absolute convergence contrary to numerical. Even though some numerical techniques can be used to find an oscillating frequency in more sophisticated circuits, the convergence of such an algorithm may be rather high, since the task is to find the roots of a polynomial equation when an initial guess is very close to the solution. Second, the approach is very fast, since analytical expressions immediately give values of all parameters. Circuit transformations are performed just one time before the optimization process (an example of calculations on each iteration step is given in [121]). Third, method does not require any additional types of analysis with any of external simulating tools either SPICE or HB. So, it well suits for home-made software realization, and any appropriate optimization algorithm may be used with the presented approach.

To optimize the oscillator performance one needs to consider several circuit parameters on each iteration step. The very first parameter is a circuit oscillating frequency. If the real solution of equation $\Im\{Z_(j\omega_0)\} = 0$ exists near the resonant frequency, then the circuit is capable of oscillating. Second, using ω_0 one can find a DC solution and the first harmonic amplitude (7.16). If a real solution exists than the oscillating sufficient conditions are fulfilled. If no solutions are found, then this variant of the oscillator is discarded. Third, using expression (7.26), the active power of a crystal resonator has to be found. This value has to fall into a certain range depending on resonator type and environmental conditions, otherwise this combination of oscillator parameters is discarded. In the case of cryogenic oscillator, in the same way the power dissipated by all the oscillator may be verified. It does not have to exceed certain levels. And finally, a circuit quality factor has to be found. Depending on the results (the solution combination of oscillator parameters), the optimization algorithm has to make a decision on the further changes of these parameters.

For oscillator optimization, derivative-free methods are the most suitable. Among them we can highlight the Nelder-Mead method, genetic algorithms and simulated annealing, which have been successfully used for optimization of high-order electro-mechanical systems [122].

7.2 Accurate Quartz-Crystal Resonator Phase Noise Simulation in ADS

While the approach proposed in the first section of the present chapter is very effective in oscillator optimization, where iterative circuit recalculations are required, for more accurate final verification of the final results it is preferable to use more sophisticated CAD tools. But, such simulation approach requires very accurate component models.

Nowadays modern commercial electronic simulators are unavoidable tools for the oscillator analysis [123]. Such engineering tools, like ADS from Agilent, cover the whole oscillator designing procedure, including the phase noise analysis. They can reduce development cost and time-to-market and can be used to clarify some oscillator intrinsic processes [124]. Indeed, not all important oscillator parameters are available for direct measurements. For example, the true phase noise of the oscillator loop alone is difficult to measure and partially hidden by the output-amplifier noise, the influence of the different loop components including the resonator itself on the resulting noise spectrum is not clearly distinguishable. So, in dielectric resonator oscillators (10-100 GHz) the active part noise dominates the resonator noise. In case of oscillators using acoustic resonators (bulk acoustic wave (BAW) up to 100 MHz, surface acoustic wave (SAW) and film bulk acoustic resonators (FBAR) up to 10 GHz), the resonator-caused noise cannot be ignored, as it is usually done (In the best case it is just added manually by the designer after simulation). For example, for BAW [3, 26, 125] and FBAR [126], resonator-caused noises are measured, but not included into resonator simulations. Obviously, this simplification degrades the close-to-carrier simulation results. In this paper the case of RF ultra-stable quartz crystal oscillators is covered. In the first section a resonator noise model is addressed from the point of view of oscillator phase noise simulation ignoring the noise origins (actually not still clearly identified). Finally, the last section discusses the influence of this type of noise on the final oscillator noise spectrum.

7.2.1 Quartz Resonator Phase Noise Modeling

The precision simulation of quartz crystal oscillators has to include a realistic phase noise model of the resonator. To do this the recent precision phase noise measurements have been used [3, 26]. Measurements are made with the interferometric bench. For all resonators a double-oven temperature control (having the same quality as that used in oscillators) is implemented in order to reduce the temperature fluctuations. The typical phase noise spectrum of a quartz crystal resonator consists of the following four zones (listed from low to high Fourier frequencies): 1) f^{-2} is a random-walk process due to residual temperature fluctuations. Even though it is not usually shown and not taken into account, it always exists [14, 105] and can limit the phase noise performances at low frequencies, according to the temperature control quality; 2) f^{-1} is the intrinsic crystal phase noise within its bandwidth [28]; 3) f^{-3} is the intrinsic crystal phase noise outside the

bandwidth; 4) f^0 is the noise floor of the measurement bench. So, for the unambiguous description of the resonator phase noise three spectrum parameters can be extracted: 1) f_T - the corner frequency between f^{-2} and f^{-1} regions, 2) the phase noise level at 1 Hz, 3) f_L - the corner frequency between f^{-1} and f^{-3} regions.

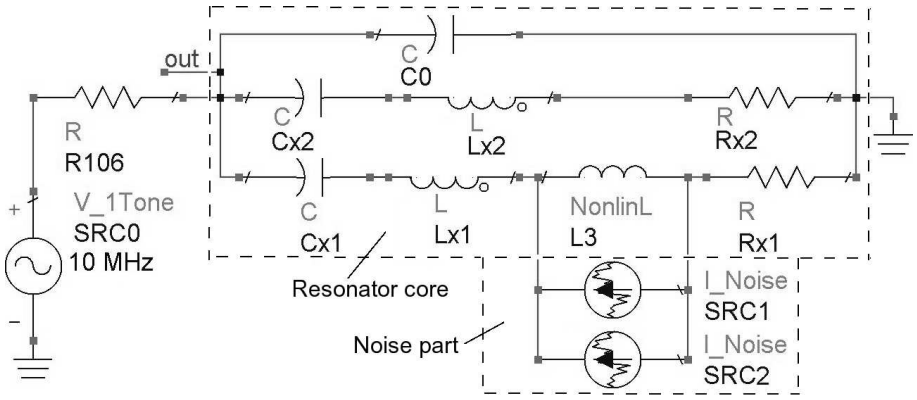

Figure 7.14: Quartz resonator noise modeling circuit. Noise sources SRC1 and SRC2 have spectral noise densities proportional to $f^{-1/2}$ and f^{-1} correspondingly

This type of measured spectrum has been implemented using a circuit shown in Fig. 7.14. The quartz crystal resonator is modeled with its conventional RLC branch (doubled here because a parasitic mode is close to the working one for doubly-rotated crystal cuts) and its parallel parasitic capacitor but including an additive current-controlled inductance, which value depends on the current of two noise sources. Since the device resonance frequency depends not only on parameters of the motional branches but also on the variable inductor, the resulting system has a parametric noise with a spectral density proportional to the squared voltage of the noise sources. So, the first source with a power spectral density $\sim f^{-\frac{1}{2}}$ is used to represent f^{-1} and f^{-3} noises for medium and high Fourier frequencies. The second one, with the PSD $\sim f^{-1}$, gives a f^{-2} slope for low frequencies. The sources parameters are adjusted to simulate the phase noise of real 10 MHz doubly-rotated BVA-type resonators measured in FEMTO-ST Institute. Fig. 7.15 presents the simulation results, which reproduce the measurement data [3, 26]. In this way the quartz crystal parametric residual fluctuations are implemented for the oscillator phase noise modeling.

It has to be noted that the chosen solution of a voltage-controlled capacitance associated with voltage noise sources is not unique. For example, a voltage-controlled capacitance associated with voltage noise sources is also relevant [127].

7.2.2 Crystal Oscillator Phase Noise Simulation

The described above model has been further used for the simulation of an actual 10 MHz ultra-stable quartz crystal oscillator designed in FEMTO-ST. This unit has a one-transistor

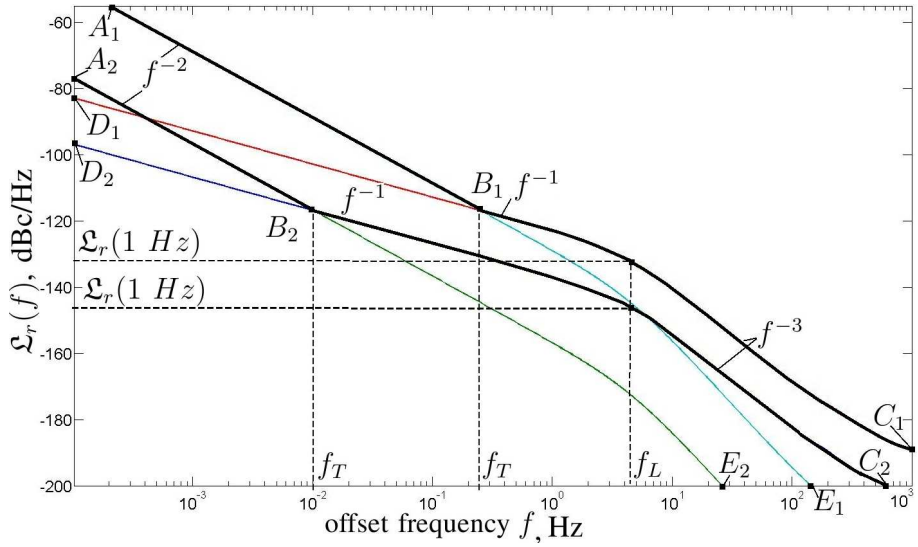

Figure 7.15: The typical phase noise spectra of a 10 MHz quartz crystal resonators of high ($A_1B_1C_1$) and medium ($A_2B_2C_2$) quality. Each spectra is an overlay of two independent PSDs, which correspond to noise sources SRC1 and SRC2: curves $A_1B_1E_1$ and $A_2B_2E_2$ originates from the source SRC2, and curves $D_1B_1C_1$ and $D_2B_2C_2$ are results of the source SRC1

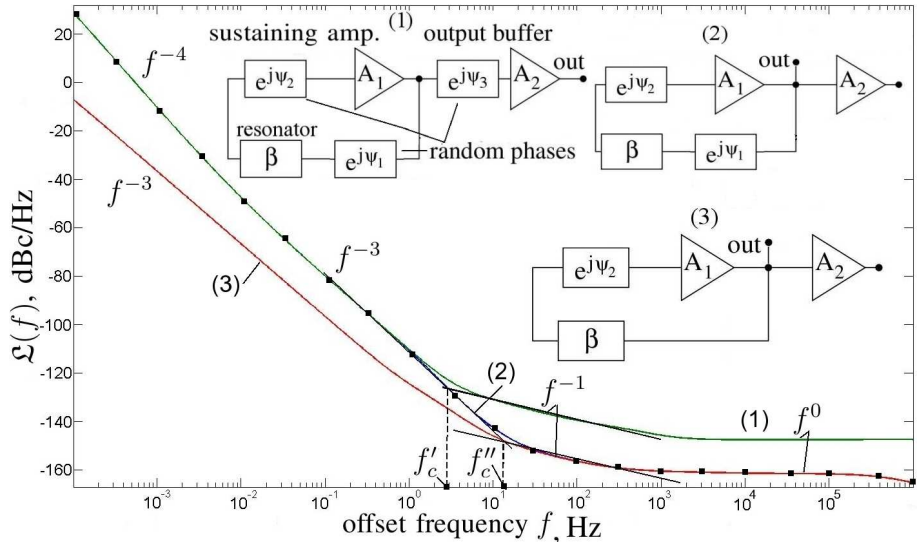

Figure 7.16: PSDs of Oscillator Phase Noise representing a 10 MHz actual one in different configurations: (1) - the oscillator PSD after the buffers, i.e. the PSD measured in reality, (2) - the oscillator PSD before the buffers (also marked with black squares), (3) - the oscillator PSD before the buffers without the resonator noise. Three generalized noise sources are present: ψ_1 - resonator phase noise, ψ_2 - sustaining amplifier noise, ψ_3 - buffer phase noise

Colpitts-type oscillation loop (the sustaining amplifier + the resonator), and a common-collector stage followed by an output cascode amplifier (i.e. two buffer stages are used to isolate the loop from the load, to match impedances and to purify the output signal).

Fig. 7.16 shows the simulated phase-noise PSD of the oscillator in different configurations with or without crystal noise, before or after the buffer stages in order to figure out the influence of the different oscillator parts. In addition to the resonator noise, thermal noise sources of all components and transistors flicker noise sources are implemented. From the practical point of view, the simulated curves correspond to the real measurements. The oscillator phase noise spectrum consists of the clear f^{-4}, f^{-3}, f^{-1} and f^{0} noises, which can be easily identified in a typical RF oscillator phase noise spectrum. The f^{-4} spectrum slope is due to the Leeson effect of the f^{-2} resonator noise. f^{-3} corresponds to the transformed f^{-1} resonator noise. The flicker and white noises of curve (1) are dominated by the noise of the output buffers, though the flicker and white noises of curve (2) are only due to the sustaining amplifier phase noise.

The first observation from these results is that white and flicker noise of the buffers overlap these types of noises of the oscillating loop. This lead to a decreasing of the corner frequency between f^{-1} and f^{-3} PSD slopes (f_c'), which can be taken for Leeson frequency by mistake [2, 1]. Actually, the Leeson effect takes place inside the oscillating loop, so the true Leeson frequency is the corner frequency between the f^{-1} and f^{-3} noises of the curve (2) - f_c'', which is hidden by the buffer noise. As a conclusion, f_c' would give unjustified high values of the loaded quality factor.

Second, as it also can be concluded comparing curves (1) and (3), the phase noise close to the carrier (both f^{-3} and f^{-4}) is predominantly due to the resonator instability. Thus, for the reliable ultra-stable oscillator noise simulation, the resonator phase noise model has to be included into the loop. The importance of the f^{-4} resulting noise depends on the quality of the temperature control in the ovenized crystal oscillator as well as in the measurement bench of resonator noise. So, neglecting it (what is usually done both in measurements and modeling) leads to poor simulation performance close to the carrier. It should be noticed that the resonator aging can hide the effect of long term temperature fluctuations, depending on their relative weights.

The proposed model of resonator phase noise is efficient for precise simulations of ultra-stable quartz oscillators. Simulations are in good agreement with both resonator and oscillator phase noise measurements. This model implements residual quartz crystal parametric noise, both due to temperature and intrinsic fluctuations. This approach provides reliable results of phase noise close to the carrier. Also, the implementation of the f^{-2} resonator noise is needed (though it is usually neglected), because it limits the system performances in many applications. Our simulations confirm that actual oscillator phase noise performances close to the carrier originate predominantly from the quartz-crystal resonator noise. In the same time, far from the carrier (f^{-1} and f^{0} noises) the system stability is mainly limited by the buffer amplifying stages. The suggested approach may be very helpful for the computer-aided ultra-stable crystal oscillator design.

7.3 Cryogenic Oscillator Implementation

Development of an actual cryogenic oscillator is related to many technical problems. First of all, this process is very limited by impossibility to modify the oscillator electronics "on-the-fly" which is absolutely required by the complexity of such systems. This means that once the DUT is installed and closed, and the temperature is decreased, one cannot change anything inside the cryocooler. In order to do any modifications the cryocooler has to be stopped, and its temperature has to be increased up to the room value. This process takes *at least 12 hours*. Once modifications are done, the DUT has to be cooled down again. This process takes *about 3.5-4 hours*. These facts mean that any schematic modification and its verification could be made only once in 24 hours. In particular, it makes almost impossible utilization of the mode-selective circuit in an oscillation loop, because it requires extremely accurate adjustment on an actual device. So, the development process of cryogenic electronic system (and oscillators in particular) is a very time-consuming and exhausting process comparing to the room temperature situation. Moreover, cryogenic devices are much less reliable, their behavior is much less predictable, and the environmental influences are much less known. So, the performance of first cryogenic crystal oscillators can hardly be compared with performances of state-of-the-art room temperature devices developed during many decades.

It has to be noted that even though the sensor temperature reaches 4K after 4 hours of cooling process, frequency stability measurements have to be made after at least additional 20 hours. This is due to very long-term time constants of cryogenerator thermal processes.

Another feature of the cryogenic oscillator development is the necessity to design a corresponding thermo-mechanical structure. This requirement is a consequence of the many issues concerning resonator and transistor temperatures, dissipated power, temperature instabilities etc.

In addition, crystal resonators working at cryogenic temperatures have many overtones and modes which can be potentially excited. And since, as it is mentioned above, the utilization of the mode-selection circuit is not possible, one cannot predict an oscillation mode *a priori*.

7.3.1 MOSFET-Based Solution

The first attempt to implement a cryogenic oscillator was made using MOSFET transistors and quartz crystal resonators originally designed for room temperature operation at 5 MHz. They are commercial q024a from BVA Industries (further, X1) and a home-made 5405 (further, X2). The mounting solution is shown in Fig. 7.17. In fact, two oscillators are implemented here. Each oscillator is mounted on a separate surface of a holder. The resonators are installed vertically, i.e. so that the resonator disks are normal to the Y

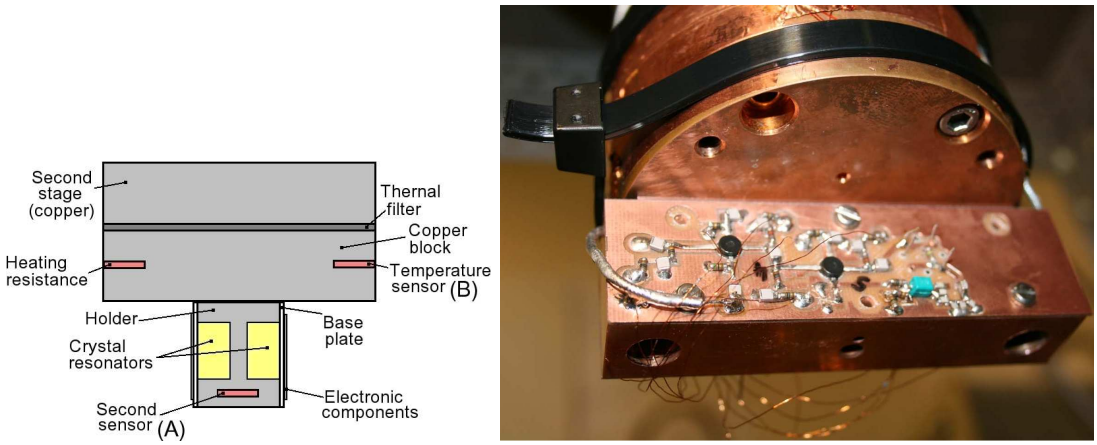

(a) Schematic view (cables and wires are not shown)

(b) Photograph

Figure 7.17: Oscillator mounting inside the cryocooler

axes (see Fig. 3.3 and Fig. 6.15). The RF signals are acquired with cables, and DC biases are provided with thin copper wires.

Table 7.1 presents different parameters and conditions of different tested oscillators. Configuration and stability results of each reference are explained in the text of the subsection.

Table 7.1: Working parameters and conditions of MOSFET-based oscillators

Reference	Regulated Temperature	Holder	V_{T1D}, V	V_{T1G1}, V	V_{T1G2}, V
X1_A1	4.6K	duraluminium	17	2.8	7.2
X1_A2	4.6K	duraluminium	17	3	7.2
X1_A3	4.6K	duraluminium	19.2	2.44	6.2
X1_A4	4.24K	copper	16	2.4	8
X1_A5	4.2K	copper	16	2.27	7.6
X1_A6	4.1K	copper	14.5	3.07	7.6
X1_A7	3.9K	copper	10	0.79	5.5
X3_A8	3.9K	copper	6	1.5	6.2
X3_A9	3.9K	copper	9.5	1.3	5.2

The oscillator circuit is shown in Fig. 7.18. This is an one-loop Collpits oscillator with one MOSFET transistor in an oscillating loop and another one in a output buffer stage (source-follower). Both transistors are biased separately, in order to achieve the best performance. In fact, bias voltages are the only means of the oscillator adjustment

at cryogenic temperatures. Moreover, the biases of the first and the second gates for both transistors are also separated.

The first attempt of oscillator implementation was made with a duraluminium holder (references X1_A1, X1_A2, X1_A3, where X1 stands for a number of an implemented resonator). This material has the lower thermal conductivity (5 $\frac{\mathrm{W}}{\mathrm{m}\cdot\mathrm{K}}$ at 4K for 6061 aluminium) and the higher specific heat (0.3 $\frac{\mathrm{J}}{\mathrm{kg}\cdot\mathrm{K}}$ at 4K for 6061 aluminium) than the copper [128]. These properties provide better filtration of the cryocooler temperature fluctuations, but they also increase an absolute temperature of two resonators. The packages of MOSFET transistor are installed in a way to have a direct mechanical and thermal connection with the holder.

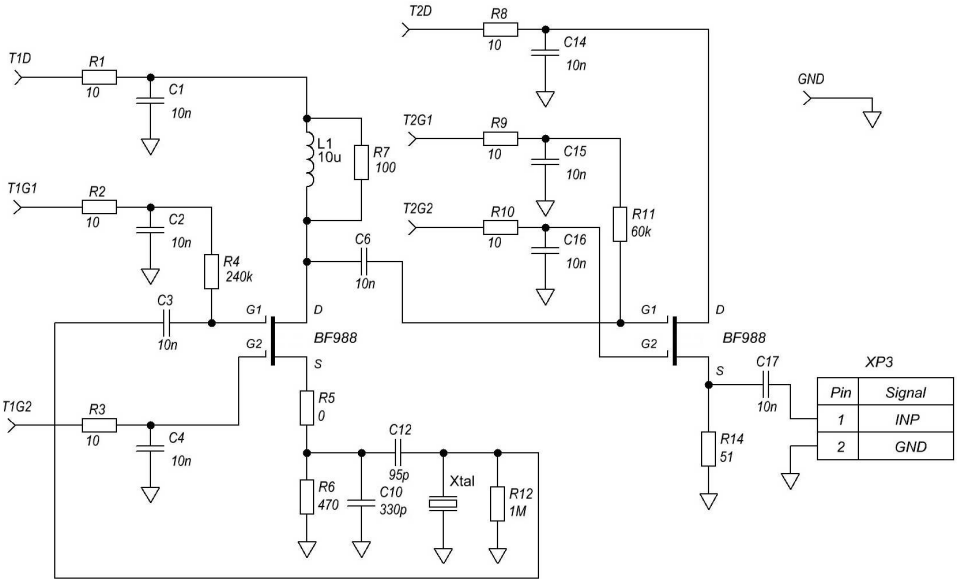

Figure 7.18: Schematic diagram of a cryogenic crystal oscillator based on a MOSFET transistor

The oscillator shown in Fig. 7.18 could be regulated to work at three resonator modes. The measured frequency stabilities in terms of the Alan deviation of these modes are shown in Fig. 7.19. These modes are 5.489680 MHz (the 3rd overtone of the B mode), 4.992987 MHz (the 3rd overtone of the C mode), 8.535128 MHz (probably, an anharmonic). These results are obtained only for one oscillator (X1) measured against the H-maser with the TSC5120A phase noise test set. All attempts to force X2 device to oscillate were unsuccessful.

The first experimental attempt showed that oscillator electronics heated up the support considerably. Though the temperature control system was regulated for working at 4.6K, and the actual temperature of the copper block reached this value, the temperature of the holder was just 14K. This fact states that an actual value of the quality factor is not high enough. In order to solve this problem the duraluminium holder is replaced with a

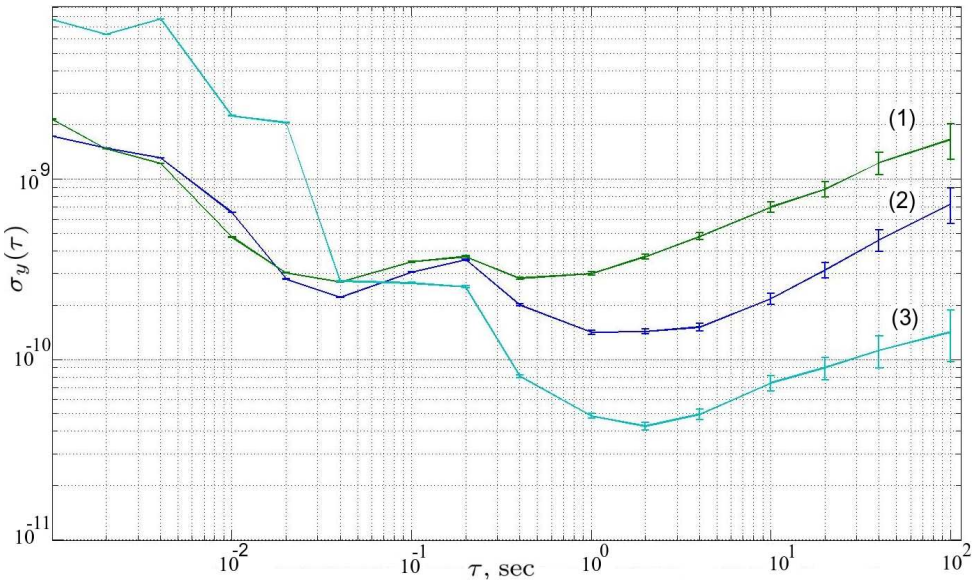

Figure 7.19: Allan deviation of the oscillator (duraluminium holder) working at different modes: (1) - 5.489680 MHz (ref. X1_A1), (2) - 4.992987 MHz (ref. X1_A2), (3) - 8.535128 MHz (ref. X1_A3)

copper holder of the same dimensions. Copper has a much higher thermal conductivity (1900 $\frac{\mathrm{W}}{\mathrm{m \cdot K}}$ at 4K) and a lower specific heat (0.1 $\frac{\mathrm{J}}{\mathrm{kg \cdot K}}$ at 4K) [128].

These oscillator solutions (references X1_A4, X1_A5, X1_A6) also can be forced to oscillate at different modes. Fig. 7.20 shows the corresponding Allan deviation plots. This time another frequency could be produced, i.e. 11.853208 MHz which is an unknown anharmonc. Though it is also present, the 3rd overtone of the B mode is not shown since it has unsatisfactory stability.

Further, two oscillators were modified to obtain a batter frequency stability. As for the oscillator X1, capacitance C12 is increased up to 150 pF and resistance R6 is decreased down to 470 Ohm. For the second oscillator, the resonator is replaced with another q024a from BVA Industries and both transistors are changed (further, this solution is referenced as X3). Also for X3, capacitance C12 is increased up to 350 pF and resistance R6 is decreased down to 470 Ohm.

Fig. 7.21(b) shows that the closest to the carrier slope of the phase noise PSD is less (about f^{-2}) than the second one from the carrier (f^{-4}). This phenomenon could be explained with the results of section 2.3. Indeed, the section states that transfer functions between some oscillator noise source and output phase noise have no an integrating multiplier, and so they do not obey the Leeson low for close-to-carrier frequencies. Moreover, these sources have higher impact into the total noise for oscillators with higher Q. So, for high-Q oscillators, noise sources without the Leeson effect could overlap the standard spectrum introducing two additional noise slopes. This is shown theoretically

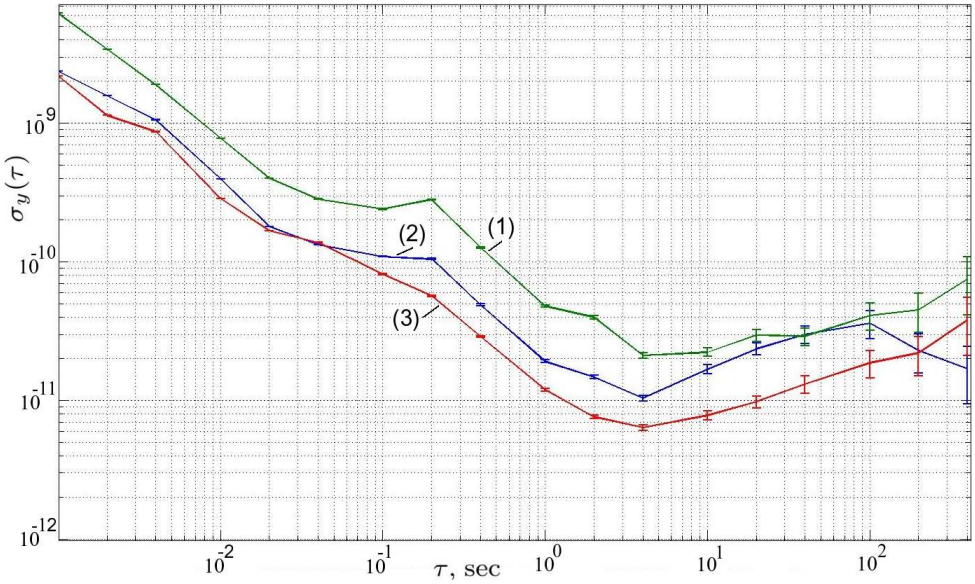

Figure 7.20: Allan deviation of the oscillator (copper holder) working at different modes: (1) - 5.039109 MHz (ref. X1_A4), (2) - 8.535124 MHz (ref. X1_A5), (3) - 11.853208 MHz (ref. X1_A6)

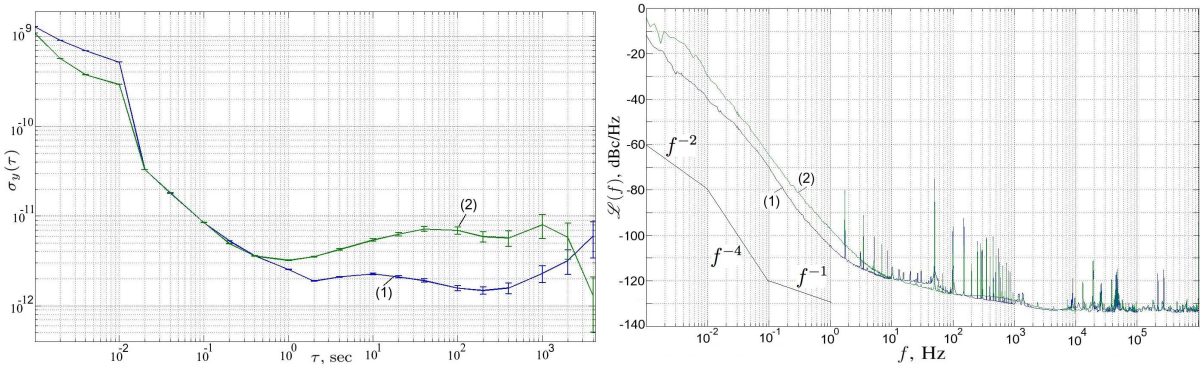

(a) Allan deviation

(b) Phase noise PSD

Figure 7.21: MOSFET-based liquid helium oscillator stability measurement results: improved ref. X1_A7 8.4430359 MHz and ref. X3_A8 8.443156 MHz

in 2.3 (see Fig. 2.10). The cryogenic oscillators have higher quality factors than their room-temperature counterparts ant, thus, they may exhibit this effect. This is the case of this optimized MOSFET oscillator. Here, the standard Leeson frequency is hidden by f^{-4} slope of the overlapping noise. But $f_L(1-\nu)$ can be estimated to be $2\cdot10^{-2}-3\cdot10^{-2}$ that is much smaller than possible f_L.

Further possible parametrical improvements and modifications did not lead to any considerable frequency stability improvement. Also, an attempt of structural improvement was made. The idea is to separate transistors and resonator in the space. To do so, the

transistors were moved from the circuit board on the copper holder to a separate board attached directly to the copper block (see Fig. 7.17(a)). The phase noise measurement results for such a device are shown in Fig. 7.22. As it is seen from the phase nose PSD, the short-term phase noise is considerably increased in comparison with previous systems. This phenomenon can be attributed to longer signal paths inside the whole circuit.

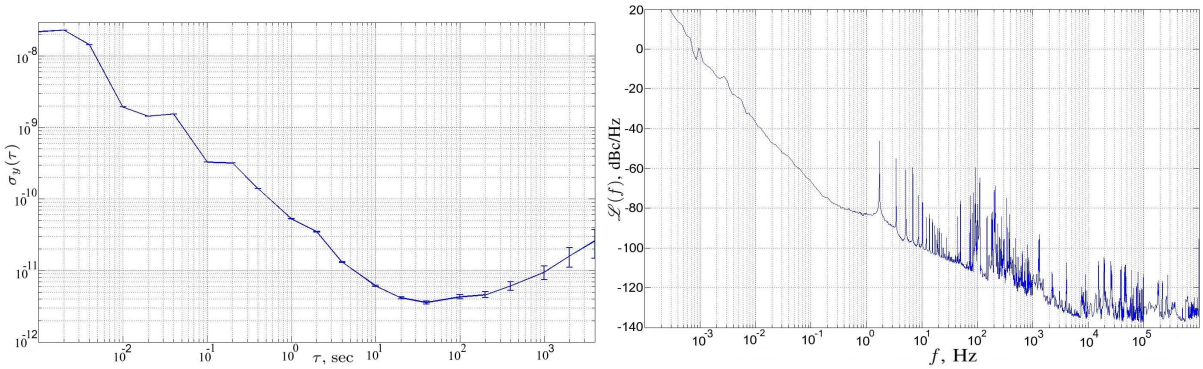

(a) Allan deviation (b) Phase noise PSD

Figure 7.22: Stability measurement results for a MOSFET-based liquid helium oscillator with modified component arrangement: improved ref. X1_A9 8.4430359 MHz

Concluding the present subsection, it could be stated that obviously the oscillator development has met the noise floor for the oscillator. This noise floor is estimated in section 6.5.7. So, the following improvement of the oscillator stability for present day resonators and environmental conditions seems unfeasible.

7.3.2 HBT-Based Solution

The present subsection presents some results and experience of utilization of SiGe heterojunction transistors as active devices for cryogenic crystal oscillators. A staring point of these investigations is an oscillator circuit shown in Fig. 7.23. This is a fully cryogenic Colpitts oscillator based on one HBT. Another transistor (MOSFET) is used only in a buffer stage used to decrease the influence of a long connecting cable on an oscillating loop. The circuit is designed to maximize the loaded quality factor. For the practical implementation, the copper holder with one board solution are used. Also, only q024a 5 MHz resonators from BVA Industries are used. Table 7.2 presents different parameters and conditions of HBT oscillator configurations.

The experiments with the first oscillator configuration (Y1_A1) show that the resonator in this circuit could be excited only on its 3rd overtone of the B mode (5.489793 MHz). The frequency stability results of the implemented oscillator are shown in Fig. 7.24 where Fig. 7.24(a) shows the phase noise spectrum and Fig. 7.24(b) presents the time domain fluctuations of the oscillating frequency. As it is clearly seen from both time and frequency domains, frequency of the oscillation signal exhibit periodic changes. This is a result of a

Table 7.2: Working parameters and conditions of HBT-based oscillators

Reference	Regulated Temperature	Holder	V_C, V	V_B, V
Y1_A1	4.3K	copper	14	14
Y2_A2	3.9K	copper	8	2.3
Y3_A3	3.9K	copper	3.8	7
Y3_A4	3.9K	copper	7.6	5.4

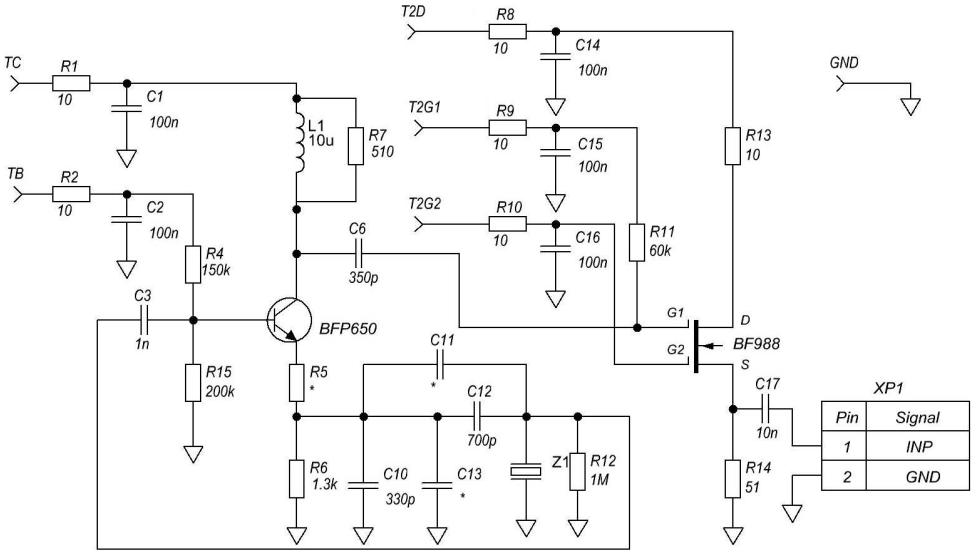

Figure 7.23: Schematic diagram of a cryogenic crystal oscillator based on a SiGe HBT

high dissipation power and the consequent amplitude-temperature fluctuations discussed in subsection 6.5.5.

In order to reduce the dissipated power of the cryogenic crystal resonator, two schematic modifications are introduced. Firstly, the resistance R6 is split into two, so that $R_{R6} =$ 1 kOm, $R_{R5} = 300$ Om. Secondly, the capacitance C12 is decreased down to 500 pF. This circuit configuration (Y2_A2, see Table 7.2) oscillates at 4.992984 MHz, i.e. the 3rd overtone of the C mode of the resonator. The measured Allan deviation and the phase noise spectral density are shown in Fig. 7.25, curves (1).

Next schematic modification is further decrease of the capacitance C12. For next two configurations (Y3_A3 and Y3_A5) this value is 300 pF. The details of these experiments are shown in Table 7.2. The oscillation frequencies are 4.992985 MHz. The corresponding frequency stability results are presented in Fig. 7.25, curves (2) and (3) correspondingly.

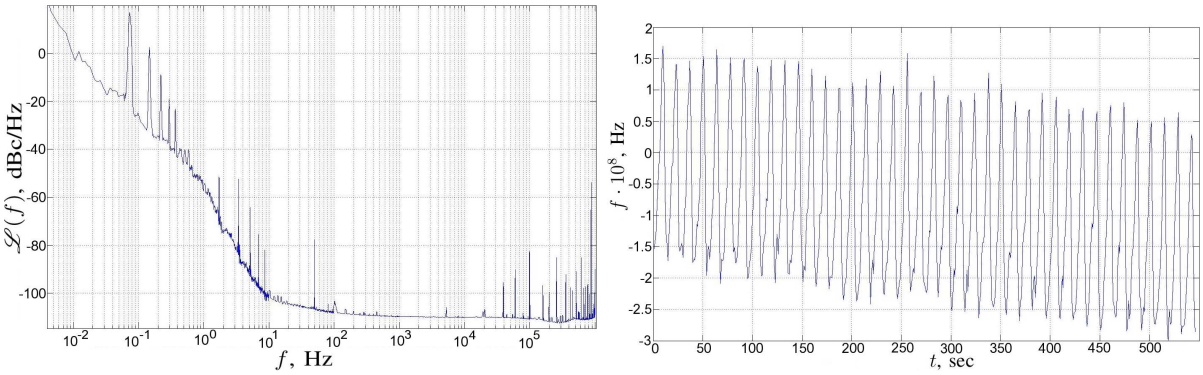

(a) Phase noise PSD (b) Time domain frequency fluctuations

Figure 7.24: Stability measurement results for the HBT-based liquid helium oscillator (Y1_A1) working at 5.489793 MHz

It is clearly seen from Fig. 7.25(b) that the white phase noise is lower in the case of a stronger oscillating signal (curve (3)) because of a better signal-to-noise ration. In the same time, close-to-carrier instabilities are higher in such cases. Indeed, curve (2) is measured for the weakest signal. The same pattern is usually observed for room temperature oscillators.

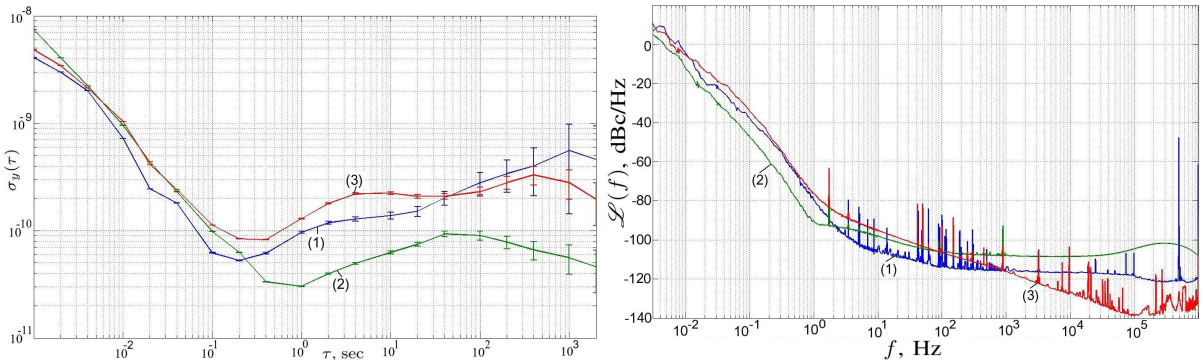

(a) Allan deviation (b) Phase noise PSD

Figure 7.25: HBT-based liquid helium oscillator stability measurement results: ref. Y2_A2, curves (1), ref. Y3_A3, curves (2), ref. Y3_A5, curves (3)

Unfortunately, the tested oscillator are excited only on the 3rd overtone of the B mode and the 3rd overtone of the C mode of their resonators. This fact determines that their frequency stability results are inferior to that of the MOSFET-based cryogenic oscillators.

The oscillator development for liquid-helium temperatures is a very time consuming task. Despite the rigorous models of electronic components (Chapters 4 and 5) and sophisticated analysis methods (sections 7.1 and 7.2), the actual behavior of cryogenic oscillators leaves many unpredictable phenomena. Nevertheless, it seems that for excited modes, the

practical frequency stability limits are achieved for the MOSFET-based oscillator (about $2 \cdot 10^{-12}$ between 1 and 1000 seconds). Though the extraordinary frequency stability have not been achieved yet (as it is predicted in section 6.5.7), the present work is a gradual step further towards hyper stable cryogenic BAW oscillators.

Conclusions et perspectives

Conclusions

The present work is a systematic research in the area of cryogenic BAW frequency sources. The work starts with general background in the field of the frequency control in general and BAW resonators in particular. The second chapter gives some theoretical investigations in the field of the resonator phase noise. The accurate model of the BAW resonator phase noise is proposed based on the averaging technique. This model relates the resonator parameter fluctuations and the output phase and amplitude noise. It is able to predict all types of phase noise spectra. Also, an influence of the devices nonlinearity is considered predicting some different possibility of both degradation and improvement of the resonator phase noise filtering properties. Additionally, the derived resonator MIMO model in the amplitude-phase space is used to investigates possible types of the oscillator PSD by generalizing the Leeson effect. The different type of spectra is predicted for high quality oscillators.

The second chapter of the thesis concerns the cryogenic test bench. In this part, two main sources of environmental instabilities are measured, characterized and analyzed. It is shown that temperature fluctuations could be a source of the white noise or the random walk. And the cryogenerator vibration is able to produce instabilities with a f^{-1} spectrum slope for low Fourier frequencies.

The third chapter of the work sheds the light on the different aspects of the BAW resonator operation at liquid helium temperatures. The main conclusions of these investigations are:

1. quality factors of quartz resonators at liquid helium temperatures increase considerably for all tested modes and overtones, the highest increase is achieved for the A-mode;
2. resonators at liquid helium temperatures operate at the Landau-Rumer regime that implies independence of Q from the frequency;
3. for the temperatures below 5K the further increase in Q is limited by device losses, but not that of the material;

4. active equivalent resistance of quartz resonators at such temperature is very low;

5. temperature-frequency characteristics of the tested modes and overtones do not have any turn-over point, the temperature sensitivity of the frequency decreases with temperature;

6. quartz resonators are subjects of considerable nonlinear effects at low temperatures which depend not only on dissipated active power but also on the Q;

7. higher overtones (such as 11th and 13th) have even higher values of Q and $Q \cdot f$ (here records for BAW devices are achieved), higher active resistances, but many close anharmonics;

8. though LD-cut resonators exhibit smaller Q, they also have higher active resistances and their amplitude-frequency effect is less pronounced.

9. present-day LGS resonators do not exhibit any increase in the quality factor between room and liquid helium temperatures;

10. though LGT resonators have higher Q values and obtain a turn-over point at liquid helium temperatures, this increase cannot justify application of cryogenic systems;

Although points 1, 2 and 7 are really fascinating and promising, points 4, 5 and 6 pose serious problems for the practical utilization of quartz devices in hyper-stable frequency sources. Indeed, without a turn-over point it is impossible to achieve a sufficient temperature stability of a frequency source system. And, considerable nonlinear effects suggest to work with lower signal levels which worsen a signal-to-noise ration. These problems are aggravated by the instabilities of the cryogenic environment.

The forth chapter presents investigation results in the area of the liquid helium electronics which is a very underinvestigated field of knowledge. The chapter presents the choice of passive and active devices. The rigorous measurement and modeling approaches are proposed. Three main types of transistors are compared. And though SiGe HBTs are an excellent choice for future applications, nowadays MOSFETs are better choice due to their robustness for current projects.

In the fifth chapter, a closed loop frequency reference based on the cryogenic quartz resonator is analyzed, simulated and implemented. The accurate model and efficient optimization procedure of the system are proposed. It is concluded that the long term frequency stability of this system depends on the feedback resonator random-walk fluctuations, and it is inverse proportional to its loaded quality factor. Actual realization of this system shows considerable problems related to the points 4, 5 and 6 of the conclusion to the chapter three. Though SC-cut resonators have higher quality factors, better frequency stability is achieved for LD-cut devices ($4 \cdot 10^{-13}$ at 100 seconds, and better than 10^{-12} between 1 and 2000 seconds). Additionally, the chapter describes an approach for the phase noise measurement of cryogenic quartz resonators. The measured noise

is higher than that in the room temperature. It is concluded that the resonator flicker noise is a consequence of its vibration and the possible white noise is due to temperature instabilities.

The last chapter of the work deals with the full cryogenic quartz oscillators. First of all, the effective modeling and optimization procedure is proposed. It is inspired by the inability of the modern simulation tools to work with the extremely high quality resonators. In addition, the resonator phase noise simulation method is proposed for commercial design tools. Finally, some oscillators are designed based on MOSFET and HBT devices. The frequency stability of the MOSFET-based oscillator reaches the limit of $2 \cdot 10^{-12}$ between 1 and 1000 seconds. The unusual type of the PSD theoretically predicted in the second Chapter is measured.

Generally speaking, BAW devices based on present day technology can be hardly utilized for hyper-stable frequency sources due to the serious problems. These problems are mainly due to their high temperature sensitivity and limiting nonlinear effects.

Perspectives

Though the future development of frequency sources based on cryogenic quartz resonators is associated with serious problems, some ways of the further development could be proposed:

- *device structure optimization* can further increase resonator quality factor down to the limits of the material losses;
- *investigation at milikelvin temperatures* may be useful to find a minimum of the frequency-temperature sensitivity;
- *design of a new optimized crystal cut* may provide a turn-over point in the temperature-frequency characteristic at the liquid helium temperatures;
- *optimization of LD-cut resonators* is a probable solution to the problem of high nonlinear effects, since this is a special cut designed for this purpose at room temperatures;
- *DUT environment improvements* (active and passive temperature stabilization systems as well as active vibration compensation) are needed to ensure better results;
- *further investigations in cryogenic SiGe HBTs* (probably, another package or on-wafer devices) may help to find more reliable device of this kind.

These solutions may play a key role in the future development of cryogenic BAW frequency sources.

Apart from the considered application in frequency sources, the results of the present work may be useful in many related fields of science. For example, the investigated resonators and materials with very low mechanical losses could find potential applications in the development of gravitational wave interferometers [7, 129], mechanical quantum resonators [130, 131], etc. These devices could also be used as vibration or temperature sensors for other types of cryogenic frequency sources, for example, sapphire cryogenic oscillators [132]. In addition, the obtained results in the area of liquid helium electronics could be used in its arising and future applications [76, 87].

Appendix A: Linear MIMO Model of a BAW Resonator in the Amplitude-Phase Space

A linear MIMO model of a BAW resonator in the magnitude-phase space derives from system (2.22) that relates averaged over a period an output signal amplitude ($M(t)$) and a phase ($\Phi(t)$) with an input signal amplitude ($u_a(t)$) and a phase ($\Phi(t)$) and resonator fluctuating parameters ($\delta(t)$, $\Omega(t)$ and $K(t)$). Neglecting small terms the system is linearized by representing each of these variables with constant ($\overline{M}$, $\overline{\Phi}$, etc) and small variable parts ($\widetilde{M}$, $\widetilde{\Phi}$, etc). So, the BAW resonator may be described in the form of matrix equation:

$$\mathbf{Y} = \mathbf{H}_i\mathbf{X}_i + \mathbf{H}_r\mathbf{X}_r, \tag{1}$$

where

$$\mathbf{Y} = \begin{pmatrix} \widetilde{M} \\ \widetilde{\Phi} \end{pmatrix}, \mathbf{X}_i = \begin{pmatrix} \widetilde{u}_a \\ \widetilde{\theta} \end{pmatrix}, \mathbf{X}_r = \begin{pmatrix} \widetilde{\delta} \\ \widetilde{\Omega} \\ \widetilde{k} \end{pmatrix}, \tag{2}$$

$$\mathbf{H}_i = \begin{pmatrix} \dfrac{\overline{k}\sin\overline{\Phi}}{\overline{\Omega}}\dfrac{\overline{\delta}s+\overline{\delta}^2+\overline{\Omega}^2}{s^2+2\overline{\delta}s+\overline{\delta}^2+\overline{\Omega}^2} & \overline{k}\overline{u}_a\sin\overline{\Phi}\dfrac{s}{s^2+2\overline{\delta}s+\overline{\delta}^2+\overline{\Omega}^2} \\ -\dfrac{\overline{\Omega}}{\overline{u}_a}\dfrac{s}{s^2+2\overline{\delta}s+\overline{\delta}^2+\overline{\Omega}^2} & \dfrac{\overline{\delta}s+\overline{\delta}^2+\overline{\Omega}^2}{s^2+2\overline{\delta}s+\overline{\delta}^2+\overline{\Omega}^2} \end{pmatrix}, \tag{3}$$

$$\mathbf{H}_r = \begin{pmatrix} -\dfrac{\overline{k}\overline{u}_a\sin\overline{\Phi}}{\overline{\Omega}}\dfrac{s+\overline{\delta}}{s^2+2\overline{\delta}s+\overline{\delta}^2+\overline{\Omega}^2} & \dfrac{-\overline{k}\overline{u}_a\sin\overline{\Phi}}{s^2+2\overline{\delta}s+\overline{\delta}^2+\overline{\Omega}^2} & \dfrac{\overline{u}_a\sin\overline{\Phi}}{\overline{\Omega}}\dfrac{\overline{\delta}s+\overline{\delta}^2+\overline{\Omega}^2}{s^2+2\overline{\delta}s+\overline{\delta}^2+\overline{\Omega}^2} \\ \dfrac{-\overline{\Omega}}{s^2+2\overline{\delta}s+\overline{\delta}^2+\overline{\Omega}^2} & \dfrac{s+\overline{\delta}}{s^2+2\overline{\delta}s+\overline{\delta}^2+\overline{\Omega}^2} & -\dfrac{\overline{\Omega}}{\overline{k}}\dfrac{s}{s^2+2\overline{\delta}s+\overline{\delta}^2+\overline{\Omega}^2} \end{pmatrix}, \tag{4}$$

So, equation (1) models response of the amplitude and the phase of the output signal ($\widetilde{M}$ and $\widetilde{\Phi}$, respectively) to small variations of the amplitude and the phase of the input signal ($\widetilde{u}_a$ and $\widetilde{\theta}$, respectively) as well as fluctuation of the device parameters ($\widetilde{\delta}$, $\widetilde{\Omega}$, $\widetilde{k}$). So, $\mathbf{X}_r$ is a vector of resonator own parameter fluctuations, and $\mathbf{X}_i$ is a vector of input signal amplitude and phase instabilities.

In addition the following relations for the model parameters are relevant:

$$\begin{cases} \overline{\delta M} = \overline{k}\overline{u}_a \cos\overline{\Phi} \\ \overline{\Omega M} = \overline{k}\overline{u}_a \sin\overline{\Phi} \end{cases} \tag{5}$$

If a nonlinear resonator is considered, formula (1) is relevant. But transfer matrix have to be redefined:

$$\mathbf{H}_i = \begin{pmatrix} \dfrac{\overline{k}\sin\overline{\Phi}}{\overline{\Omega}'} \dfrac{\overline{\delta}'s + \overline{\delta}'^2 + \overline{\Omega}'^2}{s^2 + (\overline{\delta}' + \overline{\delta}'')s + \overline{\delta}'\overline{\delta}'' + \overline{\Omega}'\overline{\Omega}''} & \overline{k}\overline{u}_a \sin\overline{\Phi} \dfrac{s}{s^2 + (\overline{\delta}' + \overline{\delta}'')s + \overline{\delta}'\overline{\delta}'' + \overline{\Omega}'\overline{\Omega}''} \\ -\dfrac{1}{\overline{u}_a} \dfrac{s\overline{\Omega}' + \overline{\Omega}'\overline{\delta}'' - \overline{\Omega}''\overline{\delta}'}{s^2 + (\overline{\delta}' + \overline{\delta}'')s + \overline{\delta}'\overline{\delta}'' + \overline{\Omega}'\overline{\Omega}''} & \dfrac{\overline{\delta}'s + \overline{\delta}'\overline{\delta}'' + \overline{\Omega}'\overline{\Omega}''}{s^2 + (\overline{\delta}' + \overline{\delta}'')s + \overline{\delta}'\overline{\delta}'' + \overline{\Omega}'\overline{\Omega}''} \end{pmatrix}, \tag{6}$$

$$\mathbf{H}_r = \begin{pmatrix} -\dfrac{\overline{k}\overline{u}_a \sin\overline{\Phi}}{\overline{\Omega}'} \dfrac{s + \overline{\delta}'}{B(s)} & \dfrac{-\overline{k}\overline{u}_a \sin\overline{\Phi}}{B(s)} & \dfrac{\overline{u}_a \sin\overline{\Phi}}{\overline{\Omega}'} \dfrac{\overline{\delta}'s + \overline{\delta}'^2 + \overline{\Omega}'^2}{B(s)} \\ \dfrac{-\overline{\Omega}''}{B(s)} & \dfrac{s + \overline{\delta}''}{B(s)} & -\dfrac{1}{\overline{k}} \dfrac{\overline{\Omega}'s + \overline{\Omega}'\overline{\delta}'' - \overline{\Omega}''\overline{\delta}'}{B(s)} \end{pmatrix}, \tag{7}$$

where $B(s) = s^2 + (\overline{\delta}' + \overline{\delta}'')s + \overline{\delta}'\overline{\delta}'' + \overline{\Omega}'\overline{\Omega}''$ and

$$\overline{\delta}' = \overline{\delta} + \lambda_1 \overline{M}^2, \quad \overline{\delta}'' = \overline{\delta} + 3\lambda_1 \overline{M}^2, \quad \overline{\Omega}' = \overline{\Omega} + \lambda_2 \overline{M}^2, \quad \overline{\Omega}'' = \overline{\Omega} + 3\lambda_2 \overline{M}^2. \tag{8}$$

For definitions of λ_1 and λ_2, please, see section 2.2. Also, in the nonlinear case, relations (5) have to be replaced by

$$\begin{cases} \overline{\delta}'\overline{M} = \overline{k}\overline{u}_a \cos\overline{\Phi}, \\ \overline{\Omega}'\overline{M} = \overline{k}\overline{u}_a \sin\overline{\Phi}, \end{cases} \tag{9}$$

Appendix B: Accelerometer Orientations and Measurement Results

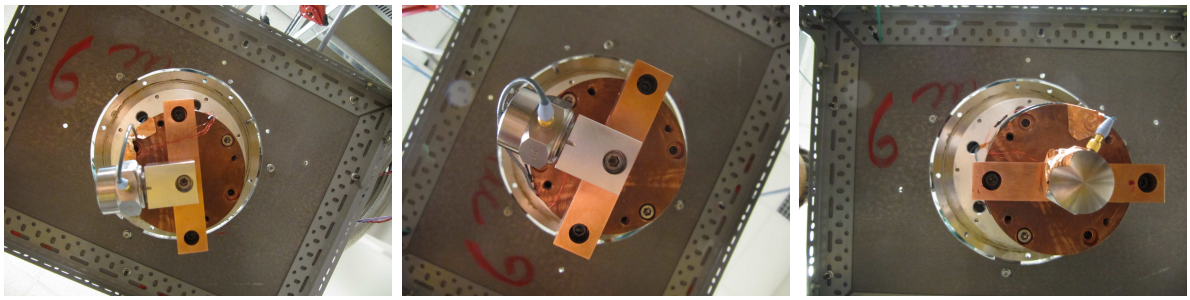

(a) First horizontal axis (b) Second horizontal axis (c) Vertical axis

Figure 1: Three variants of accelerometer orientation (bottom view)

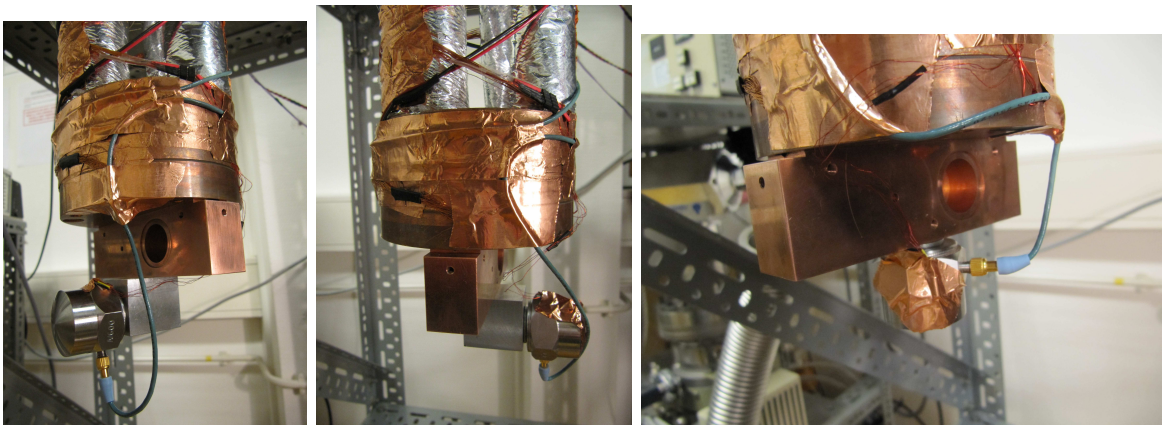

(a) First horizontal axis (b) Second horizontal axis (c) Vertical axis

Figure 2: Three variants of accelerometer orientation (side view)

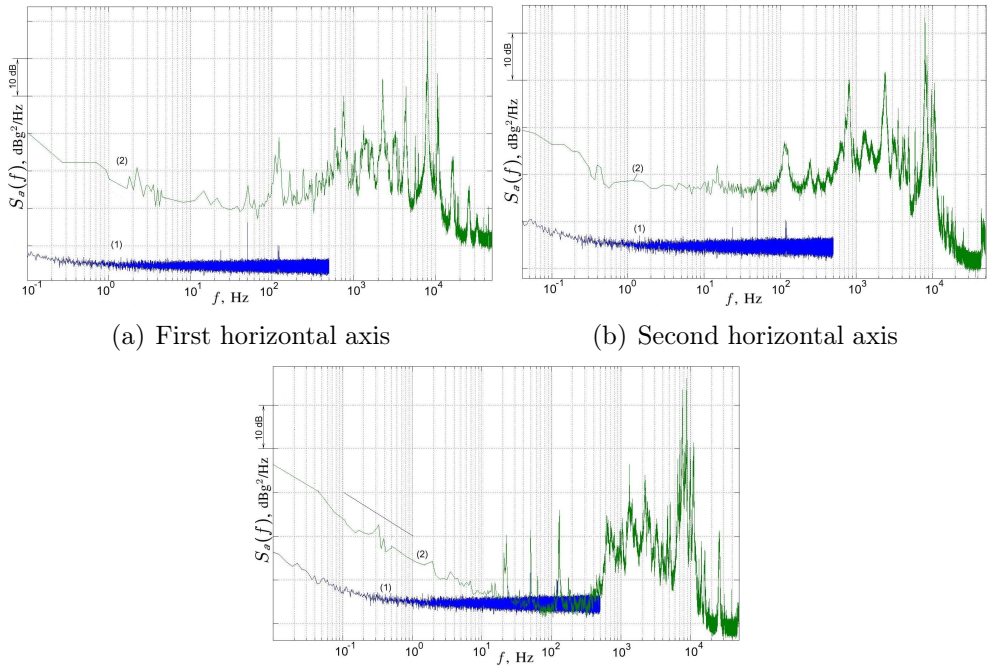

(a) First horizontal axis

(b) Second horizontal axis

(c) Vertical axis

Figure 3: Measured PSDs: measurement noise floor (1), second stage acceleration (2)

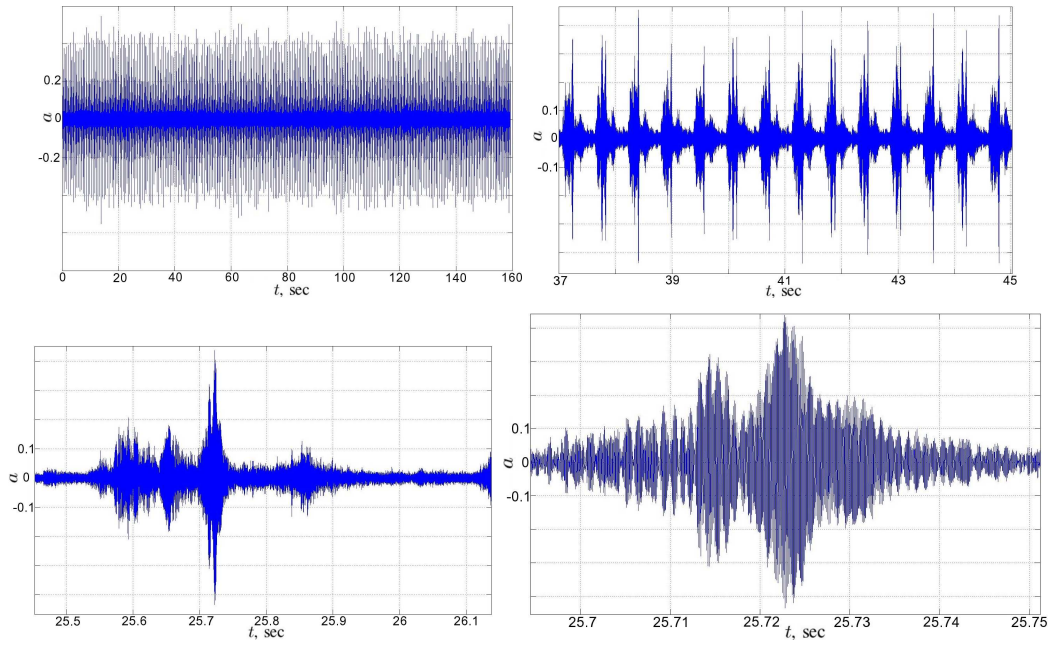

Figure 4: Second stage vibration waveforms in vertical orientation

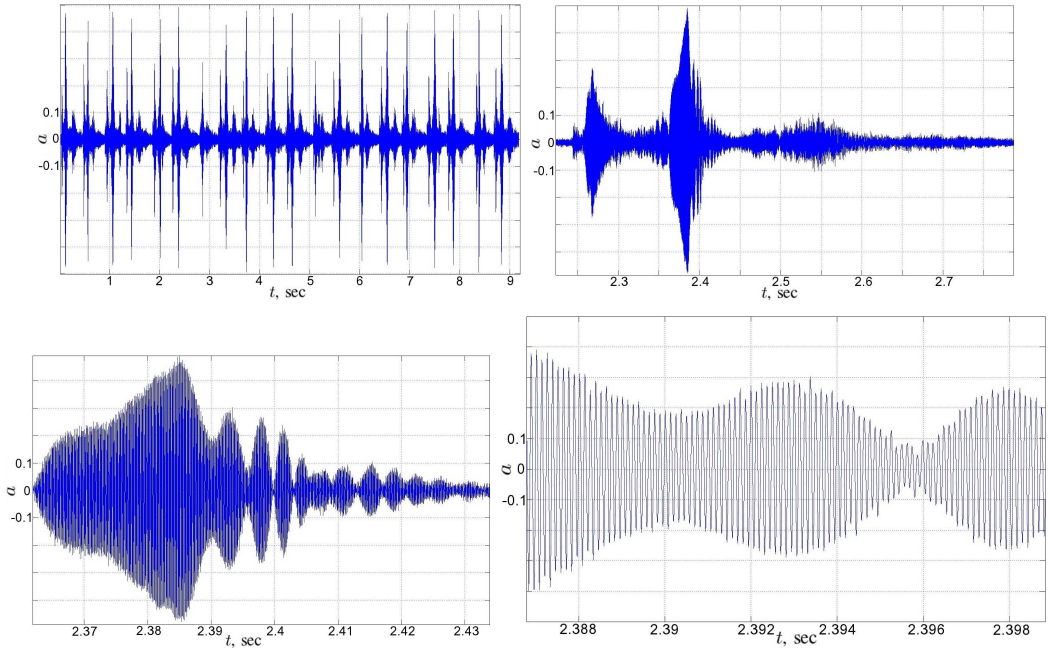

Figure 5: Second stage vibration waveforms along the first horizontal axis

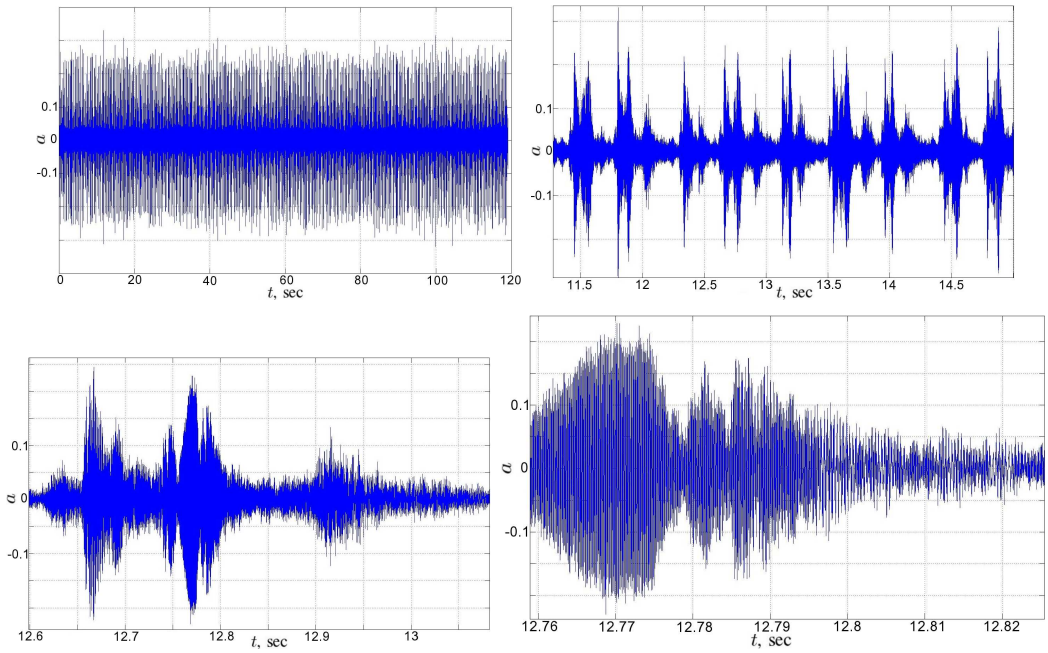

Figure 6: Second stage vibration waveforms along the second horizontal axis

Appendix C: Resistances at Cryogenic Temperatures

Table 1: YAGEO (PHYCOMP) - RC0805JR-SKE24L (SMD Resistors 0805, 1%, 150 V, 100 ppm/C, power dissipation 0.125 W) - Part 1

T_B, K	295	3.8	4.0	4.2
R, Ohm	10	12.4	12.4	12.3
R, Ohm	103.5	110.9	110.7	110.1
R, Ohm	204.5	221.0	220.8	219.7

Table 2: YAGEO (PHYCOMP) - RC0805JR-SKE24L (SMD Resistors 0805, 1%, 150 V, 100 ppm/C, power dissipation 0.125 W) - Part 2

T_B, K	295	3.6	3.8	4.0	4.2	5.0
R, kOhm	56 (nom)	123.3	120.4	117.7	115.3	107.3
R, kOhm	100 (nom)	263.7	255.5	248.5	242.1	221.0
R, kOhm	130 (nom)	290.4	283.0	276.8	271.1	251.8
R, kOhm	160 (nom)	385.6	375.0	366.2	357.8	329.4
R, kOhm	200 (nom)	486.0	472.0	460.5	450.0	414.12
R, kOhm	240 (nom)	600.0	582.0	568.0	554.0	508.2

Table 3: Temperature sensitivity of the SMD resistors measured between 4.24K and 4.16K

$R(nom)$, KOhm	56	100	130	160	200	240
$\frac{\Delta R}{\Delta K}$, kOhm/K	10.25	27.25	24.50	33.13	40.25	47.13
Sensitivity, mK^{-1}	$2.3 \cdot 10^{-5}$	$3 \cdot 10^{-5}$	$2.39 \cdot 10^{-5}$	$2.5 \cdot 10^{-5}$	$2.5 \cdot 10^{-5}$	$2.4 \cdot 10^{-5}$

Table 4: Basic Kit LMA-24-SBR02 (Metal Film Resistors MINI-MELF 0204-50, 1%, 50 ppm/K, rated power dissipation 0.25 W)

T_B, K	295	3.2	3.6	4.0	4.2	5
R, Ohm	1.6 (nom)	1.6	1.6	1.6	1.6	1.6
R, Ohm	10 (nom)	10.6	10.6	10.6	10.6	10.6
R, Ohm	100 (nom)	99.9	99.9	99.9	99.9	99.9
R, kOhm	1 (nom)	0.999	0.999	0.999	0.999	0.998
R, kOhm	100 (nom)	101.4	101.3	101.3	101.3	101.2
R, kOhm	510 (nom)	529.8	528.9	527.8	527.4	525.8

Bibliography

[1] E. Rubiola, *Phase noise and frequency stability in oscillators.* New York: Cambridge University Press, November 2009.

[2] ——, *The Leeson effect: phase noise in quasilinear oscillators.* Université Henri Poincaré, 2005.

[3] F. Sthal, S. Galliou, J. Imbaud, X. Vacheret, P. Salzenstein, E. Rubiola, and G. Cibiel, "About quartz crystal resonator noise: recent study," in *Proc. 20th International Conference on Noise and Fluctuations*, Pisa, Italy, June 2007, pp. 607–610.

[4] G. Robichon, J. Groslambert, and J. Gagnepain, "Frequency stability of quartz crystal at very low temperatures: preliminary results," in *Proc. 38nd Ann. Symp. on Freq. Cont.*, 1984, pp. 201–205.

[5] J. Vig and etc, "Panel discussion: To what extent will quartz be squeezed out by MEMS and CSAC session," in *Proc EFTF & IEEE IFCS Joint Meeting*, San Francisco, USA, May 2011.

[6] J. Vig, "Introduction to quartz frequency standards," IEEE UFFC Teaching Resources, October 1992.

[7] O. Aguiar, "Past, present and future of the resonant-mass gravitational wave detectors," *Research in Astronomy and Astrophysics*, vol. 11, no. 1, pp. 10.1088/1674–4527/11/1/001, 2011.

[8] S. Galliou, J. Imbaud, R. Bourquin, N. Bazin, and P. Abbé, "Outstanding quality factors of bulk acoustic wave resonators at cryogenic temperature," in *European Frequency and Time Forum*, 2008.

[9] ——, "Quartz crystal resonators exhibiting extremely high Q-factors at cryogenic temperatures," *Electronics Letters*, vol. 44, no. 14, pp. 889–890, 2008.

[10] J. Imbaud, "Evaluation des potentialités des matériaux du type langasite pour la réalisation d′oscillateurs ultra-stables. Etude et réalisation préliminaires d′un oscillateur cryogénique." Ph.D. dissertation, University of Franche Comté, Besancon, France, November 2008.

[11] Y. Shmaliy, *Continuous-time systems*. Dordrecht, The Netherlands: Springer, 2007.

[12] D. Popovici, F. Constantinescu, M. Maricaru, F. Hantila, M. Nitescu, and A. Gheorghe, *Modeling and simulation*. InTech, June 2008, ch. Modeling and simulation of piezoelectric devices.

[13] J. Vig and T. Meeker, "The aging of bulk acoustic wave resonators, filters, and oscillators," in *Proc. 45th Ann. Symp. Freq. Cont.*, vol. IEEE Cat. No. 91 CH2965-2, 1991, pp. 77–101.

[14] J. J. Gagnepain, M. Olivier, and F. L. Walls, "Excess noise in quartz crystal resonators," in *Annual Symposium on Frequency Control*, 1983, pp. 218–225.

[15] F. Walls and J. Vig, "Fundamental limits on the frequency stabilities of quartz crystal oscillators," *IEEE Transactions on Ultrasonics, Ferroelectrics, and Frequency Control*, vol. 42, pp. 576–589, July 1995.

[16] J. Vig, "Quartz crystal resonators and oscillators for frequency control and timing applications," Tutorial, January 2007.

[17] A. Ballato and J. Vig, "Static and dynamic frequency-temperature behavior of singly and doubly rotated, oven-controlled quartz resonators," in *Proc. 32nd Ann. Symp. on Freq. Cont.*, 1978, pp. 181–188.

[18] J. Kusters and J. Vig, "Thermal hysteresis in quartz resonators - a review," in *Proc. 44th Ann. Symp. Freq. Cont.*, vol. IEEE Catalog No. 90CH2818-3, 1990, pp. 165–175.

[19] R. Filler, "The acceleration sensitivity of quartz crystal oscillators: a review," *IEEE Transactions on Ultrasonics, Ferroelectrics and Frequency Control*, vol. 35, no. 3, May 1988.

[20] R. Filler, J. Kosinski, V. Rosati, and J. Vig, "Aging studies on quartz crystal resonators and oscillators," in *Proc. 38th Ann. Symp. on Freq. Cont.*, 1984, pp. 225–231.

[21] J. Rutman and F. L. Walls, "Characterization of frequency stability in precision frequency sources," *Proc. IEEE*, vol. 79, no. 7, pp. 952–960, 1991.

[22] J. Vig, "IEEE standard definitions of physical quantities for fundamental frequency and time metrology - random instabilities," IEEE Standards 1139-1999, 1999.

[23] M. Goryachev and S. Galliou, "Parametric model of the BAW resonator phase noise," *Ultrasonics*, vol. 51, no. 8, pp. 966–973, December 2011.

[24] S. Galliou, F. Sthal, X. Vacheret, R. Brendel, P. Salzenstein, E. Rubiola, and G. Cibiel, "A program to analyze the origin of noise in ultra-stable quartz crystal resonators," in *Proc. EFTF & IEEE IFCS Joint Meeting*, Geneva, Switzerland, 2007, pp. 1176–1181.

[25] F. Sthal, M. Mourey, F. Marionnet, and W. Walls, "Phase noise measurements of 10 MHz BVA quartz crystal resonator," *IEEE Transactions on Ultrasonics, Ferroelectrics and Frequency Control*, vol. 47, pp. 369–373, 2000.

[26] E. Rubiola, J. Groslambert, M. Brunet, and V. Giordano, "Flicker noise measurement of HF quartz resonators," *IEEE Transactions on Ultrasonics, Ferroelectrics and Frequency Control*, vol. 47, no. 2, pp. 361–368, March 2000.

[27] Y. Shmaliy, "Conversion of 1/f fluctuations in crystal resonator within an inter resonance gap," *IEEE Transactions on Ultrasonics, Ferroelectrics and Frequency Control*, vol. 46, no. 1, pp. 61–71, 1999.

[28] ——, "The noise conversion method for oscillatory systems," *IEEE Transactions on Ultrasonics, Ferroelectrics and Frequency Control*, vol. 51, no. 8, pp. 948–956, 2004.

[29] F. Sthal, S. Galliou, P. Abbe, N. Franquet, X. Vacheret, P. Salzenstein, E. Rubiola, and G. Cibiel, "Thermal characterization of crystal ovens used in phase noise measurement system," in *Proc. IEEE IFCS*, Miami, Florida, June 2006, pp. 736–739.

[30] R. Ward, "The constants of alpha quartz," in *Proc. 16th Piezoelectric Devices Conference and Exhibition*, 1992.

[31] A. Chulichkov, *Mathematical models of nonlinear dynamics*, 2nd ed. Moscow, Russia: FIZMATLIT, 2003.

[32] N. Krylov and N. Bogolyubov, *Introduction to non-linear mechanics.* Princeton: Princeton Univercity Press, 1947.

[33] A. Nayfeh and D. Mook, *Nonlinear oscillations.* USA: John Wiley&Sons, 1995.

[34] E. Rubiola and R. Brendel, "The generalization of the Leeson effect," April 2010, http://rubiola.org.

[35] W. Mason, *Piezoelectric crystals and their application to ultrasonics.* New York: D.Van Nostrand Company Inc., 1950.

[36] J. Zelenka, *Piezoelectric resonators and their applications.* New York, Amsterdam: Elsevier, 1986.

[37] M. Redwood, "Transient performance of a piezoelectric transducer," *J. Acoust. Soc. of Amer.*, vol. 33, no. 4, pp. 527–536, April 1961.

[38] R. Krimholtz, D. Leedom, and G. Matthaei, "New equivalent circuits for elementary piezoelectric transducers," *Electronics Letters*, vol. 6, no. 13, pp. 398–399, June 1970.

[39] C. Collado, E. Rocas, J. Mateu, A. Padilla, and J. O'Callaghan, "Nonlinear distributed model for bulk acoustic wave resonators," *IEEE Trans. on Microwave Theory and Techn.*, vol. 57, no. 12, pp. 3019–3029, December 2009.

[40] E. Rocas, C. Collado, J. Booth, E. Iborra, and R. Aigner, "Unified model for bulk acoustic wave resonators' nonlinear effects," in *IEEE International Ultrasonics Symposium*, Italy, Rome, 2009, pp. 880–884.

[41] *F-70H and F-70L helium compressors*, Sumitomo Heavy Industries Ltd., Allentown, USA, 2006.

[42] *4K pulse tube cryocooler RP-082A*, Sumitomo Heavy Industries Ltd., Tokyo, Japan, 2007.

[43] *SRP-082A cyocooler*, Sumitomo Heavy Industries Ltd., Tokyo, Japan, 2007.

[44] T. Flynn, *Cryogenic engineering*, 2nd ed. Marcel Dekker, 2005.

[45] *Model 332 temperature controller*, 1st ed., Lake Shore Cryotonics Inc., Westerville, USA, 2005.

[46] *ADwin Product Overview*, Jäger Computergesteuerte Messtechnik GmbH, Lorsch, Germany, 2010.

[47] A. Warner, "Ultra-precise quartz crystal frequency standards," *IRE Transactions on Instrumentation*, 1958.

[48] N. Smagin, "Quartz crystal resonators with quality factors of about $120 \cdot 10^6$ at 2K," *Izmeritel Tekh. SSSR*, vol. 9, 1960.

[49] J. Gagnepain, "Non linear mechanisms in quartz crystal resonators," Ph.D. dissertation, University of Franche Comté, Besancon, France, March 1972.

[50] G. Mossuz, "Study and achievement of a quartz crystal oscillator at very low temperature," Ph.D. dissertation, University of Franche Comté, Besancon, France, July 1975.

[51] A. E. Habti, "Study of resonators and oscillators at very low temperatures," Ph.D. dissertation, University of Franche Comté, Besancon, France, January 1993.

[52] P. Southgate, "Internal friction in germanium and silicon I: electron and impurity relaxation," *Proceedings of the Physical Society*, vol. 76, no. 3, pp. 385–397, 1960.

[53] W. Mason, *Effect of impurities and phonon process on the ultrasonic attenuation of germanium crystal quartz and silicon*, ser. Physical Acoustics. New York: Academic Press, 1965, vol. 3.

[54] D. Fraser, *Impurities and anelasticity in crystalline quartz*, ser. Physical Acoustics. Academic Press, 1968, vol. V.

[55] H. Maris, *Interactions of sound with thermal phonons in dielectric crystals*, ser. Physical Acoustics. Academic Press, 1968, vol. 5.

[56] H. Bömmel and K. Dransfeld, "Excitation and attenuation of hypersonic waves in quartz," *Physical Review*, vol. 117, no. 5, pp. 1245–1252, 1960.

[57] P. Klemens, *Effect of thermal and phonon processes on ultrasonic attenuation*, ser. Physical acoustics. New York: Academic Press, 1965, vol. 3.

[58] M. Planat and J. Gagnepain, "$1/f$ noise in quartz crystal resonator in relation with losses and frequency dispersion," *Applied Physics Letters*, vol. 50, no. 9, pp. 510–512, March 1987.

[59] J. Suter, "Acoustic loss phenomena in alpha quartz resonators over the 1.4-77K temperature range," *Journal of Applied Physics*, vol. 63, no. 11, pp. 5594–5595, June 1988.

[60] S. Galliou, J. Imbaud, M. Goryachev, R. Bourquin, and P. Abbé, "Losses in high quality quartz crystal resonators at cryogenic temperatures," *Applied Physics Letters*, vol. 98, no. 9, 2011.

[61] M. Goryachev, S. Galliou, J. Imbaud, R. Bourquin, and P. Abbé, "Recent investigations on BAW resonators at cryogenic temperatures," in *Proc EFTF & IEEE IFCS Joint Meeting*, San Francisco, USA, May 2011.

[62] A. E. Habti and F. Bastien, "Low temperature limitation on the quality factor of quartz resonators," *IEEE Transactions on Ultrasonics, Ferroelectrics and Frequency Control*, vol. 41, no. 2, pp. 250–255, 1994.

[63] M. Lewis and E.Patterson, "Microwave phonon-attenuation measurements in quartz," *Physical Review*, vol. 19, no. 3, pp. 703–711, 1967.

[64] A. Akheiser, "On the absorption of sound in solids," *Journal Physics USSR*, vol. 1, p. 277, 1939.

[65] L. Landau and G. Rumer, "Absorption of sound in solids," *Phys. Z. Sowjetunion*, vol. 11, no. 18, 1937.

[66] V. Lemanov and G. Smolenskiy, "Hypersonic waves in crystals," *Uspekhi Fizicheskikh Nauk*, vol. 108, no. 3, pp. 465–501, November 1972.

[67] S. Simons, "On the mutual interaction of parallel phonons," *Proceedings of the Physical Society*, vol. 82, no. 3, pp. 401–406, September 1963.

[68] S. McBride, H. Maris, and R. Truell, "Ultrasonic attenuation at microwave frequencies in aluminum oxide and ruby," *Journal of the Acoustical Society of America*, vol. 45, p. 1389, 1969.

[69] D. Stevens and H. Tiersten, "An analysis of doubly rotated quartz resonators utilizing essentially thickness modes with transverse variations," *Journal of the American Statistical Association*, vol. 79, no. 6, pp. 1811–1826, 1986.

[70] J. Nosek, "Drive level dependence of the resonant frequency in BAW quartz resonators and his modeling," *IEEE Transactions on Ultrasonics, Ferroelectrics and Frequency Control*, vol. 46, no. 4, pp. 823–829, July 1999.

[71] S. Galliou, F. Sthal, J. Boy, R. Bourquin, and M. Mourey, "Recent results on quartz crystal LD-cuts operating in oscillators," in *IEEE International Frequency Control Symposium*, August 2004, pp. 475–477.

[72] D. Nassour, "Influence des paramètres de construction sur le défaut d'isochronisme des résonateurs piézoéléctrique a simple ou double rotation," Ph.D. dissertation, University of Franche Comté, Besancon, France, May 1982.

[73] R. Bourquin, D. Nassour, and D. Hauden, "Amplitude frequency effect of SC-cut quartz trapped energy resonators," in *Proc. 36th Ann. Symp. on Freq. Cont.*, Philadelphia, USA, 1981, pp. 200–207.

[74] A. R. Kerr and M. Lambeth. Cryogenic (4K) measurements of some resistors and capacitors. [Online]. Available: http://www.gb.nrao.edu/electronics/edtn/edtn205.pdf

[75] G. Vasilescu, *Electronic noise and interfering signals: principles and applications*. Berlin, Germany: Springer-Verlag, 2005.

[76] E. Gutiérrez-D. and M. Deen, *Low temperature electronics: physics, devices, circuits and applications*. San Diego, CA, USA: Academic Press, 2001.

[77] M. Goryachev, S. Galliou, and P. Abbé, "Cryogenic transistor measurement and modeling for engineering applications," *Cryogenics*, vol. 50, pp. 381–389, 2010.

[78] V. Grassi, C. Colombo, and D. Camin, "Low frequency noise versus temperature spectroscopy of Si and Ge JFETs," in *Proc. of the 5th European Workshop on Low Temperature Electronics*, June 2000, pp. 37–44.

[79] P. Robertson and D. Dumin, "Ballistic transport and properties of submicrometer silicon MOSFET's from 300 to 4.2K," *IEEE Transactions on Electron Devices*, vol. 33, no. 4, pp. 494–498, 1986.

[80] B. Dierck, E. Simoen, S. Cos, J. Vermeiren, S. Claes, and G. Delerickl, "Anomalous kink-related excess noise in MOSFETs at 4.2K," *EEE Transactions on Electron Devices*, vol. 38, no. 4, pp. 907–912, 1991.

[81] R. Ward, R. Kirschman, M. Jhabvala, R. Babu, N. Das, D. Camin, V. Grassi, K. Kandiah, and J. Rosenberg, "Development of cryogenic Ge JFETs - III," in *Proc. of the 4th Workshop On Low Temperature Electronics*, June 2000.

[82] R. Kirschman, S. Lemoff, and J. Lipa, "Further evaluation of GaAs FETs for cryogenic readout," *SPIE Infrared Detectors and Instrumentation*, pp. 350–364, 1993.

[83] T. Cunninghamand and E. Fossum, "GaAs JFETs intended for deep cryogenic VL-WIR readout electronics," *Journal de Physique III*, vol. 4, pp. 147–152, 1994.

[84] J. Lee, "Recent developments in HEMT cryogenic low-noise amplifiers," 6.772 Final Project Presentation, 2003.

[85] L. Roschier and P. Hakonen, "Design of cryogenic 700 MHz HEMT amplifier," *Cryogenics*, vol. 44, pp. 783–788, 2004.

[86] J. Bautitsa, "Cryogenic HEMTs," *Low-Noise Systems*, vol. 3, pp. 6–8, 2006.

[87] M. Kiviranta, "SQUID readout and flux feedback based on a SiGe bipolar transistor at 4.2K," *Superconductor Science and Technology*, vol. 19, no. 12, pp. 1297–1302, 2006.

[88] J. Cressler and G. Niu, *Silicon-germanium heterojunction bipolar transistors*, 1st ed. Norwood: Artech House, 2003.

[89] F. Voisin, E. Bréelle, M. Piat, D. Prêle, G. Klisnick, G. Sou, and M. Redon, "Very low noise multiplexing with SQUIDs and SiGe heterojunction bipolar transistors for readout of large superconducting bolometer arrays," *Journal of Low Temperature Physics*, vol. 151, no. 3, pp. 1028–1033, 2007.

[90] J. Cressler, *Measurement and modeling of silicon heterostructure devices*, 1st ed. Boca Raton: CRC Press, 2008.

[91] C. Maiti and G. Armstrong, *Applications of silicon-germanium heterostructure devices*. Bristol: Institute of Physics Publishing, 2001.

[92] Q. Liang, R. Krithivasan, A. Ahmed, Y. Lu, Y. Li, J. Cressler, G. Niu, J. Rieh, G. Freeman, D. Ahlgren, and A. Joseph, "Analysis and understanding of unique cryogenic phenomena in state-of-the-art SiGe HBTs," *Solid-State Electronics*, vol. 50, no. 6, pp. 964–972, 2006.

[93] A. Shimunovich, P. Sakalas, M. Ramonas, M. Schroter, C. Jungemann, and W. Kraus, "Investigation of SiGe heterojunction bipolar transistor over an extreme temperature range," in *Proc. International Conference on Noise and Fluctuations*, Pisa, Italy, June 2009, pp. 309–312.

[94] M. Pospieszalski, "Extremely low-noise amplification with cryogenic FETs and HFETs: 1970-2004," *IEEE Microwave Magazine*, vol. 6, pp. 62–75, 2005.

[95] Infineon. Infineon webpage. [Online]. Available: http://www.infineon.com/cms/en/product/index.html

[96] Y. Jiahui, J. Cressler, Z. Chendong, C. Yan, N. Guofu, L. Qingqing, and A. Joseph, "An investigation of negative differential resistance and novel collector current kink effects in SiGe HBTs operating at cryogenic temperatures," *IEEE Transactions on Electron Devices*, vol. 54, no. 3, pp. 504–516, 2007.

[97] B. Woods, H. Mantooth, and J. Cressler, "SiGe HBT compact modeling for extreme temperatures," in *Proc. International Semiconductor Device Research Symposium*, December 2007, pp. 1–2.

[98] S. Haykin, *Neural networks - a comprehensive foundation*, 2nd ed. Ontario: Pearson Education, 2005.

[99] S. Weinreb, J. Bardin, and H. Mani, "Design of cryogenic SiGe low-noise amplifiers," *IEEE Transactions on Microwave Theory and Techniques*, vol. 55, no. 11, pp. 2306–2312, 2007.

[100] *5120A/5120A-01/5115A phase noise test set*, 276th ed., Symmetricom Corp., 2009.

[101] M. Goryachev, S. Galliou, P. Abbé, and V. Komine, "Oscillator frequency stability improvement by means of negative feedback," *IEEE Transactions on Ultrasonics, Ferroelectrics and Frequency Control*, vol. accepted, 2011.

[102] C. McNeilage, E. Ivanov, P. Stockwell, and J. Searls, "Review of feedback and feedforward noise reduction techniques," in *IEEE International Frequency Control Symposium*, 1998, p. 196.

[103] G. Bianchi, *Phase-locked loop synthesizer simulation.* New York: McGraw-Hill, 2005.

[104] Hewlett-Packard, "High-performance RF signal generators," 2011, a HP8643A, HP8644B, HP8664A, HP8665A, HP8665B.

[105] Y. Noguchi, Y. Teramachi, and T. Musha, "1/f frequency fluctuation of quartz crystal oscillator and temperature fluctuation," in *Annual Frequency Control Symposium*, 1981, pp. 484–491.

[106] R. E. Best, *Phase-locked loops: design, simulation and applications*, 5th ed. New York: McGraw-Hill, 2003.

[107] A. R. Conn, K. Scheinberg, and L. N. Vicente, *Introduction to derivative-free optimization.* Philadelphia: Society for Industrial and Applied Mathematics, 2009.

[108] Wenzel. (2011) Crystal oscillators. [Online]. Available: http://www.wenzel.com/oscillators.htm

[109] Pascal. (2011) Ultra low phase noise performance crystal oscillators. [Online]. Available: http://www.pascall.co.uk/

[110] D. B. Leeson, "A simple model of feed back oscillator noise spectrum," *Proc. IEEE*, vol. 54, no. 2, pp. 329–330, 1966.

[111] J. Gagnepain, J. Uebersfeld, G. Goujon, and P. Handel, "Relation between $1/f$ noise and Q-factor in quartz resonators at room and low temperatures, first theoretical interpretation," in *Proc. 35th Ann. Symp. on Freq. Cont.*, Ft. Monmouth, NJ, 1981, pp. 476–483.

[112] P. Handel, "Quantum approach to $1/f$ noise," *Phys. Rev.*, vol. 22A, pp. 745–757, 1980.

[113] ——, "Nature of $1/f$ frequency fluctuation in quartz crystal resonators," *Solid State Electronics*, vol. 22, pp. 875–876, 1979.

[114] P. Dutta and P. M. Horn, "Low-frequency fluctuations in solids: $1/f$ noise," *Rev. Mod. Phys.*, vol. 53, no. 3, pp. 497–516, 1981.

[115] L. Kiss and P. Heszler, "Handel's quantum $1/f$ noise model, based on quantum electrodynamics," *J. of Phys. C: Solid State Physics*, vol. 19, no. 27, pp. L631–L633, 1986.

[116] T. Nieuwenhuizen, D. Frenkel, and N. van Kampen, "Objections to Handel's quantum theory of $1/f$-noise," *J. of Phys. C: Solid State Physics*, vol. 35, pp. 2750–2753, 1987.

[117] M. Goryachev and S. Galliou, "Precision close-to-carrier phase noise simulation of BAW oscillators," *IEEE Transactions on Ultrasonics, Ferroelectrics and Frequency Control*, vol. 58, no. 1, pp. 6–9, January 2011.

[118] M. Goryachev, S. Galliou, and P. Abbé, "Oscillator phase noise modeling and optimization," in *Proc. 24th EFTF*, Noordwijk, Netherlands, April 2010.

[119] V. Besekersky and E. Popov, *Automatic control system theory.* Moscow, Russia: Professiya, 2004.

[120] W. Levine, *Control system fundamentals.* New York: CRC Press, 1999.

[121] J. Imbaud, S. Galliou, and P. Abbé, "Measurement of first langatate oscillators improved by an original simulating method," in *Proc. 22nd EFTF*, Toulouse, France, May 2008.

[122] G. Onwubolu and B. Babu, *New optimization techniques in engineering.* Berlin, Germany: Springer, 2004.

[123] R. Rhea, *Oscillator design and computer simulation*, 2nd ed. Atlanta: Noble Publishing Corporation, 1995.

[124] R. Quere, J. Nallatamby, A. Layec, and M. Prigent, "Low phase noise oscillator modeling in a system environment," *IEEE International Microwave Symposium Digest*, vol. 2, pp. 891–894, 2005.

[125] V. Kroupa, "Theory of $1/f$ noise - a new approach," *Physics Letters A*, vol. 336, pp. 126–132, 2005.

[126] S. Gribaldo, C. Chay, E. Tournier, and O. Llopis, "Experimental study of phase noise in FBAR resonators," *IEEE Transactions on Ultrasonics, Ferroelectrics and Frequency Control*, vol. 53, no. 11, pp. 1982–1987, November 2006.

[127] A. Howard, "Simulate oscillator phase noise," *Microwaves & RF*, p. 70, 1993.

[128] E. Marquardt, J. Le, and R. Radebaugh, "Cryogenic material properties database," in *11th International Cryocooler Conference*, Keystone, USA, June 2000.

[129] A. Grib, D. Heiert, R. Nawrodt, C. Schwardz, V. Grosse, P. Seidel, and I. Martin, "Acoustic losses in a thick quartz plate at low temperatures," *Journal of Applied Physics*, vol. 107, pp. 013 504–1–5, 2010.

[130] A. D. Armour, M. Blencowe, and K. Schwab, "Entanglement and decoherence of a micromechanical resonator via coupling to a Cooper-pair box," *Physical Review Letters*, vol. 88, no. 14, pp. 148 301–1–4, 2002.

[131] A. Cleland and M. Geller. Mechanical quantum resonators. [Online]. Available: http://web.physics.ucsb.edu/

[132] J. Hartnett, C. Locke, E. Ivanov, M. Tobar, and P. Stanwi, "Cryogenic sapphire oscillator with exceptionally high long-term frequency stability," *Applied Physics Letters*, vol. 89, pp. 203 513–1–3, 2006.

Résumé : Cette thèse présente des résultats de recherche sur des résonateurs acoustiques à ondes de volume travaillant à températures cryogéniques (de 3K à 15K dans un réfrigérateur à tube pulsé) ainsi que sur les systèmes construits autour de ces composants.
Le premier aspect concerne le fonctionnement de différents composants, dont en particulier le résonateur. Le comportement de ce dernier a fait l'objet d'une étude plus systématiquement sur la gamme de fréquence $[1-90$ MHz]. Des facteurs de qualité de $417 \cdot 10^6$ et des produit $Q \cdot f$ (facteur de qualité Q à la fréquence f) pouvant atteindre $3,07 \cdot 10^{16}$ Hz ont été mesurées pour les résonateurs à quartz, valeurs exceptionnelles qui sont des records mondiaux pour cette classe de composants. Il est montré que le facteur de qualité Q ne dépend pas de la fréquence f à ces températures, conformément à la théorie de Landau-Rumer. Les problèmes et avantages de travailler à de telles températures sont évalués. Les limitations qui s'y rattachent sont discutées. D'autres composants passifs ou actifs, tels que des transistors, sont aussi d'étudiés. Le choix des composants appropriés est fait sur la base de comparaisons de leur comportement à 4K. Les résultats sont confirmés par une modélisation d'amplificateurs cryogéniques, réalisée avec succès.
Le deuxième aspect mis en lumière dans ce travail est la modélisation et la simulation des composants et des systèmes étudiés. Le rapport présente un modèle rigoureux du bruit de phase des composants à onde acoustique de volume prenant en compte les non linéarités et basé sur la méthode de la moyenne. Ce modèle du résonateur, de type MIMO (multiple-input and multiple-output) est utilisé pour en déduire l'impact des différents paramètres d'un oscillateur sur son bruit de phase et expliquer les résultats expérimentaux. Les modèles établis pour les différents autres composants sont aussi utilisés pour simuler et optimiser des amplificateurs et oscillateurs cryogéniques.
Le troisième aspect concerne des sources de fréquence basées sur ces résonateurs à ondes de volume cryogéniques : référence passive et oscillateur cryogéniques. Les systèmes réalisés ont permis de mesurer et caractériser le bruit du résonateur dans des conditions spécifiques. Certaines sources de bruit ont ainsi été identifiées. Les systèmes à boucle d'asservissement testés ont une stabilité relative de fréquence de $4 \cdot 10^{-13}$ à 100 secondes et restent à mieux que $1 \cdot 10^{-12}$ entre 1 et 2000 s. L'oscillateur réalisé a une stabilité de $1.5 \cdot 10^{-12}$ à 200 s et meilleure que $1 \cdot 10^{-11}$ pour des temps d'intégration plus grands que 80 ms. Les limitations de ces systèmes sont discutées sur la base des données obtenues.
Mots-clés : hélium liquide, résonateurs acoustiques à ondes de volume, resonateurs à quartz, facteur de qualité, sensibilité thermique, référence passive de fréquence, oscillateur, electronique cryogénique, bruit de phase, optimisation de systèmes.

Abstract: This thesis presents the results of investigation of bulk-acoustic-wave (BAW) resonators working at cryogenic temperatures (over 3K-15K, in a pulse-tube cryocooler) along with the systems built with these devices.
The first aspect of the work is dedicated to the operation of different devices, and particularly the BAW resonators. Their behavior is more systematically studied over a frequency range of $1-90$ MHz. Quality factors of $417 \cdot 10^6$ and $Q \cdot f$-products (Q-factor at frequency f) up to $3.07 \cdot 10^{16}$ Hz have been measured for quartz resonators, outstanding values that are word records of this class of devices. It is shown that the intrinsic Q-factor does not depend of the frequency f, at these temperatures, in agreement with the Landau-Rumer theory. Problems and advantages of operating at such temperatures are assessed. Related limitations are discussed. Other passive and active electronic devices, such as transistors, are also under scope of this work. The choice of appropriate components is made based on comparison of their behavior at 4K. The results are confirmed with a successful design of liquid helium amplifiers.
The second aspect of the thesis is the modeling and simulation of the studied devices and systems. The report presents a rigorous model of the BAW device phase noise taking into account device nonlinearities based on the averaging approach. This MIMO (multiple-input and multiple-output) model is used to derive impacts of different oscillator parameters to its phase noise and to explain experimental results. Accurate models of other electronics devices working at liquid helium temperatures are also derived. They are used for simulation and optimization of cryogenic, oscillators, etc.
The third aspect concerns frequency sources based on these cryogenic BAW resonators: a cryogenic passive closed loop reference system and an oscillator. The implemented systems allowed measuring and characterizing the resonator phase noise at the given conditions. Thus, some noise sources have been identified. The tested feedback stabilization systems achieve fractional frequency stability of $4 \cdot 10^{-13}$ at 100 seconds and have stability better than 10^{-12} between 1 and 2000 seconds. The implemented oscillator exhibits frequency stability of $1.5 \cdot 10^{-12}$ at 200 seconds and better than 10^{-11} for averaging times greater than 80 ms. Limitations of these systems are discussed based on the obtained data.
Key words: liquid helium, BAW devices, quartz resonators, quality factor, temperature sensitivity, feedback frequency reference system, oscillator, cryogenic electronics, phase noise, system optimization.